University of Ljubljana

Faculty of Electrical Engineering

Helena Cindrič

Numerical modeling and treatment planning for clinical applications of electroporation

Numerično modeliranje in načrtovanje zdravljenja za klinične aplikacije elektroporacije

DOCTORAL DISSERTATION

Ljubljana, 2023

University of Ljubljana

Faculty of Electrical Engineering

Helena Cindrič

Numerical modeling and treatment planning for clinical applications of electroporation

DOCTORAL DISSERTATION

Mentor: Bor Kos, Ph.D

Ljubljana, 2023

Univerza v Ljubljani

Fakulteta za elektrotehniko

Helena Cindrič

Numerično modeliranje in načrtovanje zdravljenja za klinične aplikacije elektroporacije

DOKTORSKA DISERTACIJA

Mentor: doc. dr. Bor Kos

Ljubljana, 2023

PREFACE

This dissertation is the result of numerical modeling, data analysis, research and development related to electroporation-based tumor treatments. The work was carried out during the doctoral studies at the Laboratory of Biocybernetics, University of Ljubljana, Faculty of Electrical Engineering. The work is presented in the following six articles published in international journals:

- **Paper 1: H. Cindrič**, P. Mariappan, L. Beyer, P. Wiggermann, M. Moche, D. Miklavčič and B. Kos. Retrospective study for validation and improvement of numerical treatment planning of irreversible electroporation ablation for treatment of liver tumors, *IEEE Transactions on Biomedical Engineering*, vol. 68, no. 12, 2021.

- **Paper 2: H. Cindrič**, G. Gašljević, I. Edhemović, E. Brecelj, J. Žmuc, M. Čemažar, A. Seliškar, D. Miklavčič and B. Kos. Numerical mesoscale tissue model of electrochemotherapy in liver based on histological findings, *Scientific Reports*, vol. 12, no. 5476, 2022.

- **Paper 3:** F. H. Cornelis, **H. Cindrič**, B. Kos, M. Fujimori, E. N. Petre, D. Miklavčič, S. B. Solomon and G. Srimathveeravalli. Peri-tumoral Metallic Implants Reduce the Efficacy of Irreversible Electroporation for the Ablation of Colorectal Liver Metastases, *Cardiovascular Interventional Radiology*, vol. 43, no. 1, 2020.

- **Paper 4:** T. Jarm, T. Krmac, R. Magjarević, B. Kos, **H. Cindrič** and D. Miklavčič. Investigation of safety for electrochemotherapy and irreversible electroporation ablation therapies in patients with cardiac pacemakers, *Biomedical Engineering Online*, vol. 19, no. 85, 2020.

- **Paper 5: H. Cindrič**, B. Kos, G. Tedesco, M. Cadossi, A. Gasbarrini and D. Miklavčič. Electrochemotherapy of spinal metastases using transpedicular approach – A numerical feasibility study, *Technology in Cancer Research and Treatment*, vol. 17, 2018.
- **Paper 6: H. Cindrič**, D. Miklavčič, F. H. Cornelis and B. Kos. Optimization of transpedicular electrode insertion for electroporation-based treatments of spinal tumors, *Cancers*, vol. 14, iss. 21, no. 5412, 2022.

This research was supported by the Slovenian Research Agency (ARRS) under a Junior Researcher grant. Unless otherwise indicated, all illustrations are the work of the author.

Acknowledgements

I am deeply grateful to my mentor, Dr. Bor Kos. Thank you for your guidance, fruitful discussions, and invaluable advice, but most of all, thank you for your patience and for always being there for me when I needed help.

I would also like to thank Prof. Dr. Damijan Miklavčič for his continuous support during my PhD studies. Thank you for introducing me to the scientific world and giving me the opportunity to work on many interesting projects.

My special thanks to all the researchers and physicians with whom I worked on the papers included in this dissertation for providing the clinical data and sharing their invaluable knowledge.

I am sincerely grateful to my parents and Andraž for always being there for me and encouraging me to keep going even when things looked bleak.

Last but not least, I would like to thank all the great colleagues in the Laboratory of Biocybernetics, who made it a friendly and welcoming place to work.

Table of contents

Abstract

Electroporation is a phenomenon in which short high-voltage electric pulses are used to change the integrity of the cell membrane, thereby increasing membrane permeability. With appropriate choice of pulse parameters, the phenomenon can be reversible or irreversible. Both endpoints of electroporation are used in various clinical applications. Reversible electroporation is used in electrochemotherapy and gene electrotransfer, while irreversible electroporation is used for ablation of tumors in oncology and of cardiac tissue to treat atrial fibrillation and other arrhythmias.

Many aspects of the clinical applications of electroporation are still unresolved. Numerical models are an important tool for investigating the complex phenomena of electroporation. We can develop new treatment approaches, test new electrode designs, and analyze different clinical scenarios for their feasibility and safety. The use of numerical models also reduces the number of clinical and preclinical studies required to develop and guide the clinical treatment based on electroporation. However, before the models can be integrated into the clinical workflow, e.g., for treatment planning, they need to be validated in experiments and (pre)clinical studies.

One of the most important applications of numerical modeling is computer-assisted treatment planning. A prerequisite for the success of all electroporation-based treatments is the complete coverage of the clinical target volume with a sufficiently high electric field. Accurately determining the distribution of the electric field in the tissue, especially for deep-seated targets, is not a trivial task. Treatment planning based on patient-specific numerical models and optimization of treatment parameters, is advisable to ensure a successful treatment outcome.

Despite the technological advances, treatment planning is still not part of the routine clinical practice for electroporation-based treatments. The major limitation stems from the fact that treatment plans are currently based on preinterventional images, which can be several days or even weeks old. The development of real-time treatment planning using interventional imaging and actual electrode positions will allow real-time control of treatment parameters and outcome, and is a critical step toward introducing computer-assisted treatment planning into routine clinical practice.

The aim of this dissertation is to improve electroporation-based tumor treatments through numerical modeling and computer-assisted treatment planning. First, a brief introduction to the clinical applications of electroporation is given; then, the fundamentals of treatment planning are described, followed by an overview of the numerical approaches used in modeling the electroporation phenomenon. The main body of the dissertation consists of six original research papers published in international journals that comprise the work performed in the dissertation. The methodology and results are discussed in detail in the papers, therefore only the discussion and conclusions of the presented papers are summarized at the end of the dissertation.

Three original contributions to science are included in the dissertation. First, the numerical model of irreversible electroporation for the treatment of liver tumors was validated using real patient data. Second, the safety and efficacy aspects of electroporation-based treatments were numerically evaluated in risky clinical scenarios, such as near implanted pacemakers or in the presence of multiple metallic implants within the treatment zone. Third, an optimization algorithm for electrode placement was developed without using computationally intensive methods. The algorithm significantly reduces the time and expertise required to develop a treatment plan and is a step toward real-time treatment planning.

Key words: electroporation, electroporation-based treatments, numerical modeling, treatment planning, electrochemotherapy, irreversible electroporation, oncology, cancer treatment, tumor treatment

Razširjen povzetek v slovenščini

I Uvod

Elektroporacija je pojav, kjer s kratkimi visokonapetostnimi električnimi pulzi spremenimo strukturo celične membrane in s tem povečamo njeno prepustnost. Zunanje električno polje povzroči preureditev membranskih lipidov in s tem nastanek hidrofilnih por v membrani, kemične reakcije na membranskih lipidih in transportnih proteinih pa še dodatno prispevajo k povečanju prepustnosti membrane in omogočijo prehod ionom in molekulam, ki sicer težko ali pa sploh ne prehajajo celične membrane. Z ustrezno izbiro parametrov elektroporacije, predvsem števila in dolžine električnih pulzov ter amplitude dovedene napetosti, lahko prepustnost membrane spremenimo le začasno, kar imenujemo reverzibilna elektroporacija, ali pa trajno, kar imenujemo ireverzibilna elektroporacija. Pri reverzibilni elektroporaciji se membrane celic relativno hitro po koncu dovajanja pulzov povrnejo v prvotno stanje zato dolgoročno gledano ne zmanjšamo celične sposobnosti za delitev in delovanje. Pri ireverzibilni elektroporaciji pa celice ne morejo več popraviti membrane, kar povzroči izgubo celične funkcionalnosti in s tem celično smrt [1]–[4].

Elektroporacija ponuja številne možnosti uporabe na področjih medicine in biotehnologije [5]–[8]. V medicini se reverzibilna elektroporacija uporablja za vnos različnih molekul v celice, pri čemer sta trenutno najpomembnejši aplikaciji elektrokemoterapija in genska elektrotransfekcija [9]–[13]. Ireverzibilna elektroporacija se uporablja za ablacijo tumorjev in za ablacijo v srcu, in sicer za izolacijo pljučnih ven pri zdravljenju atrijske fibrilacije [14]–[23]. Splošno sprejeto je, da elektroporacija nastopi, ko lokalna jakost električnega polja v tkivu preseže pragovno vrednost, tj. prag reverzibilne ali ireverzibilne elektroporacije. Da dosežemo ustrezen terapevtski učinek moramo pri terapijah, ki temeljijo na elektroporaciji, zagotoviti dovolj visoko jakost polja v celotnem ciljnem volumnu

tkiva [24]. Razporeditev električnega polja v tkivu je odvisna predvsem od geometrije elektrod za elektroporacijo, strukture ter (električnih) lastnosti tkiva. Z leti so za različne aplikacije elektroporacije razvili različne modele elektrod ter protokole za dovajanje električnih pulzov.

I.1 Klinične aplikacije elektroporacije

I.1.1 Elektrokemoterapija

Elektrokemoterapija (EKT) je metoda, ki združuje kemoterapijo in reverzibilno elektroporacijo. Pri tipičnem protokolu zdravljenja z EKT najprej sistemsko ali lokalno injiciramo enkratno dozo kemoterapevtika; ko je koncentracija kemoterapevtika v tumorju najvišja, sledi dovajanje električnih pulzov v volumen tumorja [25], [26]. Reverzibilna elektroporacija poveča prepustnost membran rakavih celic, s čimer omogočimo prehod določenih kemoterapevtikov, kot sta na primer cisplatin in bleomicin, ki sicer težko ali pa sploh ne prehajajo skozi celično membrano. S tem močno povečamo znotrajcelično koncentracijo kemoterapevtika in posledično tudi njegovo citotoksičnost. Študije so pokazale, da lahko z reverzibilno elektroporacijo povečamo citotoksičnost kemoterapevtika cisplatin do osemdesetkrat [27], kemoterapevtika bleomicin pa od nekaj sto do tisočkrat [10], [28]. Za učinkovito zdravljenje je tako potreben manjši odmerek kemoterapevtika, s čimer se močno zmanjšajo stranski učinki terapije. Poleg povečane citotoksičnosti k učinkovitosti zdravljenja prispevata tudi povečan lokalni in sistemski imunski odziv ter zmanjšanje pretoka krvi v tumorju [29], [30].

Prvi in najbolj znan protokol dovajanja pulzov za EKT so leta 1991 predstavili Mir in sodelavci [9] in sestoji iz 8 pulzov dolžine 100 µs s ponavljalno frekvenco 1 Hz. Ta protokol se pri EKT uporablja še danes, vendar je v nekaterih klinično dostopnih pulznih generatorjih, kot je Cliniporator (IGEA S.P.A., Italija), prilagojen tako, da pulze namesto z 1 Hz dovajamo s ponavljalno frekvenco 5000 Hz. Električni pulzi povzročajo stimulacijo električno vzdržanih tkiv, kot so živci, mišice in srčna mišica, kar se odraža v obliki bolečine ter sunkovitega krčenja mišic. S povišanjem ponavljalne frekvence z 1 Hz na 5000 Hz bolnik občuti le en sam pulz, s čimer precej zmanjšamo neprijetne učinke terapije, hkrati pa

ne zmanjšamo učinkovitosti terapije [31], [32]. Visokonapetostni električni pulzi lahko povzročijo motnje srčnega ritma, zato je pri posegih v bližini prsnega koša dovajanje pulzov sinhronizirano z bolnikovim elektrokardiogramom (EKG) tako, da pulze dovedemo v fazi absolutne refraktorne dobe srca [33], [34]. Zaradi relativno enostavne tehnične izvedljivosti posega in dobrih kozmetičnih rezultatov se EKT uporablja predvsem za zdravljenje površinskih tumorjev. V zadnjem času pa je razvoj usmerjen tudi v zdravljenje globlje ležečih tumorjev, na primer v možganih, požiralniku, debelem črevesu, jetrih in kosteh [35]–[42].

I.1.2 Ablacija z ireverzibilno elektroporacijo

Ireverzibilna elektroporacija (IRE) se uporablja kot metoda ablacije različnih tumorjev in mehkih tkiv. V nasprotju s kemoterapijo, kjer želimo ohraniti funkcionalnost celic, pri ablaciji IRE stremimo k neposrednemu uničenju celic z električnim poljem. Učinkovitost ablacije je neposredno povezana z jakostjo lokalnega električnega polja v tkivu in s časom izpostavitve polju. Protokoli dovajanja pulzov se med študijami precej razlikujejo. Tipično se za ablacijo IRE na posamezen par elektrod dovede 70–100 pulzov dolžine 50–100 µs. Posamezne pulze dovajamo sinhronizirano z bolnikovim EKG, in sicer v fazi absolutne refraktorne dobe srca. Cilj zdravljenja z EKT je ireverzibilna elektroporacija celotnega kliničnega ciljnega volumna (tumorja z varnostnim robom) ter minimalno segrevanje tkiva in minimalni delež ireverzibilne elektroporacije v okoliškem zdravem tkivu.

V nasprotju z že uveljavljenimi termičnimi metodami ablacije, kot so ablacija z radijskimi in mikro valovi ter krioablacija, učinkovitost ablacije IRE ni odvisna od spremembe temperature tkiva. Metodo je zato mogoče uporabiti tudi v primerih, kadar termične poškodbe tkiva niso sprejemljive ali kadar je učinkovitost termičnih metod ablacije oslabljena, na primer zaradi prisotnosti velikih žil, ki prekomerno odvajajo toploto (ti. *heat sink* učinek) [33], [43]–[45]. Prednost ablacije IRE je tudi selektivnost metode; IRE uniči le membrane živih celic, preostale strukture in proteini v medceličnem prostoru pa ostanejo nepoškodovani, kar ohranja strukturo tkiva, zmanjša brazgotinjenje in omogoča hitrejšo regeneracijo tkiva [46].

Najnovejši razvoj na področju ireverzibilne elektroporacije je visokofrekvenčna

ireverzibilna elektroporacija, imenovana H-FIRE [47]–[49]. Električni pulzi, ki jih uporabljamo pri H-FIRE, se bistveno razlikujejo od pulzov, ki jih uporabljamo pri EKT in pri klasični ablaciji IRE. Tako imenovani bipolarni pulzi so sestavljeni iz dveh pulzov nasprotnih polaritet in premora med pulzi; dolžina posameznega pulza v paru je nekaj mikrosekund (1–10µs), ponavljalna frekvenca pulzov pa se giblje od 50 000 do 125 000 Hz. Zaradi krajših pulzov in višjih ponavljalnih frekvenc imajo bipolarni pulzi višji prag za stimulacijo vzdražnih tkiv (v primerjavi z monopolarnimi pulzi), s čimer se zmanjšajo mišične kotrakcije in bolečina [50]. Prav zato je H-FIRE še posebej obetavna metoda za ablacijo v srcu, in sicer za izolacijo pljučne vene pri zdravljenju atrijske fibrilacije [21]–[23], [51].

I.1.3 Genska elektrotransfekcija

Genska terapija z elektroporacijo oziroma genska elektrotransfekcija (GET) je terapija, kjer z električnimi pulzi v celice vnašamo tuj genski material – plazmidno DNK (pDNK). Namen terapije je spodbuditi proizvajanje novih proteinov ali izklop okvarjenih oziroma prekomerno izraženih genov [12], [52]–[54]. GET je večstopenjski proces, ki vključuje transport pDNK čez celično membrano, migracijo skozi citoplazmo, transport čez jedrno ovojnico in končno izražanje genov [55]. Najbolj razviti aplikaciji GET sta citokinska terapija za zdravljenje tumorjev, ter gensko cepljenje, pri katerem v mišice ali skozi kožo vnesemo pDNK, ki kodira določen antigen, in tako telo zaščitimo pred celicami, ki izražajo ta antigen [8].

Pri GET v tkivo najprej lokalno injiciramo genski material, kateremu sledi dovajanje električnih pulzov. V nasprotju s kemoterapevtiki pri EKT, molekule pDNK niso električno nevtralne in so prevelike, da bi v celice vstopile samo z difuzijo. Pri GET zato uporabljamo kombinacijo kratkih visokonapetostnih pulzov (dolžine nekaj mikrosekund) in dolgih nizkonapetostnih pulzov (dolžine nekaj milisekund). Kratki pulzi povzročijo permeabilizacijo celične membrane, dolgi pulzi pa z elektroforezno silo premaknejo negativno nabite molekule pDNK v bližino celične membrane. Zaradi elektroforezne sile pride v stik s celično membrano večje število molekul pDNK, kot bi bilo mogoče samo z difuzijo; na celični membrani tako nastanejo agregati pDNK, ki kasneje z endocitozo vstopijo v celice [54].

Optimalno doziranje genskega materiala ter protokoli dovajanja pulzov pri GET so še vedno predmet raziskav. Učinkovitost GET se namreč močno razlikuje med vrstami celic, odvisna pa je tudi od ciljnega volumna tkiva [54]. Ciljni volumen tkiva pri GET ni enostavno opredeljiv. Poleg tega (v nasprotju z EKT in ablacijo IRE) ireverzibilna elektroporacija v ciljnem volumnu ni dopustna, saj za uspešno transfekcijo potrebujemo žive celice.

I.2 Načrtovanje zdravljenja

Učinkovitost terapij, ki temeljijo na elektroporaciji, je neposredno odvisna od pokritja kliničnega ciljnega volumna (CTV, ang. *clinical target volume*) z ustrezno visokim električnim poljem – nad pragom reverzibilne ali ireverzibilne elektroporacije. V onkologiji CTV tipično obsega tumor s pasom zdravega tkiva okoli mase tumorja -– varnostni pas širine od 5 do 10 mm. Poenostavljeno gledano je elektroporacija pragovni pojav. Pri zdravljenju zato stremimo k pokritju celotnega CTV z jakostjo električnega polja nad pragom reverzibilne elektroporacije pri EKT in GET oziroma nad pragom ireverzibilne elektroporacije pri ablaciji IRE.

Pri zdravljenju površinskih tarč, kot je recimo kožni rak, za dovajanje električnih pulzov uporabljamo aplikatorje s fiksnimi elektrodami. Pri tej vrsti elektrod lahko spreminjamo le dolžino; tudi parametri pulzov so priporočeni s strani proizvajalca in jih v večini primerov ne spreminjamo. Površinski posegi so tehnično nezahtevni in sestojijo iz zaporednih dovajanj pulzov z aplikatorjem, tako da pokrijemo celoten CTV. V večini primerov ne potrebujemo predoperativnega načrtovanja zdravljenja, saj so tarče dobro vidne. Pri minimalno invazivnem zdravljenju globoko ležečih tarč, kot so recimo tumorji v jetrih, uporabljamo samostojne dolge igelne elektrode. Vstavitev elektrod je veliko bolj zahtevna kot pri aplikatorju in zahteva izkušenega intervencijskega radiologa [56]–[58]. V skladu z navodili proizvajalcev pulznih generatorjev je potrebno elektrode namestiti popolnoma vzporedno in na enako globino v telesu. Ta zahteva sicer ni pogoj za uspešno zdravljenje, vendar omogoča boljše predvidevanje nastalega električnega polja, saj je razporeditev električnega polja v tkivu močno odvisna od geometrije elektrod.

V praksi je idealno postavitev elektrod praktično nemogoče doseči; omejuje nas anatomija telesa (npr. kosti), izogniti se moramo občutljivim anatomskim strukturam, poleg tega pa se dolge tanke igelne elektrode pogosto upogibajo med vstavitvijo. Vsaka napaka pri postavitvi elektrod vpliva na porazdelitev električnega polja. Poleg geometrije elektrod na porazdelitev električnega polja v CTV vplivajo tudi sestava tkiva ter negotovost glede električnih lastnosti tkiva, ki se poleg tega med posameznimi tkivi tudi močno razlikujejo. Določanje porazdelitve električnega polja v globoko ležečih tarčah ni trivialna naloga, zato je priporočljiva uporaba računalniško podprtega načrtovanja zdravljenja [59]–[61]. Pri uporabi le-tega tudi ni potrebno, da so elektrode popolnoma vzporedne, s čimer so posegi tehnično manj zahtevni in omejujoči.

Računalniško podprto načrtovanje zdravljenja temelji na izdelavi bolnikom prilagojenih numeričnih modelov, in sicer na podlagi bolnikovih medicinskih slik. Cilj je določiti optimalno postavitev elektrod in parametre električnih pulzov, tako da zanesljivo pokrijemo CTV z dovolj visokim električnim poljem, pri čemer ne poškodujemo okoliškega zdravega tkiva. Zagotoviti moramo tudi tehnično izvedljivost posega za izbrano postavitev elektrod in parametre. Trenutno sta na voljo dve spletni orodji za izdelavo bolnikom prilagojenih načrtov zdravljenja z elektroporacijo, in sicer Visifield (www.visifield.com, Univerza v Ljubljani, Slovenija), implementiran leta 2015 [62], [63], in PIRET, implementiran leta 2022 [64]. Obe orodji omogočata izgradnjo bolnikom prilagojenih modelov na podlagi medicinskih slik ter izračun električnega polja v tkivu z metodo končnih elementov; orodje PIRET vključuje tudi izračun segrevanja tkiva. Orodji nista certificirani za uporabo v kliničnem okolju, zato se lahko uporabljata le za raziskovalne namene. Obe orodji omogočata izdelavo hipotetičnega načrta zdravljenja, vendar ne ponujata možnosti optimizacije izbranih parametrov; ocenitev ustreznosti načrta je izključno na strani uporabnika.

Trenutno pripravljamo načrte zdravljenja nekaj dni pred posegom, zato za izdelavo modelov uporabimo predoperativne slike bolnikov (MR ali CT). Na medicinskih slikah najprej izvedemo proces razgradnje, s čimer pridobimo maske pomembnih tkiv, na primer tumorja, zdravega okoliškega tkiva in žil (Slika I.1 A). Na podlagi mask tkiv nato zgradimo anatomsko pravilen 3D model (Slika I.1 B), ki ga uvozimo v program za računanje z metodo končnih elementov, na primer COMSOL Multiphysics (www.comsol.com, Comsol Inc, Švedska). Vsaki

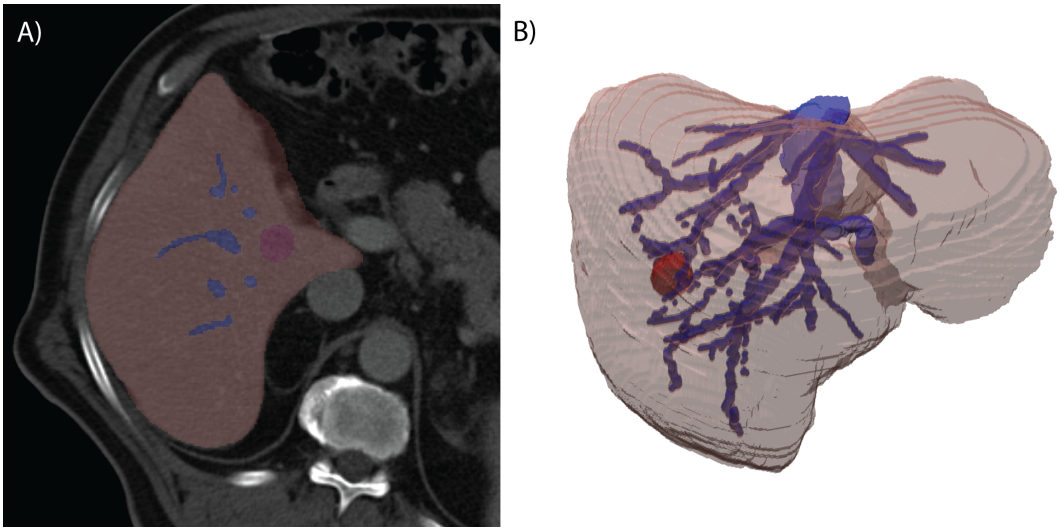

Slika I.1: A) Primer razgradnje abdominalne CT slike na maske ciljnih tkiv – jetra (rožnata), tumor (rdeča), žile (modra). B) Bolniku prilagojen anatomsko pravilen 3D model jeter s tumorjem in žilami, zgrajen iz mask ciljnih tkiv.

vrsti tkiva v modelu pripišemo električne in termične lastnosti, tako da model čim bolje odraža fizikalne lastnosti tkiva.

V naslednjem koraku moramo določiti položaje elektrod ter parametre pulzov, pri čemer moramo upoštevati potencialne anatomske in tehnične omejitve. Pri izbiri optimalnega položaja elektrod moramo določiti najboljšo pot vstavitve, njihovo končno število in položaj glede na CTV ter dolžino elektrod. Pri izbiri parametrov pulzov je najpomembnejši parameter amplituda pulzov, dovedenih na specifični par elektrod. Število in dolžina pulzov sta odvisna od vrste terapije (npr. EKT ali ablacija IRE), zato teh parametrov navadno ne optimiziramo.

Razporeditev električnega polja v modelu izračunamo z metodo končnih elementov. Metode, ki jih uporabljamo pri modeliranju elektroporacije, so podrobneje opisane v poglavju I.3 *Numerični modeli elektroporacije*. Končni načrt zdravljenja obsega grafični prikaz vstavitvene trajektorije in končnih položajev elektrod glede na CTV, izbrane amplitude napetosti in predvidene električne tokove za vsak aktiven par elektrod ter pričakovano pokritje CTV z električnim poljem nad izbrano pragovno vrednostjo. Za boljšo vizualizacijo lahko predvideno razporeditev električnega polja v tkivu prikažemo neposredno na medicinskih slikah, kot je prikazano na Sliki I.2. Načrt zdravljenja lahko združimo z navigacijskimi

ali robotskimi sistemi, kar omogoča hitrejšo in natančnejšo namestitev elektrod [65]–[67].

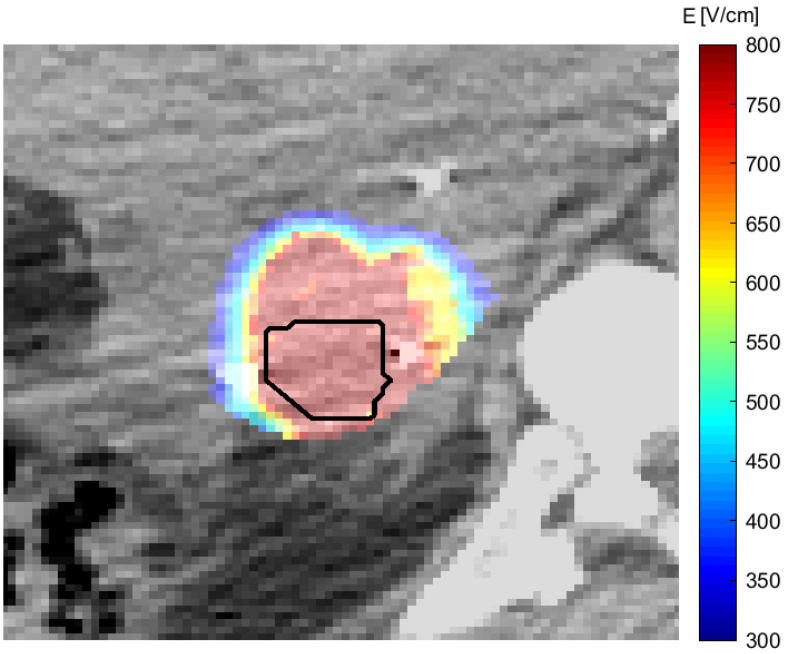

Slika I.2: Izračunano razporeditev električnega polja lahko prikažemo neposredno na medicinskih slikah. Masa tumorja je prikazana s črno. Zaradi boljše vidljivosti je električno polje skalirano na območje 300–800 V/cm, ki predstavlja območje, kjer pričakujemo reverzibilno oziroma ireverzibilno elektroporacijo v jetrih.

Računalniško podprto načrtovanje zdravljenja žal še vedno ni del klinične rutine in se zaenkrat uporablja v redkih raziskovalnih skupinah kot vodilo za intervencijske radiologe. Trenutno načrte zdravljenja večinoma pripravljamo ročno. Proces je dolgotrajen in poteka v več iteracijah, kjer po vsaki iteraciji preverimo izračunano razporeditev električnega polja v tkivu in pokritje CTV z ustrezno visokim električnim poljem, identificiramo nepokrite dele CTV ter ustrezno popravimo položaje elektrod. Tak način načrtovanja zahteva visoko raven znanja o razporeditvi polja v nehomogenem tkivu ter o vplivu položajev elektrod in parametrov pulzov na polje, zato je priprava načrtov večinoma še vedno v domeni inženirjev. Poskusi avtomatizacije postopka načrtovanja so do sedaj temeljili na uporabi genetskih algoritmov ali parametričnih študij [60], [68], [69]. Obe metodi sta časovno izredno potratni in zahtevata računalniške kapacitete, ki presegajo zmožnosti kliničnega okolja.

Ker se načrti zdravljenja pripravljajo nekaj dni pred posegom, je njihova uporabnost za intervencijske radiologe vprašljiva, saj je izredno težko postaviti elektrode popolnoma v skladu s predoperativnim načrtom. Uspešnost terapije je neločljivo povezana z razporeditvijo električnega polja v tkivu, zato vsaka napaka pri postavitvi elektrod vnaša negotovost. Uporaba sistemov za navigacijo izboljša natančnost postavitve elektrod, vendar je študij, kjer je numerično načrtovanje zdravljenja združeno s sistemi za navigacijo, le peščica [65], [66]. Če želimo računalniško podprto načrtovanje vpeljati v klinično prakso, moramo omogočiti načrtovanje v realnem času – na licu mesta, z dejanskimi položaji elektrod; le tako lahko nadzorujemo in ustrezno popravljamo parametre zdravljenja. Načrtovanje v realnem času zahteva robustne in predvsem hitre modele. Ročni postopek in uporaba genetskih algoritmov za načrtovanje v realnem času nista primerna, saj sta obe metodi časovno preveč potratni. Potreben je razvoj hitrih in enostavnih optimizacijskih algoritmov, ki lahko poenostavijo in pospešijo načrtovanje zdravljenja za terapije, ki temeljijo na elektroporaciji.

I.3 Numerični modeli elektroporacije

I.3.1 Statični modeli

Numerični modeli elektroporacije temeljijo na izračunu razporeditve električnega polja v tkivu. Tipično najprej rešimo Laplaceovo parcialno diferencialno enačbo (PDE) za električni potencial V (I.1), električno polje E pa nato izračunamo kot gradient potenciala (I.2) [70]–[72].

$$\nabla \cdot (\sigma \nabla V) = 0, \tag{I.1}$$

$$E = -\nabla V. \tag{I.2}$$

Enačbo I.1 lahko rešujemo v stanju ravnovesja (predpostavljamo, da električni pulzi trajajo neskončno dolgo), saj pri večini terapij, temelječih na elektroporaciji, uporabljamo pulze dolžine 50-100 µs, kjer pričakujemo, da vsi prehodni pojavi elektroporacije izzvenijo dolgo pred koncem pulza. Pojav elektroporacije je v model vključen preko nelinearne funkcije odvisnosti električne prevodnosti σ od jakosti lokalnega električnega polja v tkivu [70], [73]–[77].

Leta 2005 so Šel in sodelavci [70] predstavili prvi eksperimentalno podprt sekvenčni model elektroporacije, v katerem je odvisnost električne prevodnosti od jakosti električnega polja opisana s sigmoidno funkcijo. Če lokalna jakost električnega polja v tkivu preseže prag za reverzibilno elektroporacijo, se prevodnost tkiva poveča od izhodiščne vrednosti v odvisnosti od jakosti polja. Če električno polje preseže določen prag, se prevodnost poveča do največje vrednosti in se z dovedenim električnim poljem ne povečuje več [78]. Danes v večini modelov za opis povečanja prevodnosti uporabljamo takšno ali drugačno obliko sigmoidne funkcije [79]:

$$\sigma(E) = \sigma_0 \cdot (1 + sigmoid(E, E_1, E_2, A)), \tag{I.3}$$

kjer je E lokalno električno polje v tkivu, σ_0 izhodiščna električna prevodnost tkiva, E_1 prag električnega polja, pri katerem se prevodnost začne povečevati, E_2 prag električnega polja, pri katerem se prevodnost neha povečevati in A faktor največjega povečanja prevodnosti pri električnih poljih nad E_2.

Slika I.3 prikazuje primer nelinearne odvisnosti prevodnosti od električnega polja. Različna tkiva imajo zelo različne lastnosti in odziv na električno polje, zato se dinamika povečanja prevodnosti razlikuje od tkiva do tkiva. Parametri sigmoidne funkcije, in sicer σ_0, E_1, E_2 in A v enačbi I.3, so odvisni od tkiva [24], [76]. Poleg tega so študije pokazale, da sta lahko parametra E_1 in A odvisna tudi od števila pulzov [77].

I.3.2 Modeli časovne odvisnosti

V novejših študijah je pri modeliranju elektroporacije vključeno tudi segrevanje tkiva, kar zahteva izračun v časovni domeni. Medtem ko pri reverzibilni elektroporaciji termična komponenta ni posebej izrazita, pa pri ablaciji IRE v tkivo dovedemo na stotine pulzov, kar povzroči znatno Joulovo segrevanje v bližini elektrod in lahko vpliva na varnost terapije [43], [81]–[83]. Modeli v časovni domeni omogočajo tudi modeliranje različnih oblik pulzov, npr. monopolarnih, bipolarnih, eksponentnih pulzov, in dinamike dovajanja pulzov, npr. različne dolžine pulzov, zakasnitve med pulzi in ponavljalne frekvence [84]–[86]. To je pomembno za razvoj novih pulznih protokolov, na primer za H- FIRE, ali za preučevanje mehanizmov elektroporacije, npr. elektrokemičnih reakcij med dovajanjem pulzov.

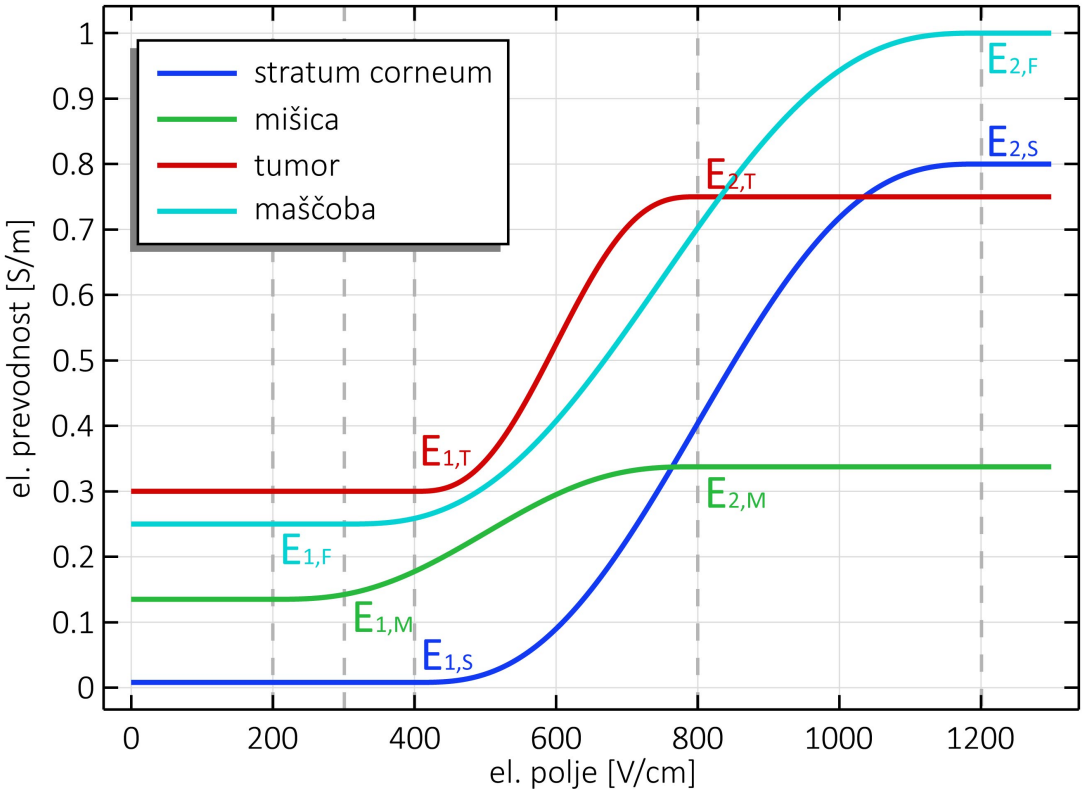

Slika I.3: Učinek elektroporacije na električno prevodnost različnih tkiv lahko opišemo s sigmoidnimi funkcijami. Izhodiščna prevodnost se začne povečevati, ko uporabljeno električno polje preseže prag za reverzibilno elektroporacijo, in doseže najvišjo vrednost polje preseže prag za ireverzibilno elektroporacijo. Reverzibilna (E1) in ireverzibilna (E2) mejna vrednost sta označeni s črtkano črto (S – rožena plast, M – mišica, T – tumor, F – maščoba). Slika je povzeta po [80].

Segrevanje tkiva med elektroporacijo najpogosteje opišemo s prilagojeno Pennesovo enačbo prenosa toplote v tkivu (I.4) [87], [88]:

$$\rho C \frac{\partial T}{\partial t} = \nabla(k \nabla T) + Q_{bio} + \sigma \left|E\right|^2 , \tag{I.4}$$

kjer so ρ, C in k gostota, toplotna kapaciteta in toplotna prevodnost tkiva, T je temperatura tkiva, t pa čas. Izraz za vir biološke toplote Q_{bio} vključuje prekrvitev in presnovno aktivnost tkiva, izraz $\sigma \left|E\right|^2$ pa predstavlja Joulovo segrevanje tkiva.

Dvig temperature tkiva vpliva tudi na električno prevodnost. Razmerje med prevodnostjo in temperaturo je običajno opisano z linearno enačbo (I.5), ki pred-

postavlja konstanten temperaturni koeficient [89], [90]:

$$\sigma(T) = \sigma_0 \cdot (1 + \alpha_T \cdot \Delta T), \tag{I.5}$$

kjer je α_T temperaturni koeficient, ΔT temperaturna razlika glede na začetno temperaturo tkiva in σ_0 izhodiščna električna prevodnost.

Dvig temperature lahko poveča električno prevodnost celo nad njeno največjo vrednost, ki jo povzroči lokalno električno polje (I.3). Dinamična električna prevodnost tkiva je torej funkcija električnega polja in temperature. Primer modeliranja te soodvisnosti je naslednja kombinacija enačb I.3 in I.5:

$$\sigma(E, T) = \sigma(E) \cdot (1 + \alpha_T \cdot \Delta T), \tag{I.6}$$

kjer $\sigma(E)$ predstavlja nelinearno povečanje zaradi učinka elektroporacije (I.3). Ob upoštevanju kombiniranega učinka elektroporacije in segrevanja postane prevodnost tkiva σ v Laplaceovi PDE (I.1) in v Pennesovi enačbi (I.4) nelinearna funkcija električnega polja in temperature $\sigma(E, T)$. V literaturi zasledimo tudi druge pristope k modeliranju kombiniranih termičnih in elektroporacijskih učinkov, saj je oba mehanizma med seboj težko z gotovostjo razmejiti [77], [91].

I.3.3 Statistični modeli

Statistični modeli predstavljajo še en možen pristop za določanje odziva tkiva na elektroporacijo. Namesto da bi učinkovitost zdravljenja ovrednotili na podlagi praga električnega polja, izračunamo statistično verjetnost preživetja celic pri določeni izpostavitvi polju. Pri modeliranju elektroporacije se najpogosteje uporablja model Peleg-Fermi [57], [92]–[95]. Verjetnost preživetja celic S in verjetnost celične smrti P izračunamo na naslednji način:

$$S(E, n) = \frac{1}{1 + exp\left(\frac{E - E_c(n)}{B(n)}\right)}, \tag{I.7}$$

$$P(E, n) = 1 - S(E, n), \tag{I.8}$$

kjer je n število pulzov, E je lokalno električno polje, E_c je kritično električno polje, pri katerem umre 50 % prizadetih celic, B pa je faktor oblike, ki določa velikost prehodnega območja.

Parametra E_c in B sta funkciji števila pulzov in ju je potrebno eksperimentalno določiti za vsako tkivo posebej. Narava računa verjetnosti omogoča medsebojni produkt različnih verjetnosti, s čimer dobimo nižjo verjetnost preživetja celic. To lahko s pridom uporabimo v primerih, ko je tkivo kumulativno izpostavljeno pulzom iz različnih parov elektrod; ob daljši izpostavljenosti električnemu polju se namreč zniža verjetnost preživetja celic.

Verjetnost celične smrti zaradi termičnih poškodb lahko določimo s časovno integracijo Arrheniusove konstante reakcijske hitrosti (I.9), ki jo pretvorimo v verjetnost celične smrti P (I.10):

$$\Omega(t) = \int_0^{t_{end}} \zeta \cdot exp\left(\frac{-E_a}{R \cdot T(t))}\right) dt, \tag{I.9}$$

$$P = 100 \cdot \left(1 - e^{-\Omega(t)}\right), \tag{I.10}$$

kjer ζ predstavlja frekvenčni predfaktor, E_a je aktivacijska energija, R je univerzalna plinska konstanta, P pa je verjetnost celične smrti, izražena v odstotkih.

I.4 Namen doktorske disertacije

Namen doktorske disertacije je izboljšati zdravljenje z elektroporacijo s pomočjo numeričnega modeliranja in računalniško podprtega načrtovanja zdravljenja. Numerični modeli so pomembno orodje za analizo kompleksnih interakcij v biološkem tkivu med elektroporacijo. Omogočajo nam raziskovanje novih pristopov zdravljenja, preizkušanje novih oblik elektrod ter analizo različnih kliničnih scenarijev z vidika izvedljivosti in varnosti. Računalniški eksperimenti z numeričnimi modeli omogočajo preizkušanje velikega števila parametrov in lahko tako usmerjajo poskuse, kar lahko bistveno zmanjša število poskusov ali predkliničnih testov in pospeši razvoj terapij, ki temeljijo na elektroporaciji.

Ena najpomembnejših aplikacij numeričnega modeliranja je računalniško podprto načrtovanje zdravljenja. Predpogoj za uspeh vseh terapij, ki temeljijo na elektroporaciji, je popolna pokritost kliničnega ciljnega volumna z dovolj visokim električnim poljem. Natančna določitev porazdelitve električnega polja v tkivu,

zlasti za globoko ležeče tarče, ni enostavna naloga. Za zagotovitev uspešnega izida zdravljenja je priporočljivo načrtovanje zdravljenja, ki temelji na bolnikom prilagojenih numeričnih modelih in optimizaciji parametrov zdravljenja.

Preden lahko numerične modele uporabimo v dejanskih kliničnih aplikacijah, npr. za načrtovanje zdravljenja, jih je potrebno validirati z eksperimenti in (pred)kliničnimi podatki. Namen te disertacije je bil validirati razviti numerični model ireverzibilne elektroporacije v jetrih z uporabo dejanskih kliničnih podatkov. Cilj validacije je določiti sposobnost razvitega numeričnega modela za napovedovanje rezultatov zdravljenja ter zagotoviti, da je dovolj zanesljiv in natančen za klinične potrebe, da ga lahko uporabimo za načrtovanje zdravljenja v rutinski klinični praksi.

Številni vidiki kliničnih aplikacij elektroporacije še niso ustrezno raziskani; npr. toplotni učinek ireverzibilne elektroporacije še ni temeljito kvantificiran, prisotnost vsadkov s kovinskimi deli pa še vedno velja za kontraindikacijo za zdravljenje z elektroporacijo. Z numeričnimi modeli bomo raziskali izvedljivost ter varnostni vidik elektrokemoterapije in ablacije z ireverzibilno elektroporacijo v različnih in potencialno nevarnih kliničnih situacijah, z namenom izboljšanja varnosti in dostopnosti zdravljenja z elektroporacijo.

Kljub tehnološkemu napredku računalniško podprto načrtovanje zdravljenja še vedno ni del rutinske klinične prakse pri zdravljenju z elektroporacijo; glavna omejitev izhaja iz dejstva, da se načrti trenutno izdelujejo pred posegom. Razvoj načrtovanja zdravljenja v realnem času z uporabo dejanskih položajev elektrod bo omogočil neposreden nadzor parametrov zdravljenja in izida zdravljenja v realnem času, kar je ključni korak k uvedbi računalniško podprtega načrtovanja zdravljenja v rutinsko klinično prakso. Namen disertacije je raziskati načine, kako narediti numerične modele in postopke načrtovanja zdravljenja dovolj hitre in robustne, da bi jih sčasoma lahko uporabljali v realnem času.

II Znanstveni članki

Delo, opravljeno med doktorskim študijem, je predstavljeno v šestih izvirnih znanstvenih člankih, objavljenih v mednarodnih revijah. Metodologija in rezultati so podrobno predstavljeni in obravnavani v člankih. V sklopu razširjenega povzetka v slovenskem jeziku so povzeti razprave in zaključki vsakega od člankov.

Cilj prvega članka [96] je bil validirati numerični model za načrtovanje zdravljenja na osnovi elektroporacije z uporabo kliničnih podatkov. V ta namen smo numerično rekonstruirali 18 kliničnih primerov ablacije tumorjev v jetrih z ireverzibilno elektroporacijo (ablacija IRE) in izračunali izid zdravljenja z dopolnjenim numeričnim modelom za načrtovanje zdravljenja. Rezultate simulacije smo primerjali s kliničnim odzivom v tkivu, kot ga vidimo na kontrolnih slikah MR, zajetih šest tednov po posegu. Določili smo prag električnega polja *in silico*, ki je najbolj ustrezal uspešni ablaciji ciljnega tkiva *in vivo*, vidni na kontrolnem slikanju. Ovrednotili smo tudi stopnjo segrevanja tkiva pri ablaciji IRE in pokazali uporabnost načrtovanja zdravljenja za izboljšanje zdravljenja. V tej študiji smo razvili in izpopolnili sofisticirano metodo za validacijo numeričnega modela za načrtovanje zdravljenja z ablacijo IRE. Na podlagi rezultatov študije lahko zasnujemo prospektivno klinično študijo, s katero lahko pridobimo potrebne podatke za nadaljnjo validacijo modela ter zagotovitev zadostne natančnosti za klinične potrebe.

V drugem članku [97] smo raziskovali, kako heterogena zgradba jetrnega parenhima vpliva na porazdelitev električnega polja med elektrokemoterapijo (EKT). Razvili smo model jeter na mezo nivoju, ki vključuje jetrne makro- in mikrostrukture in je primerljiv z mikroskopskimi vzorci tkiva. Numerično smo rekonstruirali štiri posege EKT v zdravih prašičjih jetrih, izvedene v nedavni *in*

vivo študiji [98]. Porazdelitev električnega polja in segrevanje tkiva smo izračunali z numeričnim modelom za načrtovanje zdravljenja na osnovi elektroporacije ter polje primerjali s histopatološkimi spremembami, opaženimi na mikroskopskih vzorcih tkiva. Izvedli smo parametrično študijo, kjer smo raziskali, ali vključitev mikrostruktur jetrnega parenhima v model in variabilnost njihovih električnih lastnosti vplivajo na porazdelitev električnega polja na nivoju, ki je pomemben za primerjavo z mikroskopskimi vzorci. Poleg tega smo določili pragove električnega polja, ki se najbolje ujemajo s histopatološkimi spremembami, opaženimi v tkivu po EKT. Izračunali smo tudi stopnjo segrevanja tkiva pri EKT in verjetnost nastanka termičnih poškodb tkiva, pri čemer smo se osredinili zlasti na občutljive anatomske strukture.

Iz varnostnih razlogov so terapije, ki temeljijo na elektroporaciji, kontraindicirane pri bolnikih, ki imajo v bližini kliničnega ciljnega volumna prisotne kovinske vsadke, kot so srčni spodbujevalniki in kirurške sponke. Kovinski vsadki imajo veliko višjo električno prevodnost kot biološko tkivo in lahko vplivajo na porazdelitev in jakost električnega polja pri elektroporaciji ter na segrevanje tkiva. V tretjem članku ([99] smo raziskovali učinke kovinskih kirurških sponk v bližini območja ablacije na varnost in učinkovitost ablacije IRE kolorektalnih metastaz v jetrih (CRLM). Raziskava je sestavljena iz dveh delov. Prvi del obsega retrospektivno statistično analizo 25 bolnikov z CRLM zdravljenih z ablacijo IRE. Identificirali smo parametre, med drugim tudi prisotnost kovinskih kirurških sponk v bližini področja ablacije, ki so kandidati za determinante lokalnega napredovanja tumorja po ablaciji IRE. Drugi del študije je obravnavan v tej disertaciji. Podskupino osmih bolnikov, štirih s kovinskimi sponkami v neposredni bližini tumorja in štirih brez sponk, smo analizirali z uporabo numeričnih modelov. Izdelali smo bolnikom prilagojene modele ter numerično ovrednotili vpliv sponk na lokalno porazdelitev električnega polja, segrevanje tkiva in verjetnost celične smrti.

Četrti članek [100] nadalje raziskuje prisotnost kovinskih vsadkov v bližini območja zdravljenja. V tej študiji smo obravnavali dve vprašanji: ali lahko elektroporacijski pulzi zmotijo delovanje vsajenega srčnega spodbujevalnika in ali lahko kovinsko ohišje srčnega spodbujevalnika vpliva na razporeditev električnega polja v tkivu in s tem ogrozi učinkovitost in varnost terapije. Drugo vprašanje smo raziskali s pomočjo numeričnega modeliranja fizikalnih pogojev, ki jih pričakujemo pri elektroporaciji v bližini vsajenega srčnega spodbujevalnika, in

je obravnavano v tej disertaciji. Raziskali smo dve metodi zdravljenja podkožnega tumorja v bližini vsajenega srčnega spodbujevalnika: elektrokemoterapijo in ablacijo IRE. Pri obeh metodah smo preučili tri scenarije: vpliv spodbujevalnika, če je kovinsko ohišje v električnem stiku z eno izmed elektrod; vpliv spodbujevalnika, ki je v bližini tumorja, a ni v stiku z elektrodami; kontrolni scenarij brez prisotnosti srčnega spodbujevalnika.

V petem članku [101] smo zasnovali nov pristop za zdravljenje tumorjev v hrbtenici, tj. transpedikularni pristop, ki združuje elektrokemoterapijo z že uveljavljenimi tehnikami vstavljanja pedikularnih vijakov za stabilizacijo hrbtenice. Z numeričnim modeliranjem smo raziskali izvedljivost in varnost novega pristopa zdravljenja. Študija temelji na treh kliničnih primerih tumorjev v hrbtenici z različnimi stopnjami vpletenosti hrbteničnega kanala. Za vse tri primere smo ustvarili bolnikom prilagojene numerične modele ter pripravili načrt zdravljenja s transpedikularnim pristopom. Izračunali smo porazdelitev električnega polja v tumorju in okoliškem tkivu ter določili predviden izid zdravljenja in morebitne poškodbe hrbtenjače in živcev. Študija prikazuje, kako je mogoče numerično modeliranje uporabiti za raziskovanje novih pristopov zdravljenja.

V šestem članku [102] je predstavljen algoritem za optimizacijo položajev elektrod (in napetosti) na podlagi prostorske informacije o porazdelitvi električnega polja v kliničnem ciljnem volumnu (CTV). Postopek načrtovanja zdravljenja je v glavnem sestavljen iz določanja najboljših možnih položajev elektrod in amplitud napetosti, s katerimi zagotovimo pokritje in s tem terapevtski učinek v celotnem CTV. Postopek načrtovanja se večinoma še vedno izvaja ročno, kar zahteva visoko raven strokovnega znanja ali uporabo računsko zahtevnih genetskih algoritmov. V tej študiji smo razvili algoritem za avtomatsko določitev položajev elektrod za EKT tumorjev v hrbtenici brez uporabe računalniško intenzivnih metod. Z uporabo algoritma se čas in strokovno znanje uporabnika, ki sta potrebna za izdelavo načrta zdravljenja, znatno zmanjšata.

III Razprava

III.1 Validacija modela ablacije tumorjev v jetrih z ireverzibilno elektroporacijo

Veliko število parametrov v kompleksnih numeričnih modelih uvaja določeno stopnjo negotovosti, zato je treba validirati natančnost in robustnost modelov, preden jih je mogoče uporabiti za klinične aplikacije. Prvi del mojega doktorskega študija je bil posvečen validaciji numeričnega modela ablacije tumorjev v jetrih z ireverzibilno elektroporacijo (ablacija IRE) na podlagi obstoječih kliničnih podatkov; rezultati razsikave so predstavljeni v prvem članku (Cindrič *et al* 2022, str. 69–82) [96].

Predhodno razvit numerični model [60], [63], [103], [104] smo posebej prilagodili za zdravljenje tumorjev v jetrih z ablacijo IRE. Glavna razlika s statičnimi modeli, ki se pretežno uporabljajo za načrtovanje zdravljenja, je dodatek računanja v časovni domeni, kar je omogočilo izračun segrevanja tkiva in termičnih poškodb med terapijo. Razlika med dolžino pulza (običajno 100 µs) in periodo pulza (običajno približno 1 s) obsega več velikostnih razredov, zato modeliranje posameznih pulzov z računskega vidika ni izvedljivo. V praksi je dovajanje posameznih pulzov sinhronizirano z bolnikovim EKG, pulze dovajamo v sekvencah po 10, čemur sledi premor, potreben za polnjenje pulznega generatorja. V modelu smo zato združili sekvence 10 pulzov v en sam dolg pulz, kateremu sledi premor dolžine treh EKG ciklov bolnika. Izraz za segrevanje tkiva smo ustrezno prilagodili razmerju dolžine in periode pulzov, ti. *duty cycle* pristop, predstavljen v [75]. Premori za sekvencami pulzov v model vnašajo tudi pomembno dinamiko hlajenja tkiva med ablacijo.

Prilagojen numerični model smo uporabili v retrospektivni študiji, v kateri smo numerično rekonstruirali 18 kliničnih primerov IRE ablacije tumorjev v jetrih ter izračunali pričakovani izid zdravljenja. Rezultate simulacije smo primerjali s kliničnim odzivom v tkivu, kot ga vidimo na kontrolnih MR slikah, zajetih šest tednov po posegu. Namen študije je bil določiti prag *in silico* električnega polja v numeričnem modelu, pri katerem pričakujemo popolno ablacijo tkiva *in vivo*, in s tem validirati uporabnost numeričnega modela za načrtovanje zdravljenja tumorjev v jetrih z ablacijo IRE. Za vsak rekonstruiran kliničen primer smo z upragovljanjem električnega polja pridobili šest simuliranih volumnov ablacije, ki ustrezajo jakosti električnega polja *in silico* 400–900 V/cm. Simulirane volumne smo primerjali z volumni ablacije, ki smo jih ročno obrisali na kontrolnih slikah MR (v nadaljevanju segmentiran volumen ablacije).

V standardni klinični praksi je prvo kontrolno slikanje MR zajeto 24 ur po ablaciji in je namenjeno oceni tehnične uspešnosti posega. Naslednje kontrolno slikanje je zajeto 6 tednov po posegu in služi prvi oceni kliničnega odziva tumorja na zdravljenje. Prvotno smo nameravali za primerjavo s simuliranimi rezultati uporabili prve kontrolne slike (24 ur po posegu), saj naj bi le-te bolje prikazale dejanski volumen tkiva, kjer pričakujemo uspešno ablacijo. Žal je bilo zaradi velikega edema na področju ablacije nemogoče z gotovostjo identificirati nekrotično tkivo, zato slik ni bilo mogoče uporabiti za primerjavo z izračuni. Za validacijo smo zato uporabili T1-utežene kontrolne slike MR, zajete 6 tednov po ablaciji.

Izbrana metrika za primerjavo simuliranih in segmentiranih volumnov ablacije je bila površinska deviacija, izračunana kot povprečna absolutna napaka (AAE) med površinama obeh volumnov. Na podlagi rezultatov podobne študije radiofrekvenčne ablacije tumorjev v jetrih [105] sklepamo, da AAE < 4 mm med simuliranim in segmentiranim volumnom ablacije zadostuje za klinične zahteve. Najnižja srednja vrednost AAE v naši študiji je bila 5,6 mm $\pm$ 1,5 mm, pridobljena s pragom *in silico* električnega polja 900 V/cm. Iz literature vemo, da je prag 900 V/cm višji od praga, ki je potreben za popolno ablacijo IRE jetrnega tkiva, ki se nahaja v območju 500–700 V/cm [58], [103], [106]–[108]. Slika III.1 A prikazuje primerjavo segmentiranih in simuliranih volumnov ablacije pri šestih pragovih električnega polja. Vidimo, da so simulirani volumni konsistentno večji od segmentiranih volumnov. Slika III.1 B prikazuje izračunane AAE za posamezne rekonstruirane klinične primere pri šestih pragovih električnega polja.

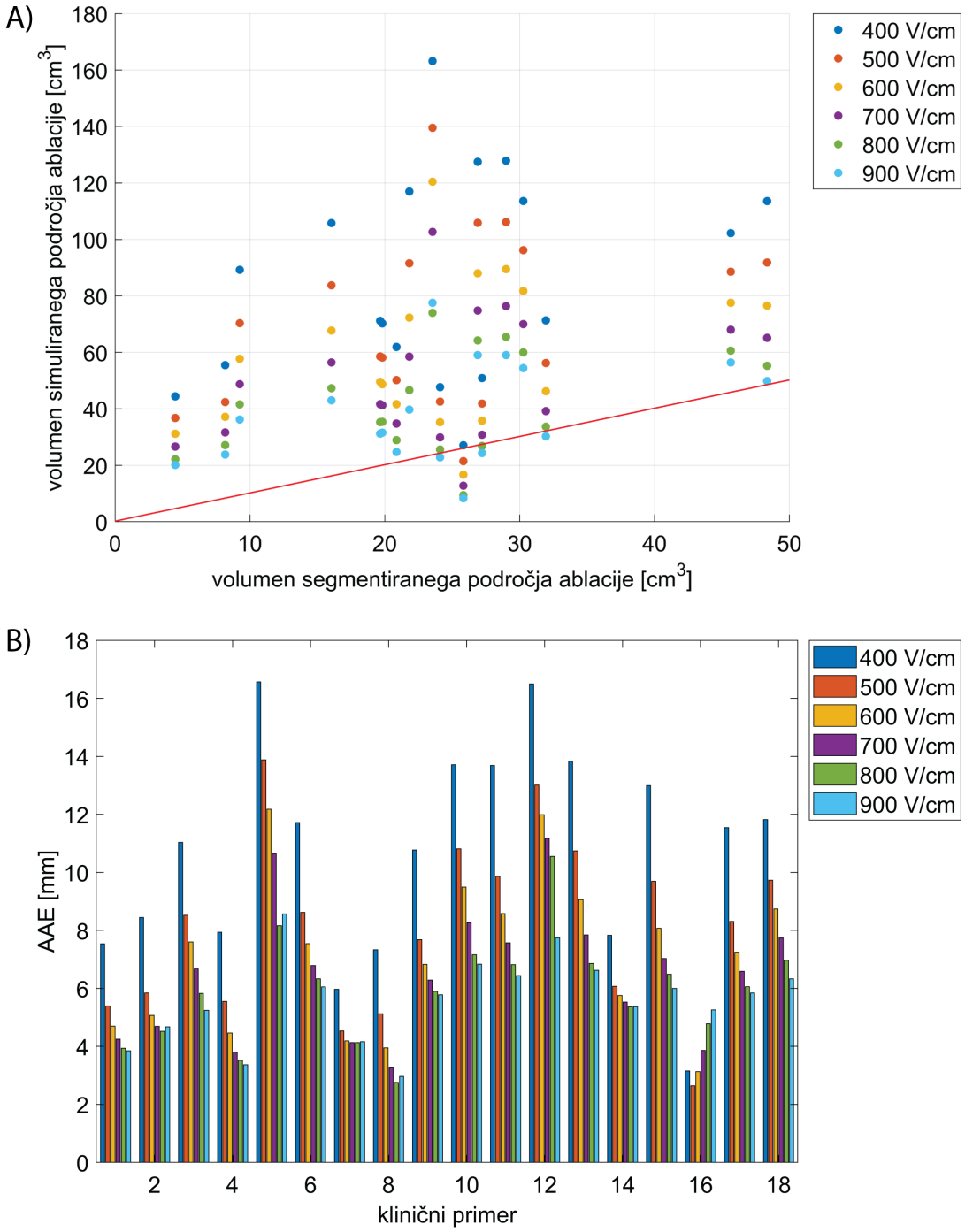

Slika III.1: A) Primerjava simuliranih volumnov ablacije in segmentiranih volumnov ablacije, pridobljenih iz kontrolnih slik MR 6 tednov po posegu. Rdeča linija označuje enakost obeh volumnov. B) Povprečna absolutna napaka (AAE) med simualiranimi in segmentirani volumni ablacije za posamezne klinične primere. Rezultati so prikazani pri šestih različnih pragovih *in silico* električnega polja.

V nasprotju s termičnimi metodami ablacije, kjer zlahka razmejimo nekrotično tkivo od zdravega, je pri ablaciji IRE zaradi dinamike celjenja tkiva težko določiti dejansko področje ablacije na kontrolnih slikah. Nedavni študiji ablacije IRE primarnih [109] in sekundarnih [110] tumorjev v jetrih sta pokazali, da se področje ablacije v prvih 2–4 tednih po posegu zelo hitro krči, kar je najverjetneje posledica celjenja. Padia in sodelavci v [109] poročajo o izrazitem krčenju področja ablacije, zlasti v prvih štirih tednih po posegu IRE. Barabasch in sodelavci v [110] prav tako poročajo o hitrem krčenju področja ablacije v prvih dveh tednih po posegu in o zmernem zmanjšanju v naslednjih tednih. Sklepamo, da se je v naši klinični skupini področje ablacije v šestih tednih do drugega kontrolnega slikanja že precej skrčilo. Ker je numerični model namenjen izračunu področja ablacije na dan posega, domnevamo, da je prag, ki smo ga določili v tej študiji, v veliki meri precenjen. Naši rezultati kažejo, da lezije, vidne na slikah MR, zajetih šest tednov po posegu, predstavljajo področja tkiva, ki je bilo med terapijo izpostavljeno električnim poljem jakosti vsaj 900 V/cm. Domnevamo, da bi lahko dosegli boljšo korelacijo s simuliranimi volumni pri nižjih pragovih električnega polja (npr. 500—700 V/cm), če bi imeli za validacijo na voljo kontrolne slike, zajete prej kot v šestih tednih po posegu, na primer v prvem ali drugem tednu. Tako bi lahko kvantificirali sposobnost modela za napoved izida zdravljenja in s tem validirali model za uporabo pri načrtovanju ablacije IRE v jetrih.

Čeprav ablacija IRE velja za ne termično metodo, je več študij pokazalo znatno segrevanje tkiva in ponekod celo termične poškodbe tkiva pri klasičnih protokolih ablacije IRE [43], [83], [88], [111]. Termične poškodbe tkiva so lahko problematične, saj se ablacija IRE pogosto uporablja v primerih, kjer je le-te niso sprejemljive. V rekonstruiranih primerih smo numerično ovrednotili termični učinek ablacije IRE. Rezultati so pokazali znatno segrevanje tkiva, zlasti v bolj klinično zahtevnih primerih, kjer je bilo uporabljenih veliko elektrod (tj. dovedenih veliko pulzov). Simulacije so v 7 od 18 rekonstruiranih primerov pokazale zadostno segrevanje za povzročitev termičnih poškodb v več kot 50 % volumna tumorja. Verjetno je, da model do neke mere precenjuje obseg termičnih poškodb. Ker pa so deli tkiva med ablacijo IRE kumulativno izpostavljeni stotinam pulzov, sta neželeno segrevanje in termično povzročena nekroza neizogibni. Največji dvig temperature smo opazili ob površini elektrod, kjer je gostota toka največja. Pri načrtovanju zdravljenja moramo zato paziti, da elektrode niso v stiku ali v nepo-

sredni bližini anatomskih struktur, ki so močno občutljive na termične poškodbe, kot so recimo živci in stene črevesja.

V študiji smo pokazali tudi uporabnost načrtovanja zdravljenja za izboljšanje prihodnjih posegov, na primer za zmanjšanje morebitnih termičnih učinkov. Za optimizacijo in pripravo hipotetičnega načrta zdravljenja sta bila izbrana dva primera, v katerih smo ocenili visok odstotek termičnih poškodb. V obeh primerih nam je uspelo odpraviti termično komponento ablacije, pri čemer nismo zmanjšali pokritosti kliničnega ciljnega volumna (CTV) z električnim poljem. V tej študiji smo optimizirali le amplitude napetosti dovedenih pulzov, medtem ko so položaji elektrod ostali enaki prvotnim posegom.

V tej študiji smo razvili sofisticirano metodo za validacijo numeričnega modela za načrtovanje ablacije IRE. Na podlagi rezultatov študije lahko zasnujemo prospektivno klinično študijo, tako da zagotovimo potrebne podatke za validacijo napovedne sposobnosti modela in zagotovimo zadostno robustnost in natančnost za izpolnjevanje kliničnih potreb. Baza podatkov, ki vsebuje informacije o rekonstruiranih kliničnih primerih, bolnikom prilagojene 3D anatomske modele in računske rezultate, je javno dostopna v spletnem repozitoriju https://doi.org /10.6084/m9.figshare.12961646.v1.

III.2 Elektrokemoterapija v jetrih na mezo nivoju

Za boljše razumevanje fizikalnega pojava elektroporacije se razvijajo numerični modeli na različnih ravneh, od obsežnih modelov tkiva za načrtovanje zdravljenja [59], [70], [71], [103] do modelov gosto zloženih celic [112]–[115], modelov posameznih celic in modelov elektroporacije celične membrane [3], [116]. Predpogoj za uspeh zdravljenja z elektroporacijo je popolna pokritost CTV z dovolj visokim električnim poljem. Porazdelitev električnega polja v biološkem tkivu je močno odvisna od električnih lastnosti tkiv v CTV; to je še posebej pomembno pri heterogenih organih, kjer ima prevodnost različnih tkiv širok razpon vrednosti [59], [107], [117], [118]. Jetra so zelo heterogen organ, prežet z mrežo krvnih žil in žolčnih poti. Jetrni parenhim ima posebno mikrostrukturo, ki jo sestavljajo funkcionalne enote, ti. jetrni lobuli ali jetrni režnjiči, ki obdajajo mrežo centralnih

ven (CV). Lobuli so povezani z mrežo vezivnega tkiva, krvnih žil in žolčnih vodov (portalne triade), imenovano medlobularna pregrada. Več študij je že pokazalo, kako pomembno je pri izdelavi modelov upoštevati makrostrukture jeter, kot so velike krvne žile in žolčevodi [106], [107], [119].

V drugem članku (Cindrič *et al.* 2022, str. 83–96) smo raziskovali, ali heterogena struktura jetrnega parenhima vpliva na porazdelitev električnega polja in s tem na izid zdravljenja z elektrokemoterapijo (EKT). Zgradili smo model jeter na mezo nivoju, ki vključuje tako makro- kot mikrostrukturo jeter in je primerljiv z mikroskopskimi slikami jeter. Za pridobitev realistične geometrije smo numerično rekonstruirali štiri posege EKT v zdravih prašičjih jetrih, ki so bili izvedeni v nedavni *in vivo* študiji [98]. Posebno pozornost smo namenili izbiri mikroskopskih vzorcev (slik), in sicer smo vzorce izbrali tako, da je bilo v območje zdravljenja vključenih več večjih jetrnih žil in portalnih prostorov. Porazdelitev električnega polja smo izračunali s predhodno razvitim numeričnim modelom za načrtovanje zdravljenja z elektroporacijo v jetrih ter polje primerjali s histopatološkimi spremembami, opaženimi na mikroskopskih slikah vzorcev tkiva po EKT.

Ker električne lastnosti posameznih mikrostruktur (tj. jetrnih lobulov, medlobularne pregrade in CV) niso znane, smo izvedli parametrično študijo prevodnosti posameznih struktur. Ugotavljali smo, ali vključitev jetrnih mikrostruktur in spremenljivost njihove električne prevodnosti vplivata na porazdelitev električnega polja v meri, ki je pomembna za primerjavo z mikroskopskimi slikami in posledično s histopatološkimi ugotovitvami. Slika III.2 prikazuje primer električnega polja, izračunanega s heterogenim modelom jetrnega parenhima na mezo nivoju (ki vključuje mikrostrukture jeter), v primerjavi s homogenim modelom jetrnega parenhima (ki se običajno uporablja pri načrtovanju zdravljenja). Pri heterogenem modelu opazimo vrh jakosti električnega polja na zunanjem robu svetline CV, kar je posledica veliko večje prevodnosti krvi v primerjavi z okoliškim tkivom; sledi padec električnega polja na območju svetline CV. Zmanjšanje električnega polja je opaziti tudi na območju medlobularne pregrade. Numerični model je skladen tudi s histološkimi ugotovitvami; poškodbe so bile namreč izrazitejše v osrednjem predelu lobulov, pri čemer CV na poškodovanih območjih niso bile več vidne. Predvidevamo, da je poškodba v osrednjem območju lobulov posledica porušitve osrednjega ožilja (CV) zaradi visokega električnega polja, medtem ko so zunanji deli lobulov manj prizadeti, saj je periferno ožilje (medlobularna

pregrada) še delujoče.

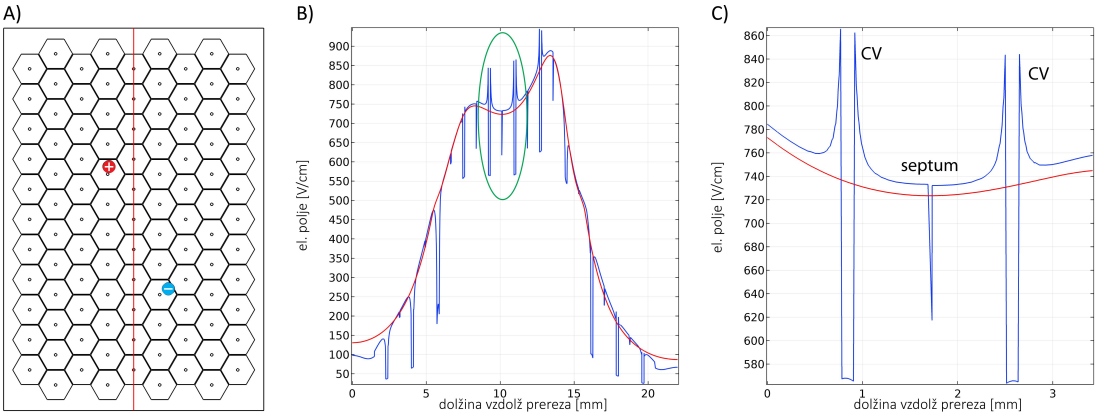

Slika III.2: A) Model jetrnega parenhima na mezo nivoju, sestavljen iz heksagonalnih jetrnih lobulov, centralnih ven (CV) in medlobularne pregrade. Model prikazuje dve elektrodi – rdečo katodo in modro anodo. Rdeča linija prikazuje prerez, vzdolž katerega smo primerjali jakosti električnega polja. B) Primerjava jakosti električnega polja, izračunanega s heterogenim modelom parenhima na mezo nivoju (modra), in popolnoma homogenim modelom parenhima (rdeča). Polje je izračunano vzdolž linije prereza, ki prečka več CV in medlobularnih pregrad. C) Približan izsek modela, označen z zeleno na sliki B), prikazuje področje dveh lobulov s CV ter medlobularno pregrado med njima. Vidimo izrazit padec na področju svetlin CV in pregrade ter zvišano jakost polja na zunanjem robu svetlin CV. Slika je povzeta po [97].

V primeru, prikazanem na Sliki III.2, je povprečna relativna napaka med električnim poljem, izračunanim s heterogenim in homogenim modelom jetrnega parenhima, 7 % s standardnim odklonom 12 %, mediana relativne napake pa je 3 %. Nizka mediana napake kaže na to, da med modeloma ni bistvene razlike v skupni porazdelitvi električnega polja. Glede na rezultate parametrične študije bi vključitev medlobularne pregrade bistveno vplivala na porazdelitev skupnega električnega polja le, če je prevodnost pregrade veliko nižja (npr. 10 %) od prevodnosti okoliškega jetrnega tkiva. Takšen scenarij je zaradi sestave medlobularne pregrade zelo malo verjeten. Naši rezultati kažejo, da mikrostrukture jeter ne vplivajo bistveno na porazdelitev električnega polja na mezo nivoju, zato za načrtovanje zdravljenja z elektroporacijo zadostuje uporaba homogenega modela jetrnega parenhima.

Histološki pregled vzorcev tretiranih prašičjih jeter je pokazal akutne spremembe v tkivu z jasno razmejitvijo po conah. Na območju neposredno okoli mesta vstavitve elektrode je vidna koagulacijska nekroza s popolno izgubo mikrostrukture jeter (temno sivo senčenje na Sliki III.3 B, D). Okoli tega območja je območje delno poškodovanega jetrnega parenhima, ki ga pripisujemo ireverzibilni elektroporaciji tkiva (svetlo sivo senčenje na Sliki III.3 B, D). Električno polje, izračunano z modelom na mezo nivoju s homogenim modelom jetrnega parenhima, smo primerjali z mikroskopskimi slikami tretiranega območja in določili pragove, ki najbolje ustrezajo videzu obeh con akutnih sprememb. Povprečen prag *in silico* električnega polja, ki najbolje ustreza območju delno poškodovanega jetrnega parenhima, je 810 V/cm (modri obrisi na Sliki III.3 B, D), kar zadostuje za povzročitev ireverzibilne elektroporacije jetrnega tkiva [70], [107], [120]. Povprečen prag *in silico* električnega polja, ki najbolje ustreza območju koagulacijske nekroze, je 1225 V/cm (rdeči obrisi na Sliki III.3 B, D). Kljub nekrotičnemu videzu tkiva so Zmuc *et al* predpostavili, da je malo verjetno, da bi bile te spremembe posledica segrevanja tkiva med dovajanjem pulzov, kar so sedaj potrdili tudi naši izračuni, saj v modelih ni bilo opaziti bistvenega segrevanja tkiva. Najvišja izračunana temperatura je dosegla 47 °C, vendar le za zelo kratek čas, kar ni bilo dovolj, da bi povzročilo termične poškodbe tkiva. Nekroza, opažena v naših vzorcih, je lahko povezana s spremembami pH v okolici elektrod, vendar so za potrditev te domneve potrebne nadaljnje raziskave.

Če povzamemo, smo v tej študiji potrdili, da mikrostrukture jeter (jetrni lobuli, medlobularna pregrada in centralne vene) ne vplivajo bistveno na porazdelitev električnega polja na mezo nivoju, zato je uporaba homogenega modela jetrnega parenhima primerna za numerične izračune električnega polja, ki se uporabljajo za načrtovanje zdravljenja z elektroporacijo. Vendar je treba v model vključiti velike jetrne žile in prostore portalne vene, saj te makrostrukture pomembno vplivajo na porazdelitev električnega polja, kot je bilo predlagano že prej.

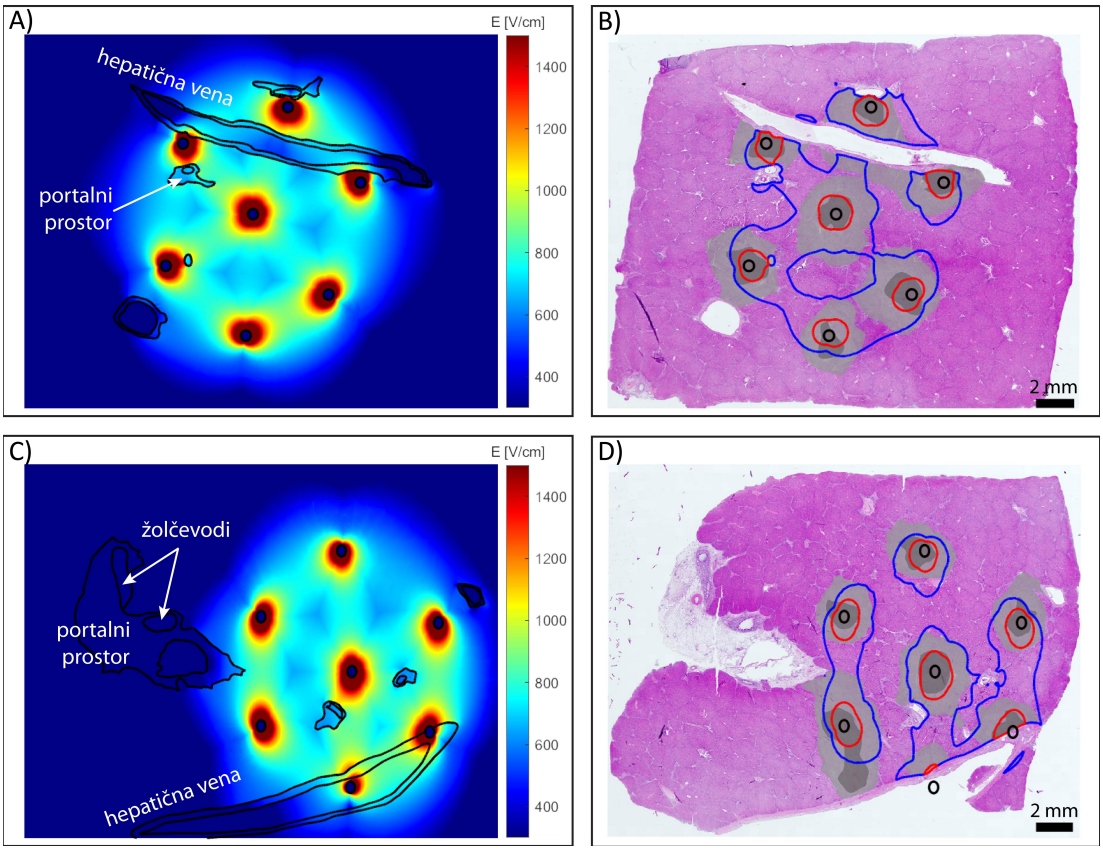

Slika III.3: Rezultati rekonstrukcije dveh primerov elektrokemoterapije prašičjih jeter. A, C) Porazdelitev električnega polja, izračunanega s homogenim modelom jetrnega parenhima. Makrostrukture jeter (večje žile in portalni prostori) so obrisane s črno barvo. B, D) Histopatološke spremembe v jetrih po elektrokemoterapiji. Cona koagulacijske nekroze, vidna na mikroskopski sliki, je senčena s temno sivo bravo, cona delno poškodovanega parenhima je senčena s svetlo sivo barvo. Prag električnega polja v numeričnem modelu, ki se najbolje prilega coni koagulacijske nekroze, znaša 1225 V/cm in je na sliki obrisan z rdečo barvo. Prag električnega polja v numeričnem modelu, ki se najbolje prilega coni delno poškodovanega tkiva, znaša 810 V/cm in je na sliki obrisan z modro barvo. Slika je povzeta po [97].

III.3 Ali prisotnost kovinskih vsadkov vpliva na varnost in učinkovitost zdravljenja z elektroporacijo?

Kot varnostni ukrep je uporaba zdravljenja z elektroporacijo kontraindicirana pri bolnikih s kovinskimi vsadki, kadar se le-ti nahajajo v neposredni bližini CTV. Zaradi visoke električne prevodnosti lahko prisotnost kovinskih vsadkov močno spremeni porazdelitev električnega polja, kar lahko povzroči nezadostno pokritje CTV. Poveča se lahko tudi tveganje za termične poškodbe okoliškega tkiva, zlasti med ablacijo IRE. Vpliv kovinskih vsadkov na varnost in učinkovitost EKT in ablacije IRE je bil raziskan v dveh študijah.

V tretjem članku (Cornelis *et al*, str. 97–108) smo raziskali učinek kovinskih kirurških sponk pri ablaciji IRE kolorektalnih metastaz v jetrih (CRLM). Pri bolnikih s ponavljajočimi se metastazami so zaradi predhodnih posegov v jetrih pogosto prisotne kovinske kirurške sponke. Po podatkih podjetja Angiodynamics (Latham, NY, ZDA), proizvajalca pulznega generatorja NanoKnife za ablacijo IRE, velja prisotnost kakršnih koli vgrajenih naprav s kovinskimi deli kot kontraindikacija za zdravljenje [121]. Kljub temu je prisotnost manjših vsadkov, kot so kirurške sponke, v praksi pogosto spregledana. Naša hipoteza je bila, da tudi kirurške sponke vplivajo na učinkovitost ablacije CRLM z IRE in da je mogoče s pomočjo bolnikom prilagojenih numeričnih modelov opredeliti vpliv kovinskih vsadkov na rezultate zdravljenja.

Rekonstruirali smo osem kliničnih primerov CRLM zdravljenih z ablacijo IRE – štirih s kovinskimi kirurškimi sponkami v bližini področja ablacije in štirih brez kovinskih sponk. Pri primerih s sponkami smo izvedli tudi kontrolne izračune brez sponk in tako ovrednotili njihov učinek na lokalno porazdelitev električnega polja, segrevanje tkiva in verjetnost celične smrti. Primerjava izračunov s sponkami in brez sponk ni pokazala bistvenih razlik v pokritju tumorja z jakostjo električnega polja nad pragom IRE. Ob podrobnejšem pregledu smo opazili, da prisotnost kovinskih sponk povzroči mikroskopska popačenja v porazdelitvi električnega polja v tkivu (Slika III.4 A). Opazili smo zmanjšanje jakosti električnega polja v neposredni bližini sponk (< 1 mm), z največjim zmanjšanjem v središču sponke vzdolž njene longitudinalne osi (Slika III.4 B). Čeprav je na prvi pogled zanemarljivo, lahko takšno popačenje električnega polja zmanjša učinkovitost zdravljenja, če so

tumorske celice prisotne na območjih znotraj sponk in okoli njih.

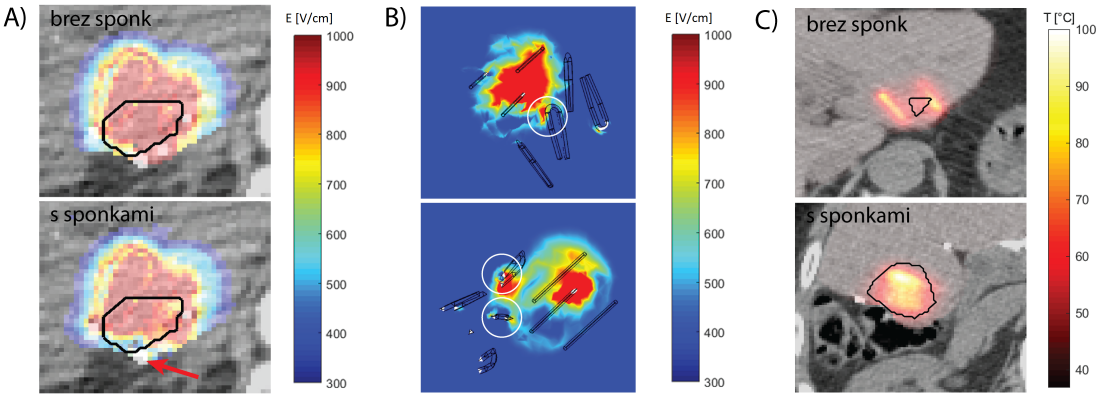

Slika III.4: A) Razporeditev električnega polja v modelu brez kovinskih kirurških sponk (zgoraj) in s sponkami (spodaj, puščica). B) Sponke vplivajo na jakost električnega polja v svoji neposredni bližini. Na nekaterih predelih je jakost polja povečana, v središču vzdolž longitudinalne osi sponke pa jakost polja zaradi učinka Faradayeve kletke izrazito upade. C) Pri protokolih pulzov, ki se trenutno uporabljajo pri ablaciji IRE, je prisotno znatno segrevanje tkiva, ki zadostuje za nastanek termičnih poškodb.

Čeprav ima IRE pretežno netermični mehanizem uničevanja celic, naši modeli kažejo, da so termične poškodbe prisotne v znatnem delu tretiranega tkiva ne glede na prisotnost kovinskih sponk (Slika III.4 C). Domnevamo, da je za to lahko odgovoren agresivni protokol dovajanja pulzov, ki se trenutno uporablja pri ablaciji IRE. Ker je kovina dober toplotni in električni prevodnik, ne pričakujemo neposrednega segrevanja kovinskih sponk. Kakršno koli segrevanje sponke je posledica prevajanja toplote iz okoliškega tkiva; poleg tega lahko kovinska sponka deluje celo kot ponor toplote in zmanjša toplotno energijo, ki se sprošča v tkivo [122].

Učinke kovinskih vsadkov na ablacijo IRE so preučevali v več kliničnih študijah. Neal in sodelavci [123] niso ugotovili škodljivih učinkov brahioterapevtskih semen na porazdelitev električnega polja v prostati ali zmanjšane učinkovitosti ablacije IRE. Po drugi strani pa je predklinična *in vivo* študija Ben-Davida in sodelavcev [124] pokazala, da lahko prisotnost kovine v območju ablacije IRE popači velikost in obliko področja ablacije. Scheffer in sodelavci [125] ter Dunki-Jacobs in sodelavci [111] so pokazali, da lahko IRE povzroči lo-

kalno segrevanje tkiva, pri čemer prisotnost kovine poveča nevarnost termičnih poškodb na mestu zdravljenja. Predhodne ugotovitve dopolnjujemo s poročilom, da prisotnost kovinskih kirurških sponk lahko vpliva na učinkovitost ablacije IRE pri zdravljenju CRLM, vendar se zdi, da sponke ne vplivajo na varnost ablacije.

Dva glavna proizvajalca klinično odobrenih pulznih generatorjev, in sicer IGEA S.p.A. (Carpi MO, Italija) za sistem Cliniporator, ki se uporablja pri EKT, in Angiodynamics (Latham, NY, ZDA) za sistem NanoKnife, ki se uporablja za ablacijo IRE, trdita, da so vsajeni srčni spodbujevalniki kontraindikacija za zdravljenje z elektroporacijo [121], [126]. V četrtem članku (Jarm *et al*, 2020, str. 109–128) smo numerično raziskali vpliv prisotnosti vgrajenega srčnega spodbujevalnika s kovinskim ohišjem na učinkovitost in varnost EKT in ablacije IRE podkožnega tumorja. Za obe možnosti zdravljenja smo preučili tri scenarije: srčni spodbujevalnik v stiku z eno od elektrod, srčni spodbujevalnik v bližini tumorja, vendar brez stika z elektrodami, in kontrolni scenarij brez srčnega spodbujevalnika.

Prisotnost srčnega spodbujevalnika ima podoben učinek pri obeh metodah zdravljenja. Slika III.5 prikazuje izračunano razporeditev električnega polja v tkivu in maksimalno temperaturo tkiva za primer ablacije IRE. Brez stika z elektrodami prisotnost srčnega spodbujevalnika nima bistvenega vpliva na porazdelitev celotnega električnega polja in dovedenega električnega toka v primerjavi s kontrolnim scenarijem. Spremembe električnega polja opazimo predvsem v zdravem tkivu v neposredni bližini spodbujevalnika (Slika III.5 B), medtem ko električno polje v tumorju ostane bolj ali manj nespremenjeno. Poleg tega nismo opazili dodatnega segrevanja tkiva v primerjavi s kontrolnim scenarijem (Slika III.5 D, E). Če je srčni spodbujevalnik v stiku z eno izmed elektrod, deluje celotno ohišje kot velika elektroda, s čimer se močno poveča poraba električnega toka. Izračunani tok je bil tako za približno 50 % večji v primerjavi s kontrolno situacijo; večja poraba toka poveča tveganje za prekoračitev maksimalnih dovoljenih vrednosti toka in s tem prekinitve dovajanja pulzov. Pri obeh metodah zdravljenja je električno polje na splošno višje, opazimo pa tudi znatno povečan delež IRE v zdravem tkivu v bližini mesta stika s spodbujevalnikom (Slika III.5 C). V bližini elektrod opazimo tudi višje temperature. Pri EKT povišanje temperature ni tako izrazito, pri ablaciji z IRE pa je na mestu druge aktivne elektrode v paru (s kontaktno elektrodo) opaziti znatno povišanje temperature (Slika III.5

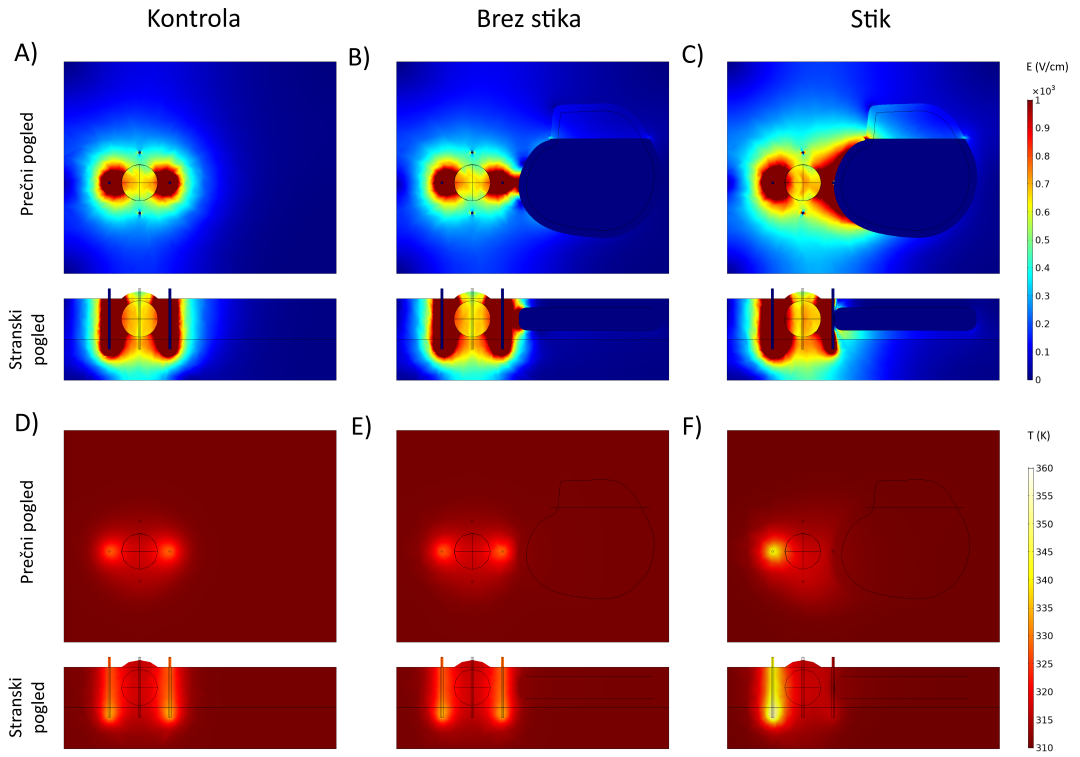

Slika III.5: Vpliv prisotnosti srčnega spodbujevalnik v bližini ablacije podkožnega tumorja z IRE. Prikazano je električno polje in maksimalna temperatura tkiva v treh scenarijih: srčni spodbujevalnik je v stiku z eno izmed elektrod (A, D), srčni spodbujevalnik je v bližini tumorja, vendar ni v stiku z elektrodami (B, E), in kontrolni scenarij brez srčnega spodbujevalnika (C, F). Slika je povzeta po [100].

F). To opažanje je skladno z rezultati predhodne študije [125], kjer so ob prisotnosti kovinskega vsadka opazili povečano segrevanja v okolici elektrod. Samo kovinsko ohišje srčnega spodbujevalnika se med terapijo ne segreje, temveč deluje kot toplotni odvodnik, kar vidimo tudi na Sliki III.5 F, zato so termične poškodbe zaradi segrevanja kovinskega ohišja malo verjetne.

Naša študija je pokazala, da prisotnost srčnega spodbujevalnika s kovinskim ohišjem ne vpliva na pokritost tumorja, ne glede na stik z elektrodo, zato ne bi smela zmanjšati učinkovitosti zdravljenja z elektroporacijo. Študijo je treba obravnavati kot preliminarno, zato je treba ugotovitve dodatno validirati z eksperimenti. Kljub temu bodo ti rezultati pripomogli k večji dostopnosti zdravljenja

z elektroporacijo za bolnike z vsajenimi srčnimi spodbujevalniki.

III.4 Nov pristop k zdravljenju tumorjev v hrbtenici

Kosti, zlasti hrbtenica, so eno najpogostejših mest za nastanek metastaz. Pojavnost metastaz v hrbtenici pri bolnikih z rakom lahko doseže do 70 %, odvisno od vrste primarnega tumorja. Predklinične in klinične študije so pokazale, da je mogoče metastaze v kosteh učinkovito zdraviti z elektrokemoterapijo (EKT), pri čemer so poročali o znatnem zmanjšanju bolečine brez neželenih nevroloških simptomov, povezanih z zdravljenjem [127]–[130]. V petem članku (Cindrič *et al* 2018, str. 129–144) smo predstavili nov, minimalno invaziven pristop za zdravljenje metastaz v hrbtenici z EKT, tj. transpedikularni pristop, pri katerem igelne elektrode za EKT vstavimo v telo vretenca skozi pedikle, podobno kot pri vstavitvi pedikularnih vijakov pri operaciji za stabilizacijo hrbtenice. Elektrode so krajše od tistih, ki se trenutno uporabljajo za elektroporacijo kosti, in sicer 1 cm namesto 3 cm, kar omogoča natančnejše lociranje tumorja. Slika III.6 prikazuje primer vstavitve elektrod s transpedikularnim pristopom. Namen študije je bil numerično ovrednotiti izvedljivost in varnost predlaganega pristopa za zdravljenje metastaz v hrbtenici.

V raziskavi smo uporabili tri reprezentativne klinične primere tumorjev v hrbtenici z različnimi stopnjami vpletenosti telesa vretenca, pedikla in hrbteničnega kanala. Za vse tri primere smo na podlagi medicinskih slik bolnikov izdelali anatomsko pravilne numerične modele in za vsak primer pripravili individualni načrt zdravljenja. Numeričen model elektroporacije temelji na vrednostih električne prevodnosti tkiva in povečanju le-te zaradi elektroporacije. Podatki, zlasti o povečanju prevodnosti med elektroporacijo, so redki, poročane vrednosti pa se med študijami precej razlikujejo. Za natančno določitev funkcij povečanja električne prevodnosti za kostno in tumorsko tkivo smo uporabili eksperimentalne podatke iz predklinične študije na ovčjih vretencih [129] ter iz prvega kliničnega primera tumorja v hrbtenici, zdravljenega z EKT [128]. Izračunali smo porazdelitev električnega polja v tumorju in okoliškem tkivu; kot ciljni prag električenga polja smo določili vrednost 400 V/cm. Ocenili smo tudi morebitno tveganje za poškodbe živcev.

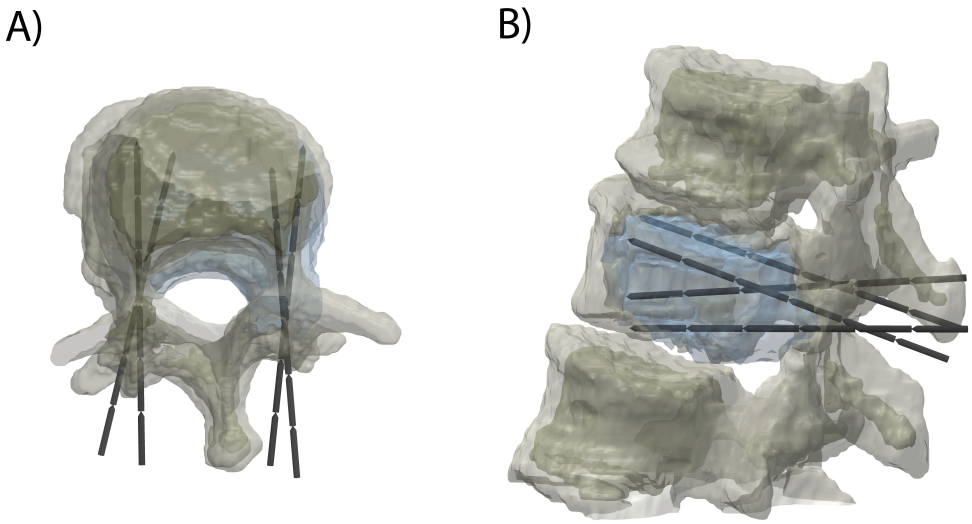

Slika III.6: Postavitev elektrod s transpedikularnim pristopom za EKT tumorja v 11. torakalnem vretencu. A) Prečni pogled in B) stranski pogled. Posamezni kratki segmenti elektrod nakazujejo retrakcijo le-teh med posegom, v primerih, ko je potrebno tumor pokriti v več segmentih. Slika je povzeta po [101].

Pokritost tumorja z izbranim pragom za EKT kostnega tkiva, 400 V/cm, je bila v dveh primerih > 99 %, v tretjem primeru pa > 98,9 %, kar smo obravnavali kot uspešno zdravljenje. Tumorsko tkivo, ki ni bilo pokrito z zadostnim električnim poljem, se je nahajalo na robu mase tumorja. V enem izmed primerov, kjer je tumor zrasel v hrbtenični kanal, je izračun pokazal IRE v 12,4 mm^3 hrbtenjače, kar bi lahko predstavljalo tveganje za poškodbo živcev. Vendar je treba upoštevati, da pragovi za elektroporacijo različnih tkiv še vedno v veliki meri niso znani; v modelih uporabljamo zelo stroge pragove, da bi se izognili preveč optimistični napovedi zdravljenja ali podcenitvi nevarnosti poškodb. Verjetno je, da tkivo hrbtenjače tudi v tem primeru ne bi bilo poškodovano. Izračuni kažejo, da je bil velik del tumorskega tkiva (34–63 %) izpostavljen dovolj visokemu električnemu polju, da bi povzročilo IRE. Kljub temu to ni zaskrbljujoče, saj so študije pokazale, da IRE dolgoročno ne vpliva na mehansko trdnost kosti [127], [129], [131], pojavljajo pa se tudi dokazi, da apoptotična celična smrt, povzročena z elektroporacijo, celo spodbuja osteogenezo (rast nove kosti) [132]. Uporaba elektrod s krajšimi prevodnimi deli omogoča natančnejše lociranje tumorskega

tkiva, kar zmanjšuje poškodbe okoliškega tkiva in znižuje dovedene električne tokove, s tem pa tudi negativne stranske učinke zdravljenja. Pri izdelavi načrta zdravljenja smo za optimizacijo amplitud dovedene napetosti uporabili genetski algoritem, položaji elektrod pa so bili določeni ročno in niso bili optimizirani. Uporaba algoritma za optimizacijo položajev elektrod bi morda pripomogla k še boljši pokritosti tumorja s še manjšim tveganjem za poškodbe živcev.

Rezultati te študije kažejo, da je predlagani pristop k zdravljenju učinkovit in da je tveganje za nevrološke poškodbe majhno, če se večina tumorja nahaja v telesu vretenca. Če se tumor nahaja zunaj telesa vretenca in v območju pedikla, je uspešno zdravljenje še vedno izvedljivo, vendar je potrebno obsežnejše načrtovanje, pri čemer je treba posebno pozornost nameniti morebitni vpletenosti hrbtenjače in živcev. Ob skrbni izbiri bolnikov je predlagani pristop k zdravljenju metastaz v hrbtenici obetavna metoda zdravljenja, ki jo je treba še naprej raziskovati. Pri vstavljanju elektrod skozi pedikle gre za podobno tehniko kot pri že uveljavljenih ortopedskih posegih; vstavljanje pritrdilnih vijakov je najpogostejša tehnika pri operacijah stabilizacije hrbtenice [133]. Razvito tehnologijo za samodejno načrtovanje trajektorije vijakov in medoperativno vodenje posega bi lahko potencialno uporabili za vstavljanje elektrod za EKT [134]–[136], kar bi olajšalo uvedbo transpedikluarnega pristopa v klinično prakso.

III.5 Optimizacija položajev elektrod za zdravljenje tumorjev v hrbtenici

Šesti članek (Cindrič *et al.* 2022, str. 145–162) nadgrajuje koncept transpedikularnega pristopa za EKT tumorjev v hrbtenici, ki je bil predhodno predstavljen v [41], [101]. Splošni postopek načrtovanja zdravljenja je v osnovi sestavljen iz določitve najboljših možnih položajev elektrod in amplitud napetosti, s katerimi zagotovimo zdravljenje celotnega kliničnega ciljnega volumna (CTV). Ta postopek se še vedno izvaja večinoma ročno, kar zahteva visoko raven strokovnega znanja ali uporabo računsko zahtevnih genetskih algoritmov. Ta študija je eden izmed prvih poskusov uporabe prostorske informacije o porazdelitvi električnega polja v tkivu za optimizacijo postavitve elektrod in amplitude pulzov brez uporabe računsko zahtevnih metod optimizacije.

Načrtovanje zdravljenja z elektroporacijo je še vedno v zgodnji fazi razvoja. Načrti zdravljenja se oblikujejo pred posegom, položaji elektrod in amplitude napetosti pa se še vedno določajo predvsem ročno. Ta postopek običajno zahteva več iteracij, pri katerih operater med izračunavanjem spreminja položaje elektrod. Po vsaki iteraciji mora operater vizualno preveriti električno polje (običajno prikazano na medicinski sliki), določiti potencialno nezadostno pokrite predele CTV, ustrezno spremeniti položaj elektrod in izračun ponoviti. Celoten postopek se nato ponavlja, dokler ni celoten CTV pokrit z dovolj visokim električnim poljem. Tak pristop zahteva visoko raven strokovnega znanja o porazdelitvi električnega polja v nehomogenem tkivu ter o vplivih postavitve elektrod in parametrov pulzov na le-to. Poleg tega lahko iterativni postopek traja vsaj 30 minut, pogosto še več.

Pri razvoju algoritma smo sledili konceptu ročnega pristopa, vendar je bil cilj postopek avtomatizirati tako, da je potreben čim manjši vložek operaterja. Algoritem izračuna porazdelitev električnega polja v CTV, identificira nezadostno pokrita območja in te informacije uporabi za iterativno premikanje elektrod iz začetnih položajev tako, da sčasoma pokrije celoten CTV. Algoritem je modularen in zajema več zahtev; npr. zagotoviti moramo ustrezno razdaljo med elektrodami, da bi se izognili kratkim stikom; prav tako je intuitivno premikati elektrode proti težišču tumorja ali proti velikim območjem nezadostno pokritega tkiva. Upoštevane so tudi tehnične omejitve tržno dostopnega pulznega generatorja za EKT. Slika III.7 prikazuje blokovni diagram razvitega algoritma.

Zaradi varnostnih razlogov so pragovi za elektroporacijo, ki se uporabljajo v praksi, na splošno precej visoki in včasih je pri večjih tumorjih težko pokriti celoten CTV. Če upoštevamo varnostni pas okoli tumorja, na zunanjem robu CTV pričakujemo zelo malo ali nič rakavih celic; zato uvedemo ti. mehko pokritje CTV. Vsakemu elementu v CTV smo dodelili utež glede na razdaljo od meje tumorja, pri čemer se uteži linearno zmanjšujejo proti zunanjemu robu CTV. Pri pokritju upoštevamo utežen prag za elektroporacijo, kar pomeni, da je na zunanjem robu CTV sprejemljivo tudi polje, ki je nižje od prvotnega praga.

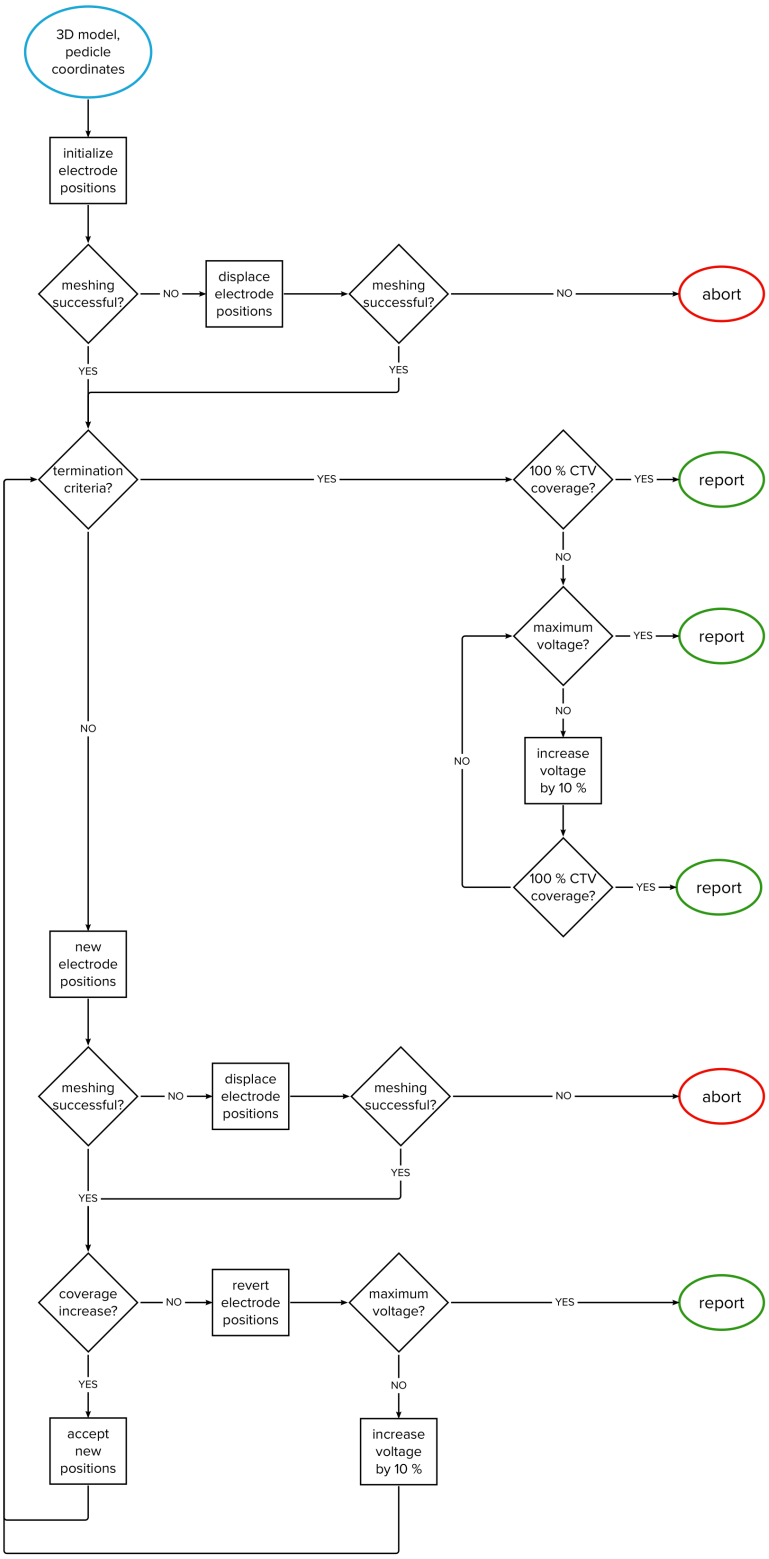

Slika III.7: Blokovni diagram algoritma za optimizacijo postavitve elektrod in amplitude napetosti pri transpedikularenm pristopu. Slika je povztea po [102].

Pragovi elektroporacije, ki se trenutno uporabljajo pri načrtovanju zdravljenja, so le zelo groba ocena; sam prag je težko določljiva lastnost, na katero med drugim vplivajo biološka variabilnost, stanje vzorca tkiva in metoda merjenja, zato v literaturi zasledimo veliko različnih vrednosti, celo za isto vrsto tkiva. Prag elektroporacije tkiva je odvisen tudi od protokola pulzov, ki se uporablja pri zdravljenju, in od kumulativnega časa izpostavljenosti tkiva v primerih z več elektrodami. Študije kažejo, da lahko pride do elektroporacije pri nižjih pragovih, če povečamo čas izpostavljenosti z več in/ali daljšimi pulzi.

Delovanje algoritma smo preizkusili na realističnih modelih vretenc spodnjega torakalnega in ledvenega dela hrbtenice. Modele smo ustvarili na podlagi medicinskih slik bolnikov, ki smo jim pozneje dodali sintetične sferične modele tumorjev različnih velikosti; skupaj smo tako dobili 108 testnih modelov. Algoritem je uspešno deloval pri različnih delih hrbtenice, pri različnih velikostih tumorjev in na različnih lokacijah tumorjev v telesu vretenca. Časovno najzahtevnejši korak postopka optimizacije je izdelava anatomskega modela na podlagi medicinskih slik, vendar je ta korak potreben tudi pri drugih konceptih načrtovanja zdravljenja. Ko je model končan, mora operater na bolnikovi medicinski sliki izbrati dve točki za vsak pedikel (Slika III.8), parametri zdravljenja pa so nato samodejno izračunani v nekaj minutah. Povprečni čas iskanja rešitve z algoritmom je bil 71 s (razpon: 17–253 s), povprečno število iteracij pa 4,9 (razpon: 1–15). To je znatno izboljšanje v primerjavi z iskanjem rešitve z genetskim algoritmom, ki zahteva vsaj 100 generacij (enakovredno iteracijam algoritma), ali z ročnim pristopom, ki traja vsaj 30 minut. V predlaganem algoritmu avtomatiziramo iterativni postopek, zato se od operaterja zahteva veliko manj znanja.

Glavna omejitev te študije je pomanjkanje validacije na realističnih tumorjih v hrbtenici. Preden lahko vzpostavimo delovni postopek načrtovanja zdravljenja, je treba opraviti validacijo na resničnih kliničnih primerih, bodisi prospektivno bodisi retrospektivno. Druga omejitev je, da trenutna izvedba algoritma omogoča uporabo le dveh elektrod, kar omejuje njegovo uporabo za tumorje, ki se nahajajo predvsem v telesu vretenc, tj. v zgodnejših fazah bolezni. Ta študija služi kot prikaz koncepta, da je mogoče položaje elektrod določiti (pol)avtomatsko na podlagi prostorske informacije o porazdelitvi električnega polja v ciljnem tkivu. Algoritem je trenutno zasnovan za EKT (z ustrezno prilagoditvijo praga električnega polja tudi za ablacijo IRE) tumorjev v vretencih s transpedikularnim pristopom,

vendar bi ga bilo mogoče prilagoditi za druga anatomska mesta. Izvorna koda algoritma in vsi modeli tumorjev vretenc, ustvarjeni v tej študiji, so javno dostopni v spletnem repozitoriju https://doi.org/10.6084/m9.figshare.21270111.v1.

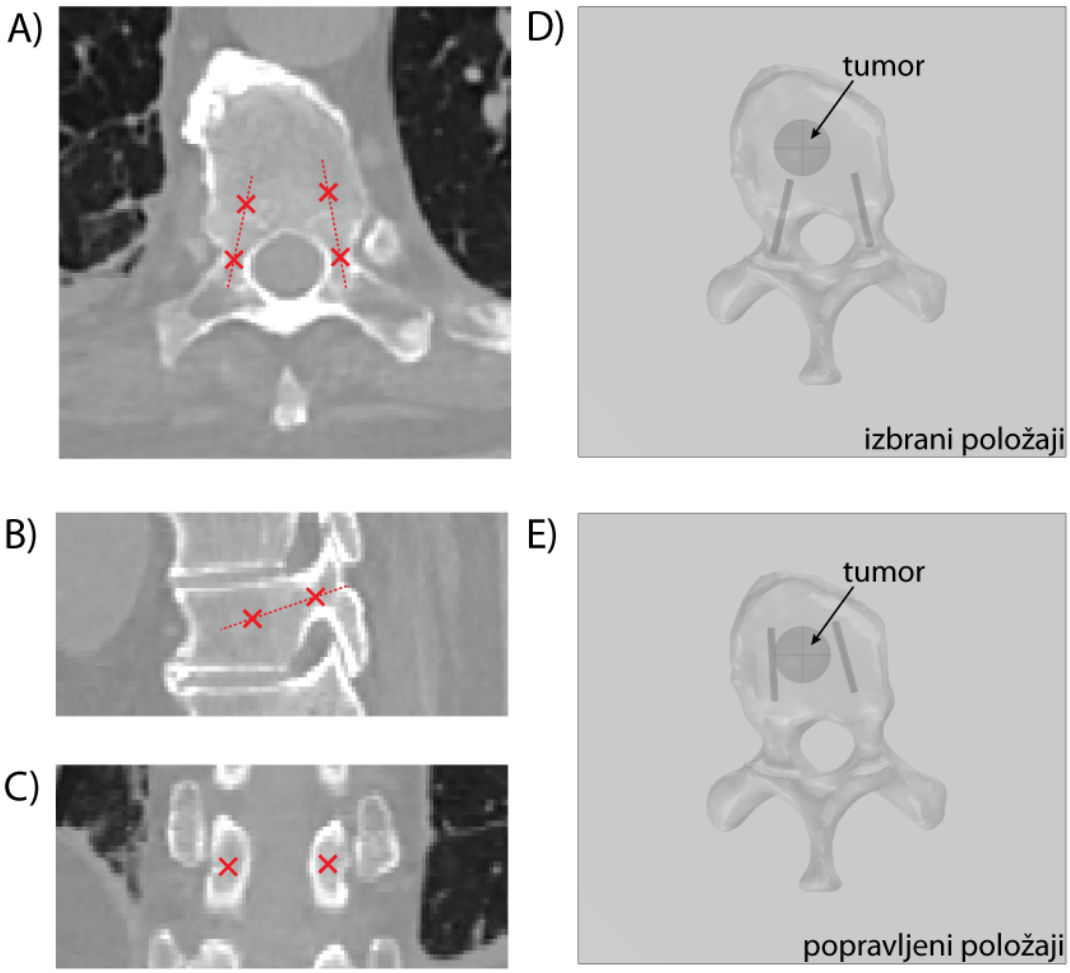

Slika III.8: Primer izbire točk za začetne položaje elektrod na A) aksialni, B) sagitalni in C) koronarni rezini CT slike torakalnega vretenca. D) Geometrija modela v programu COMSOL Multiphysics, ki prikazuje torakalno vretence in sferični tumor z začetnimi položaji elektrod, pridobljenimi iz izbranih točk. E) Popravljeni položaji elektrod po prvi iteraciji algoritma. Slika je povzeta po [102].

IV Zaključek

Klinična uporabnost načrtovanja zdravljenja za zdravljenje z elektroporacijo je bila predhodno že dokazana. Vendar numerični model, ki se uporablja za načrtovanje zdravljenja za ablacijo z ireverzibilno elektroporacijo (ablacija IRE), še ni bil sistematično validiran. Razvili smo izpopolnjeno metodo za validacijo numeričnega modela z uporabo kliničnih podatkov bolnikov, katerih jetrni tumorji so bili zdravljeni z ablacijo IRE. Na podlagi primerjave območja ablacije, ki ga je napovedal numerični model, z dejanskim območjem ablacije, zaznanim na kontrolnem slikanju bolnikov, smo določili prag električnega polja *in silico*, ki se je najbolje ujemal s področjem uspešne ablacije *in vivo*. Naši rezultati kažejo, da lezije, vidne na kontrolnem slikanju z magnetno resonanco 6 tednov po posegu, predstavljajo območja tkiv, ki so bila med zdravljenjem izpostavljena lokalnemu električnemu polju jakosti vsaj 900 V/cm ali več. Študijo sta omejevala retrospektivna narava in neugoden čas kontrolnega slikanja. Ker je numerični model namenjen izračunu območja ablacije na dan zdravljenja, je primerjava s kontrolnimi slikami šest tednov po posegu povzročila precenitev praga IRE, zato nismo mogli učinkovito validirati napovedne sposobnosti modela. Kljub temu je na podlagi metodologije in rezultatov, predstavljenih v tem delu, mogoče učinkovito zasnovati prospektivno klinično študijo, ki bo zagotovila potrebne podatke za nadaljnjo validacijo numeričnega modela in zagotovila zadostno natančnost za klinične potrebe.

Razvili smo tudi model na mezo nivoju, ki je primerljiv z mikroskopskimi slikami, ter ocenili, ali heterogena mikrostruktura jetrnega parenhim ter variabilnost električnih lastnosti le-tega vplivata na električno polje na ravni, ki je pomembna za načrtovanje zdravljenja. Potrdili smo, da mikrostruktura jetrnega parenhima ne vpliva bistveno na porazdelitev električnega polja in da je uporaba popolnoma

homogenega modela jetrnega parenhima primerna za načrtovanje zdravljenja z elektroporacijo. Kljub temu je treba v model vključiti velike jetrne žile in portalne prostore, saj te makrostrukture pomembno vplivajo na porazdelitev električnega polja, kot je bilo predlagano že prej. Poleg tega smo določili prage električnega polja *in silico* , ki so skladni s histopatološkimi spremembami, opaženimi na mikroskopskih posnetkih po zdravljenju. Povprečni prag električnega polja, ki je najbolje ustrezal območju koagulacijske nekroze, je znašal 1225 V/cm, povprečni prag, ki je najbolje ustrezal območju delno poškodovanega jetrnega parenhima, pripisanega IRE, pa 805 V/cm.

Numerični modeli so pomembno orodje za raziskovanje novih pristopov k zdravljenju, preskušanje novih oblik elektrod in analiziranje različnih kliničnih scenarijev brez potrebe po testiranju na živalih in kliničnih raziskavah. Med doktorskim študijem sta bili izvedeni dve študiji, ki sta preučevali različne vidike učinkovitosti in varnosti elektrokemoterapije (EKT) in ablacije IRE v kliničnih scenarijih, ki se pogosto pojavljajo v praksi. Po navodilih proizvajalcev pulznih generatorjev so kovinski vsadki kontraindikacija za zdravljenje z elektroporacijo. Pokazali smo, da je tveganje za neuspeh zdravljenja ali za varnostne težave ob prisotnosti vgrajenega srčnega spodbujevalnika zanemarljivo. Naši rezultati naj bi pripomogli k temu, da bo zdravljenje z elektroporacijo bolnikom bolj dostopno. Po drugi strani pa smo pokazali, da lahko pri metastazah v jetrih prisotnost kovinskih sponk v območju zdravljenja zmanjša učinkovitost zdravljenja zaradi učinka Faradayeve kletke. Glede na te ugotovitve prisotnosti kirurških sponk ne smemo zanemariti pri odločanju o možnostih zdravljenja. Pokazali smo, da prisotnost kovinskih vsadkov ne povzroča dodatnega segrevanja, vendar smo izpostavili tudi nezanemarljiv termični učinek ablacije IRE. Ablacija IRE se pogosto predstavlja kot netermična metoda, zato je obetavna opcija za uporabo na anatomskih mestih, kjer termične poškodbe tkiva niso sprejemljive. Medicinsko skupnost je treba seznaniti s termično komponento ablacije IRE in potrebo po nadzoru temperature med posegom.

Razvili smo tudi nov pristop za zdravljenje metastaz v hrbtenici z EKT ter numerično ovrednotili učinkovitost in varnost pristopa. Zdravljenje metastaz v hrbtenici je še posebej zapleteno zaradi vloge hrbtenice pri podpori in gibanju telesa ter vpletenosti hrbtenjače in živcev. Operacija ostaja najpogostejša izbira za zdravljenje, vendar je povezana s številnimi tveganji in ni vedno izvedljiva.

Zato so potrebni novi in manj agresivni načini zdravljenja metastaz v hrbtenici, da bi bolnikom olajšali simptome in izboljšali kakovost življenja. Pokazali smo, da je lahko EKT s transpedikularnim pristopom varno in minimalno invazivno zdravljenje metastaz v hrbtenici. Rezultati te študije zagotavljajo podlago in dokaze, ki spodbujajo nadaljnjo analizo in preizkuse te potencialne možnosti za zdravljenje sicer težko ozdravljive bolezni.

Zadnji del disertacije je bil namenjen optimizaciji numeričnega modela elektroporacije za izpolnjevanje zahtev načrtovanja zdravljenja v realnem času. Glavni cilj pri načrtovanju zdravljenja z elektroporacijo je določiti najboljši možen položaj elektrod in amplitudo napetosti, ki zagotavljata zdravljenje celotnega kliničnega ciljnega volumna. Ta postopek se še vedno izvaja večinoma ročno ali z računsko zahtevnimi genetskimi algoritmi. Zlasti slednja metoda ni primerna za načrtovanje zdravljenja v realnem času. Razvili smo algoritem za optimizacijo položajev elektrod na podlagi prostorske informacije o porazdelitvi električnega polja v ciljnem tkivu. Algoritem je trenutno zasnovan za EKT tumorjev v hrbtenici s transpedikularnim pristopom, vendar bi ga bilo mogoče prilagoditi tudi za druga anatomska mesta. Algoritem uspešno deluje pri različnih segmentih hrbtenice, različnih velikostih tumorjev in na različnih mestih znotraj telesa vretenc, predvsem pa bistveno skrajša čas in strokovno znanje, ki sta potrebna za izdelavo načrta zdravljenja za EKT tumorjev v hrbtenici.

V Izvirni prispevki k znanosti

Validacija in dopolnitev numeričnega modela za načrtovanje zdravljenja na osnovi elektroporacije

Numerični model za načrtovanje zdravljenja z elektroporacijo še ni bil sistematično potrjen za ablacijo z ireverzibilno elektroporacijo (ablacija IRE). Razvili smo dovršeno metodo za validacijo numeričnega modela z uporabo kliničnih podatkov bolnikov, katerih jetrni tumorji so bili zdravljeni z ablacijo IRE. Zaradi retrospektivne narave študije in neugodnega časa kontrolnega slikanja nismo mogli učinkovito validirati napovedne sposobnosti modela. Kljub temu lahko na podlagi metodologije in rezultatov, predstavljenih v tem delu, učinkovito oblikujemo prospektivno klinično raziskavo, ki bo zagotovila potrebne podatke za popolno validacijo numeričnega modela in zadostno natančnost za klinične potrebe. Podatkovna baza, ki vsebuje vse segmentacije slik, izračunane 3D porazdelitve električnega polja, 3D površinske modele jeter, tumorjev in ablacijskih volumnov, je javno dostopna v spletnem repozitoriju in se lahko uporablja za prihodnje raziskave.

Razvili smo numerični model jeter na mezo nivoju, primerljiv z mikroskopskimi slikami vzorcev, s katerim smo ocenili, ali heterogena struktura jetrnega parenhima in spremenljivost električnih lastnosti mikrostruktur parenhima vplivata na električno polje na ravni, ki je pomembna za načrtovanje zdravljenja. Pokazali smo, da mikrostruktura jetrnega parenhima ne vpliva bistveno na porazdelitev električnega polja na mezo nivoju in da je uporaba popolnoma homogenega modela jetrnega parenhima primerna za načrtovanje zdravljenja z elektroporacijo. Poleg tega smo določili pragove električnega polja *in silico*, ki so skladni s histopatološkimi spremembami, vidnimi na mikroskopskih posnetkih po zdravljenju,

in sicer območje koagulacijske nekroze in območje delno poškodovanega jetrnega parenhima, ki ga je mogoče pripisati IRE.

Numerična evalvacija varnosti in novih pristopov zdravljenja na osnovi elektroporacije

Raziskali smo učinkovitost in varnost elektrokemoterapije (EKT) in ablacije IRE v dveh pogostih kliničnih scenarijih: prisotnost kovinskih kirurških sponk v jetrih v bližini področja ablacije in zdravljenje v bližini vsajenega srčnega spodbujevalnika. Pokazali smo, da ablacija IRE lahko povzroči tudi termične poškodbe tkiva, kar se lahko izkaže za škodljivo, če se pri načrtovanju postopka ne upošteva. Nazadnje smo razvili nov pristop za zdravljenje metastaz v hrbtenici z EKT s transpedikularnim pristopom. Numerično smo ocenili učinkovitost in varnost pristopa ter dokazali, da je predlagani pristop varna in minimalno invazivna opcija za zdravljenje metastaz v hrbtenici. Rezultati te študije zagotavljajo podlago in dokaze, ki spodbujajo nadaljnjo analizo in eksperimentiranje s to potencialno možnostjo zdravljenja sicer težko ozdravljive bolezni.

Optimizacija numeričnega modela elektroporacije in priprava koncepta za računalniško podprto načrtovanje zdravljenja v realnem času

Zadnji del doktorskega študija je bil namenjen optimizaciji numeričnega modela elektroporacije, da bi se približali zahtevam načrtovanja zdravljenja v realnem času. Razvili smo algoritem za določitev optimalnih položajev elektrod in amplitud napetosti za EKT tumorjev v hrbtenici s transpedikularnim pristopom. Ta študija je bila prvi poskus uporabe prostorske informacije o porazdelitvi električnega polja v tkivu za določitev optimalnih parametrov zdravljenja. Pokazali smo, da algoritem bistveno skrajša čas in strokovno znanje, potrebno za izdelavo načrta zdravljenja. Z algoritmom je bil povprečni čas za iskanje optimalnih parametrov zdravljenja 71 s, najdaljši čas pa 253 s, kar zadostuje za izračun v realnem času. Pričakujemo, da bo razviti algoritem pomembno prispeval k razvoju računalniško podprtega načrtovanja zdravljenja v realnem času. Izvorna koda algoritma in vsi modeli, ustvarjeni v tej študiji, so javno dostopni v spletnem repozitoriju in se lahko uporabijo za prihodnje raziskave.

Numerical modeling and treatment planning for clinical applications of electroporation

1 Introduction

Electroporation is a phenomenon in which short high-voltage electric pulses are used to alter the integrity of the cell membrane and consequently increase membrane permeability. Under the influence of an electric field, membrane lipids are redistributed to form hydrophilic pores, and chemical reactions take place on the lipids and transport proteins that further increase permeability and allow the passage of various molecules that would otherwise not pass through the membrane or would do so with difficulty. With appropriate choice of pulse parameters – namely, the amplitude, duration and number of applied pulses – the phenomenon can be either reversible or irreversible. In reversible electroporation, the cell membranes quickly return to their original state and the cells' ability to divide and function is not affected in the long term, whereas in irreversible electroporation, the cells lose their functionality and die [1]–[4].

Electroporation has attracted interest for applications in medicine, biotechnology, and food processing [5]–[8]. Currently, the most developed application of electroporation in medicine is reversible electroporation used to facilitate the transport of various molecules into cells; the most notable treatments being electrochemotherapy (ECT) and gene electrotransfer (GET) [9]–[13]. Also gaining considerable interest is irreversible electroporation (IRE), which is used as a focal ablation method for the treatment of tumors in oncology and for pulmonary vein isolation in the treatment of atrial fibrillation [14]–[23]. It is generally accepted that reversible and irreversible electroporation occur in tissue at a certain electric field strength, i.e., the reversible and irreversible electroporation threshold. Complete coverage of the target tissue volume with an electric field above the reversible or irreversible threshold is therefore required to achieve a therapeutic effect in electroporation-based treatments [24]. The distribution of the electric

field in the tissue depends mainly on the electrode geometry and electrical properties of tissues. Over the years, various electrode designs and configurations have been developed to meet different therapeutic requirements, and a wide range of pulse protocols are used in practice.

1.1 Clinical applications of electroporation

1.1.1 Electrochemotherapy

Electrochemotherapy (ECT) combines chemotherapy with reversible electroporation with the goal of increasing the anti-tumor effect of the chemotherapeutic agent. In this treatment, a single dose of a chemotherapeutic agent is administered either systemically or locally, followed by the delivery of electric pulses to the tumor volume when the concentration of the drug in the tumor reaches its peak [25], [26]. The membrane permeability of cells is temporarily increased, allowing transport of chemotherapeutic agents across the membrane into the cells and thus increasing the uptake of the drug. Non-permeable (bleomycin) or poorly permeable (cisplatin) chemotherapeutic agents with intracellular target are used for this purpose. Studies have shown that electroporation can increase the cytotoxic effect of cisplatin by 80-fold [27] and that of bleomycin by a hundred to a thousand-fold [10], [28], which reduces the necessary dose of the chemotherapeutic agent and thus reduces the negative side effects of the treatment. In addition to the increased cytotoxic effect the vascular effects of electroporation and involvement of the immune response have been identified as contributing factors to treatment efficacy [29], [30].

The first and most widely known pulse protocol for ECT was introduced in 1991 by Mir *et al* [9] and consists of 8 rectangular pulses of 100 µs duration and a pulse repetition rate of 1/s. This protocol is still used today in ECT, but in some commercially available devices, such as the Cliniporator (IGEA S.P.A., Italy), it has been adapted to deliver pulses at a higher pulse repetition rate of 5000/s instead of 1/s. The application of electric pulses causes stimulation of (electrically) excitable tissues such as muscles, nerves, and cardiac muscle near the treatment zone, resulting in muscle contractions and acute pain. Studies have shown that

increasing the pulse repetition rate from 1/s to 5000/s significantly reduces muscle stimulation and associated adverse effects without compromising treatment efficacy [31], [32]. Moreover, to avoid the risk of triggering cardiac arrhythmias during thoracic procedures, pulse delivery is synchronised with the patient's electrocardiogram, so that the pulses are delivered in the absolute refractory period [33], [34].

ECT has been used mainly to treat superficial tumors because of the ease of application and good cosmetic results of the treatment. Recently, however, deeper tumors, such as those in the brain, liver, esophagus, colon, and bones [35]–[42] are being investigated as possible targets for ECT. In ECT, the optimal treatment is considered to be reversible electroporation in the entire clinical target volume (tumor with a safety margin) with minimal electroporation in the surrounding healthy tissue.

1.1.2 Irreversible electroporation ablation

Irreversible electroporation (IRE) is used as a focal ablation method for various soft tissues and tumors. This treatment aims at direct destruction of the target tissue with the electric field; for this purpose, a higher amplitude and number of pulses than in ECT are used, prolonging the exposure of the cells to the electric field. Pulse protocols vary from study to study, but typically 70–100 electric pulses are used per pair of electrodes, and the duration of each pulse being 50–100 µs. Pulse delivery is synchronized with the patient's electrocardiogram so that pulses are delivered in the absolute refractory period to minimize the risk of inducing arrhythmias. According to the manufacturer's instructions (of pulse generators), the pulse amplitude is usually determined by a fixed voltage-to-distance ratio and the distance between the paired electrodes. In IRE ablation, the optimal treatment is considered to be irreversible electroporation of the entire clinical target volume (tumor with a safety margin) with minimal tissue heating and minimal irreversible electroporation of the surrounding healthy tissue.

Because the cell-killing mechanism of IRE is not temperature dependent, IRE ablation is a treatment of choice when established thermal ablation methods such as radiofrequency and microwave ablation cannot be used safely or their efficacy

is limited. For example, when anatomical structures are present within or near the treated area that are sensitive to thermal damage (e.g., bile ducts or intestinal wall), or when large blood vessels reduce the effectiveness of thermal ablation due to the heat sink effect [33], [43]–[45]. An important benefit of IRE is also that only the cell membranes are affected, while other structures in the intercellular space remain intact, which preserves the integrity of the tissue resulting in reduced scarring and allowing faster tissue regeneration [46].

The most recent development in pulse protocols for IRE is the so-called high-frequency IRE or H-FIRE [47]–[49]. In H-FIRE, bipolar pulses are used instead of monopolar pulses used in the classic IRE (and ECT) protocols. The bipolar pulses consist of two pulses of opposite polarity separated by a pause. The duration of a single polarity pulse and the delay between pulses are in the range of a few microseconds (1–10 µs), and the repetition rate of the bipolar pulses is in the range of 50000-125000/s. The short duration of the pulses and the higher repetition rate offer several advantages over longer monopolar pulses, such as a higher threshold for stimulating excitable tissues, thereby reducing pain and muscle contractions [50]. H-FIRE is particularly promising for cardiac use, namely for pulmonary vein isolation in the treatment of atrial fibrillation [21]–[23], [51].

1.1.3 Gene electrotransfer

In gene electrotransfer (GET), we use electrical pulses to introduce protein-encoding plasmid DNA (pDNA) into tumor or healthy cells to produce a protein or shut down a defective or overexpressed gene [12], [52]–[54]. GET is a multi-step process involving interaction of pDNA with the cell membrane, translocation across the cell membrane, migration through the cytoplasm, translocation across the nuclear envelope, and finally gene expression [55]. The two most developed GET applications in oncology are cytokine therapy, in which cytokine-encoding plasmids are introduced into tumor cells, and DNA vaccination, in which pDNA encoding a specific antigen is administered intramuscularly or intradermally to protect the body from cancer cells expressing that antigen [8].

The pDNA is injected locally into the target tissue a few seconds before the pulses are applied. Unlike the chemotherapeutic agents in ECT, the pDNA

molecules are not electrically neutral and are too large to enter the cells by diffusion. Therefore, a combination of short (microsecond range) high-voltage pulses and long (millisecond range) low-voltage pulses are used to permeabilize the cell membrane and electrophoretically deliver the pDNA to the target site, respectively. The electrophoretic force acts on the negatively charged pDNA during pulse delivery, bringing a greater number of pDNA molecules into contact with the cell membrane than would be possible by diffusion alone. Plasmid DNA aggregates form at the cell membrane, which later enter the cells by endocytosis [54].

The optimal dose of pDNA and pulse protocols for GET are still under development; the efficiency of GET varies widely between cell types, and the causes of these differences are not well understood [54]. Unlike in ECT and IRE ablation, the target tissue volume is not as easily defined for GET. In addition, irreversible electroporation within the target volume is not tolerated in GET because cells must survive to successfully express the transfected gene.

1.2 Treatment planning

The success of electroporation-based treatments depends on good coverage of the clinical target volume (CTV) with a sufficiently high electric field. The CTV may represent the tumor mass with the safety margin in tumor treatment, the volume of soft tissue to be ablated in cardiac ablation, or the tissue volume to receive the genetic material in gene therapy. Electroporation is considered a threshold phenomenon, so the entire CTV should be covered with an electric field above the reversible electroporation threshold for ECT and GET or irreversible electroporation threshold in the case of IRE ablation.

Superficial targets, such as skin tumors, are generally treated using applicators with fixed geometry needle electrodes. With this type of applicators, the treatment parameters are already established, and the procedure consists of multiple pulse deliveries with the applicator to cover the entire CTV. Superficial procedures are not technically very demanding and generally do not require treatment planning, as targets can be identified visually. For minimally invasive treatment

of deep-seated targets, such as tumors in the liver, multiple single-needle electrodes are used in pairs. This type of electrodes are the most versatile; however, its placement is challenging and requires an experienced interventional radiologist [56]–[58]. According to the manufacturer's instructions (and current teachings), the electrodes should be placed parallel to each other and at the same depth. These requirements, however, are not mandatory for a successful treatment, but allow intuitive prediction of the resulting electric field.

In reality, ideal parallel electrode placement is difficult to achieve due to anatomical constraints and bending of the electrodes. Any error in electrode placement will affect the distribution of the electric field. In addition to the electrode geometry, the dielectric properties of tissue and their uncertainty and variability also have a significant effect on the resulting distribution of the electric field in the CTV. Therefore, determining the distribution of the electric field in deep-seated targets is not a trivial task. Therefore, it is advisable to apply some form of treatment planning to ensure a successful treatment outcome [59]–[61]. The use of computer-assisted treatment planning also eliminates the need for electrodes to be fully parallel, making the procedures less constraining.

Treatment planning based on numerical modeling and computation of electric field has shown promise in helping clinicians performing electroporation-based treatments. The main goal in creating a treatment plan is to determine the optimal electrode placement and pulse parameters to reliably cover the entire CTV and minimise damage to surrounding tissues. We also need to ensure that the electrode placement and pulse delivery are technically feasible. In 2015, Visifield (www.visifield.com, University of Ljubljana, Slovenia) launched the first online tool for creating patient-specific plans for EP-based treatments [62], [63]. However, the tool is currently intended for research and provides proof of concept and is not available for clinical use. In 2022, PIRET, an offline platform for irreversible and reversible electroporation therapies [64], was made available for research under a partnership agreement with the developer. While both tools allow the user to create and visualise a hypothetical treatment plan, neither provides any optimization of the treatment parameters; the creation of the treatment plan is therefore left entirely to the user.

Currently, patient-specific treatment plans are based on patients' preinterven-

tional images, which can be several days or even weeks old. In a typical planning workflow, the patient's preinterventional images (MRI or CT) are first segmented into tissues of interest, for example, the tumor mass, surrounding healthy tissue, and other important nearby anatomical structures such as blood vessels, bile ducts, and nerves. Then, an anatomically accurate 3D numerical model is created from the segmented tissue masks and imported into finite element analysis software, for example, COMSOL Multiphysics (www.comsol.com, Comsol Inc, Sweden) or FreeFem++ (https://freefem.org/, UPMC, France) [137]. The model is finalized by assigning electrical and thermal properties to each tissue in the model to reflect the physical conditions in the body as closely as possible.

The next step is to determine the electrode positions and pulse parameters, while taking into account any anatomical and technical constraints. Determining the electrode placement involves planning the best path of insertion to avoid delicate anatomical structures, determining the number of electrodes to be used, their position within and around the target, and the exposure length (i.e., the length of the conducting part). The most important parameter to be determined for pulse delivery is the voltage amplitude to be delivered to specific electrode pairs. The length and number of pulses can also be set. However, these parameters are application specific and are usually not optimised during the treatment planning phase.

The electric field distribution is then computed in the model using the finite element method. The numerical methods for calculating the electric field during electroporation are discussed in more detail in Section 1.3 *Numerical models of electroporation*. The finalized treatment plan provides the physician with a graphical representation of the trajectory of electrode insertion and final electrode placement, the optimal pulse parameters to be delivered to specific electrode pairs, the expected electric current consumption, and a visualization of the expected electric field distribution in the tissue and coverage of the CTV. The treatment plan can be coupled with navigation or robotic systems to allow faster and more precise placement of electrodes [65]–[67].

Currently, treatment plans are still mainly prepared "manually". This process usually requires several iterations where the operator changes the electrode positions between computations. After each iteration, the operator must visually

inspect the electric field (usually as an overlay over the medical image), determine the potentially undertreated areas of the CTV, reposition the electrodes accordingly, and repeat the process. This approach requires a high level of expertise, as the distribution of the electric field in inhomogeneous tissue and the impact of electrode positioning and pulse parameters are not always intuitive. Most attempts to optimize this process are based on either genetic algorithms or parametric sweeps [60], [68], [69], which are time-consuming and require significant computational power.

Because treatment plans are generated from preinterventional images prior to surgery, they are of limited use to the clinician. The patient's physique may change dramatically between the preinterventional and interventional phases, for example, due to weight loss or tumor growth. In addition, the patient's position during the procedure is often different from that during preinterventional imaging, which can lead to organ deformities. Therefore, accurate placement of the electrodes according to the pretreatment plan is often difficult to achieve. Coupling the preinterventional treatment plan with navigation systems contributes to more accurate electrode placement [65], [66]. However, to truly realize the potential of treatment planning, the entire process would need to be shifted from the preinterventional phase to the interventional phase. In other words, the plan would need to be created during the intervention based on actual electrode placement and with real-time control of the applied parameters. The manual approach to treatment planning or the use of genetic algorithms are not viable options for real-time planning, as both approaches are too time-consuming.The use of low-cost optimization algorithms would simplify and accelerate the search for optimal treatment parameters for electroporation-based treatments.

1.3 Numerical models of electroporation

1.3.1 Stationary models

Numerical models of electroporation are based on solving the Laplace partial differential equation (PDE) for the electric potential V in stationary conditions (Eq. 1.1) [70]–[72].

$$\nabla \cdot (\sigma \nabla V) = 0 \tag{1.1}$$

$$E = -\nabla V \tag{1.2}$$

Currently, most electroporation-based treatments use 50–100 µs long pulses, which means that all transient phenomena of electroporation have settled long before the end of the pulse and stationary conditions can be used for the computation of the electric field. The electric field E is derived (Eq. 1.2) from the computed electric potential V and the electrical conductivity σ of the medium, i.e. the biological tissue. The phenomenon of electroporation is implemented in the model by a nonlinear increase of the tissue electrical conductivity due to the local electric field [70], [73]–[77].

In 2005, Šel *et al* [70] presented the first experimentally supported sequential model of electroporation in which the dependence of electrical conductivity on electric field strength was modelled using a sigmoid function. If the local electric field strength in the tissue exceeds the threshold for reversible electroporation, the conductivity of the tissue increases from its baseline value as a function of the field strength. If the electric field exceeds a certain threshold, the conductivity increases to its maximum value and does not increase further with the applied electric field [78]. Most models today use some form of a sigmoid function to describe the increase in conductivity [79]:

$$\sigma(E) = \sigma_0 \cdot (1 + sigmoid(E, E_1, E_2, A)), \tag{1.3}$$

where E is the local electric field in the tissue, σ_0 is the baseline electrical conductivity of the tissue, E_1 is the threshold electric field at which conductivity starts increasing, E_2 is the electric field at which the conductivity stops increasing, and A is the factor of maximum conductivity increase at electric fields above E_2. Figure 1.1 shows an example of the dynamic conductivity as a function of the electric

field strength. Different tissues have very different properties and responses to the electric field, so the dynamics of the conductivity increase vary from tissue to tissue. Therefore, the parameters of the sigmoid function, namely σ_0, E_1, E_2, and A in Equation 1.3, are tissue dependent [24], [76]. Moreover, studies have shown that the parameters E_1 and A may also depend on the number of pulses [77].

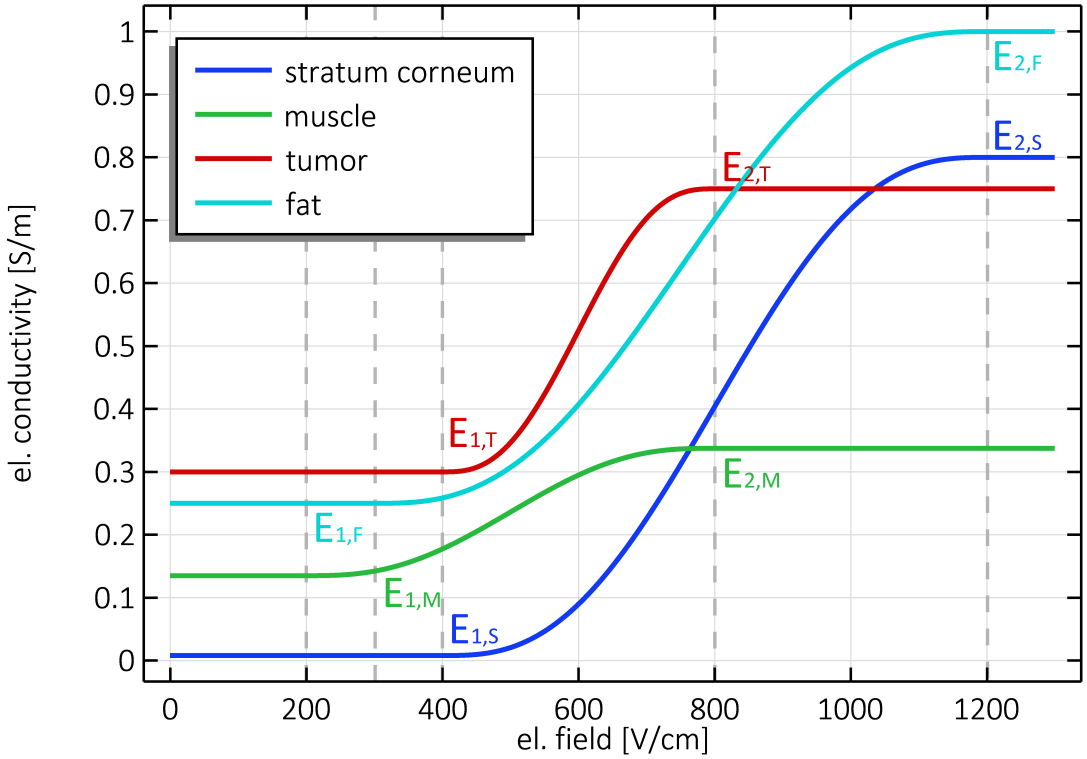

Figure 1.1: The effect of electroporation on the electrical conductivity of different tissues can be described by sigmoidal functions. The baseline conductivity starts to increase when the applied electric field exceeds the threshold for reversible electroporation, and reaches a maximum when the field exceeds the threshold for irreversible electroporation. The reversible (E_1) and irreversible (E_2) thresholds are indicated by dashed lines (S – stratum corneum, M – muscle, T – tumour, F – fat). The figure is reproduced from [80].

1.3.2 Time domain models

In recent studies, tissue heating during electroporation is also included in the model, which requires a computation in the time domain. While the thermal component is not particularly pronounced in reversible electroporation, hundreds of pulses are delivered to the tissue in IRE ablation, resulting in significant Joule heating near the electrodes, which can affect treatment safety [43], [81]–[83]. In addition, time domain models allow modeling of different pulse shapes, e.g., monopolar, bipolar, and exponential pulses, as well as the dynamics of pulse delivery, e.g., pulse length, delay between pulses, and repetition rate [84]–[86]. This is important for the development of new pulse protocols, such as for H- FIRE, or the study of electroporation mechanisms, e.g., the electrochemical reactions during pulse delivery.

Tissue heating during electroporation is most commonly modelled with the modified Pennes' bioheat equation (Eq. 1.4) [87], [88]:

$$\rho C \frac{\partial T}{\partial t} = \nabla(k \nabla T) + Q_{bio} + \sigma \left|E\right|^2, \tag{1.4}$$

where ρ, C and k are density, heat capacity, and thermal conductivity of tissue, respectively, T is tissue temperature, and t is time. The bioheat source term Q_{bio} represents blood perfusion and metabolic activity, and $\sigma \left|E\right|^2$ is the Joule heating term.

Tissue electrical conductivity is also a function of the temperature. The relationship between the conductivity and the temperature rise is usually described by a linear equation (Eq. 1.5) that assumes a constant temperature coefficient [89], [90]:

$$\sigma(T) = \sigma_0 \cdot (1 + \alpha_T \cdot \Delta T), \tag{1.5}$$

where α_T is the temperature coefficient, ΔT is the temperature difference with respect to the initial tissue temperature and σ_0 is the baseline electrical conductivity.

Increased temperature can increase electrical conductivity even beyond its maximum value caused by the local electric field (Eq. 1.3). The dynamic electrical conductivity of tissue is therefore a function of both the electric field and

temperature. Equation 1.6 shows an example of modeling this co-dependence by a combination of Equations 1.3 and 1.5:

$$\sigma(E,T) = \sigma(E) \cdot (1 + \alpha_T \cdot \Delta T), \tag{1.6}$$

where $\sigma(E)$ represents the nonlinear increase due to the electroporation effect (Eq. 1.3). Considering the combined effect of electroporation and heating, the tissue conductivity becomes a nonlinear function of the electric field and temperature $\sigma(E,T)$ in the Laplace PDE (Eq. 1.1) and the Pennes bioheat equation (Eq. 1.4), respectively. Other approaches to modeling the combined thermal and electroporation effects have been explored as well [77], [91]. It needs to be acknowledged, though, that it is difficult to decouple the two dependencies.

1.3.3 Statistical models of cell survival

Statistical models are another possible approach to determine tissue response to electroporation. Rather than evaluating the efficacy of the treatment based on a fixed electric field threshold, we can calculate the probability of cell survival. The Peleg-Fermi model is the most commonly used statistical model for electroporation [57], [92]–[95]. The probability of cell survival S and cell death P are calculated as follows:

$$S(E,n) = \frac{1}{1 + exp\left(\frac{E - E_c(n)}{B(n)}\right)}, \tag{1.7}$$

$$P(E,n) = 1 - S(E,n), \tag{1.8}$$

where n is the number of pulses, E is the local electric field, E_c is the critical electric field at which 50 % of targeted cells die, and B is the shape factor defining the size of the transition zone. The parameters E_c and B are functions of the number of pulses and must be determined experimentally for each tissue. The nature of the probability calculation allows multiplying different probabilities, where resulting product gives an equal or lower probability of cell survival. This can be used to model scenarios where the target tissue is cumulatively exposed to pulses from independent pairs of electrodes, since the probability of cell survival decreases with prolonged exposure to the electric field.

The probability of cell death due to thermal damage is also determined by a statistical model. The most common method is to integrate the Arrhenius reaction rate constant over the treatment time period (Eq. 1.9) and transforming it into probability of cell death (Eq. 1.10):

$$\Omega(t) = \int_0^{t_{end}} \zeta \cdot exp\left(\frac{-E_a}{R \cdot T(t))}\right) dt, \tag{1.9}$$

$$P = 100 \cdot (1 - exp(-\Omega(t)), \tag{1.10}$$

where ζ represents the pre-exponential frequency factor, E_a is the activation energy, R is the universal gas constant, and P is the probability of cell death expressed in percentage.

1.4 Aims of the dissertation

The overarching aim of this dissertation is to improve electroporation-based treatments through numerical modeling and computer-assisted treatment planning. Numerical models are an important tool for analyzing complex phenomena in biological tissue during electroporation. They allow us to investigate new treatment approaches, test new electrode designs, and analyze different clinical scenarios, their feasibility and safety. Computational experiments with numerical models also allow testing a large number of parameters and thus can guide experiments, which can significantly reduce the number of experiments or preclinical tests and facilitate the development of electroporation-based treatments.

One of the most important applications of numerical modeling is computer-assisted treatment planning. A prerequisite for the success of all electroporation-based treatments is the complete coverage of the clinical target volume with a sufficiently high electric field. Accurately determining the distribution of the electric field in tissue, especially for deep-seated targets, is not a trivial task. Treatment planning based on patient-specific numerical models and optimization of treatment parameters is advisable to ensure a successful treatment outcome.

Before numerical models can be used in actual clinical applications, e.g., for treatment planning, they need to be validated using experimental and

(pre)clinical data. Therefore, the aim of this dissertation was to validate the developed numerical model of irreversible electroporation ablation in the liver using existing clinical data. The goal of the validation is to determine the ability of the developed numerical model to predict treatment outcomes, to ensure that it is sufficiently robust and accurate for clinical needs and can ultimately be used for patient-specific treatment planning in routine clinical practice.

Many aspects of the clinical applications of electroporation have yet to be adequately explored. For example, the heat-generating effect of irreversible electroporation has not been thoroughly quantified, or the presence of implanted devices with metallic parts is still considered a contraindication to electroporation-based treatments. We will use numerical models to investigate the feasibility and safety aspects of electrochemotherapy and irreversible electroporation ablation in different and potentially compromising clinical situations, with the aim of improving the safety and accessibility of electroporation-based treatments.

Despite technological advances, treatment planning is still not part of routine clinical practice for electroporation-based treatments; the major limitation stems from the fact that plans are currently created prior to the procedure. The development of real-time treatment planning using actual electrode positions will allow real-time control of treatment parameters and treatment outcome, and is a critical step toward introducing computer-assisted treatment planning into routine clinical practice. The final aim of this dissertation is to explore ways to make numerical models and treatment planning procedures fast and robust so that they can eventually be used in real-time.

2 Research papers

The work carried out during the doctoral studies is presented in six original scientific papers published in international journals. At the beginning of this chapter, a brief overview of the research and the connection between the works is given. The methodology and results are presented and discussed in detail in the papers; therefore, the main part of this chapter consists of the published papers.

The main objective of the first paper *Retrospective study for validation and improvement of numerical treatment planning of irreversible electroporation ablation for treatment of liver tumors* (Cindrič *et al.* 2021) was to validate the numerical model for planning electroporation-based treatments using clinical data. For this purpose, we numerically reconstructed 18 clinical cases of irreversible electroporation (IRE) ablation of liver tumors and calculated the treatment outcome using a previously developed and improved numerical model for treatment planning. We compared the simulation results with the clinical response in the tissue as seen on 6-week follow-up imaging, and determined the *in silico* electric field threshold in the numerical model that corresponded to successful ablation of the target tissue *in vivo* as seen on follow-up imaging. In addition, we evaluated the heat-generating effect of the classic IRE ablation protocol and demonstrated the utility of treatment planning to improve future procedures. In this study, we developed a sophisticated method to validate the numerical model for treatment planning. Based on these results, a future prospective study can be effectively designed to provide the necessary data to further validate the model and ensure sufficient accuracy to meet clinical needs.

In addition to planning electroporation-based treatments, numerical modelling is an essential tool for investigating new treatment approaches, testing

new electrode designs, and analysing different clinical scenarios without the need for animal testing and clinical trials. This was the main topic of the following four papers.

In the second paper *Numerical mesoscale tissue model of electrochemotherapy in liver based on histological findings* (Cindrič *et al.* 2022), we investigated how the heterogeneous anatomical structure of the liver affects the distribution of the electric field during electrochemotherapy (ECT). We created a mesoscale model of the liver that incorporates both liver macro- and microstructures and is comparable to findings from microscopic images. We numerically reconstructed four ECT procedures in a healthy porcine liver, performed in a recent *in vivo* animal model study [98]. The electric field distribution and tissue heating were calculated using the previously developed numerical model for planning electroporation-based treatments and the results were compared with the histopathological changes observed in the microscopic tissue samples. We performed a parametric study to determine whether the microstructures of the liver (hepatic lobules, interlobular septa, and centrilobular veins) and the variability of their electrical conductivity affect the distribution of the electric field to a degree relevant for comparison with histopathological findings. Moreover, we determined the electric field thresholds that best matched the histopathological changes observed in the tissues after ECT, namely the zone of coagulation necrosis and a zone of partially damaged liver parenchyma. We also evaluated the temperature rise and the likelihood of thermal damage to the tissue, focusing particularly on sensitive anatomical structures such as vessels and bile ducts.

For safety reasons, electroporation-based treatments remain contraindicated for patients with implanted metallic implants, such as pacemakers and stents, near the treated region. Metallic implants have a much higher electrical conductivity than biological tissue and may affect the distribution and strength of the electric field during electroporation as well as the heating of the tissue. In the third paper *Peri-tumoral Metallic Implants Reduce the Efficacy of Irreversible Electroporation for the Ablation of Colorectal Liver Metastases* (Cornelis *et al.* 2019), we investigated the effects of metallic surgical clips within the ablation zone on the safety and efficacy of percutaneous IRE ablation of colorectal liver metastases (CRLM). The study consists of two parts. In the first part, a retrospective statistical analysis was performed on 25 patients in whom IRE was

used to treat 29 CRLM. Several parameters, including the presence of metallic implants within 1 cm of the ablation zone, were assessed as determinants of local tumor progression after treatment with IRE. In the second part of the study, which is addressed in this dissertation, a subset of eight patients, four with metallic implants in close proximity to the tumor and four without, were studied using patient-specific numerical models to determine local electric field distribution, tissue heating, and the probability of cell death around the implants. We have shown that patient-specific numerical models can be used as a tool to determine the mechanism by which metallic implants affect IRE treatment outcome.

The fourth paper *Investigation of safety for electrochemotherapy and irreversible electroporation ablation therapies in patients with cardiac pacemakers* (Jarm *et al.* 2020), further investigates the presence of metallic implants near the treatment zone. Two questions were investigated in this study: can the electroporation pulses interfere with the implanted pacemaker, and can the metal housing of the pacemaker alter the distribution of the electric field in the tissue in a way that compromises the efficacy and safety of the treatment? The second question was investigated by numerical modeling of the physical conditions when electroporation pulses are applied near the implanted pacemaker and is addressed in this dissertation. Two scenarios for the treatment of a subcutaneous tumour in the vicinity of an implanted pacemaker were studied: electrochemotherapy and irreversible electroporation ablation. In both scenarios, the influence of a metal-encased pacemaker with and without contact to one of the electrodes was studied and compared with a control scenario without a pacemaker. The influence on the electric field distribution as well as the tissue heating was investigated.

In the fifth paper *Electrochemotherapy of spinal metastases using transpedicular approach – A numerical feasibility study* (Cindrič *et al.* 2018), we used numerical modeling to investigate the feasibility and safety of a new less invasive treatment approach. We developed a novel approach for the treatment of spinal metastases, namely the transpedicular approach, which combines electrochemotherapy with already established technologies for the insertion of fixation screws in spinal surgery. In this study, three clinical cases of spinal tumours with varying degrees of spinal canal involvement were investigated. One of the cases was previously presented in [128]. Anatomically accurate patients-specific numerical models were created for all three cases, and numerical calculations of the

distribution of the electric field in the tumour and surrounding tissue were performed to determine the treatment outcome and potential damage to the spinal cord and nerves. This study shows how numerical modeling can be used to investigate new treatment approaches.

One of the most important applications of numerical modeling is computer-assisted treatment planning. Despite the technological advances in numerical modeling and simulation, computer-assisted treatment planning is still not part of standard clinical practice. The final part of this research focuses on optimising numerical modeling to improve the treatment planning process aiming towards real-time treatment planning.

The sixth paper *Optimization of transpedicular electrode insertion for electroporation-based treatments of vertebral tumors* (Cindrič *et al.* 2022) presents an algorithm for optimizing electrode positions (and voltage amplitudes) based on spatial information about the electric field distribution in the target tissue. The treatment planning process mainly consists of determining the best possible electrode positions and voltage amplitudes to ensure treatment of the entire clinical target volume. This process is still mainly performed manually, which requires a high level of expertise, or the use of computationally intensive genetic algorithms. In this study, we developed an algorithm to optimize electrode positions for electrochemotherapy of vertebral tumors without using computationally intensive methods. By using the algorithm, the amount of time and user expertise required to create a treatment plan for vertebral tumors is significantly reduced. The use of fast and robust algorithms improves and accelerates the treatment planning process, contributing to the development of real-time treatment planning for electroporation-based treatments.

2.1 Paper 1

Title: **Retrospective study for validation and improvement of numerical treatment planning of irreversible electroporation ablation for treatment of liver tumors**

Authors: **Helena Cindrič**, Panchatcharam Mariappan, Lukas Beyer, Philipp Wiggermann, Michael Moche, Damijan Miklavčič and Bor Kos

Publication: *IEEE Transactions on Biomedical Engineering*, vol. 68, no. 12, pp. 3513-3524, December 2021

Impact factor: 4.756 (2021)

Quartile: Q2

Rank: 37/98 (Biomedical Engineering)

DOI: https://doi.org/10.1109/TBME.2021.3075772

IEEE TRANSACTIONS ON BIOMEDICAL ENGINEERING, VOL. 68, NO. 12, DECEMBER 2021 3513

Retrospective Study for Validation and Improvement of Numerical Treatment Planning of Irreversible Electroporation Ablation for Treatment of Liver Tumors

Helena Cindrič, Panchatcharam Mariappan, Lukas Beyer, Philipp Wiggermann, Michael Moche, Damijan Miklavčič, and Bor Kos

Abstract*—*Objective: **The aims of this study were to determine the electric field threshold that best fits the local response to irreversible electroporation (IRE) ablation of hepatic tumors as seen in follow-up MRI; to numerically evaluate the heat generating effect of IRE; and to demonstrate the utility of treatment planning to improve procedures in the future. *Methods:* 18 cases of hepatic tumors treated with IRE ablation were numerically reconstructed and treatment outcome was computed with a numerical treatment planning framework. Simulated ablation volumes were compared to ablation volumes segmented from 6-week follow-up MRI. Two cases with a high thermal component were selected for numerical optimization. *Results:* The best fit between segmented and simulated ablation zones was obtained at 900 V/cm threshold with the average absolute error of 5.6 $\pm$ 1.5 mm. Considerable heating was observed in 7/18 cases, where >50% of tumor volume experienced heating likely to cause thermal damage. In the selected two cases, thermal damage was eliminated with adjustment of applied voltages. *Conclusion:* Lesions visible on MRI 6 weeks post IRE represent areas that experienced an electric field of 900 V/cm or higher. This threshold is higher than previously reported for IRE of hepatic tumors. It is likely the 6-week follow-up period was too long and the ablation zone has already shrunk considerably, resulting in overestimation of the threshold. *Significance*: We developed a sophisticated method for validation of the numerical treatment planning framework. A future prospective study can be effectively designed based on the findings of this study.**

***Index Terms*—Irreversible electroporation (IRE), liver tumors, numerical modelling, treatment planning, tumor ablation.**

Manuscript received November 20, 2020; revised February 24, 2021 and April 16, 2021; accepted April 17, 2021. Date of publication April 27, 2021; date of current version November 22, 2021. This work was supported by Slovenian Research Agency (ARRS) through the Research Program – Electroporation-based Technologies and Treatments under Grant P2-0249. *(Corresponding author: Bor Kos.)*

Helena Cindrič and Damijan Miklavčič are with the Faculty of Electrical Engineering, University of Ljubljana, Slovenia.

Panchatcharam Mariappan is with the Department of Mathematics and Statistics, Indian Institute of Technology Tirupati, India.

Lukas Beyer is with the Department of Diagnostic and Interventional Radiology, Ernst von Bergmann Hospital, Germany.

Philipp Wiggermann is with the Institute of Radiology and Nuclear Medicine, Hospital Braunschweig, Germany.

Michael Moche is with the Department for Interventional Radiology, Helios Park-Klinikum Leipzig, Germany.

Bor Kos is with the Faculty of Electrical Engineering, University of Ljubljana, Ljubljana, Slovenia (e-mail: bor.kos@fe.uni-lj.si).

This article has supplementary downloadable material available at https://doi.org/10.1109/TBME.2021.3075772, provided by the authors.

Digital Object Identifier 10.1109/TBME.2021.3075772

I. Introduction

IRREVERSIBLE electroporation (IRE) ablation is a relatively new modality for ablation of deep-seated tumors and soft tissues [1]. Short high voltage electrical pulses are delivered to the target tissue, causing a disruption in cell membrane structural integrity and increased permeability, which leads to the loss of cell homeostasis. The affected cells cannot recover from the loss of membrane functionality and eventually die in a process similar to apoptosis [2]–[4]. IRE ablation is being evaluated for ablation of various deep-seated tumors such as in liver, pancreas, prostate and kidney [5]–[8]. Unlike in conventional ablation modalities, the success of IRE ablation does not depend on the change in target tissue temperature [1], [9]. Thus it presents an alternative treatment option in cases where the use of thermal ablation modalities is contraindicated due to risk of thermal damage to sensitive nearby structures or when the presence of heat sinks reduces ablation efficacy [7], [10], [11].

A prerequisite for successful IRE ablation is complete coverage of clinical target volume with a sufficiently high electric field (threshold). Needle electrodes are used for delivery of electric pulses and the electric field distribution in tissue mostly depends on the electrode configuration and applied voltage magnitude. Currently, the estimated threshold for IRE of hepatic tumors is around 600 V/cm, however, studies report thresholds in the range of 500-700 V/cm [12]–[15]. Furthermore, the electroporation threshold depends on the number and duration of delivered pulses – with a higher number of pulses or longer pulses a lower electric field strength will suffice [16], [17].

According to the recommendations of the current manufacturer, the electrodes need to be placed around the tumor parallel to each other and on the same depth to ease the prediction of electric field distribution. This is often difficult to achieve in practice, causing uncertainties in ablation zone appearance

[18], [19]. In order to avoid undertreatment of the target tissue, voltages higher than strictly required and multiple sessions with additional electrodes or electrode retractions are often used in practice to produce a larger ablation zone. There is currently no method for real-time monitoring of ablation efficacy. In some studies on IRE ablation of pancreatic cancer a 12-15 A increase in electric current of was suggested as an indicator for successful irreversible electroporation. In order to achieve this increase in electric current additional (hundreds of) pulses are applied to tissue [20], [21]. While this method may be feasible for successful ablation in the pancreas, the implementation of the specific current increase of 12-15 A might not be an appropriate endpoint for all tumor types and locations [22]. Several experimental studies have also shown that current protocols may lead to a considerable Joule heating and thermal damage in the vicinity of electrodes. This may impact treatment safety if the electrodes are positioned in the immediate vicinity or touching certain anatomical structures susceptible to thermal damage – for example in the liver thermal damage to bile ducts can result in life threatening complications [23]–[25].

A numerical treatment planning tool that predicts ablation zone *a priori* presents an option for overcoming the uncertainties in the treatment area (especially undertreatment) and avoiding potential thermal damage to nearby critical structures. Furthermore minimizing thermal damage of targeted tissue, i. e. tumor, facilitates both immune response and faster resolution of ablated tissue. A patient specific numerical model is developed from the patient's medical imaging and a treatment plan is then prepared, completed with an optimized number and positioning of the electrodes and applied voltages. Thus complete coverage of target volume with a sufficiently high electric field is ensured, avoiding undertreatment of the target area, while (thermal) damage to surrounding tissue is minimized. The clinical practicality of numerical modelling for treatment planning has already been shown [12], [15], [26], however, further validation using clinical data and a robustness analysis of developed treatment plans are needed in order to introduce numerical treatment planning into clinical routine.

In this retrospective study, 18 cases of hepatic tumors treated with IRE ablation were numerically reconstructed and treatment outcome was computed with the numerical treatment planning framework, which was developed previously [12], [27]–[29]. Simulated ablation volumes were extracted from computed 3D electric field distribution and compared to actual ablation volume determined from follow-up MRI. The main objective of our study was to determine the electric field threshold in the numerical model, which best fits the clinical response in target tissue obtained from follow-up imaging. This would allow us to determine at which electric field threshold *in silico* we expect a complete ablation *in vivo* and therefore validate the outcome prediction of the treatment planning framework for IRE ablation of hepatic tumors. Furthermore, we investigated the thermal component of IRE ablation in our dataset and demonstrated the potential of treatment planning to ensure complete coverage of target area while avoiding thermal damage, and to improve and shorten future IRE procedures.

II. Materials and Methods

A. Case Selection Eligibility Criteria

A review of patients who underwent IRE ablation of primary and secondary liver tumors at the author's institution between 2015 and 2018 was performed. Cases were selected for the numerical study based on the availability of data for numerical reconstructions – the accessibility of pre-interventional contrast-enhanced CT (CECT), complete peri-interventional CT scans with all electrode positions visible, follow-up imaging and complete reports of delivered IRE protocols (active electrode pairs, applied voltage magnitude, number and duration of applied pulses, retraction/replacement of electrodes). A total of 18 cases were eligible for reconstruction – 12 cases of primary liver cancer (HCC) and 6 cases of various liver metastases. The tumor characteristics and procedure data for all 18 cases are available in supplementary materials in Table E4. The patient data used in this retrospective study is from clinical procedures performed in the past. All the patient data used in this study was completely anonymized and IRB approval was therefore not required according to local regulations.

B. Ablation Procedure and Follow-up

Patients underwent percutaneous irreversible electroporation ablation of primary and secondary hepatic tumors. A multiphase (arterial and portal venous phase) contrast-enhanced CT (CECT) and/or multiphase MRI was acquired up to 30 days prior to the procedure. The number of needle electrodes, insertion trajectories and placement were decided by the interventional radiologist based on pre-and peri- interventional imaging.

IRE procedures were performed with the NanoKnife system (AngioDynamics, Latham, NY, USA) using 4–6 electrodes (1.2 mm diameter, 2 cm active length) per ablation. After needle insertion, a native CT scan was taken to confirm the needle placement. Pulse parameters were defined according to AngioDynamics guidelines with applied voltage ranging from 1200 to 3000 V. Generally, 100 pulses of 90 μs were delivered per electrode pair in sequences of 10 pulses, followed by delay for recharge of the pulse generator. Delivery of each single pulse was synchronized with the absolute refractory period of patients' ECG cycle using AccuSync. The delivered current and voltage were recorded automatically by the pulse generator with a specified hardware precision of 3% [30]. The successful delivery of all pulses was considered as procedure endpoint. All procedures were performed under general anesthesia with muscle relaxation.

The first follow-up imaging was performed on the first working day after intervention with an abdominal CT and contrast enhanced T1W MRI. Consequent follow-up MRI was performed at approximately 6 week post- and 3 months post-intervention.

C. Numerical Reconstruction

Patients' pre-interventional CECT and peri-interventional native CT (showing electrode positions) were used for the numerical reconstructions of IRE procedures. First, the

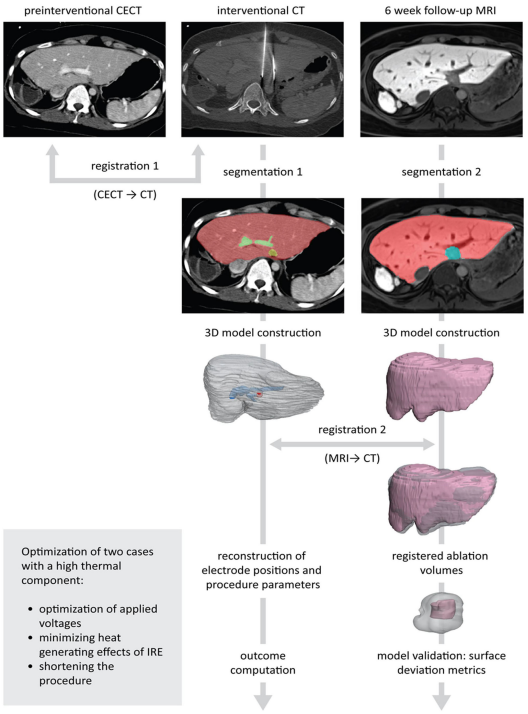

Fig. 1. Study design and steps. Three sets of patient images were used for the numerical reconstruction of each case: pre- and peri-interventional CT for the reconstruction of the IRE procedure and approximately 6 week follow-up MRI for comparison of the simulated and the actual ablation zone. All three sets had to be registered into the same imaging domain, the domain of the peri-interventional CT, which also served as the computation domain in the numerical model. Validation of the model was performed through a comparison of the simulated and the actual ablation zone segmented from follow-up MRI using surface deviation metrics.

pre-interventional CECTs were registered into the spatial domain of the peri-interventional CT, which served as the computational domain (Fig. 1). Rigid registration with mutual information criterion was selected for registration using the registration tool in ITK-SNAP software [31]. Tissues of interest – tumor volume, liver parenchyma and major blood vessels in the vicinity of the treated area (< 3 cm from tumor border) – were then manually segmented on registered CECT (Fig. 2(A)). All segmentations were performed in ITK-SNAP and were inspected and verified by an experienced radiologist.

For each patient, a 3D anatomically correct numerical model was built based on segmented tissue masks from CECT (Fig. 1). Final positions of needle electrodes were determined from peri-interventional CT (Fig. 2(B)) and introduced into the model. Treatment parameters, namely active electrode pairs, applied voltage, number and duration of delivered pulses and potential electrode re-placement or retraction (in cases where multiple sessions were required) were determined from treatment reports. Measurements of delivered currents and actual voltage of electrical pulses delivered were extracted from the NanoKnife pulse generator and used for validation of computed electric currents (Fig. 2(D)).

Treatment outcome was computed using the numerical framework for planning of electroporation based treatments [12], [27]. COMSOL Multiphysics v5.4 (Comsol Inc., Sweden) was used for numerical computations, however, the model construction and simulation set up was performed in MATLAB R2018b (MathWorks, USA) via LiveLink connector.

Electric field distribution in the target tissue is computed indirectly by solving the stationary partial differential equation for electric potential [32], [33]. The stationary model is supplemented with the modified Pennes' bioheat transfer equation solved in time domain, which includes the Joule heating term and bioheat term [34], [35]. The electrical conductivity of modelled tissues is affected by both electroporation phenomenon and heating electroporation is implemented in the model through a non-linear electric field dependent increase in tissue base electrical conductivity [36]. The thermal dependence of electrical conductivity is modelled with a constant factor of increase of 1.0%/ °C. The bioheat term of the Pennes equation represents tissue perfusion and metabolic activity, however, when electroporation occurs tissue perfusion decreases significantly due to vascular lock effect [37]. The delays after each sequence of ten pulses are an important part of the heating/cooling dynamics during IRE ablation and were therefore accounted for in our model.

The electric field distribution is calculated separately for each active electrode pair used in the procedure. The final electric field distribution *in situ* is determined by combining the maximal electric field contributions from all electrode pairs (cumulative coverage of target tissue). Thermal damage in target tissue is determined by integrating the Arrhenius kinetics equation over the treatment time period [38]. The kinetic parameters of the equation were selected to expose the most alarming thermal effects which start at temperatures above 50°C, namely, protein denaturation [39], [40]. The threshold for thermal damage was 90 % probability of cell death as determined by the integration. For each case, the results of the reconstruction consist of a final 3D electric field distribution as experienced by tissue, the temporal evolution of tissue temperature and a 3D map of thermal damage probability.

A more detailed description of the model and equations used in the computation is available in supplementary materials. All selected tissue properties and model parameters are available in supplementary materials in Tables E1 and E2. All segmented tissue masks (interventional CECT and follow-up MRI), 3D surface models of liver, tumors and segmented ablation zones, and 3D electric field distributions are available for download in the associated data repository.[1]

D. Model Validation

For each case, we extracted six isosurfaces from the 3D electric field distribution, which correspond to threshold values of 400-900 V/cm (100 V/cm steps). These simulated ablation

[1]https://doi.org/10.6084/m9.figshare.12961646.v1

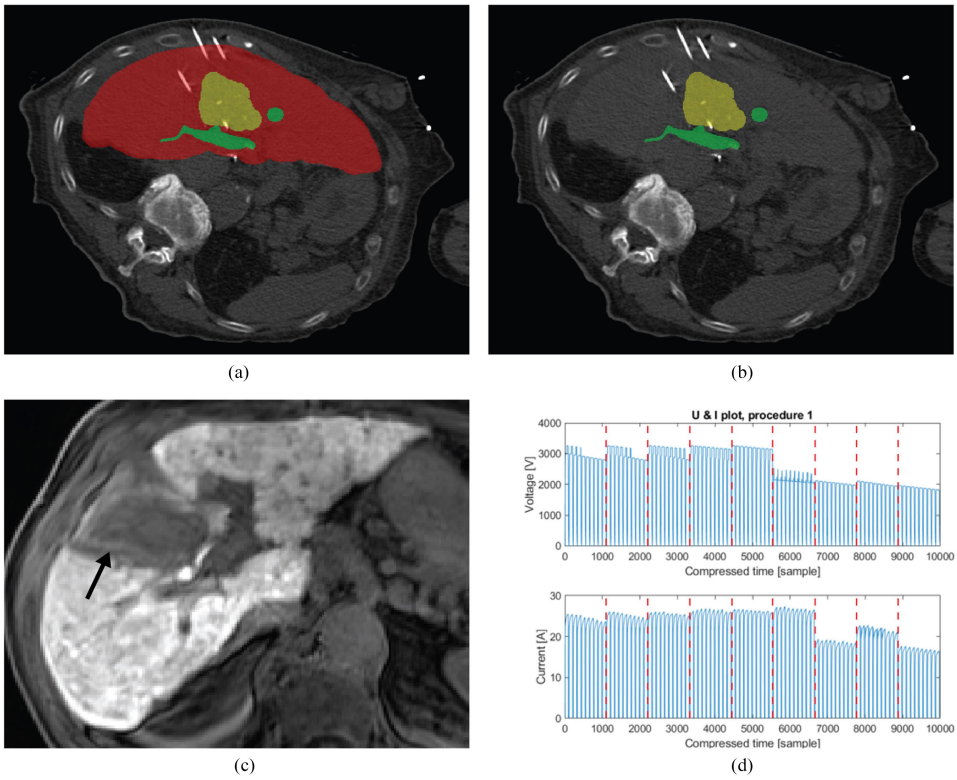

Fig. 2. An example of tissue segmentation, electrode placement and follow-up imaging for one of the reconstructed cases (case P14 in Table E4 in supplementary materials). In this particular case, the tumor was very large, therefore two consecutive sessions were performed with 2 cm electrode retraction in between sessions. A) Tissue segmentation overlay on pre-interventional CECT (yellow – tumor, green – vessels, red – liver parenchyma). B) Native interventional CT with visible needle electrode positions. C) Seven week follow-up late phase T1W MRI. Ablation zone is visible as hypo-enhanced region with a hyper-intense rim (arrow). D) An example of voltage and electric current measurements recovered from NanoKnife device. Nine electrode pairs were used in this case with 100 pulses delivered to each pair in each session. Only the first 10 pulses of each pair are shown to highlight the difference in voltage magnitude applied to different pairs – there was no voltage decrease visible in the subsequent 90 pulses. Electrode pairs are separated with dashed lines.

volumes were then compared with ablation volumes segmented from follow-up MRI. Six week follow-up T1W MRI (median 5.5 weeks, range 4–12 weeks) was chosen for model validation, since 1-day follow-up was not suitable for segmentation due to edema and poor visibility and 3-month follow-up was too long. The hepatic capsule and ablation volume (zone) were manually segmented on the MRI using ITK-SNAP software. The ablation zone is visible on the late hepatobiliary phase as a hypo-intense region with a peripheral hyper-intense rim (Fig. 2(C)).

In order to compare the segmented and simulated ablation volumes, the follow-up MRI needed to be registered into the spatial domain of peri-interventional CT (Fig. 1). Due to the multimodal nature of images, the registration was performed using hepatic capsule masks. Segmented masks from CT and MR were transformed into 3D liver models, which were then registered using Materialise 3-matic software (Materialise NV, Belgium). The registration resulted in the alignment of segmented and simulated ablation volumes to a common coordinate system on which the analysis of surface deviation between the volumes was then performed (Fig. 1). Average absolute error (AAE) was chosen as the measure of surface deviation and was calculated for each combination of segmented ablation surface and simulated ablation surface at 400-900 V/cm thresholds. AAE is a measure to find how on average two objects differ and is calculated as follows:

$$AAE = \frac{\sum_i w_i |d_i|}{\sum_i w_i} \cdot \tag{1}$$

In (1), per-face metrics are computed by trilinear interpolation from the distance level set (d) at the center of the face and weighted (w) over the area of the triangle face.

E. Statistical Analysis

The statistical analysis was performed in MATLAB using the Statistics and Machine Learning Toolbox. Difference between HCC and metastatic tumor subgroups were calculated using the

Wilcoxon rank sum test (Mann-Whitney test). Correlations between segmented ablation size and average absolute error (AAE) for both subgroups and for the whole dataset were calculated using the Spearman's rank correlation coefficient.

F. Treatment Planning/Case Optimization Example

In order to demonstrate how treatment planning could improve future IRE procedures, two cases, in which the reconstructions suggested a high percentage of thermal damage in the target tissue, were selected for optimization and development of a hypothetical treatment plan. In this study only applied voltage magnitudes were optimized.

In the first selected case, 6 electrodes were used in the original procedure, constituting 10 active electrode pairs. Retraction of the electrodes (1.5 cm) was also performed thus resulting in two successive deliveries of 100 pulses to all electrode pairs (i.e., 200 pulses delivered altogether). In the optimized plan, the original electrode placement was preserved. However, electrode retraction was omitted and longer conductive electrode tip was used instead – 3 cm as opposed to the original 2 cm tip. These additional changes were based on previous experience and were not subject to further optimization. In the second case, 6 electrodes were used in the procedure forming 10 active electrode pairs and no retraction was performed. The original electrode placement without further modifications was used in the optimized plan as well.

Optimization of applied voltage magnitudes to electrode pairs was performed in MATLAB by calculating the minimum of a nonlinear criterion function F (2). The criterion function was constructed to ensure complete IRE of clinical target volume (CTV), while minimizing IRE of the surrounding healthy tissue and preventing a large current draw. The threshold for IRE of tumor and healthy liver tissue was set to 600 V/cm according to the literature [12]–[14], [41], [42].

$$F = -1000 \cdot V_{CTV_{PP}} + 10 \cdot \frac{V_{LIVER}}{3 \cdot V_{CTV}} + \sum_{all\ pairs} f(I), \tag{2}$$

$$f(I) = 2^{I - I_{CUT}}, \tag{3}$$

In (2) $V_{CTV \cdot PP}$ stands for the fraction of CTV experiencing IRE, V_{CTV} and V_{LIVER} are the CTV and volume of healthy tissue experiencing IRE respectively, and *f(I)* is the nonlinear function representing electric current limitation (3). The contribution of *f(I)* to the criterion function F is negligible until the calculated current I exceeds the cutoff value I_{CUT} (set to 40 A in our case). If this happens, the contribution of *f(I)* rapidly increases thus eliminating the pairs that would potentially cause a high current draw. The weights in the criterion function were selected arbitrarily but with respect to individual demands for IRE.

In a single iteration of the optimization process new voltages were selected for all electrode pairs from a pool of possible values ranging from 1500 V to 3000 V (only multiples of 100 V were allowed as candidates to speed up the process). The stationary model was computed using the new voltages and the criterion function was evaluated. The process was repeated until a minimum of the criterion function was reached.

Only the computation of the stationary electric field was used in the optimization, since heating is directly dependent on delivered energy, or in other words, changing (lowering) the applied voltage will also change (lower) the delivered energy and therefore heat. The addition of heating computation in time domain would not significantly improve the accuracy of the criterion function while it would significantly increase the necessary computation resource and optimization time.

The selected voltages resulting in the function minimum were considered as the optimized treatment parameters (plan). The compete model with computation of heating in time domain was then computed to evaluate the thermal component in the optimized plan. Lastly, the percentage of volume, where the probability of thermal damage exceeded 90 %, was calculated and compared to the original results from the reconstruction.

TABLE I
COMPARISON OF MEASURED AND COMPUTED MEAN ELECTRIC CURRENTS AND ROOT MEAN SQUARED ERROR (RMSE) FOR EACH CASE

Case	Mean measured current (A)	Mean computed current (A)	RMSE (A)
P1	37.5	26.9	12.3
P2	20.9	18.7	3.8
P3	36.7	35.3	9.6
P4	30.0	29.3	9.4
P5	26.3	29.8	4.6
P6	23.3	30.6	14.0
P7	26.3	21.1	5.8
P8	27.2	29.5	5.2
P9	33.6	23.3	12.0
P10	22.8	22.1	8.8
P11	27.0	24.1	4.2
P12	26.3	28.8	3.9
P13	21.7	23.5	5.8
P14	29.0	38.2	15.0
P15	40.4	24.0	17.3
P16	28.2	23.4	5.1
P17	21.4	22.0	3.4
P18	26.8	35.3	13.3

III. RESULTS

For each reconstructed case, the computed electric current for all electrode pairs was compared to the current measurements recovered from NanoKnife pulse generator. Table I shows the mean electric current value (averaged over all active electrode pairs) and root mean squared error (RMSE) for all 18 reconstructed cases. The average relative error of the pair-to-pair comparison of measured and computed electric current is 28.9%.

Percentage of tumor volume and clinical target volume (CTV) covered with the electric field of and above a specific threshold value (400–900 V/cm) was calculated (further on referred to as

TABLE II
PERCENTAGE OF TUMOR VOLUME COVERED IN THE ELECTRIC FIELD OF (OR ABOVE) SPECIFIC THRESHOLD (400—900 V/CM) AND PERCENTAGE OF TUMOR VOLUME SUBJECTED TO THERMAL DAMAGE. MEAN, STANDARD DEVIATION, MEDIAN AND RANGE ARE CALCULATED OVER THE WHOLE DATA SET OF 18 TUMOR CASES

Coverage	Mean [%]	Standard deviation [%]	Median [%]	Range [%]
400 V/cm	97	6.2	100	76-100
500 V/cm	94	9.7	100	68-100
600 V/cm	90	13.3	98	58-100
700 V/cm	83	17.0	89	41-100
800 V/cm	75	20.0	75	32-100
900 V/cm	65	22.0	64	21-100
Thermal damage	48	32.9	37	5-100

TABLE III
PERCENTAGE OF CLINICAL TARGET VOLUME (CTV) COVERED IN THE ELECTRIC FIELD OF (OR ABOVE) SPECIFIC THRESHOLD (400—900 V/CM) AND PERCENTAGE OF CTV SUBJECTED TO THERMAL DAMAGE. MEAN, STANDARD DEVIATION, MEDIAN AND RANGE ARE CALCULATED OVER THE WHOLE DATA SET OF 18 TUMOR CASES.

Coverage	Mean [%]	Standard deviation [%]	Median [%]	Range [%]
400 V/cm	94	11.3	99	54-100
500 V/cm	90	13.6	96	47-100
600 V/cm	85	15.8	89	40-100
700 V/cm	78	17.5	78	34-100
800 V/cm	71	18.8	70	28-100
900 V/cm	64	19.6	62	22-100
Thermal damage	36	24.5	29	3-87

coverage) as well as the percentage of thermal damage. CTV is considered as tumor volume with 5 mm and 10 mm safety margin for HCC and metastases, respectively. The mean and median coverage and thermal damage were calculated (along with standard deviation and range) over all cases and are shown in Table II for tumor volume and Table III for CTV. Detailed results for each case separately are available in supplementary materials in Tables E5 and E6. According to Tables II and III the best coverage is achieved with the lowest electric field of 400 V/cm at 97% and 94% mean volume coverage for tumor and CTV respectively, followed closely by 500 V/cm threshold, where the mean volume coverage was 94 % and 90 % for tumor and CTV respectively.

At the highest studied threshold – 900 V/cm – the mean volume coverage of tumor and CTV was 65% and 64% respectively. We extracted six isosurfaces from the electric field data, which correspond to 400-900 V/cm thresholds, thus simulating different ablation volumes. We compared the simulated ablation volumes to segmented ablation volumes from 6-week follow-up MRI. Fig. 3 shows simulated ablation volumes with respect to segmented ablation volumes. Ideally, the two volumes would be the same; however, the numerically predicted size of the ablation is always larger than the ablation seen on follow-up MRI. There is only one case, where the segmented ablation was larger than the simulated ablation. For better clarity, only data for 600 V/cm and 900 V/cm electric field thresholds is shown on Fig. 3; our results indicate the best fit is achieved at 900 V/cm, however, in

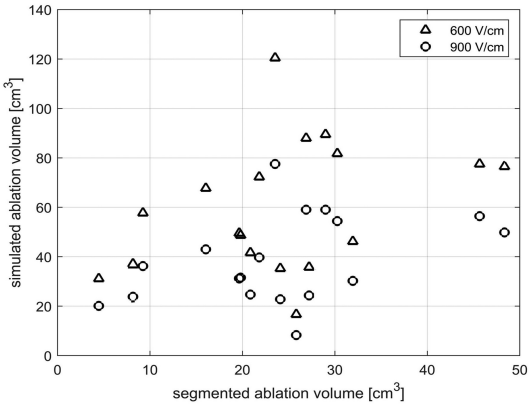

Fig. 3. Simulated ablation volume size obtained at 600 V/cm and 900 V/cm thresholds compared to the segmented ablation volume size.

TABLE IV
MEAN AND MEDIAN SURFACE DEVIATION AND RESPECTIVE DATA RANGE BETWEEN THE TWO ABLATION VOLUMES (SEGMENTED AND SIMULATED) FOR EACH OF THE SIX ELECTRIC FIELD THRESHOLDS. THE SELECTED MEASURE OF ABLATION ZONE COMPARISON IS THE AVERAGE ABSOLUTE ERROR (AAE)

Threshold	Median AAE [mm]	Standard deviation [mm]	Median AAE [mm]	Range [mm]
400 V/cm	9.4	3.4	9.8	2.6-15.6
500 V/cm	8.1	3.0	8.4	2.6-13.9
600 V/cm	7.1	2.6	7.4	3.1-12.2
700 V/cm	6.5	2.3	6.6	3.3-11.2
800 V/cm	5.9	1.8	6.0	2.8-10.6
900 V/cm	5.6	1.5	5.8	3.0-8.6

current literature lower thresholds (600-700 V/cm) for IRE of hepatic tissue are reported [12], [14], [15].

Surface deviation – average absolute error (AAE) – was calculated for each combination of segmented and simulated volumes in order to determine the best fit between the two volumes and consequently determine the *in silico* electric field value that corresponds to successful ablation of the treated tissue. AAE is lower when the segmented ablation is larger or when the electric field threshold is higher (smaller simulated ablation zone). Mean and median AAE of the overall 18 cases for each electric field threshold were calculated and are shown in Table IV along with respective standard deviations and ranges. Since the ablation zone sizes vary between the cases in our dataset, we also normalized the AAE with the diameter of the segmented ablation zone to obtain a relative value for AAE. Normalized results are presented in table E3 in Section 2 of supplementary materials. Fig. 4 shows the calculated AAE for all 18 cases with respect to segmented ablation volumes.

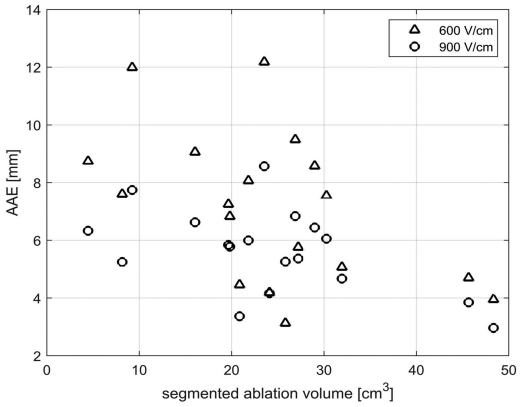

Fig. 4. Average absolute error (AAE) of surface deviation between simulated ablation volume (at 600 V/cm and 900 V/cm threshold) and ablation volume segmented from approximately 6-week follow-up MRI.

As in Fig. 3, only data for 600 V/cm and 900 V/cm electric field thresholds are shown for clarity. The results for all thresholds are provided in section 2 of the Supplementary materials.

We evaluated whether there is a statistically significant difference in AAE and electric field coverage between the metastatic and HCC tumors. The difference in calculated AAE between the two subgroups, and calculated coverage of tumor volume and CTV between the two subgroups was evaluated using the Mann-Whitney test (Wilcoxon rank sum test). No statistical difference between the two subgroups was found. Correlation between segmented ablation size and AAE for both subgroups and for the whole dataset was calculated using the Spearman's rank correlation coefficient. According to the test, there is a strong negative correlation between AAE and segmented ablation volume in the metastatic group which is statistically significant for 800 V/cm ($p = 0.033$). There is a negative correlation in the HCC group but it is not statistically significant. In the whole dataset, there is a negative correlation between AAE and segmented ablation volume, which is also statistically significant for 800 V/cm ($p = 0.047$). Correlation between segmented and simulated ablation size for both subgroups and for the whole dataset was calculated using the Spearman's rank correlation coefficient. According to the test, there is a weak positive correlation between segmented and simulated ablation size in the HCC group, but it is not statistically significant. There is no correlation in the metastatic group.

Our simulations show considerable Joule heating resulting in thermal damage of target tissue. There are 5 out of 18 cases where >50 % of CTV is thermally damaged, 7 out of 18 cases where >50 % of tumor volume is thermally damaged and 4 out of 18 cases where >90 % of tumor volume is thermally damaged (data is available in supplementary materials). The average and median volume percentage of thermal damage along with the standard deviation and data range are shown in Tables II and III for tumor volume and CTV respectively.

In our dataset, thermal damage was observed in cases that were clinically challenging and therefore more pulses were delivered to tissue – either due to electrode retraction or overall higher number of electrodes used for ablation. The numerical framework was used to design a treatment plan for two selected cases that exhibited a high thermal component with the aim of reducing thermal damage while preserving the coverage of target tissue. The threshold determined from fitting the computed results to follow-up imaging in this study was originally intended to be used in the optimization of the two selected cases as well. However, since the determined threshold is much higher than expected and reported in literature, we decided to use 600 V/cm as the threshold for IRE of tumor and healthy tissue. This value is in the middle of the range reported in literature (500-700 V/cm) and corresponds better with the clinical outcomes of our patient sample, since 14/18 cases had complete response identified 6 weeks post IRE (see Tables II and III and Tables E4-E6 in the Supplementary materials). In both cases, we were able to eliminate the thermal component completely by lowering the applied voltage magnitude. In Case 1, the voltages were lowered from the original range of 2405-3000 V to a lower range of 1700-1900 V and in Case 2 from the original span of 2310-3000 V to a lower span of 1800-2000 V. Table V shows the percentage of tumor volume and CTV experiencing thermal damage and coverage of both respective volumes with an electric field strength of 600 V/cm for both the original simulation (reconstruction) and simulation with optimized voltages. In both cases tumor coverage remained at 100%, while in Case 2 CTV coverage was 3 percentage points lower in the optimized simulation. In both cases, thermal damage of tissue was practically eliminated.

Furthermore, in Case 1, where electrode retraction was initially performed, longer electrodes were used in the simulation (3 cm instead on 2 cm) rendering retraction unnecessary and therefore potentially shortening the procedure duration. The optimization also resulted in lower electric currents in both cases. Fig. 5 shows an example of computed results for Case 2. Electric field distribution and maximum computed temperature in tissue are shown for original and optimized simulation as an overlay on the patient's peri-interventional CT images. Panels B and D show a significant reduction in tissue heating, while panels A and C show little alteration in electric field distribution and almost no change in coverage of target tissue with and electric field sufficient to cause IRE.

IV. Discussion

In this retrospective study, 18 clinical cases of IRE ablation of hepatic tumors were numerically reconstructed and treatment outcome was computed using a numerical tool for treatment planning. The aim of our study was to determine the *in silico* electric field threshold in the numerical model, that corresponds to successful ablation of target tissue *in vivo* as visible on follow-up imaging. A complete response is not necessarily considered as 100% cell death due to IRE alone. There are additional mechanisms contributing to tumor eradication, for example immune response and vascular lock, which are still being investigated [43]–[47]. Furthermore, electric field threshold should not be

TABLE V
PERCENTAGE OF TUMOR VOLUME AND CTV EXPERIENCING THERMAL DAMAGE AND COVERAGE WITH AN ELECTRIC FIELD OF 600 V/CM IN THE ORIGINAL SIMULATIONS (RECONSTRUCTIONS) AND THE OPTIMIZED SIMULATIONS

	Thermal damage				Coverage with 600 V/cm			
	Tumor volume		CTV		Tumor volume		CTV	
	original	optimized	original	optimized	original	optimized	original	optimized
Case 1	92 %	0 %	70 %	0 %	100 %	100 %	100 %	100 %
Case 2	90 %	4.6 %	63 %	2.5 %	100 %	100 %	99 %	96 %

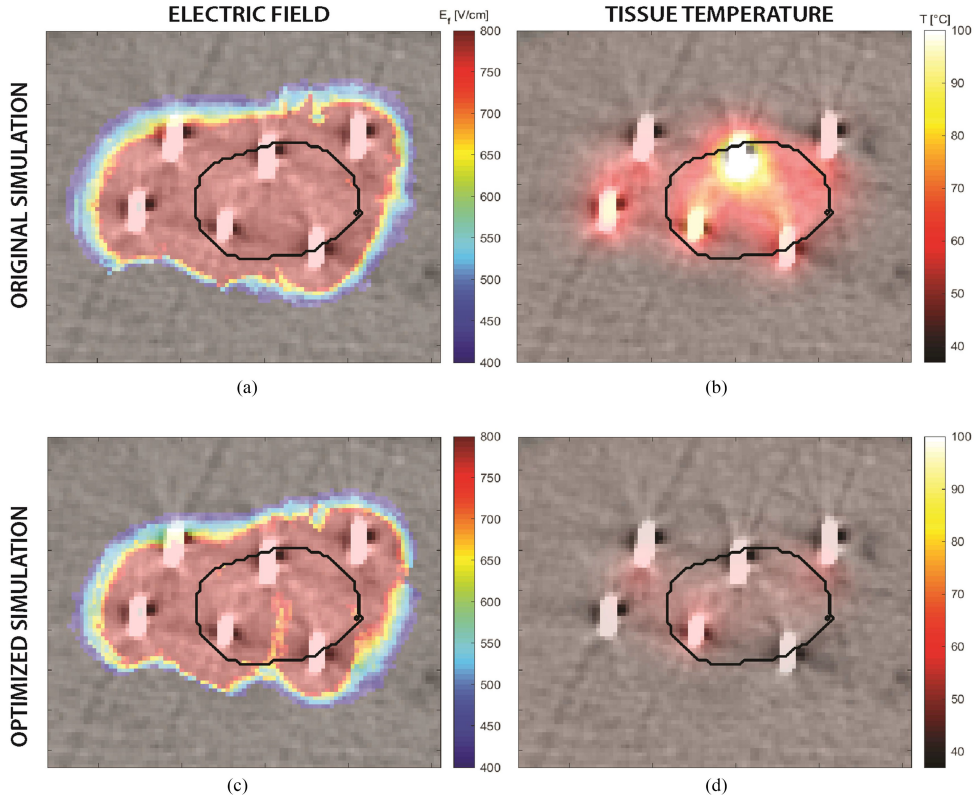

Fig. 5. Results of numerical optimization for Case 2. Computed electric field distribution and tissue temperature are represented as an overlay on patient's peri-interventional CT with six visible needle electrodes. Tumor volume is outlined in black. Panels A and B show the results of the original simulation (reconstruction). Computation indicates considerable heating, resulting in almost complete thermal ablation of tumor volume (see Table V). Temperatures around the electrodes reach up to 100 °C. Panels C and D show results after optimization of applied voltages. Tissue coverage with sufficiently high electric field remains mostly unaffected and should not negatively affect treatment success (A, C) while tissue heating is practically eliminated (B, D).

mistaken with the voltage-to-distance ratio used for calibration of delivered voltage magnitude, recommended by manufacturers of pulse generators, which has the same unit of V/cm. The electric field in our model is considered as the local electric field as experienced by cells/tissue *in situ*.

For each case, six simulated ablation volumes were extracted, corresponding to *in silico* electric field thresholds of 400–900 V/cm, and compared to ablation volumes segmented from follow-up MRI acquired approximately 6 weeks after IRE procedure. The chosen metric for ablation zone comparison was surface deviation calculated as an average absolute error (AAE). In a study by Moche *et al*. [48] a similar approach was employed to evaluate the integrability of the simulation tool for prediction of radiofrequency ablation (RFA) zones in the liver. The authors report a mean AAE of 3.4 mm $\pm$ 1.7 mm that was considered accurate enough for clinical demands. In our study, the lowest mean AAE was 5.6 mm $\pm$ 1.5 mm (standard deviation) for simulated ablation volume at 900 V/cm. It is important to note that [48] was a prospective study accounting also for the computational

demands, therefore a better correlation between computed and segmented volumes is expected than in a retrospective study.

Based on existing literature we know that a 900 V/cm threshold is higher than what is required for complete ablation of hepatic tissue with irreversible electroporation. The threshold for IRE of hepatic tumors is estimated to be somewhere between 500–700 V/cm [12]–[14], [41], [42]. With longer pulses or higher number of pulses, lower amplitudes are needed for the same fraction of electroporated cells [16], [17]. An increase in tissue temperature, which is the result of Joule heating during IRE, presumably also decreases the threshold for electroporation [35]. However, if we observe our data at lower thresholds, there is an even larger deviation between segmented and simulated ablation volumes, with simulated volumes being larger than segmented volumes. There are several possible reasons for this discrepancy. As opposed to RFA where the necrotic tissue is easily demarcated from viable tissue and its appearance on follow-up imaging does not change within the studied time frame, the healing dynamics (and consequential shrinkage) of electroporated tissue make the determination of actual ablation zone size on follow-up imaging difficult. It is therefore difficult to determine with certainty the region where apoptotic and necrotic cell death due to irreversible electroporation occur, which presumably contributes to a higher error in surface deviation when compared to the study on RFA. Furthermore, it is most likely that the 6-week follow-up period was too long and the ablation zone has already shrunk considerably. It is possible that a part of the lesion visible on 6-week follow-up represents thermal damage; however, it is practically impossible to distinguish between thermal necrosis and IRE apoptosis/necrosis on the MRI.

Recent studies on MRI findings after IRE ablation of liver metastases [49] and HCC [50] have shown that the ablation zone shrinks rapidly in size in the first 2–4 weeks after the procedure. Barabasch *et al*. [49] report an increase in ablation size in the first 24h after IRE with the mean ablation size being 836% of target lesion size one day after IRE. In the two weeks after the IRE procedure, a rapid decrease in ablation size was observed and a moderate decrease was observed afterwards. Furthermore, the rim enhancement visible on T1w and T2w MRI disappeared within 6 weeks in 21 out of 37 patients in the study. Padia *et al*. [50] also report a marked decrease of ablation zone size especially in the first 4 weeks after IRE procedure. The authors point out that early MRI (1 day post-IRE) may overestimate the appearance of the ablation zone, since both reversibly and irreversibly electroporated tissue may accumulate the gadolinium contrast agent, if the latter is present before the delivery of pulses [51].

One of the main advantages of irreversible electroporation is the preservation of the extracellular matrix and connective tissue. This quality promotes the use of electroporation in the vicinity of sensitive anatomical structures and also enables healing of treated tissue. The healing dynamics, however, are patient specific and are closely connected to the health of the liver organ and presumably also depend on patients' age and overall health status. The healing ability of cirrhotic liver is distinctively decreased which suggests the shrinking of the ablation zone might be slower in cases with cirrhotic liver (common in HCC cases) than in cases where the liver organ tissue is healthy (common in metastatic disease). Our results, however, did not show a statistically significant difference between the healthy (metastases) and cirrhotic (HCC) liver group. Although this may also be due to small sample size – 6 cases of metastases versus 12 cases of HCC. Animal experiments show fast resolution of IRE tissue within two weeks from procedure. However, two electrodes and a variety of pulse protocols were used in the experiments, resulting in a less pronounced thermal component [52]. Apart from the much larger volume of affected tissue in our study (compared to animal studies), it is also possible that the thermal component slows down the resolution of IRE lesion.

Our model is designed to compute the electric field distribution at the time of treatment. We conclude that the threshold of 900 V/cm determined in our study does not represent the actual biological manifestation of IRE which would be beneficial for treatment planning. Our results indicate that lesions visible on MRI 6 weeks post IRE represent tissue areas that experienced a local electric field strength of 900 V/cm or higher during treatment. We hypothesize that a more beneficial correlation with contours at lower electric field thresholds (e.g., 500-700 V/cm) would be achieved if follow up at an earlier time point were available for comparison with simulated ablation volumes. Kos *et al*. [12] compared simulated electric field distribution with findings from contrast enhanced CT on the day of IRE procedure and achieved good overlap with the ablation volume at 700 V/cm threshold. Gallinato *et al*. [15] compared simulated electric field distribution with MRI findings 3 days after IRE procedure and achieved a good fit between isocontours at 500 V/cm threshold and the hypo-enhanced area seen on T1w MRI. Based on the collective knowledge on the estimated threshold for IRE of hepatic tissue and MRI findings from Barabasch *et al*. and Padia *et al*. we assume the best time point for comparison with our computed results would be somewhere between 1 to 2 weeks after IRE procedure. Based on the results of a similar study on RFA of hepatic tumors, an AAE of <4 mm between simulated and actual (segmented) ablation volume should be sufficient for clinical demands and would effectively validate the numerical model.

A future prospective study utilizing multiple follow-up examinations, for example 3 to 5 days (when the inflammation should already subsided), 1 week and 2 weeks post IRE, would enable comparison of computed electric field to ablation size at different time points post IRE and would allow the determination of a more realistic electric field threshold beneficial for treatment planning. However, such a study might be ethically questionable due to repeated exposure of patients to contrast media and would also be quite costly. When a better time point for follow-up image acquisition is determined, a validation of the model performance and sensitivity should be performed in a prospective study and on a larger sample of patients including various liver diseases. Diffusion weighted imaging (DWI) was shown to represent the electroporated zone in early MRI quite well [53] and it does not require a contrast agent or radiation, so it could potentially present a possible solution for multiple follow-up sessions. Another recent pre-clinical study investigated the

trans-catheter intra-arterial perfusion MRI (TRIP-MRI) as a potential biomarker for differentiating reversibly and irreversibly electroporated zones. The study showed promising results in rabbit liver and warrants further investigation [54].

When interpreting the computed results we must, however, also consider the limitations of the numerical models currently in use, which mainly stem from uncertainties in the electrical properties of biological tissues. Whereas electrical conductivities of normal tissues have been measured abundantly (although with a large dispersion of values), properties of various malignant tissues, especially at low frequencies, are still reported with considerable uncertainty. Furthermore, the dynamics and extent of electrical conductivity increase during electroporation are still not well determined and are being actively studied [55]. The retrospective nature of our study is a major drawback and largely contributes to the error in our results. The reconstruction process was limited by missing documentation on needle positions and administered pulse protocols (see "Case selection" section of Materials and Methods), the follow-up intervals were different between patients, image registration (especially multimodal) also produces a certain error. The variance in dielectric properties of tissues and possible errors in the reconstruction of active electrode pairs affects the error in computed electric current (Table I). In a future prospective study, complete imaging of all needle positions (including retracted needles), as well as correct needle numbering would need to be recorded. Lastly, cases that are treated with IRE ablation are usually clinically more challenging, since IRE is still mostly considered only as a "last resort" procedure when other techniques are contraindicated or exhausted. Therefore, a large variance was to be expected in our dataset. In the future, a prospective study would be more appropriate to gather the necessary data to perform a similar analysis and determine a more realistic electric field threshold.

Also investigated in our study was the possible thermal damage due to IRE. Although IRE ablation is considered a non-thermal technique, several studies have shown mild hyperthermic as well as thermal ablation effects during and after IRE [23], [35], [38], [56], [57]. It has been demonstrated that mild hyperthermic effects might even positively affect treatment outcome by presumably lowering the electroporation threshold [58]. However, thermal ablation component could potentially be problematic, since IRE is currently presented as a non-thermal modality for use in cases and anatomical locations, where thermal damage is not acceptable. Our computed results showed considerable heating present in some of the cases – especially in the more clinically challenging cases where many electrodes/pulses were delivered. The highest increase in temperature was observed, as expected, in the vicinity of the electrodes, where the current density is the highest. It is possible, that our model overestimates the extent of thermal damage. Although the Arrhenius equation is quite popular for assessing thermal damage, it is prone to overestimation of cell death at the mild-hyperthermic temperatures, as the kinetic parameters are difficult to define and not well documented for hepatic tissue. Another limitation is the uniform initial perfusion across the tissue, as it underestimates the cooling from the larger blood vessels. Nevertheless, since parts of tissue are cumulatively exposed to hundreds of pulses, undesired heating and thermal necrosis is inevitable, and can negatively affect treatment safety, should the electrodes be in contact or in the immediate vicinity of critical anatomical structures.

Numerical computations and treatment planning in the two selected cases demonstrate the ability to perform IRE ablation without potentially damaging thermal effects. In the two selected cases with a presumably high thermal damage fraction, we were able to eliminate the thermal damage entirely while retaining a complete coverage of the target volume. In this study, only the applied voltage magnitudes were optimized. Another option for decreasing the temperature rise is the reduction of active electrode pairs. Due to uncertainties in ablation zone size, multiple sessions with electrode retraction are often used in clinical practice. In one of the selected cases, we were able to eliminate electrode retraction achieving complete coverage of tumor volume and safety margin in one session, thus also shortening the total procedure time.

Treatment plans in their current realization are usually prepared a few days ahead of intervention using patients' preinterventional imaging. Their usefulness for the interventional radiologist is limited since exact electrode placement according to the plan is often hard to achieve due to anatomical constraints and other technical difficulties. Furthermore, variability in dielectric properties of healthy and tumor tissue directly affect the electric field distribution and therefor influence the treatment efficacy. To ensure that the treatment success is not affected by these factors, a certain safety margin needs to be utilized when preparing the treatment plan. A robustness analysis of the treatment planning for percutaneous IRE is needed to evaluate the impact of errors in electrode positioning and variations in applied voltage and pulses on the effectiveness of the treatment. Despite current limitations, numerical modelling and treatment planning are important tools in understanding and improving electroporation-based treatments. Introduction of numerical treatment planning into clinical practice has the potential to improve the future procedures: we can numerically determine beforehand whether the procedure is feasible or not, optimization of electrode number and active pairs can make the procedure quicker and technically less difficult and the use of lower voltages can avoid high currents and thermal damage. One of the challenges which need to be overcome, however, is the difficulty in placing the electrodes in agreement with the pretreatment plan [59]. Electrode insertion is still mainly performed freehandedly and very few studies can be found where electrode placement is coupled with navigation systems [18], [59]–[61]. We believe combining numerical treatment planning with commercially available navigation systems would even further advance the clinical routine for IRE ablation.

V. Conclusion

In conclusion, the aim of our study was to validate the previously developed numerical framework for the purpose of treatment planning of irreversible electroporation ablation of hepatic tumors – more specifically, to correlate the computed electric field distribution with ablation zone appearance on 6-week follow-up MRI. Our study was limited by its retrospective

nature and a rather late time of follow-up imaging, as the ablation zone has presumably already shrunk in the 6 weeks following the ablation. Since the numerical model is intended to compute the ablation size on the day of treatment, a large error is present in the results and we were therefore not able to effectively validate the model. However, our results indicate that lesions visible on MRI 6 weeks post IRE represent tissue areas that experienced a local electric field strength of 900 V/cm or higher during treatment. Furthermore, we developed and polished a sophisticated method for validation of the numerical treatment planning software. Based on our findings, a future prospective study can be effectively designed, therefore providing the necessary data to further validate the model and ensure sufficient accuracy for clinical demands. A complete database, containing all image segmentations, computed 3D electric field distributions, and 3D surface models of liver, tumors and ablation volumes is also available in the supplementary materials.

Acknowledgment

The authors would like to thank Lukas Lürken, for his help in gathering the missing patient data and for verification of tissue segmentation. The study was conducted within the Infrastructural Centre "Cellular Electrical Engineering", which is part of the Network of Research and Infrastructural Centres of University of Ljubljana (MRIC UL IP-0510).

References

[1] R. V. Davalos *et al.*, "Tissue ablation with irreversible electroporation," *Ann. Biomed. Eng.*, vol. 33, no. 2, pp. 223–231, Feb. 2005.
[2] T. Kotnik *et al.*, "Membrane electroporation and electropermeabilization: Mechanisms and models," *Annu. Rev. Biophys.*, vol. 48, pp. 63–91, May. 2019.
[3] M. L. Yarmush *et al.*, "Electroporation-based technologies for medicine: Principles, applications, and challenges," *Annu. Rev. Biomed. Eng.*, vol. 16, pp. 295–320, Jul. 2014, doi: 10.1146/annurev-bioeng-071813-104622.
[4] L. Rems and D. Miklavčič, "Tutorial: Electroporation of cells in complex materials and tissue," *J. Appl. Phys.*, vol. 119, no. 20, May 2016, Art. no. 201101, doi: 10.1063/1.4949264.
[5] H. J. Scheffer *et al.*, "Irreversible electroporation for nonthermal tumor ablation in the clinical setting: A systematic review of safety and efficacy," *J. Vasc. Interv. Radiol. JVIR*, vol. 25, no. 7, pp. 997–1011, Jul. 2014, doi: 10.1016/j.jvir.2014.01.028.
[6] M. R. Meijerink *et al.*, Eds., *Irreversible Electroporation in Clinical Practice*. Cham, Switzerland: Springer International Publishing, 2018.
[7] K. N. Aycock and R. V. Davalos, "Irreversible electroporation: Background, theory, and review of recent developments in clinical oncology," *Bioelectricity*, vol. 1, no. 4, pp. 214–234, Dec. 2019, doi: 10.1089/bioe.2019.0029.
[8] B. Geboers *et al.*, "High-Voltage electrical pulses in oncology: Irreversible electroporation, electrochemotherapy, gene electrotransfer, electrofusion, and electroimmunotherapy," *Radiology*, vol. 295, no. 2, pp. 254–272, May 2020, doi: 10.1148/radiol.2020192190.
[9] M. Distelmaier *et al.*, "Midterm safety and efficacy of irreversible electroporation of malignant liver tumors located close to major portal or hepatic veins," *Radiology*, vol. 285, no. 3, pp. 1023–1031, Aug. 2017, doi: 10.1148/radiol.2017161561.
[10] N. Verloh *et al.*, "Similar complication rates for irreversible electroporation and thermal ablation in patients with hepatocellular tumors," *Radiol. Oncol.*, vol. 53, no. 1, pp. 116–122, Mar. 2019, doi: 10.2478/raon-2019-0011.
[11] E. I. Cohen *et al.*, "Technology of irreversible electroporation and review of its clinical data on liver cancers," *Expert Rev. Med. Devices*, vol. 15, no. 2, pp. 99–106, Feb. 2018, doi: 10.1080/17434440.2018.1425612.
[12] B. Kos *et al.*, "Careful treatment planning enables safe ablation of liver tumors adjacent to major blood vessels by percutaneous irreversible electroporation (IRE)," *Radiol. Oncol.*, vol. 49, no. 3, pp. 234–241, Sep. 2015, doi: 10.1515/raon-2015-0031.
[13] M. Marčan *et al.*, "Effect of blood vessel segmentation on the outcome of electroporation-based treatments of liver tumors," *PLoS ONE*, vol. 10, no. 5, May 2015, Art. no. e0125591, doi: 10.1371/journal.pone.0125591.
[14] R. Qasrawi *et al.*, "Anatomically realistic simulations of liver ablation by irreversible electroporation: Impact of blood vessels on ablation volumes and undertreatment," *Technol. Cancer Res. Treat.*, vol. 16, no. 6, pp. 783–792, Dec. 2017, doi: 10.1177/1533034616687477.
[15] O. Gallinato *et al.*, "Numerical workflow of irreversible electroporation for deep-seated tumor," *Phys. Med. Biol.*, vol. 64, no. 5, Mar. 2019, Art. no. 055016, doi: 10.1088/1361-6560/ab00c4.
[16] G. Pucihar *et al.*, "Equivalent pulse parameters for electroporation," *IEEE Trans. Biomed. Eng.*, vol. 58, no. 11, pp. 3279–3288, Nov. 2011, doi: 10.1109/TBME.2011.2167232.
[17] Z. Qin *et al.*, "Irreversible electroporation: An in vivo study with dorsal skin fold chamber," *Ann. Biomed. Eng.*, vol. 41, no. 3, pp. 619–629, Mar. 2013, doi: 10.1007/s10439-012-0686-1.
[18] L. P. Beyer *et al.*, "Stereotactically-navigated percutaneous irreversible electroporation (IRE) compared to conventional IRE: A prospective trial," *PeerJ*, vol. 4, Aug. 2016, Art. no. e2277, doi: 10.7717/peerj.2277.
[19] L. P. Beyer *et al.*, "Evaluation of a robotic system for irreversible electroporation (IRE) of malignant liver tumors: Initial results," *Int. J. Comput. Assist. Radiol. Surg.*, vol. 12, no. 5, pp. 803–809, May 2017, doi: 10.1007/s11548-016-1485-1.
[20] R. C. G. Martin *et al.*, "Irreversible electroporation in locally advanced pancreatic cancer: A call for standardization of energy delivery," *J. Surg. Oncol.*, vol. 114, no. 7, pp. 865–871, Dec. 2016, doi: 10.1002/jso.24404.
[21] E. M. Dunki-Jacobs *et al.*, "Evaluation of resistance as a measure of successful tumor ablation during irreversible electroporation of the pancreas," *J. Amer. College Surg.*, vol. 218, no. 2, pp. 179–187, Feb. 2014, doi: 10.1016/j.jamcollsurg.2013.10.013.
[22] A. H. Ruarus *et al.*, "Conductivity rise during irreversible electroporation: True permeabilization or heat?," *Cardiovasc. Intervent. Radiol.*, vol. 41, no. 8, pp. 1257–1266, Aug. 2018, doi: 10.1007/s00270-018-1971-7.
[23] E. M. Dunki-Jacobs *et al.*, "Evaluation of thermal injury to liver, pancreas and kidney during irreversible electroporation in an in vivo experimental model," *Brit. J. Surg.*, vol. 101, no. 9, pp. 1113–1121, Aug. 2014, doi: 10.1002/bjs.9536.
[24] M. Faroja *et al.*, "Irreversible electroporation ablation: Is all the damage nonthermal?," *Radiology*, vol. 266, no. 2, pp. 462–470, Feb. 2013, doi: 10.1148/radiol.12120609.
[25] P. G. K. Wagstaff *et al.*, "Irreversible electroporation of the porcine kidney: Temperature development and distribution," *Urol. Oncol. Seminars Original Investigations*, vol. 33, no. 4, pp. 168.e1–168.e7, Apr. 2015, doi: 10.1016/j.urolonc.2014.11.019.
[26] P. A. Garcia *et al.*, "Predictive therapeutic planning for irreversible electroporation treatment of spontaneous malignant glioma," *Med. Phys.*, vol. 44, no. 9, pp. 4968–4980, Jun. 2017, doi: 10.1002/mp.12401.
[27] M. Marčan *et al.*, "Web-based tool for visualization of electric field distribution in deep-seated body structures and planning of electroporation-based treatments," *Biomed. Eng. Online*, vol. 14, pp. 1–13, Aug. 2015, doi: 10.1186/1475-925X-14-S3-S4.
[28] B. Kos *et al.*, "Robustness of treatment planning for electrochemotherapy of deep-seated tumors," *J. Membrane Biol.*, vol. 236, no. 1, pp. 147–153, Jul. 2010, doi: 10.1007/s00232-010-9274-1.
[29] A. Županič *et al.*, "Treatment planning of electroporation-based medical interventions: Electrochemotherapy, gene electrotransfer and irreversible electroporation," *Phys. Med. Biol.*, vol. 57, no. 17, pp. 5425–5440, Sep. 2012, doi: 10.1088/0031-9155/57/17/5425.
[30] D. Miklavčič *et al.*, "Towards treatment planning and treatment of deep-seated solid tumors by electrochemotherapy," *Biomed. Eng. OnLine*, vol. 9, pp. 10, Feb. 2010, doi: 10.1186/1475-925X-9-10.
[31] P. A. Yushkevich *et al.*, "User-guided 3D active contour segmentation of anatomical structures: Significantly improved efficiency and reliability," *NeuroImage*, vol. 31, no. 3, pp. 1116–1128, Jul. 2006, doi: 10.1016/j.neuroimage.2006.01.015.
[32] J. F. Edd and R. V. Davalos, "Mathematical modeling of irreversible electroporation for treatment planning," *Technol. Cancer Res. Treat.*, vol. 6, no. 4, pp. 275–286, Aug. 2007, doi: 10.1177/153303460700600403.
[33] D. Šel *et al.*, "Sequential finite element model of tissue electropermeabilization," *IEEE Trans. Biomed. Eng.*, vol. 52, no. 5, pp. 816–827, May 2005, doi: 10.1109/TBME.2005.845212.

[34] H. H. Pennes, "Analysis of tissue and arterial blood temperatures in the resting human forearm," *J. Appl. Physiol.*, vol. 85, no. 2, pp. 93–122, Aug. 1948, doi: 10.1152/jappl.1948.1.2.93.

[35] P. Agnass *et al.*, "Mathematical modeling of the thermal effects of irreversible electroporation for in vitro, in vivo, and clinical use: A systematic review," *Int. J. Hyperth.*, vol. 37, no. 1, pp. 486–505, Apr. 2020, doi: 10.1080/02656736.2020.1753828.

[36] N. Pavšelj *et al.*, "The course of tissue permeabilization studied on a mathematical model of a subcutaneous tumor in small animals," *IEEE Trans. Biomed. Eng.*, vol. 52, no. 8, pp. 1373–1381, Aug. 2005, doi: 10.1109/TBME.2005.851524.

[37] T. Jarm *et al.*, "Antivascular effects of electrochemotherapy: Implications in treatment of bleeding metastases," *Expert Rev. Anticancer Ther.*, vol. 10, no. 5, pp. 729–746, May 2010, doi: 10.1586/era.10.43.

[38] P. A. Garcia *et al.*, "A numerical investigation of the electric and thermal cell kill distributions in electroporation-based therapies in tissue," *PloS One*, vol. 9, no. 8, Aug. 2014, Art. no. e103083, doi: 10.1371/journal.pone.0103083.

[39] C. Rossmanna and D. Haemmerich, "Review of temperature dependence of thermal properties, dielectric properties, and perfusion of biological tissues at hyperthermic and ablation temperatures," *Crit. Rev. Biomed. Eng.*, vol. 42, no. 6, pp. 467–492, May 2014.

[40] J. A. Pearce, "Relationship between arrhenius models of thermal damage and the CEM 43 thermal dose," in *Proc. Energy-based Treat. Tissue Assess. V*, Feb. 2009, pp. 718104, doi: 10.1117/12.807999.

[41] O. Gallinato *et al.*, "Numerical modelling challenges for clinical electroporation ablation technique of liver tumors," *Math. Model. Nat. Phenom.*, vol. 15, pp. 1–18, Feb. 2020, doi: 10.1051/mmnp/2019037.

[42] R. E. Neal *et al.*, "In vivo irreversible electroporation kidney ablation: Experimentally correlated numerical models," *IEEE Trans. Biomed. Eng.*, vol. 62, no. 2, pp. 561–569, Feb. 2015, doi: 10.1109/TBME.2014.2360374.

[43] R. E. Neal *et al.*, "Improved local and systemic anti-tumor efficacy for irreversible electroporation in immunocompetent versus immunodeficient mice," *PloS One*, vol. 8, no. 5, May 2013, Art. no. e64559, doi: 10.1371/journal.pone.0064559.

[44] V. M. Ringel-Scaia *et al.*, "High-frequency irreversible electroporation is an effective tumor ablation strategy that induces immunologic cell death and promotes systemic anti-tumor immunity," *EBioMedicine*, vol. 44, pp. 112–125, Jun. 2019, doi: 10.1016/j.ebiom.2019.05.036.

[45] C. Bastianpillai *et al.*, "Harnessing the immunomodulatory effect of thermal and non-thermal ablative therapies for cancer treatment," *Tumor Biol.*, vol. 36, no. 12, pp. 9137–9146, Dec. 2015, doi: 10.1007/s13277-015-4126-3.

[46] H. J. Scheffer *et al.*, "Irreversible electroporation of locally advanced pancreatic cancer transiently alleviates immune suppression and creates a window for antitumor t cell activation," *Oncoimmunology*, vol. 8, no. 11, Aug. 2019, Art. no. 1652532, doi: 10.1080/2162402X.2019.1652532.

[47] T. Polajzer *et al.*, "Analysis of damage-associated molecular pattern molecules due to electroporation of cells in vitro," *Radiol. Oncol.*, vol. 54, no. 3, pp. 317–328, Jul. 2020, doi: 10.2478/raon-2020-0047.

[48] M. Moche *et al.*, "Clinical evaluation of in silico planning and real-time simulation of hepatic radiofrequency ablation (ClinicIMPPACT trial)," *Eur. Radiol.*, vol. 30, no. 2, pp. 934–942, Feb. 2020, doi: 10.1007/s00330-019-06411-5.

[49] A. Barabasch *et al.*, "Magnetic resonance imaging findings after percutaneous irreversible electroporation of liver metastases: A systematic longitudinal study," *Invest. Radiol.*, vol. 52, no. 1, pp. 23–29, Jan. 2017, doi: 10.1097/RLI.0000000000000301.

[50] S. A. Padia *et al.*, "Irreversible electroporation in patients with hepatocellular carcinoma: Immediate versus delayed findings at MR imaging," *Radiology*, vol. 278, no. 1, pp. 285–294, Jan. 2016, doi: 10.1148/radiol.2015150031.

[51] M. Kranjc *et al.*, "In situ monitoring of electric field distribution in mouse tumor during electroporation," *Radiology*, vol. 274, no. 1, pp. 115–123, Jan. 2015, doi: 10.1148/radiol.14140311.

[52] J. A. Vogel *et al.*, "Time-Dependent impact of irreversible electroporation on pancreas, liver, blood vessels and nerves: A systematic review of experimental studies," *PloS One*, vol. 11, no. 11, 2016, Art. no. e0166987, doi: 10.1371/journal.pone.0166987.

[53] F. Mahmood *et al.*, "Diffusion-weighted MRI for verification of electroporation-based treatments," *J. Membrane Biol.*, vol. 240, no. 3, pp. 131–138, Apr. 2011, doi: 10.1007/s00232-011-9351-0.

[54] L. Pan *et al.*, "Transcatheter intraarterial perfusion MRI approaches to differentiate reversibly electroporated penumbra from irreversibly electroporated zones in rabbit liver," *Acad. Radiol.*, vol. 27, no. 12, pp. 1727–1733, Dec. 2020, doi: 10.1016/j.acra.2020.01.008.

[55] Y. Zhao *et al.*, "Development of a multi-pulse conductivity model for liver tissue treated with pulsed electric fields," *Front. Bioeng. Biotechnol.*, vol. 8, May 2020, doi: 10.3389/fbioe.2020.00396, Art. no. 396.

[56] W. van den Bos *et al.*, "Thermal energy during irreversible electroporation and the influence of different ablation parameters," *J. Vasc. Interv. Radiol. JVIR*, vol. 27, no. 3, pp. 433–443, Mar. 2016, doi: 10.1016/j.jvir.2015.10.020.

[57] T. J. O'Brien *et al.*, "Effects of internal electrode cooling on irreversible electroporation using a perfused organ model," *Int. J. Hyperth.*, vol. 35, no. 1, pp. 44–45, May 2018, doi: 10.1080/02656736.2018.1473893.

[58] C. M. Edelblute *et al.*, "Controllable moderate heating enhances the therapeutic efficacy of irreversible electroporation for pancreatic cancer," *Sci. Rep.*, vol. 7, no. 1, Sep. 2017, Art. no. 11767, doi: 10.1038/s41598-017-12227-4.

[59] I. Fuhrmann *et al.*, "Navigation systems for treatment planning and execution of percutaneous irreversible electroporation," *Technol. Cancer Res. Treat.*, vol. 17, Jan. 2018, Art. no. 1533033818791792, doi: 10.1177/1533033818791792.

[60] A. Grošelj *et al.*, "Coupling treatment planning with navigation system: A new technological approach in treatment of head and neck tumors by electrochemotherapy," *Biomed. Eng. Online*, vol. 14, pp. 1–14, Sep. 2015, doi: 10.1186/1475-925X-14-S3-S2.

[61] L. P. Beyer *et al.*, "Evaluation of a robotic system for irreversible electroporation (IRE) of malignant liver tumors: Initial results," *Int. J. Comput. Assist. Radiol. Surg.*, vol. 12, no. 5, pp. 803–809, May 2017, doi: 10.1007/s11548-016-1485-1.

2.2 Paper 2

Title: **Numerical mesoscale tissue model of electrochemotherapy in liver based on histological findings**

Authors: **Helena Cindrič**, Gorana Gasljevic, Ibrahim Edhemovic, Erik Brecelj, Jan Zmuc, Maja Cemazar, Alenka Seliskar, Damijan Miklavcic and Bor Kos

Publication: *Scientific Reports*, vol. 12, no. 6476, pp. 1-11, April 2022

Impact factor: 4.996 (2021)

Quartile: Q1

Rank: 19/73 (Multidisciplinary Sciences)

DOI: https://doi.org/10.1038/s41598-022-10426-2

www.nature.com/scientificreports

scientific reports

Check for updates

OPEN

Numerical mesoscale tissue model of electrochemotherapy in liver based on histological findings

Helena Cindric[1], Gorana Gasljevic[2], Ibrahim Edhemovic[2,3], Erik Brecelj[2], Jan Zmuc[2,3], Maja Cemazar[2,4], Alenka Seliskar[5], Damijan Miklavcic[1] & Bor Kos[1]✉

Electrochemotherapy (ECT) and irreversible electroporation (IRE) are being investigated for treatment of hepatic tumours. The liver is a highly heterogeneous organ, permeated with a network of macro- and microvasculature, biliary tracts and connective tissue. The success of ECT and IRE depends on sufficient electric field established in whole target tissue; therefore, tissue heterogeneity may affect the treatment outcome. In this study, we investigate electroporation in the liver using a numerical mesoscale tissue model. We numerically reconstructed four ECT experiments in healthy porcine liver and computed the electric field distribution using our treatment planning framework. We compared the computed results with histopathological changes identified on microscopic images after treatment. The mean electric field threshold that best fitted the zone of coagulation necrosis was 1225 V/cm, while the mean threshold that best fitted the zone of partially damaged liver parenchyma attributed to IRE was 805 V/cm. We evaluated how the liver macro- and microstructures affect the electric field distribution. Our results show that the liver microstructure does not significantly affect the electric field distribution on the level needed for treatment planning. However, major hepatic vessels and portal spaces significantly affect the electric field distribution, and should be considered when planning treatments.

Electrochemotherapy (ECT) is a localized tumour treatment that combines the use of chemotherapeutic agents with the application of short high-voltage electric pulses to tissue. The application of pulses causes a transient increase in cell membrane permeability—reversible electroporation—that facilitates the transport of ions and molecules to which the membrane is otherwise impermeable or poorly permeable. Reversible electroporation significantly enhances the local cytotoxic effect of agents with intracellular targets, such as bleomycin and cisplatin[1–4]. ECT is already an established treatment for cutaneous and subcutaneous tumours (e.g. skin malignancies, head and neck tumours), due to its high effectiveness, relatively simple application and good cosmetic results[5,6]. Based on its effectiveness for superficial lesions, ECT is now also being investigated for treatment of various deep-seated tumours[2,3,7,8]. A significant part of recent studies is focused on treatment in the liver; results indicate that ECT is a feasible and effective treatment option for primary[9–11] and secondary liver tumours[12–15].

A prerequisite for a successful electroporation-based treatment is complete coverage of target tissue volume with sufficiently high electric field. For this purpose, numerical models of various scales are being developed for accurate prediction of electroporation in target tissue; from bulk tissue models used for treatment planning[16–19], to models of densely packed cells[20–23], models of single cells, and models of cell membrane electroporation[24,25]. The liver is a highly heterogeneous organ, permeated with a network of blood vessels and biliary tracts. Several studies have already shown the importance of considering liver macrostructures (large blood vessels and bile ducts), when constructing models for electroporation-based treatments in the liver[26–28]. Moreover, liver parenchyma has a distinct microstructure consisting of functional units called hepatic lobules, each containing a centrilobular vein (CV). Hepatic lobules relate to a network of connective tissue, blood vessels and bile ducts (portal triads), called the interlobular septa. For modelling purposes, the lobules are usually represented as prisms with hexagonal cross sections of 1000–2000 µm diameter with CVs in the center (80–187 µm diameter), and separated by gaps (~ 50 µm) representing the interlobular septa[29,30]. The electric field distribution depends on the electrical properties of the medium. This is especially important when treating target volumes that contain

[1]Faculty of Electrical Engineering, University of Ljubljana, Trzaska cesta 25, 1000 Ljubljana, Slovenia. [2]Institute of Oncology Ljubljana, Zaloska cesta 2, 1000 Ljubljana, Slovenia. [3]Faculty of Medicine, University of Ljubljana, Vrazov trg 2, 1000 Ljubljana, Slovenia. [4]Faculty of Health Sciences, University of Primorska, Polje 42, 6310 Izola, Slovenia. [5]University of Ljubljana, Veterinary Faculty, Gerbiceva ulica 60, 1000 Ljubljana, Slovenia. ✉email: bor.kos@fe.uni-lj.si

Sample/model	Electrode geometry	Threshold [V/cm]		DSC [/]	
		Zone A	Zone B	Zone A	Zone B
S1	Hexagonal	1230	760	0.71	0.74
S2	Hexagonal	1150	800	0.65	0.70
S3	Linear	1260	770	0.67	0.85
S4	Linear	1260	890	0.75	0.87

Table 1. Computed electric field threshold with the best Sørensen-Dice similarity coefficient (DSC) for Zone A (mechanical damage and coagulation necrosis) and Zone B (damage caused by IRE).

tissues with significantly different conductivities, as the majority of voltage drop, and consequently electric field strength, occurs in tissues with low conductivity[18,27,31,32]. The natural heterogeneity of the liver structure may have an impact on the electric field distribution and consequently on the outcome of electroporation-based treatments in liver.

In this study, we investigate ECT in the liver using a mesoscale tissue model that is comparable to findings from microscopic images after treatment. In a recent translational animal model study[33], we examined whether ECT with bleomycin causes clinically significant damage to normal liver tissue with respect to large blood vessels and bile ducts. In our present study, we numerically reconstructed four of the experiments performed in that study[33], and computed the electric field distribution in tissue with our previously developed treatment planning framework[19,34–36]. The aim of this study was to compare the computed electric field distribution with the histopathological changes observed in tissue after treatment, and to evaluate how the liver structures affect the electric field distribution. We determined the electric field thresholds that best correspond to the changes present in tissue after ECT, and evaluated the temperature increase and probability of thermal damage to tissue, with special focus on sensitive anatomical structures such as vessels and bile ducts. We investigated whether the liver microstructure (i.e. hepatic lobules, septa and CVs) and the variability in its' electrical conductivity affect the electric field distribution in any extent relevant for comparison with histopathological findings.

Results

Electric field thresholds and tissue heating. We reconstructed four experiments of liver ECT from the study reported previously[33] and computed the electric field distribution and heating in treated tissue. We fitted the computed electric field to the microscopic images and determined the thresholds that best fit the two zones of histopathological changes observed in the samples—Zone A, immediately surrounding the electrode insertion site that exhibits coagulation necrosis with complete loss of liver microstructure, and Zone B of partially damaged liver parenchyma. The electric field thresholds corresponding to the two zones for each reconstructed case are presented in Table 1 along with their respective Sørensen-Dice similarity coefficients. The mean thresholds were 1225 ± 52 V/cm for Zone A and 805 ± 59 V/cm for Zone B. The threshold for Zone A encapsulates the potential temperature-related changes and electro-chemical changes at the treated site, while threshold for Zone B is attributed mainly to damage caused by irreversible electroporation (IRE). Figures 1, 2 show the computed electric field distribution and the determined zones for hexagonal and linear geometry electrodes respectively.

There was no significant heating observed in tissue. With linear geometry electrodes, the temperature did not exceed 41 °C anywhere in the tissue, while in case of hexagonal electrodes the temperature reached 47 °C only at the electrode surface. Probability of thermal damage was determined by integrating the Arrhenius equation over the time of treatment and was $< 1\%$ everywhere in tissue in all four cases; therefore, the tissue necrosis observed in Zone A is not considered to be a direct consequence of elevated temperature in tissue. Nevertheless, a map of maximum temperature distribution for all four cases is shown in Supplementary Fig. S3.

Liver microstructure and variability in electric properties. We evaluated how the liver microstructure—hepatic lobules, septa and centrilobular veins (CV)—affects the electric field distribution. We compared the electric field distribution computed with numerical models incorporating a varying degree of geometrical detail of the liver parenchyma: a heterogeneous model (hepatic lobules, septa and CVs), a semi-homogenous model (homogeneous hepatic tissue with CVs) and a fully homogenous model (only hepatic tissue). Detailed description of the models is provided in the Methods sub-section "Liver microstructure and parametric study of tissue properties".

Figure 3 shows an example of the electric field, computed with the heterogeneous and homogeneous models. In this example, the septa had the same conductivity function shape as the vessel wall (see Supplementary Tables S1 and S2). When crossing the septum domain we observe a drop in electric field strength, however, it resumes its previous value immediately after leaving the septum (Fig. 3b,c). When crossing the domain of the CV we observe a spike at the edge of the CV lumen, which is a consequence of a much higher conductivity of blood within the lumen compared to surrounding tissue, and then a drop in electric field strength in the CV lumen respectively (Fig. 3b,c). This effect was also reported in previous studies on smaller vessels and capillaries[37]. In this example the mean relative error between electric field computed with a heterogeneous model and a fully homogenous model is 7% with a standard deviation of 12%, while the median relative error is 3%. The mean relative error between the electric field computed with a semi-homogenous and a fully homogenous model is 3% with a standard deviation of 10%, while the median relative error is 0.5%.

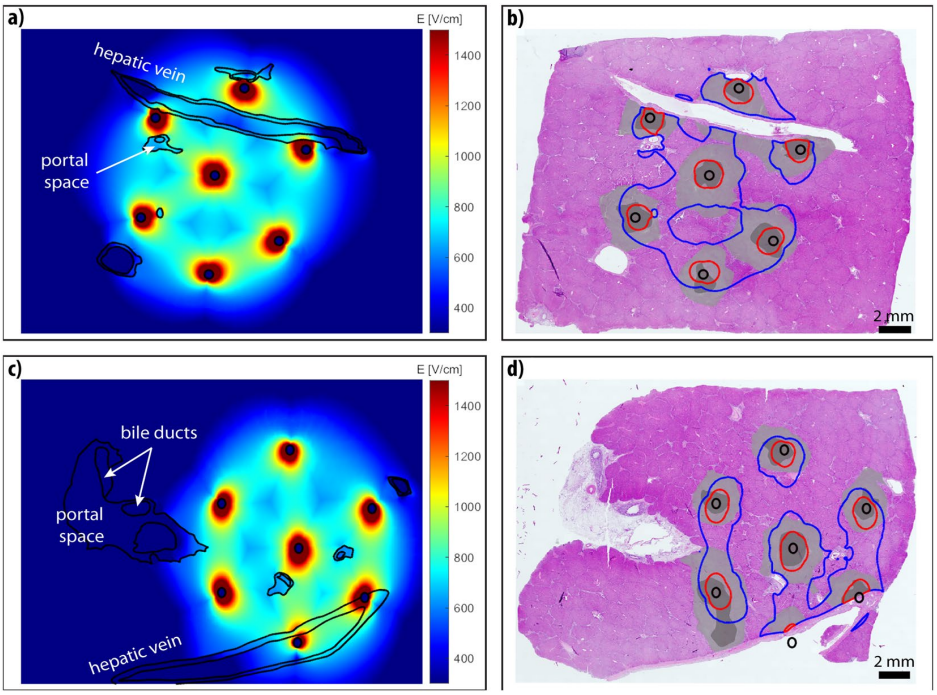

Figure 1. Reconstruction results of cases S1 (**a**, **b**) and S2 (**c**, **d**) with hexagonal geometry electrodes. (**a**, **c**) Computed electric field distribution. Geometric entities are outlined in black. (**b**, **d**) Segmented Zone A (dark grey) and Zone B (light gray), and computed Zone A (red contour) and Zone B (blue contour) shown as an overlay on the microscopic image of the treated area.

Using the heterogeneous model, we performed a parametric study, to evaluate how the differences in conductivity of the septa affect the electric field distribution and determined thresholds for Zones A and B. Electric field was computed for all combinations of parameter values of the septa conductivity function (see Methods Section "Liver microstructure and parametric study of tissue properties"), resulting in 72 computations. The electric field thresholds for Zones A and B were calculated for each combination and results were compared to thresholds determined with the semi homogeneous and fully homogeneous models. Row 1 of Table 2 shows the median and mean electric field thresholds, range and standard deviation for both zones, obtained in the parametric study with the heterogeneous model. Rows 2 and 3 of Table 2 show the electric field thresholds for both zones, obtained with the semi-homogeneous and homogeneous models, respectively. We can see that the threshold for Zone B is not affected by any of the parameters studied. If the base conductivity of the septa is much lower than the conductivity of the lobules (e.g., 10% of its base value), the threshold for Zone A is lower than in the homogenous models (660 ± 22 V/cm vs. 850 V/cm respectively). If the base conductivity of the septa is equal or higher than the conductivity of lobules, the threshold for Zone A does not significantly differ from the thresholds from the homogenous models (853 ± 8 V/cm vs. 850 V/cm respectively). The size and location of the transition zone do not affect the threshold. Although the exact conductivity of the interlobular septa is not known, we hypothesize that their conductivity is higher than the conductivity of the lobules because the septa consist of connective tissues, blood vessels and bile ducts. Therefore, we can assume the septa does not affect the electric field thresholds at the mesoscale.

Discussion

In this study, we compare the electric field distribution, computed in a mesoscale tissue model, with the histopathological changes observed in healthy hepatic tissue after ECT. We numerically reconstructed four ECT procedures, performed in a recent in vivo animal study by Zmuc et al.[33] and examined how the liver macro- and microstructures affect the electric field distribution. We also investigated the tissue temperature increase due to Joule heating and its' potential effect on the nearby vessels and bile ducts.

The four studied samples are different from the ones presented in our previous study; special attention was given to select samples where several major hepatic vessels were involved in the treatment area. In three cases at least one electrode was inserted directly into the vessel, while in the fourth case (sample S1) the electrodes were positioned around one of the hepatic veins. The presence of these hepatic vessels affects the gross electric field distribution. In Figs. 1–2, we can see an increase in electric field strength at the side of the vessel perpendicular

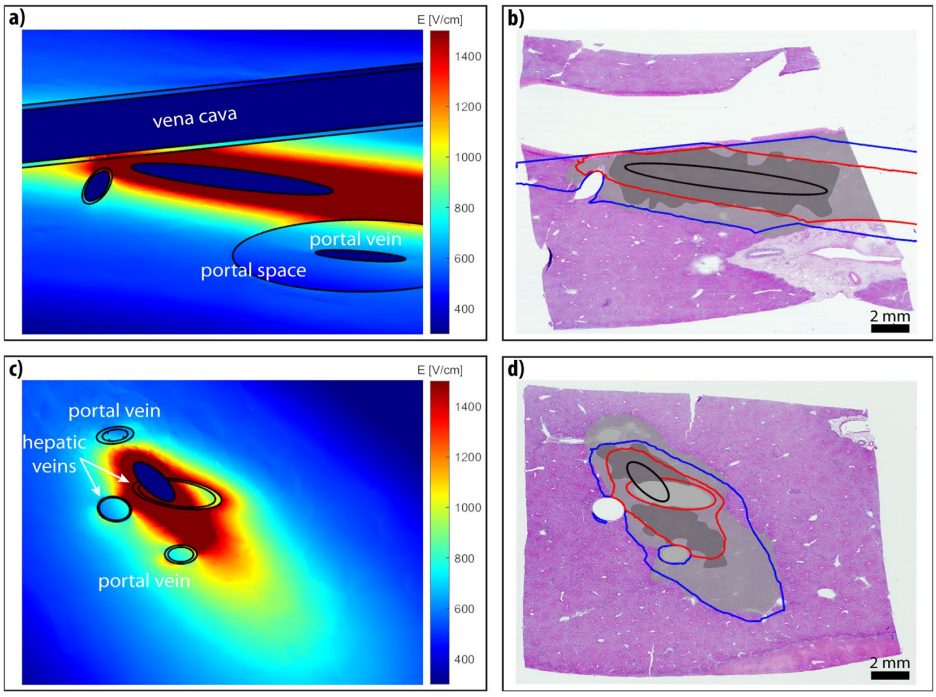

Figure 2. Reconstruction results of cases S3 (**a**, **b**) and S4 (**c**, **d**) with linear geometry electrodes. (**a**, **c**) Computed electric field distribution in a slice of the 3D model, corresponding to the microscopic image. Geometric entities are outlined in black. (**b**, **d**) Segmented Zone A (dark grey) and Zone B (light gray), and computed Zone A (red contour) and Zone B (blue contour) shown as an overlay on the microscopic image of the treated area.

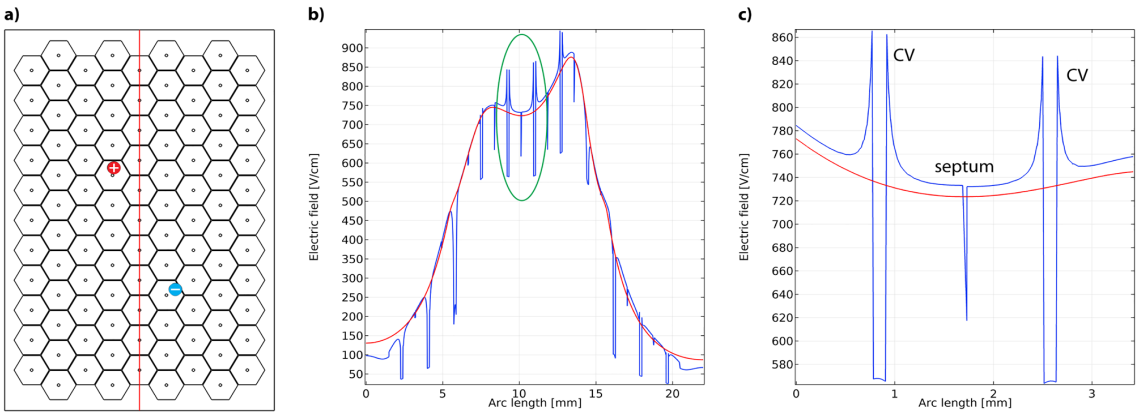

Figure 3. (**a**) A section of the model, showing two electrodes (red–cathode, blue–anode) and the cut-line (red vertical line). **(b)** Electric field strength along the cut-line crossing several septa and centrilobular veins (CV). (**c**) A close up of a section (indicated in green on panel (**b**) showing two lobules with CVs separated by a septum. Red lines on panels (**b**) and (**c**) show the electric field computed with a completely homogenous model.

Model	Zone A threshold [V/cm]		Zone B threshold [V/cm]	
	median (range) [V/cm]	mean ± std [V/cm]	median (range) [V/cm]	mean ± std [V/cm]
Heterogeneous (parametric study)	840 (640–860)	810 ± 70	480 (480–490)	480 ± 2
Semi-homogeneous	850	/	480	/
Homogeneous	850	/	470	/

Table 2. Electric field thresholds for Zones A and B determined with models with different level of geometric detail. Only one section of the model, containing one active electrode pair, was computed due to computational complexity.

to the electrodes, and a decrease in field strength at the side parallel to the electrode. This effect is most notable around the lower portal vein in Fig. 2c. Our findings are in agreement with previous studies[26–28], indicating that presence of larger vessels should not be overlooked, when computing the electric field for electroporation-based treatments. In samples S1, S2 and S4 larger portal spaces containing bile ducts were present in vicinity of the treated zone, however, no damage was observed in the histological examination of the samples. The portal space constitutes mainly of supportive connective tissue (type I collagen fibers, lymphatics, cholangioles) with a higher base electrical conductivity than the surrounding liver parenchyma (0.26 S/m compared with 0.091 S/m[19,27,38]) and is therefore exposed to a lower electric field strength than its surroundings..

No significant tissue heating was observed in our models. This comes at no surprise, since only a small number of pulses is used in ECT. The highest computed temperature reached 47 °C in sample S1 with hexagonal electrodes, but only immediately at the surface of the electrode that was positioned in the hepatic vein. In case of the linear geometry electrodes, the temperature did not exceed 41 °C, since a significantly lower number of pulses is cumulatively applied and a slower repetition rate is used. Probability of thermal damage according to Arrhenius kinetics equation was < 1% everywhere in tissue for all four cases.

In our previous study[33], we investigated whether ECT with bleomycin causes clinically significant damage to normal liver tissue. Upon histological examination of explanted liver samples, acute changes with clear zonation were observed in the tissue. The area immediately surrounding the electrode insertion site exhibited coagulation necrosis with complete loss of liver microstructure (Zone A; Zones 1–2 in the paper by Zmuc et al.). Surrounding this area was a zone of partially damaged liver parenchyma, which was attributed to irreversible electroporation (IRE) of tissue (Zone B; Zone 3 in the paper by Zmuc et al.). No histological changes were observed in areas exposed to reversible electroporation. Furthermore, the addition of bleomycin (electrochemotherapy) did not cause any difference compared with samples only treated with electric pulses. In our current study, we fitted the computed electric field to the microscopic images of the treated area to determine the threshold values that best fit the appearance of the Zones A and B.

The mean electric field threshold that best fits the appearance of Zone A is 1225 V/cm. Although histological examination of Zone A revealed changes characteristic of coagulation necrosis, in Zmuc et al. we postulated that it is not likely these changes were caused by tissue heating during pulse delivery, which was now also confirmed by our computations. In recent years the role of pH changes in cell death mechanisms is being investigated in electroporation-based treatments[39–44]. The pH change is attributed to the ion transport, which results in a strong acidification at the site of the anode and alcalinization at the site of the cathode, which result in necrotic regions near the electrode insertion site. The necrosis in Zone A observed in our samples may be related to the pH changes around the electrodes, however, further research is needed to verify this speculation. The appearance of Zone B is most likely caused by IRE of tissue. Even though lower pulse amplitudes and pulse number are used in ECT, an area of irreversibly electroporated tissue is also present around the electrodes. Our computations show the best fit with Zone B is achieved with electric field strength of 810 V/cm, which is sufficient to cause IRE of hepatic tissue with reversible electroporation pulse protocols[16,27,45].

In Zmuc et al.[33], the estimated thresholds for Zone A were 1500 V/cm for linear and 1200 V/cm for hexagonal electrodes. The electroporated volume and electric field threshold depend on the number and duration of applied electric pulses (i. e. exposure time). With one pair of linear electrodes significantly less pulses are cumulatively delivered to tissue compared to hexagonal electrodes (8 pulses vs. 96 pulses respectively), therefore, a higher threshold for linear geometry electrodes is expected[24]. In present study, however, we found no significant difference between the thresholds for linear and hexagonal electrodes for both zones. We achieved good agreement with the original study for the hexagonal electrodes, however, for linear electrodes our threshold was approximately 300 V/cm lower. The discrepancy between the results could be due to sample selection bias. Although the data was obtained from the same experiments, the thresholds in the present study were determined on samples located at the sites of major hepatic vessels and bile ducts, whereas in the previous study[33] the thresholds were determined on samples located exclusively in the liver parenchyma and obtained from a different animal. Biological variability and different methods of threshold determination are among the main reasons for the different threshold values reported in literature[16,19,45–48]. Lastly, in Zmuc et al., the thresholds were estimated by matching the radius of Zone A to the distance obtained from the image of field distribution. For electric fields of such high intensity (> 800 V/cm), the transition zone is very short and even an error of 1 mm in the estimated zone radius can result in a difference of 150 V/cm in the electric field threshold. However, in the present study, we used a refined image-based fitting method for threshold determination with a step of 10 V/cm.

In the second part of the study, we investigated whether the microscopic structure of the liver (i.e. hepatic lobules, septa, CVs) and the differences in electrical conductivity of these microstructures affect the electric field

distribution during ECT on a level relevant for comparison with microscopic images. The result of our study show, that the inclusion of the liver microstructures does not significantly affect the computed electric field. There is a localized drop in field strength observed in the domain of the septa and CVs (Fig. 3), however, these domains are composed mainly of connective tissue and microvasculature and do not contain cells targeted by electroporation-based treatments, therefore the treatment success should not be negatively affected. When compared to a fully homogenous tissue model (with electrical properties of hepatic lobules, see Table S1 in supplementary materials) there is no significant difference in computed electric field strength. According to the results of our parametric study, the only scenario, where the inclusion of the septa would significantly affect the gross electric field distribution, is if the conductivity of the septa is much lower than the conductivity of surrounding hepatic tissue (e.g. 10%; 0.0091 S/m compared to 0.091 S/m for the septa and lobules, respectively). However, the interlobular septa consist of connective tissue, venules, arterioles and bile ducts, which suggests the conductivity of the septa is in fact higher than the surrounding tissue. Our findings confirm there is no significant difference in gross electric field distribution and the determined thresholds for Zones A and B regardless of the inclusion of the septa and CVs in the model.

In the previous study[33], Zmuc et al. observed that the damage in Zone B was not distributed equally, as it was more pronounced in the centri- and midlobular areas. This observation might be explained by taking into consideration the vascularization of the hepatic lobules. At the center of each lobule there is a centrilobular vein surrounded by sinusoids (capillaries), while the "wall" of the lobule consists of the vascularized septa and portal tracts. Blood flows through the lobule walls, traverses the sinusoids, and flows into the centrilobular vein[29]. In Fig. 3, we can see pronounced spikes in electric field strength at the lumen of the CVs, which could cause damage to the vessel. This is also in agreement with the histological findings, as the CVs were no longer visible in the damaged areas of Zone B. In the domains of the septa however, the electric field is lower compared to surrounding tissue, which could spare the microvasculature. It is possible that the damage in the centrilobular domain is due to disruption of central vasculature of the lobules, while the outer parts of the lobules are less affected due to still functional vasculature. When evaluating the electric field distribution at a mesoscale, these local fluctuations in electric field strength were not significant.

Our study was mainly limited by its retrospective nature. While in case of hexagonal electrodes, the positions of the electrodes were easily discernible in the histological samples, the soft liver tissue was somewhat deformed during electrode insertion, therefore the inter-electrode distances in the samples were no longer 7.3 mm in all locations within the samples. Already a 1–2 mm difference in inter-electrode distance resulted in significant difference in the determined electric field thresholds. We applied scaling and shearing deformations to the 2D models, however, we were unable to completely eliminate the deformation, therefore small differences in inter-electrode distance remained. On the other hand, in case of linear geometry electrodes, we were able to fix the inter-electrode distance in the model to 2 cm. However, only one electrode site was visible in the sample and the position of the counter electrode had to be determined to the best of our ability, based on the shape of the Zones A and B.

In conclusion, we confirmed that the liver microstructure (hepatic lobules, interlobular septa and centrilobular veins) does not significantly affect the electric field distribution at a mesoscale. The use of a fully homogeneous model of the liver parenchyma is suitable for the numerical computations of electric field in the liver organ, needed for planning electroporation-based treatments. However, major hepatic vessels and portal spaces should be included in the model, as these macrostructures significantly affect the electric field distribution, as already suggested before[27].

Methods

Animal experiments. The animal experiments were performed in the scope of a recent in vivo animal model study by Zmuc et al.[33], which is reported in accordance with ARRIVE guidelines for reporting of research involving animals. All experiments were performed in accordance with the relevant guidelines and regulations. Regulatory approval for this study was obtained from the National Ethics Committee at The Administration of the Republic of Slovenia for Food Safety, Veterinary, and Plant Protection (U34401-1/2017/4; approval date: 17.03.2017). Experiments were performed on healthy pig liver; six pigs were treated with ECT with bleomycin and two pigs received pulses only, serving as control. The pulses were delivered with the Cliniporator pulse generator (IGEA, Italy) using either fixed hexagonal geometry electrodes or two linear geometry electrodes with 2 cm spacing. The following ECT protocols were used: for linear geometry electrodes 8×100 µs, 2000 V electric pulses were delivered with a 1/s repetition rate; for fixed hexagonal geometry electrodes 96×100 µs, 730 V electric pulses were delivered with a 5000/s repetition rate. The applied voltage in both electrode geometries corresponded to a 1000 V/cm voltage-to-distance ratio. Two days after the procedure the liver was explanted, cut and fixed in formaldehyde. After 24 h, the specimens were cut into 2–3 µm thick samples, stained with H&E and microscopically examined and photographed. Further details regarding the experiments, treatment protocols and histological analysis are described in[33].

Numerical reconstructions. For our present study, four histological samples from two animals treated with ECT with bleomycin were selected for numerical reconstruction and analysis. The samples were selected from procedures performed at the sites of the major hepatic vessels and portal spaces, and therefore differ from the samples in the work of Zmuc et al. Fig. 4 shows the microscopic images of the selected samples 2 days post treatment. Animal 1 (Fig. 4a,b) was treated with hexagonal geometry electrodes (pig #2 from Zmuc et al.). In sample S1, electrodes were inserted in the liver parenchyma abutting the hepatic vein (a) and in sample S2, two electrodes were inserted into the hepatic vein (b). Animal 2 (Fig. 4c,d) was treated with linear geometry electrodes (pig #1 from Zmuc et al.). In sample S3, one of the electrodes was inserted into the vena cava (c) and

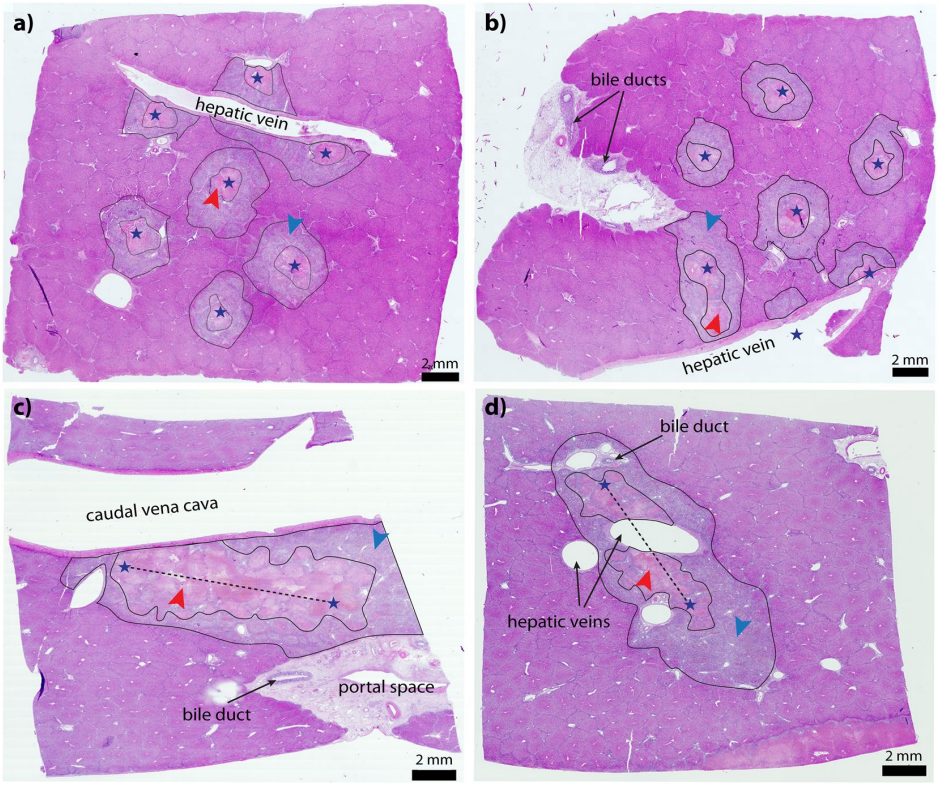

Figure 4. Microscopic images of treated liver 2 days post ECT. Electrode insertion sites are denoted with stars and dashed lines. Portal spaces and major hepatic vessels are contained in the treatment zone. Zones A (red arrowhead) and B (blue arrowhead) are outlined in black. (**a**, **b**) Samples S1 and S2 of animal 1, treated with hexagonal geometry electrodes. (**c**, **d**) Samples S3 and S4 of animal 2, treated with linear geometry electrodes. Since the second electrode was 2 cm away, it is always far from the field of view of these histological sections, so they are not visible.

in sample S4 into one of the major hepatic veins (d). The zones of acute changes in the liver parenchyma were identified in the microscopic images. In the work of Zmuc et al., three zones were identified: the central cavity caused by electrode insertion (Zone 1), the surrounding zone of coagulation necrosis with complete loss of liver microstructure (Zone 2), and a zone of partially damaged liver parenchyma attributed to IRE (Zone 3). In this study, we focus only on Zones 2 and 3 because Zone 1 is caused by mechanical damage by the electrodes and is always included in Zone 2. To avoid confusion regarding numbering, we changed the zoning to Zone A (Fig. 4, red arrows), which corresponds to Zones 1–2, and Zone B (Fig. 4, blue arrows), which corresponds to Zone 3 in the original article[33]. A pathologist manually outlined the two zones in microscopic images. The outlined images were imported to Adobe Illustrator CS4 where major haptic vessels, vessel walls, portal spaces and bile ducts were manually outlined as well, and electrode insertion trajectories were determined. The outlines were saved in vector format (Fig. 5a,b) and imported into COMSOL Multiphysics to construct the geometry for the numerical models.

In case of hexagonal electrodes, the sections were cut perpendicular to the electrode orientation and all 7 electrodes were visible; therefore, we were able to construct a 2D model directly from the imported vector images (Fig. 5a). Electrodes were modelled as circles with a 0.7 mm diameter. In case of linear electrodes, only one electrode of the pair was visible, and the sample was not cut perpendicular to the electrodes, therefore a 3D model was required. The vector image was imported into the work plane in the 3D model, and the vessels, bile ducts and portal spaces were modelled with geometrical primitives (cylinders and spheroids) so that the intersection of the primitives with the work plane overlapped with the outlined anatomical structures (red intersections on Fig. 5b). Electrodes were modelled as cylinders with a 1.2 mm diameter and 3 cm active length. The orientation of the first electrode was determined from the microscopic image, and the counter electrode (second electrode of the pair) was modelled completely parallel at a distance of 2 cm. Since the position of the counter electrode could not be determined from the microscopic images, we determined its position by rotating it in 5° steps around the first electrode at the circumference of 2 cm, and comparing the appearance of the computed electric field to the

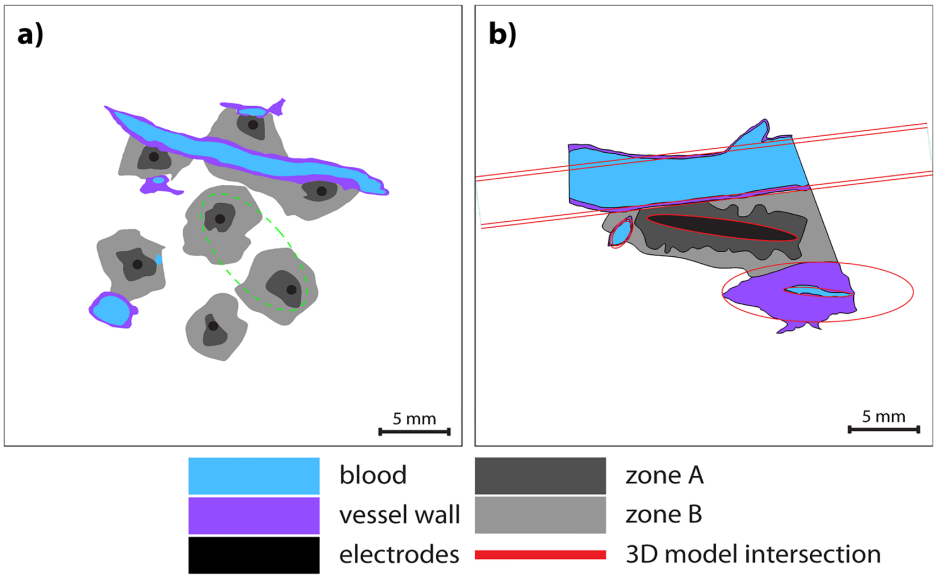

Figure 5. Numerical model geometries. (**a**) 2D model geometry of sample S1 is constructed directly from the outlined microscopic image. Green circle indicates the section of the model, used in the parametric study of septa electrical conductivity. (**b**) A slice from the simplified 3D model with linear electrodes. The location of the slice corresponds to the microscopic image of sample S3. Intersections of the geometric entities with the outlined microscopic image are shown in red.

segmented zones (see Methods Section "Electric field distribution and threshold determination"). The angle that resulted in the highest Sørensen-Dice similarity coefficient was selected as the final model.

Electric field distribution and threshold determination. COMSOL Multiphysics was used for computation of electric field and temperature distribution during the procedures. The computation process is described in detail in[19,34–36]. Briefly, the model consists of solving the partial differential equation for electric potential distribution in steady state form. Electrical conductivity is a non-linear function of the local electric field, and is represented by a smoothed step function, specific to each tissue modelled. To evaluate tissue heating during treatment, the modified Pennes' bioheat equation[49] is solved in time domain. The power dissipation density from the stationary computation is used as the heat source. The duty cycle approach is used to shorten computation times[50]. In hexagonal electrode geometry, the electric field and temperature for each electrode pair is computed separately, and the contributions from all 12 pairs are then superimposed to reproduce the final field distribution. Local conductivity increase due to electric field is independent between the pairs (each computation starts with base conductivity). The heat dissipation process is much slower than electroporation phenomenon, therefore the base conductivity for the following electrode pair computations is increased due to increased temperature. For a more detailed explanation of the modeling approach, see Supplementary materials Section "Numerical model and computation".

The computed electric field and temperature distributions were imported into MATLAB for comparison with the segmented microscopic images. The 2D model was already identical to the microscopic image of the sample (Fig. 5a), while in the 3D model, the plane corresponding to the microscopic image of the sample was extracted for evaluation (Fig. 5b). For each of the four sample models, the similarity between the computed electric field and the segmented microscopic zones was calculated using the Sørensen-Dice similarity coefficient (DSC)[51]. DSC calculates the similarity between two binary images (masks) and takes a value between 0 and 1. A similarity of 1 means that the masks match perfectly. We compared the masks of Zones A and B with masks representing isocontours of the electric field at selected thresholds (field masks). The process is shown in Fig. S2 of the supplementary materials. The masks of Zones A and B were extracted directly from the outlines of the microscopic images (Fig. S2, top row), while the field masks were obtained by applying a specific threshold to the computed electric field distribution. Thresholds ranging from 300 to 1500 V/cm were applied in steps of 10 V/cm, resulting in 121 field masks (Fig. S2, middle row). DSC was calculated between each zone mask and the 121 field masks, resulting in 121 DSC values for each zone (Fig. S2, bottom row). A higher DSC value indicates a greater similarity between the isocontour of the field obtained with the respective threshold level and the shape of the segmented zone. Therefore, the two electric field thresholds that yielded the highest DSC value were set as the thresholds for Zones A and B, respectively.

Liver microstructure and parametric study of tissue properties. In order to evaluate, how the liver microstructures and the variability in electrical properties of these structures affect the computed electric field distribution we constructed a 2D model incorporating the hexagonal liver architecture. A hexagonal structure representing the hepatic lobules and interlobular septa was constructed using Adobe Illustrator CS4. The modelled lobule diameter was 1950 μm, CV diameter was 150 μm and septum thickness was 50 μm (Fig. 3 a). Positions of the electrodes were taken from sample S1 with parenchymal hexagonal electrodes. The liver macro- and microstructures are several magnitudes apart in size, which significantly increases the computational difficulty. Therefore, the computations were performed only in one section of the sample containing a single electrode pair (green circle in Fig. 5a). The geometry was imported into COMSOL Multiphysics where a 2D numerical model was constructed for the computation of electric field.

Three models with a varying degree of geometrical details were computed; a heterogeneous model incorporating the whole liver microstructure (hepatic lobules, septa and CVs), a semi-homogeneous model consisting of homogeneous hepatic tissue with CVs, and a fully homogeneous model consisting only of hepatic tissue. In order to eliminate error due to meshing, identical geometry (whole liver microstructure) was used in all three models; the homogeneous effect was achieved by matching the conductivity of the septa and CVs to the conductivity of the lobules.

The change in electrical conductivity due to electroporation of each modelled structure is approximated in COMSOL as a smoothed step function, with the following parameters: base electrical conductivity (σ_0), factor of conductivity increase, center (E_C) and size (E_W) of the transition zone. The parameters of the electrodes and all tissues except for the septa were taken from previous works[19,27,36], and are listed in Supplementary Table S1. The electrical conductivity of the interlobular septa is unknown, therefore, we performed a parametric study, using the heterogeneous model, where we varied all four parameters of the conductivity function. The base conductivity was defined as a fraction of base conductivity of hepatic lobules, while the factors of conductivity increase and values of E_C and E_W were taken from conductivity functions of hepatic lobules and vessel wall. All studied parameter values are listed in Supplementary Table S2.

We computed the electric field for each set of parameters of the heterogeneous model (72 combinations in total) and for the semi-homogenous and homogeneous models. Then we calculated the similarities between the computed electric fields and segmented Zones A and B of sample S1 (see Fig. 5a) and compared the thresholds determined by the different models (see Methods Section "Electric field distribution and threshold determination").

Ethics declarations. The animal experiments were performed in the scope of our previously published animal study by Zmuc et al. (J. Zmuc et al. Sci Rep, 2019. 9:3649), which is reported in accordance with ARRIVE guidelines for reporting of research involving animals. All experiments were performed in accordance with the relevant guidelines and regulations. Regulatory approval for the study was obtained from the National Ethics Committee at The Administration of the Republic of Slovenia for Food Safety, Veterinary, and Plant Protection (U34401-1/2017/4; approval date: 17.03.2017).

Data availability

The datasets generated during and/or analysed during the current study are available from the corresponding author on a reasonable request.

Received: 15 October 2021; Accepted: 7 April 2022
Published online: 20 April 2022

References

1. Miklavčič, D., Čorović, S., Pucihar, G. & Pavšelj, N. Importance of tumour coverage by sufficiently high local electric field for effective electrochemotherapy. *Eur. J. Cancer Suppl.* **4**, 45–51 (2006).
2. Miklavčič, D., Mali, B., Kos, B., Heller, R. & Serša, G. Electrochemotherapy: From the drawing board into medical practice. *Biomed Eng Online* **13**, 29 (2014).
3. Campana, L. G. *et al.* Electrochemotherapy - Emerging applications technical advances, new indications, combined approaches, and multi-institutional collaboration. *Eur. J. Surg. Oncol.* **45**, 92–102 (2019).
4. Geboers, B. *et al.* High-voltage electrical pulses in oncology: Irreversible electroporation, electrochemotherapy, gene electrotransfer, electrofusion, and electroimmunotherapy. *Radiology* **295**, 254–272 (2020).
5. Spratt, D. E. *et al.* Efficacy of skin-directed therapy for cutaneous metastases from advanced cancer: A meta-analysis. *JCO* **32**, 3144–3155 (2014).
6. Campana, L. G. *et al.* Electrochemotherapy of superficial tumors – Current status: Basic principles, operating procedures, shared indications, and emerging applications. *Semin. Oncol.* **46**, 173–191 (2019).
7. Probst, U., Fuhrmann, I., Beyer, L. & Wiggermann, P. Electrochemotherapy as a new modality in interventional oncology: A review. *Technol. Cancer Res. Treat.* **17**, 1533033818785329 (2018).
8. Granata, V. *et al.* Electroporation-based treatments in minimally invasive percutaneous, laparoscopy and endoscopy procedures for treatment of deep-seated tumors. *Eur. Rev. Med. Pharmacol. Sci.* **25**, 3536–3545 (2021).
9. Tarantino, L. *et al.* Percutaneous electrochemotherapy in the treatment of portal vein tumor thrombosis at hepatic hilum in patients with hepatocellular carcinoma in cirrhosis: A feasibility study. *World J. Gastroenterol.* **23**, 906–918 (2017).
10. Djokic, M. *et al.* Electrochemotherapy as treatment option for hepatocellular carcinoma, a prospective pilot study. *Eur. J. Surg. Oncol.* **44**, 651–657 (2018).
11. Djokic, M. *et al.* A prospective phase II study evaluating intraoperative electrochemotherapy of hepatocellular carcinoma. *Cancers (Basel)* **12**, E3778 (2020).
12. Edhemović, I. *et al.* Intraoperative electrochemotherapy of colorectal liver metastases. *J. Surg. Oncol.* **110**, 320–327 (2014).
13. Tafuto, S. *et al.* Electrochemotherapy as a new approach on pancreatic cancer and on liver metastases. *Int. J. Surg.* **21**, S78–S82 (2015).

14. Coletti, L. *et al.* Safety and feasibility of electrochemotherapy in patients with unresectable colorectal liver metastases: A pilot study. *Int. J. Surg.* **44**, 26–32 (2017).
15. Edhemovic, I. *et al.* Intraoperative electrochemotherapy of colorectal liver metastases: A prospective phase II study. *Eur. J. Surg. Oncol.* **46**, 1628–1633 (2020).
16. Šel, D. *et al.* Sequential finite element model of tissue electropermeabilization. *IEEE Trans. Biomed. Eng.* **52**, 816–827 (2005).
17. Edd, J. F. & Davalos, R. V. Mathematical modeling of irreversible electroporation for treatment planning. *Technol. Cancer Res. Treat.* **6**, 275–286 (2007).
18. Miklavčič, D. *et al.* Towards treatment planning and treatment of deep-seated solid tumors by electrochemotherapy. *Biomed. Eng. Online* **9**, 10 (2010).
19. Kos, B., Voigt, P., Miklavcic, D. & Moche, M. Careful treatment planning enables safe ablation of liver tumors adjacent to major blood vessels by percutaneous irreversible electroporation (IRE). *Radiol. Oncol.* **49**, 234–241 (2015).
20. Gowrishankar, T. R. & Weaver, J. C. Electrical behavior and pore accumulation in a multicellular model for conventional and supra-electroporation. *Biochem. Biophys. Res. Commun.* **349**, 643–653 (2006).
21. Murovec, T., Sweeney, D. C., Latouche, E., Davalos, R. V. & Brosseau, C. Modeling of transmembrane potential in realistic multicellular structures before electroporation. *Biophys. J.* **111**, 2286–2295 (2016).
22. Dermol-Černe, J. & Miklavčič, D. From cell to tissue properties—modeling skin electroporation with pore and local transport region formation. *IEEE Trans. Biomed. Eng.* **65**, 458–468 (2018).
23. Pavlin, M., Leben, V. & Miklavčič, D. Electroporation in dense cell suspension—Theoretical and experimental analysis of ion diffusion and cell permeabilization. *Biochimica et Biophys. Acta BBA Gen. Subj.* **1770**, 12–23 (2007).
24. Pucihar, G., Miklavcic, D. & Kotnik, T. A time-dependent numerical model of transmembrane voltage inducement and electroporation of irregularly shaped cells. *IEEE Trans. Biomed. Eng.* **56**, 1491–1501 (2009).
25. Kotnik, T., Rems, L., Tarek, M. & Miklavčič, D. Membrane electroporation and electropermeabilization: Mechanisms and models. *Ann. Rev. Biophys.* https://doi.org/10.1146/annurev-biophys-052118-115451 (2019).
26. Golberg, A., Bruinsma, B. G., Uygun, B. E. & Yarmush, M. L. Tissue heterogeneity in structure and conductivity contribute to cell survival during irreversible electroporation ablation by "electric field sinks". *Sci. Rep.* **5**, 8485 (2015).
27. Marčan, M., Kos, B. & Miklavčič, D. Effect of blood vessel segmentation on the outcome of electroporation-based treatments of liver tumors. *PLoS ONE* **10**, e0125591 (2015).
28. Qasrawi, R., Silve, L., Burdío, F., Abdeen, Z. & Ivorra, A. Anatomically realistic simulations of liver ablation by irreversible electroporation: Impact of blood vessels on ablation volumes and undertreatment. *Technol. Cancer Res. Treat.* **16**, 783–792 (2017).
29. Bonfiglio, A., Leungchavaphongse, K., Repetto, R. & Siggers, J. H. Mathematical modeling of the circulation in the liver lobule. *J. Biomech. Eng.* **132**, 111011 (2010).
30. Singh, J., Sharma, A., Sarma, K., Suri, S. & Malik, M. R. A quantitative histological study of the liver of pig (Sus scrofa). **94**, 14–16 (2017).
31. Campana, L. G. *et al.* Effect of tissue inhomogeneity in soft tissue sarcomas: From real cases to numerical and experimental models. *Technol. Cancer. Res. Treat.* **17**, 1533033818789693 (2018).
32. Denzi, A. *et al.* Modeling the positioning of single needle electrodes for the treatment of breast cancer in a clinical case. *Biomed. Eng. Online* **14**, S1 (2015).
33. Zmuc, J. *et al.* Large liver blood vessels and bile ducts are not damaged by electrochemotherapy with bleomycin in pigs. *Sci. Rep.* **9**, 3649 (2019).
34. Marčan, M., Pavliha, D., Kos, B., Forjanič, T. & Miklavčič, D. Web-based tool for visualization of electric field distribution in deep-seated body structures and planning of electroporation-based treatments. *Biomed. Eng. Online* **14 Suppl 3**, S4 (2015).
35. Kos, B. Treatment Planning for Electrochemotherapy and Irreversible Electroporation of Deep-Seated Tumors. In *Handbook of Electroporation* (ed. Miklavčič, D.) 1001–1017 (Springer International Publishing, 2017). doi:https://doi.org/10.1007/978-3-319-32886-7_2.
36. Cindric, H. *et al.* Retrospective study for validation and improvement of numerical treatment planning of irreversible electroporation ablation for treatment of liver tumors. *IEEE Trans. Biomed. Eng.* https://doi.org/10.1109/TBME.2021.3075772 (2021).
37. Sersa, G. *et al.* Vascular disrupting action of electroporation and electrochemotherapy with bleomycin in murine sarcoma. *Br. J. Cancer* **98**, 388–398 (2008).
38. Duck, F. A. *Physical properties of tissue: A comprehensive reference book*. (Institute of Physics and Engineering in Medicine, 2012).
39. Turjanski, P. *et al.* The role of pH fronts in reversible electroporation. *PLoS ONE* **6**, e17303 (2011).
40. Maglietti, F. *et al.* The role of Ph fronts in tissue electroporation based treatments. *PLoS One* **8**, (2013).
41. Olaiz, N. *et al.* Tissue damage modeling in gene electrotransfer: The role of pH. *Bioelectrochemistry* **100**, 105–111 (2014).
42. Rubinsky, L., Guenther, E., Mikus, P., Stehling, M. & Rubinsky, B. Electrolytic effects during tissue ablation by electroporation. *Technol. Cancer Res. Treat.* **15**, NP95–NP103 (2016).
43. Guenther, E. *et al.* Toward a clinical real time tissue ablation technology: Combining electroporation and electrolysis (E2). *Peer J.* **8**, e7985 (2020).
44. Mahnič-Kalamiza, S. & Miklavčič, D. Scratching the electrode surface: Insights into a high-voltage pulsed-field application from in vitro & in silico studies in indifferent fluid. *Electrochim. Acta* **363**, 137187 (2020).
45. Miklavčič, D., Šemrov, D., Mekid, H. & Mir, L. M. In vivo electroporation threshold determination. In *Proceedings of the 22nd Annual International Conference of the IEEE Engineering in Medicine and Biology Society (Cat. No.00CH37143)* vol. 4 2815–2818 vol.4 (2000).
46. Yao, C. *et al.* Bipolar microsecond pulses and insulated needle electrodes for reducing muscle contractions during irreversible electroporation. *IEEE Trans. Biomed. Eng.* **64**, 2924–2937 (2017).
47. Sano, M. B. *et al.* Towards the creation of decellularized organ constructs using irreversible electroporation and active mechanical perfusion. *Biomed. Eng. Online* **9**, 83 (2010).
48. Edd, J. F., Horowitz, L., Davalos, R. V., Mir, L. M. & Rubinsky, B. In vivo results of a new focal tissue ablation technique: Irreversible electroporation. *IEEE Trans. Biomed. Eng.* **53**, 1409–1415 (2006).
49. Agnass, P. *et al.* Mathematical modeling of the thermal effects of irreversible electroporation for in vitro, in vivo, and clinical use: A systematic review. *Int. J. Hyperthermia* **37**, 486–505 (2020).
50. Neal, R. E., Garcia, P. A., Robertson, J. L. & Davalos, R. V. Experimental characterization and numerical modeling of tissue electrical conductivity during pulsed electric fields for irreversible electroporation treatment planning. *IEEE Trans. Biomed. Eng.* **59**, 1076–1085 (2012).
51. Sørensen, T. J. *A method of establishing groups of equal amplitude in plant sociology based on similarity of species content and its application to analyses of the vegetation on Danish commons* (Munksgaard, 1948).

Acknowledgements

The Slovenian Research Agency (ARRS), grants P3-0003, P4-0053, P2-0249, and 17-MR.R910 supported this work. The funder had no role in the study design, data analysis, decision to publish or preparation of the manuscript. Research was performed in the infrastructure center 'Cellular Electrical Engineering' at the University of Ljubljana MRIC UL I0–0022.

Author contributions

H.C., B.K. and D.M. designed the study. H.C. performed the numerical reconstructions, computations and analysed the results. GG performed the histopathological analysis of the liver samples. I.E., E.B., J.Z., M.C. and A.S. performed the animal experiments. H.C. wrote the original manuscript draft with additional editing done by B.K., D.M., G.G. and M.C. All authors read and approved the final manuscript.

Competing interests

D.M. is the inventor of several patents pending and granted, is receiving royalties and is consulting for different companies and organizations, which are active in electroporation and electroporation-based technologies and therapies. The rest of authors report no conflict of interest.

Additional information

Supplementary Information The online version contains supplementary material available at https://doi.org/10.1038/s41598-022-10426-2.

Correspondence and requests for materials should be addressed to B.K.

Reprints and permissions information is available at www.nature.com/reprints.

Publisher's note Springer Nature remains neutral with regard to jurisdictional claims in published maps and institutional affiliations.

2.3 Paper 3

Title: **Peri-tumoral Metallic Implants Reduce the Efficacy of Irreversible Electroporation for the Ablation of Colorectal Liver Metastases**

Authors: Francois H. Cornelis, **Helena Cindrič**, Bor Kos, Masashi Fujimori, Elena N. Petre, Damijan Miklavčič, Stephen B. Solomon, Govindarajan Srimathveeravalli

Publication: *Cardiovascular Interventional Radiology*, vol. 43, no. 1, pp. 84-93, January 2020

Impact factor: 2.740 (2020)

Quartile: Q3

Rank: 71/134 (Radiology, Nuclear Medicine and Medical Imaging)

DOI: https://doi.org/10.1007/s00270-019-02300-y

Cardiovasc Intervent Radiol
https://doi.org/10.1007/s00270-019-02300-y

CLINICAL INVESTIGATION NON-VASCULAR INTERVENTIONS

Peri-tumoral Metallic Implants Reduce the Efficacy of Irreversible Electroporation for the Ablation of Colorectal Liver Metastases

Francois H. Cornelis[1,2] · Helena Cindrič[3] · Bor Kos[3] · Masashi Fujimori[1] · Elena N. Petre[1] · Damijan Miklavčič[3] · Stephen B. Solomon[1] · Govindarajan Srimathveeravalli[4,5]

Received: 2 April 2019 / Revised: 21 July 2019 / Accepted: 27 July 2019

Abstract
Purpose To evaluate the effect of peri-tumoral metallic implants (MI) on the safety and efficacy of percutaneous irreversible electroporation (IRE) of colorectal liver metastasis (CRLM).
Materials and Methods In this retrospective study, 25 patients (12 women, 13 men; MI: 13, no MI: 12) were treated for 29 CRLM. Patient characteristics, tumor location and size, treatment parameters and the presence of MI were evaluated as determinants of local tumor progression (LTP) with the competing risks model (univariate and multivariate analyses). Patient-specific computer models were created to examine the effect of the MI on the electric field used to induce IRE, probability of cell kill and potential thermal effects.
Results Patients had a median follow-up of 25 months, during which no IRE-related major complications were reported. Univariate analysis showed that tumor size (> 2 cm), probe spacing (> 20 mm) and the presence of MI ($p < 0.05$) were significant predictors of time to LTP, but only the latter was found to be an independent predictor on multivariate analysis (sub-hazard ratio = 6.5; [95% CI 1.99, 21.4]; $p = 0.002$). The absence of peri-tumoral MI was associated with higher progression-free survival at 12 months (92.3% [56.6, 98.9] vs 12.5% [2.1, 32.8]). Computer simulations indicated significant distortions and reduction in electric field strength near MI, which could have contributed to under-treatment of the tumor.
Conclusions Peri-tumoral MI increases the risk of treatment failure following IRE of CRLM.

Keywords Liver · Colorectal metastasis · Irreversible electroporation · Survival · Local tumor progression · computer simulations

Introduction

Irreversible electroporation (IRE) has been evaluated for the ablation of primary [1–3] and metastatic tumors [4, 5] in the liver that cannot be treated with thermal ablation because of safety or efficacy concerns. The largely non-thermal tumor killing effect of IRE has allowed its use for the treatment of tumors abutting the bile duct and large blood vessels in the liver [6, 7]. Early studies report efficacious local control of colorectal liver metastases (CRLM) using IRE [4, 5], and tumor diameter greater than 3 cm has been reported to be the only independent risk factor for local tumor progression following ablation [3]. Patients selected to undergo ablation of their CRLM may have undergone prior treatment such as surgical resection

✉ Govindarajan Srimathveeravalli
govind@umass.edu

1 Department of Radiology, Memorial Sloan-Kettering Cancer Center, 1275 York Avenue, New York, NY 10065, USA

2 Tenon Hospital, ISCD, Sorbonne Université, 4 Rue de la Chine, 75020 Paris, France

3 Faculty of Electrical Engineering, University of Ljubljana, Tržaška 25, 1000 Ljubljana, Slovenia

4 Department of Mechanical and Industrial Engineering, University of Massachusetts, Amherst, MA 01003, USA

5 Institute for Applied Life Sciences, University of Massachusetts, Amherst, MA 01003, USA

Published online: 05 August 2019

and can therefore have surgical clips, biliary stents or other metallic implants in the vicinity (< 1 cm) of the tumor to be treated. Metallic implants (MI) have substantially greater electrical conductivity than the tumor or healthy liver and may influence the distribution and strength of the electric field applied during IRE [8, 9]. The presence of MI can also create pockets of high current density, leading to undesirable effects such as electrical arcing and localized heating [8]. While the presence of large MI such as stents is a contraindication to the application of IRE as per manufacturer IFU, the presence of small MI such as surgical clips at the site of ablative treatment is a common clinical scenario in the management of unresectable liver malignancies. Therefore, the objective of this study was to understand the effect of metallic implants on the safety and efficacy of percutaneous IRE of CRLM. Our hypothesis was that MI will reduce the efficacy of CRLM ablation with IRE and that patient-specific computer models can be used as a novel tool to identify the mechanism by which MI affect IRE outcomes.

Material and Methods

Patient Selection and Eligibility Criteria

Retrospective review of all patients who underwent IRE of their CRLMs at our institution, a tertiary cancer center, between 2011 and 2015 was performed under a HIPAA-compliant, IRB-approved protocol.

Treatment

The decision to use IRE to treat patients' CRLMs was entirely at the IR physician's discretion and was driven by the tumor's proximity to large (> 3 mm) blood vessels or major bile ducts, where thermal ablation would increase the risk of complications or LTP. All procedures were performed while the patients were under general anesthesia and deep muscle relaxation, and electric pulse delivery was synchronized to the patient's electrocardiogram. All treatments were performed with the NanoKnife system (Angiodynamics, NY, USA), using CT guidance for electrode placement by two interventional radiologists with more than 15 years of experience performing percutaneous ablation and 7 years of experience performing IRE in patients. Electrode geometry and treatment parameters were selected with the intent to treat the tumor while achieving a minimum of 5-mm ablation margin. Triphasic CT was performed immediately after ablation to evaluate technical success of the ablation. Complete coverage of the tumor and a 5-mm ablation margin with a non-enhancing region on immediate post-treatment CT imaging was defined as the ablation endpoint. All patients included in this study received systemic chemotherapy as per standard of care for their disease status during the follow-up period.

Imaging Follow-up and Local Tumor Progression

Triphasic liver CT imaging was performed within 4–8 weeks after IRE ablation and every 2–4 months thereafter through the follow-up period. IRE success was defined as the absence of irregular peripheral or nodular enhancement within 1 cm of the ablated area at the first imaging follow-up. Imaging appearance indicating otherwise was considered treatment failure with residual tumor at the first imaging follow-up (4–8 weeks) [10]. Evidence of new abnormal tumor tissue (i.e., tumor recurrence) within 1 cm from the ablation zone observed on contrast-enhanced CT images obtained after the first imaging follow-up and confirmed by review was considered local tumor progression (LTP). This approach is consistent with the guidelines on reporting of tumor ablation [10, 11]. Positron emission tomography (PET) was performed at 6 and 12 months following ablation, and the presence of increased SUV uptake was considered positive evidence of local tumor progression. Procedure-related complications and side effects were noted and classified on the basis of criteria proposed by the Society of Interventional Radiology [12], CIRSE complication classifications [13] and the National Cancer Institute Common Terminology Criteria Adverse Events (CTCAE, version 4.0). The operating interventional radiology physicians retrospectively reviewed imaging assessments. Evidence of tumor recurrence up to 1 cm from the ablation zone seen on contrast-enhanced CT images and confirmed by the review was considered LTP.

Numerical calculations

A subset of all patients included in the study, four with MI in the vicinity of ablation zone (up to 1 cm from the tumor and or the electrodes) and four without, were selected for evaluation of treatment delivery with computer simulations. The number of ablation probes used for the treatment (≤ 4) and the availability of complete intra-procedural treatment parameters data were used to select the subset of patients for evaluation with computer simulations. The selected datasets and corresponding treatment parameters (voltage, electrode spacing and exposure, and the number of pulses) were exported to Visifield [14]. Visifield is a web-based tool for visualizing in vivo distribution of electric fields during electroporation-based treatments. Patients' pre-procedural CT images were manually segmented by an experienced radiologist (M.F.) to demarcate the tumor, liver parenchyma, major anatomic landmarks

such as blood vessels and to define positions and orientations of any metallic surgical clips in the treatment vicinity (Fig. 1A). Intra-procedural CT images were registered to pre-procedural images and used to determine the positions of IRE electrodes during treatment (Fig. 1B). A 3D numerical model was built for each patient and tumor (Fig. 1C). Electric field distribution was computed using a nonlinear model of electric field dependent tissue conductivity. Tissue heating was taken into account by solving the Pennes' bioheat equation. Electrical and thermal properties of the modeled tissues (e.g., liver, blood and tumor density, thermal capacity and conductivity, etc.) were compiled from the literature in the previous work [15]. The electric field was computed for each electrode pair present in the treatments. The total extent of the ablation zone was evaluated by combining the maximal computed electric field in situ from all electrode pairs [16], and regions that may have experienced insufficient field strength for complete ablation were identified. Probability of cell death due to irreversible electroporation was calculated using a statistical Peleg–Fermi model, which also takes into account the number of applied electrical pulses [17]. Model parameters were adjusted to best describe the properties of liver tissue during IRE treatment. The probability of cell death due to thermal damage was calculated using the Arrhenius equation [18]. The volume of the tumor experiencing electric field greater than the critical threshold, where the probability of cell death due to IRE or thermal damage was > 0.9, were calculated as the percentage of the pre-treatment tumor volume.

Statistical Analysis

Median follow-up time was determined based on patients who were alive at the end of the review period. Survival rates were calculated by using the Kaplan–Meier method and were stratified for gender, tumor location, tumor size (> 2 cm), the number of ablation probes (> 3), treatment parameters (probe spacing > 2 cm, treatment voltage < 2500 V, pulse length < 100 microseconds, the number of pulses applied < 90) and the presence of metallic surgical clips within 1 cm from the tumor margin. Variables that showed statistical significance at univariate analysis were subsequently analyzed with a multivariate model. As patient death may occur prior to evidence of LTP on imaging, LTP predictors were adjusted for competing factors for death using the Fine–Gray competing risks regression model [19]. This analysis enabled us to identify specific factors contributing to the risk of LTP by modeling sub-distribution functions of LTP, death without LTP, along with the associated hazard rates (HR) and the sub-hazard ratio (sHR). Results of this analysis is shown along with the Kaplan–Meyer technique for comparison. Differences in electric field coverage, cell death probability and thermal damage in simulation models within (clips vs. no clips) and between patients were assessed with a Mann–

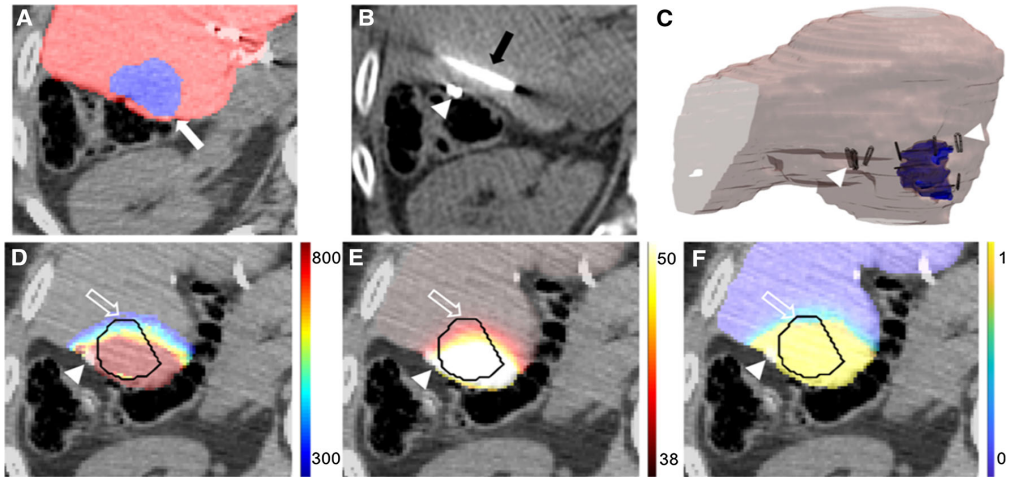

Fig. 1 Workflow of patient-specific simulation models. **A** Pre-treatment CT images were segmented to extract the tumor (white arrow) and surrounding parenchyma. **B** Intra-treatment CT imaging is used to identify the location of clips (arrowhead) and ablation probes (black arrow). **C** The segmented images are converted to 3D models, and arrowheads indicate location of surgical clips relative to the tumor (outlined in blue). Calculation of **D** electric field distribution (units in V/cm), **E** thermal damage (units degree centigrade) and **F** cell kill probability (fraction 0–1) in the tumor and margin (outline arrow). The tumor is outlined in black, axial cross sections selected to show the tumor at the largest cross section and the relative location of the surgical clips (arrowhead)

Whitney *U* test. Data were analyzed with a commercially available statistical software (Stata, version 12.0; Stata, College Station, Texas).

Results

The study enrolled 25 consecutive patients who underwent IRE of 29 CRLMs. Among these patients, 13 had MI in the peri-tumoral region and 12 did not have MI. All patients completed follow-up and were included in the analysis. Patient and tumor characteristics and treatment parameters used to perform IRE are given in Tables 1 and 2, respectively.

Clinical Outcomes

IRE treatment failure was observed in 13.8% of tumors (4/29) at the first post-ablation CECT scan (Fig. 2A–F) performed 4–8 weeks following treatment, and all cases with residual tumor were patients with MI (Fig. 2D–E). Subsequent tumor progression was observed in 58.6% of tumors (17/29) during the median follow-up period of 25 months (Fig. 3A–C) wherein all patients had MI. The cumulative survival without LTP was 48.3% [95% confidence interval (CI) 29.5, 64.8] and 40.5% [22.6, 57.7] at the 12- and 24-month follow-ups, respectively. Univariate analysis suggested tumor size > 2 cm ($p = 0.003$), probe spacing > 2 cm ($p = 0.018$) and the presence of metallic clips within 1 cm of ablation probes ($p = 0.001$) to be significant predictors of time to LTP. Gender of the patient ($p = 0.997$), the tumor location ($p = 0.445$), the number of probes used for the treatment ($p = 0.252$), treatment voltage < 2500 V ($p = 0.582$), pulse length < 100 microseconds ($p = 0.830$) or the number of pulses applied < 90 pulses ($p = 0.830$) was not found to be determinant of LTP. On subsequent multivariate analysis, only the presence of metallic clips (HR 29.5; $p = 0.002$) was found to be an independent predictor of shorter time to LTP (Table 3). As patient death may have occurred before imaging evidence of LTP could be gathered, a competing analysis was performed. The resulting sHR of the presence of metallic clips as predictor of LTP was still significant (sHR 6.5, 95% CI 1.99, 21.4, $p = 0.002$). Kaplan–Meier survival curve of LTP is displayed in Fig. 4 A. In the absence of metallic clips in the vicinity of ablation, the progression-free survival rate was 92.3% (56.6, 98.9) at 6–36 months. In the presence of metallic clips, the progression-free survival rate was 18.8% (4.6, 40.3) at 6 months, 12.5% (2.1, 32.8) at 12 months, and 0% after. Overall survival rate was 82.8% [63.4, 92.4] at 12 months, 61.3% [40.1, 76.5] at 24 months, and 26.8% [12, 44.2] at 36 months (Fig. 4B). Progression of disease was the cause of death in all patients, and assessed variables were not found to be predictors of overall survival, including tumor size of greater than 2 cm (HR 1.92; [0.78–4,7]; $p = 0.154$) and the presence of metallic clips (HR 2; [0.81–4,92]; $p = 0.132$).

Treatment-related complications of grade > 3 were not observed. Six complications with grade < 3 occurred following the procedures. This included pneumothoraxes ($n = 5$, 4 requiring drainage), and 1 case of urinary retention. Complication related to injury of the liver, blood vessels of the liver, bile ducts, small bowel or duodenum was not observed.

Table 1 Patient and tumor characteristics

Characteristics	MI	No MI
No. of patients	13	12
No. of lesions	17	12
Age (years)	51.7 ± 10.7	61 ± 12.7
Sex	7 males/6 females	6 males/6 females
Tumor size (cm)	2.80 ± 0.76	1.45 ± 0.78

Data are expressed as mean values ± standard deviation

Table 2 Treatment characteristics, recorded from the IRE generator

No. of probes	3 (2–6)
Probe spacing (mm)	15 (10–25)
Treatment voltage (V)	1890 (1050–3000)
Num. pulses per probe	90 (70–90)
Pulse width (μS)	90 (90–100)
Impedance change (ohms)	− 13.5 (− 3.7 to − 38.5)
Peak current (A)	27.5 (8.9–50)
Cumulative energy delivered (J)	406.8 (74.5–938.2)

Data are expressed as median values ± standard deviation, and range is given in parenthesis

Simulation Outcomes

Ablation was considered technically successful if the electric field strength exceeded the threshold for IRE in the liver (500 V/cm) [20] and the probability of cell death was > 0.9 in the tumor and the margin (Fig. 1D–F). In patients with MI, the electric field was computed with and without the clips to isolate the specific impact of these clips on ablation outcomes (Fig. 5A–C). The presence of metallic clips resulted in a reduction in electric field strength in their immediate surrounding microscopic volume, with maximum distortion at the middle of the clip, along the longitudinal axis. The reduction in electric field strength at the site of such distortions was sufficient to

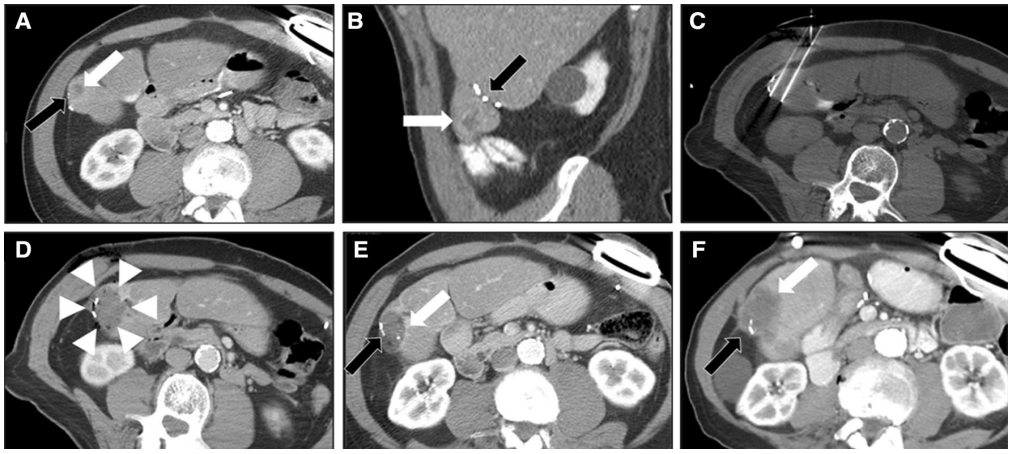

Fig. 2 Example of CRLM treated with IRE in patient number two who had surgical clips in the treatment region. **A**, **B** Pre-treatment CT image showing tumor location (white arrow) and relative location of the surgical clips (black arrow). **C** Intra-treatment CT image showing ablation probe placement. **D** Immediate post-IRE image showing technical treatment success (arrowheads). Tumor recurrence (white arrow) on CECT at **E** 8 and **F** 24 months following IRE, abutting the metallic implant (black arrow)

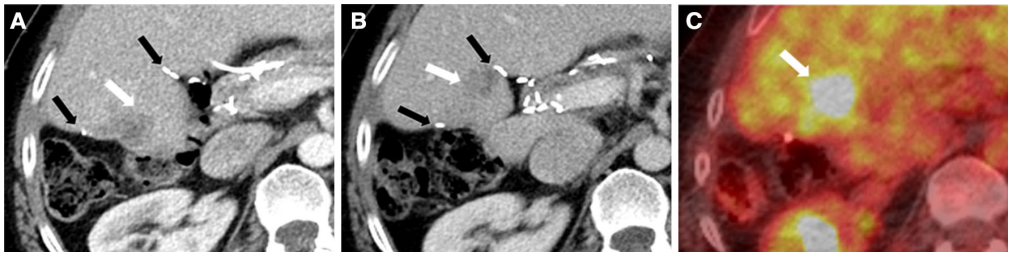

Fig. 3 Example of CRLM treated with IRE in patient number one who had surgical clips in the treatment region. **A** Pre-treatment CT image showing tumor location (white arrow) and the relative location of the surgical clips (black arrow). Local tumor progression (white arrow) assessed with **B** CT imaging and **C**. PET imaging at 12 months post-IRE

Table 3 Univariate and multivariate analyses of factors associated with local tumor progression by using regression models

	Univariate analysis *p* value	Multivariate analysis		
		HR	95% CI	*p* value
Size (> 2 cm)	0.003	1.65	0.6–4.9	0.364
Distance of probes (> 20 mm)	0.018	0.99	0.3–3.5	0.996
Metallic implants	0.001	29.5	3.5–247.2	0.002

All examined variables displayed significance at univariate analysis and multivariate analysis. Multivariate analysis data were calculated with the regression model

reduce the efficacy of cell death (Fig. 5D). Such distortions in the electric field strength were restricted to < 1 mm away from the clip (Fig. 5E, F), and no difference was found in gross volume of tumor experiencing electric field at the critical threshold when comparing simulations performed with, and without the clips ($p = 0.8852$, Table 4).

Correlation of Simulation: Clinical Outcomes

Based on computed electric field coverage and cell death probability, simulation results from patient-specific models correlated with clinical outcomes, predicting LTP in all patients with metallic surgical clips (Figs. 2E, 3D, 5D). Two patients without clips and all four patients having clips were seen to have inadequate electric field coverage

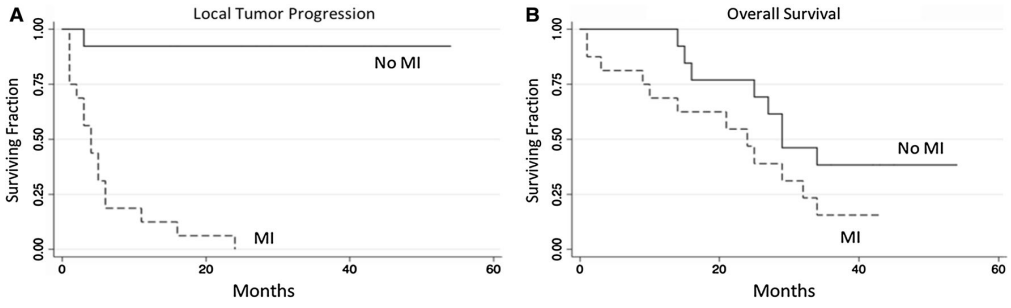

Fig. 4 Kaplan–Meier estimate of (**A**). local tumor progression-free survival (HR 29.5; [3.5–47.2]; $p = 0.002$) and (**B**). overall survival (HR 2; [0.81–4.92]; $p = 0.132$). after IRE with or without presence of metallic implants within 1 cm from the tumor margin

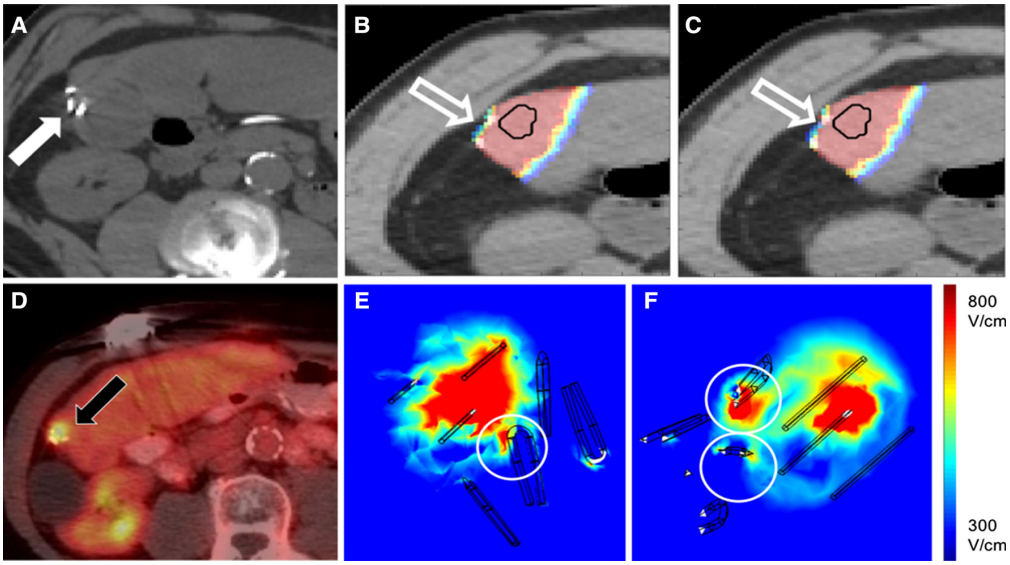

Fig. 5 Simulation model constructed for patient number two. **A** Pre-IRE image showing the location of surgical clips within the treatment region (white arrow). Estimate of electric field coverage when simulations were performed **B** without or **C** with the surgical clips (outline arrows). **D** Local tumor progression observed on PET imaging at 24 months post-IRE (black arrow). **E**, **F** Computed electric field distribution in target tissue, distortions are visible in the vicinity of the clips (circles)

in the tumor, and the margin, however, having cell death in $> 95\%$ of tumor volume seemed to improve local tumor control in patients without clips. Overall, there was no statistically significant difference in the percentage volume of the tumor experiencing electric field coverage greater than the critical threshold (MI: $78.2 \pm 16\%$ vs no MI: $91.6 \pm 8.8\%$, $p = 0.3123$) or the estimated probability of cell death within the ablation (MI: $81.4 \pm 18.7\%$ vs no MI: $96.5 \pm 1.9\%$, $p = 0.1939$) between the two patient groups, with the presence of clips being the only differentiating factor.

Risk of Thermal Damage from MI

Due to the large number of pulses delivered during IRE treatment, thermal damage could be observed in a significant volume of target tissue. However, the percentage volume of the tumor where cell kill was expected due to thermal damage was completely enclosed within the volume of cell death from IRE (Fig. 6A–D). In patients having clips, simulations performed with ($60.9 \pm 18.1\%$) and without the clips ($60.8 \pm 18.2\%$, $p = 0.8852$) did not reveal a difference in the degree of thermal damage, stemming from the presence of metal in the treatment region. Likewise, there was no difference in the volume of

Table 4 Electric field coverage and cell kill probability in tumor volume

Patient #	Electric field coverage* (%)		IRE cell kill** (%)		Thermal cell kill*** (%)	
	No clips	Clips	No clips	Clips	No clips	Clips
1	94.57	94.63	93.61	93.87	86.74	86.68
2	59.32	58.94	55.70	55.51	51.90	52.09
3	71.26	71.18	79.53	81.03	59.34	59.84
4	87.98	87.35	96.89	96.53	45.66	44.75
5	98.71	–	95.76	–	68.63	–
6	87.04	–	95.37	–	35.19	–
7	81.44	–	95.62	–	29.90	–
8	99.48	–	99.48	–	90.63	–

*Percentage of tumor volume covered with electric field of at least 500 V/cm

**Percentage of tumor volume with cell death probability above 0.9 due to irreversible electroporation alone (Peleg–Fermi model adapted from [17])

***Percentage of tumor volume with cell death probability above 0.9 due to thermal damage alone

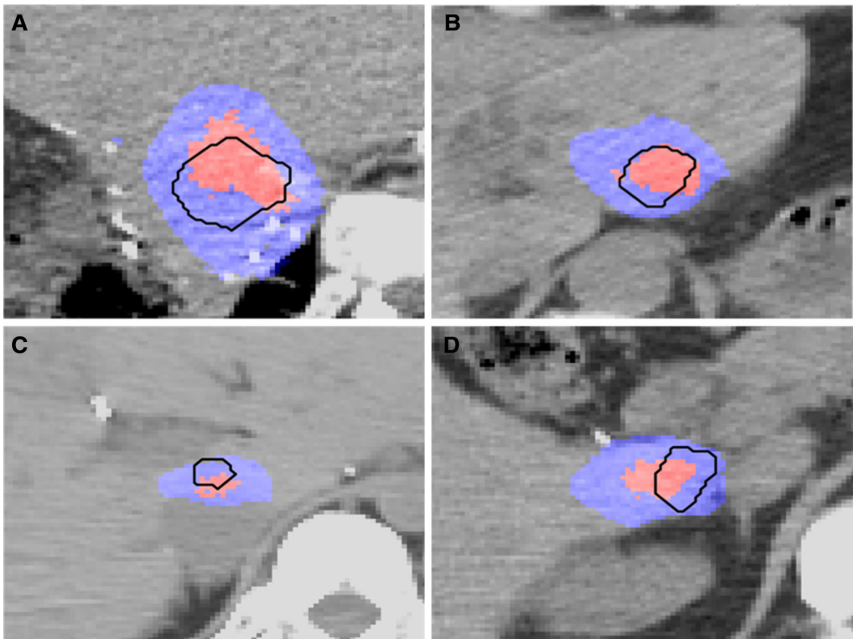

Fig. 6 Volume of thermal damage during IRE in **A** patient number four, **B** patient number five, **C** patient number six and **D** patient number seven. The tumor is outlined in black, the region of thermal damage is depicted in red, and the total region of IRE is shown in blue. Tissue was considered ablated (thermally or by IRE) if cell kill probability was above 0.9

thermal damage within the ablation between the two patient cohorts ($p = 0.8852$).

Discussion

CRLM often presents as infiltrative disease, with high risk of recurrence at the surgical margin in patients having unfavorable mutational status [21, 22]. Anatomic location of the surgical margin can influence choice of loco-regional treatment to manage recurrent disease. IRE has emerged as potential choice for the management of these patients as the technique can be safely applied in delicate anatomic locations even if the tumor involves critical structures [2, 6, 7, 23]. Tumor size has been previously identified as a predictor of LTP in IRE [3], which was confirmed in our analysis as well. Our results suggest that IRE requires further optimization and refinement when treating CRLM, especially when the treatment site has MI such as surgical clips. As evidenced by our experience, application of IRE without adjusting treatment parameters to account for the

presence of metallic surgical clips reduces treatment efficacy.

IRE in patients using the NanoKnife system is contraindicated in the presence of large MI such as stents as per the manufacturer's instruction for use. However, the impact of smaller MI such as surgical clips was largely considered negligible. Our simulation results suggest that the presence of MI in tissue being treated with IRE can distort both the electrical and thermal field distributions, resulting in an unpredictable ablation zone. This consideration has resulted in multiple preclinical studies evaluating the safety and impact of the presence of metallic implants on IRE treatment. Using a tuber model, Neal et al. [24] evaluated the impact of metallic seeds on electric field distribution and the ablation volume, reporting no deleterious effects. However, in vivo preclinical evaluation by Ben-David et al. [9] has shown the presence of metal in the IRE treatment zone can distort the size and shape of the ablation. Scheffer et al. [8] and Dunki-Jacobs et al. [25] have then shown that IRE can cause localized heating, with the presence of metal increasing thermal damage at the treatment site. In a case report, Månsson et al. [26] present contraindication to the use of IRE in patients who have bare metal stents from the elevated risk of severe adverse events. We add to these prior results by reporting that the presence of metallic surgical clips can impact the efficacy of IRE when treating CRLM in a clinical setting but does not seem to impact ablation safety.

Ablation with IRE is amenable to numerical modeling, which has been validated in multiple preclinical and clinical studies as a tool for predicting the safety and efficacy of this technique [14–16, 27–29]. However, the use of simulation tools for treatment planning for IRE is not standard of care and is not performed in current clinical practice. In this study, we employ patient-specific numerical models as a tool to understand the etiology and factors underlying IRE failure when used to treat CRLM patients having metallic surgical clips at the site of ablation. We observed that metallic clips induce microscopic distortions in the electric field used to perform IRE while having negligible effect on the overall volume of tissue experiencing electric field strength above the critical threshold. We also found that the electric field coverage was often inadequate for the tumor and its margin irrespective of the metallic clip's presence, which may explain tumor recurrence away from the location of MI in some patients. Despite inadequate coverage, LTP was not observed in patients without clips possibly because of higher estimated cell kill probability. The cell death probability calculations takes into account the number of pulses delivered into a tissue and increased pulse numbers seems to improve tumor control even in regions of reduced electric field strength which is consistent with theory [10, 30]. Ablation with IRE involves interplay between different treatment parameters (voltage, pulse duration and the number of pulses applied) and IRE planning based only on electric field coverage may therefore be inadequate to ensure successful treatment. Our experimental findings suggest incorporation of simulation for planning can assist in appropriate probe placement and optimization of electrode geometry prior to pulse delivery. Appropriate electrode orientation with respect to the metallic implant may reduce distortions in the electric field, thereby minimizing the impact of MI on ablation outcomes.

While increasing pulse application has been seen as a way to increase the efficacy of IRE, any benefit from increased pulse application has to be carefully considered in light of associated thermal damage during IRE consistent with previous calculations and recent ex vivo experiments [18, 31]. While IRE has a predominantly non-thermal cell kill mechanism [32], all our simulations suggested the existence of thermal damage in a considerable volume of the treated tissue. Since metal is a good thermal and electrical conductor, the presence of metallic implants at the treatment site does not result in their direct heating but increases the thermal energy deposited into the tissue surrounding the implant. Such localized heating can reduce the safety associated with IRE [8, 25], which often is the motivating rationale when selecting this treatment technique for use in specific clinical conditions. Precise treatment planning, with use of patient-specific simulation models prior to treatment delivery, can improve electrode positioning and treatment parameter selection to improve treatment outcomes even in patients having metallic implants at the treatment site.

Our study is limited by its retrospective nature and the small number of patients included. Likewise, the patient-specific simulation models were performed only in a subset of all patients that were treated at our center, potentially limiting the generalizability of our findings. Expanding the data with additional patients and simulation models can increase our knowledge of IRE for the treatment of CRLM, which will be the focus of future studies. As a retrospective study, with an inherent patient selection bias, we are unable to control for the volume or number of metallic implants in the ablation or evaluate the effect in different types of clips based on material (stainless steel vs. titanium).

In conclusion, the presence of metallic surgical clips within 1 cm from the tumor margin is associated with increased risk of treatment failure after IRE of CRLM, but safety is not affected. Potentially, increasing pulse application can offset electric field distortion in the presence of metallic implants, but this may reduce the non-thermal benefits of IRE. The results of this study emphasize the importance of an adequate patients' selection and a detailed treatment planning process, which could help to reduce the

tumor recurrences while avoiding complications after percutaneous IRE of CRLM.

Acknowledgements The authors acknowledge the support of NIH Cancer Center Support Grant (P30 CA008748) for core laboratory services that were used for the presented work. The authors acknowledge the support of the National Cancer Institute of the National Institutes of Health under Award Numbers U54CA137788/U54CA132378, and the Slovenian Research Agency (ARRS), Slovenia Program P2-0249, Grant Z3-7126 and Bilateral Slovenian-USA project BI-US/18-19-002. SBS is a consultant to BTG, Johnson & Johnson, XACT, Adegro and Medtronic. SBS is a consultant to BTG, Johnson & Johnson, XACT, Adgero, Innobaltive, and Medtronic. SBS has funding support from GE Healthcare, Ethicon, Elesta and Angiodynamics, and holds stock in Aperture Medical.

Compliance with Ethical Standards

Conflict of interest The authors declare that they have no conflict of interests.

Ethical Approval All procedures were performed in accordance with the ethical standards of the institutional or national research committee, and with the Helsinki declaration and its later amendments or comparable ethical standards.

Informed Consent For this type of study, informed consent is not required.

Consent for Publication For this type of study, consent for publication is not required.

References

1. Kingham TP, Karkar AM, D'Angelica MI, et al. Ablation of perivascular hepatic malignant tumors with irreversible electroporation. J Am Coll Surg. 2012;215(3):379–87.
2. Cannon R, Ellis S, Hayes D, Narayanan G, Martin RCG. Safety and early efficacy of irreversible electroporation for hepatic tumors in proximity to vital structures. J Surg Oncol. 2013;107(5):544–9.
3. Niessen C, Igl J, Pregler B, et al. Factors associated with short-term local recurrence of liver cancer after percutaneous ablation using irreversible electroporation: a prospective single-center study. J Vasc Interv Radiol. 2015;26(5):694–702.
4. Scheffer HJ, Nielsen K, van Tilborg AAJM, et al. Ablation of colorectal liver metastases by irreversible electroporation: results of the COLDFIRE-I ablate-and-resect study. Eur Radiol. 2014;24(10):2467–75.
5. Schoellhammer HF, Goldner B, Merchant SJ, Kessler J, Fong Y, Gagandeep S. Colorectal liver metastases: making the unresectable resectable using irreversible electroporation for microscopic positive margins—a case report. BMC Cancer. 2015;15(1):271.
6. Dollinger M, Zeman F, Niessen C, et al. Bile duct injury after irreversible electroporation of hepatic malignancies: evaluation of MR imaging findings and laboratory values. J Vasc Interv Radiol. 2016;27(1):96–103.
7. Silk MT, Wimmer T, Lee KS, et al. Percutaneous ablation of peribiliary tumors with irreversible electroporation. J Vasc Interv Radiol. 2014;25(1):112–8.
8. Scheffer HJ, Vogel JA, van den Bos W, et al. The influence of a metal stent on the distribution of thermal energy during irreversible electroporation. PLoS ONE. 2016;11(2):e0148457.
9. Ben-David E, Ahmed M, Faroja M, et al. Irreversible electroporation: treatment effect is susceptible to local environment and tissue properties. Radiology. 2013;269(3):738–47.
10. Rems L, Miklavčič D. Tutorial: Electroporation of cells in complex materials and tissue. J Appl Phys. 2016;119(20):201101.
11. Goldberg SN, Grassi CJ, Cardella JF, et al. Image-guided tumor ablation: standardization of terminology and reporting criteria. Radiology. 2005;235(3):728–39.
12. Ahmed M, Solbiati L, Brace CL, et al. Image-guided tumor ablation: standardization of terminology and reporting criteria—a 10-year update. Radiology. 2014;273(1):241–60.
13. Filippiadis DK, Binkert C, Pellerin O, Hoffmann RT, Krajina A, Pereira PL. CIRSE quality assurance document and standards for classification of complications: the CIRSE classfication system. Cardiovasc Intervent Radiol. 2017;40(8):1141–6.
14. Marčan M, Pavliha D, Kos B, Forjanič T, Miklavčič D. Web-based tool for visualization of electric field distribution in deep-seated body structures and planning of electroporation-based treatments. Biomed Eng Online. 2015;14(Suppl 3):S4.
15. Kos B, Voigt P, Miklavcic D, Moche M. Careful treatment planning enables safe ablation of liver tumors adjacent to major blood vessels by percutaneous irreversible electroporation (IRE). Radiol Oncol. 2015;49(3):234–41.
16. Garcia PA, Kos B, Rossmeisl JH, Pavliha D, Miklavčič D, Davalos RV. Predictive therapeutic planning for irreversible electroporation treatment of spontaneous malignant glioma. Med Phys. 2017;44(9):4968–80.
17. Dermol J, Miklavčič D. Mathematical models describing chinese hamster ovary cell death due to electroporation in vitro. J Membr Biol. 2015;248(5):865–81.
18. Garcia PA, Davalos RV, Miklavcic D. A numerical investigation of the electric and thermal cell kill distributions in electroporation-based therapies in tissue. PLoS ONE. 2014;9(8):e103083.
19. Donoghoe MW, Gebski V. The importance of censoring in competing risks analysis of the subdistribution hazard. BMC Med Res Methodol. 2017;17(1):52.
20. Gallinato O, de Senneville BD, Seror O, Poignard C. Numerical workflow of irreversible electroporation for deep-seated tumor. Phys. Med. Biol. 2019;64(5):055016.
21. Margonis GA, Sasaki K, Andreatos N, et al. KRAS mutation status dictates optimal surgical margin width in patients undergoing resection of colorectal liver metastases. Ann Surg Oncol. 2017;24(1):264–71.
22. Akyuz M, Aucejo F, Quintini C, Miller C, Fung J, Berber E. Factors affecting surgical margin recurrence after hepatectomy for colorectal liver metastases. Gland Surg. 2016;5(3):263–9.
23. Vroomen LGPH, Petre EN, Cornelis FH, Solomon SB, Srimathveeravalli G. Irreversible electroporation and thermal ablation of tumors in the liver, lung, kidney and bone: What are the differences? Diagn Interv Imaging. 2017;98(9):609–17.
24. Neal RE, Smith RL, Kavnoudias H, et al. The effects of metallic implants on electroporation therapies: feasibility of irreversible electroporation for brachytherapy salvage. Cardiovasc Intervent Radiol. 2013;36(6):1638–45.
25. Dunki-Jacobs EM, Philips P, Martin RCG. Evaluation of thermal injury to liver, pancreas and kidney during irreversible electroporation in an in vivo experimental model. Br J Surg. 2014;101(9):1113–21.
26. Månsson C, Nilsson A, Karlson B-M. Severe complications with irreversible electroporation of the pancreas in the presence of a metallic stent: a warning of a procedure that never should be performed. Acta Radiol Short Rep. 2014. https://doi.org/10.1177/2047981614556409.

27. Yarmush ML, Golberg A, Serša G, Kotnik T, Miklavčič D. Electroporation-based technologies for medicine: principles, applications, and challenges. Annu Rev Biomed Eng. 2014;16:295–32020.
28. O'Brien TJ, Bonakdar M, Bhonsle S, et al. Effects of internal electrode cooling on irreversible electroporation using a perfused organ model. Int J Hyperthermia. 2018;35:44–55.
29. Faroja M, Ahmed M, Appelbaum L, et al. Irreversible electroporation ablation: is all the damage nonthermal? Radiology. 2013;266(2):462–70.
30. Edhemović I, Brecelj E, Gasljevic G, et al. Intraoperative electrochemotherapy of colorectal liver metastases. J Surg Oncol. 2014;110(3):320–7.
31. Edhemovic I, Gadzijev EM, Brecelj E, et al. Electrochemotherapy: a new technological approach in treatment of metastases in the liver. Technol Cancer Res Treat. 2011;10(5):475–85.
32. Djokic M, Cemazar M, Popovic P, et al. Electrochemotherapy as treatment option for hepatocellular carcinoma, a prospective pilot study. Eur J Surg Oncol. 2018;44(5):651–7.

2.4 Paper 4

Title: **Investigation of safety for electrochemotherapy and irreversible electroporation ablation therapies in patients with cardiac pacemakers**

Authors: Tomaž Jarm , Tadej Krmac, Ratko Magjarević, Bor Kos, **Helena Cindrič** and Damijan Miklavčič

Publication: *BioMedical Engineering OnLine*, vol. 19, no. 85, pp. 1-18, November 2020

Impact factor: 2.819 (2021)

Quartile: Q3

Rank: 55/90 (Biomedical Engineering)

DOI: https://doi.org/10.1186/s12938-020-00827-7

Jarm et al. BioMed Eng OnLine (2020) 19:85
https://doi.org/10.1186/s12938-020-00827-7

BioMedical Engineering OnLine

RESEARCH Open Access

Investigation of safety for electrochemotherapy and irreversible electroporation ablation therapies in patients with cardiac pacemakers

Tomaz Jarm[1*], Tadej Krmac[1], Ratko Magjarevic[2], Bor Kos[1], Helena Cindric[1] and Damijan Miklavcic[1]

*Correspondence: tomaz.jarm@fe.uni-lj.si
[1] University of Ljubljana, Faculty of Electrical Engineering, Trzaska 25, 1000 Ljubljana, Slovenia
Full list of author information is available at the end of the article

Abstract

Background: The effectiveness of electrochemotherapy of tumors (ECT) and of irreversible electroporation ablation (IRE) depends on different mechanisms and delivery protocols. Both therapies exploit the phenomenon of electroporation of the cell membrane achieved by the exposure of the cells to a series of high-voltage electric pulses. Electroporation can be fine-tuned to be either reversible or irreversible, causing the cells to either survive the exposure (in ECT) or not (in IRE), respectively. For treatment of tissues located close to the heart (e.g., in the liver), the safety of electroporation-based therapies is ensured by synchronizing the electric pulses with the electrocardiogram. However, the use of ECT and IRE remains contraindicated for patients with implanted cardiac pacemakers if the treated tissues are located close to the heart or the pacemaker. In this study, two questions are addressed: can the electroporation pulses interfere with the pacemaker; and, can the metallic housing of the pacemaker modify the distribution of electric field in the tissue sufficiently to affect the effectiveness and safety of the therapy?

Results: The electroporation pulses induced significant changes in the pacemaker ventricular pacing pulse only for the electroporation pulses delivered during the pacing pulse itself. No residual effects were observed on the pacing pulses following the electroporation pulses for all tested experimental conditions. The results of numerical modeling indicate that the presence of metal-encased pacemaker in immediate vicinity of the treatment zone should not impair the intended effectiveness of ECT or IRE even when the casing is in direct contact with one of the active electrodes. Nevertheless, the contact between the casing and the active electrode should be avoided due to significant tissue heating at the site of the other active electrode for the IRE protocol and may cause the pulse generator to fail to deliver the pulses due to excessive current draw.

Conclusions: The observed effects of electroporation pulses delivered in close vicinity of the pacemaker or its electrodes do not indicate adverse consequences for either the function of the pacemaker or the treatment outcome. These findings should

contribute to making electroporation-based treatments accessible also to patients with implanted cardiac pacemakers.

Keywords: Electrochemotherapy of tumors, Irreversible electroporation, Non-thermal ablation therapy, Cardiac pacemaker, Implantable devices, Safety, Numerical modeling, Experimental work

Background

Electroporation

When biological cells are exposed to electric pulses with intensity above certain threshold, the induced transmembrane voltage leads to electroporation—a physical phenomenon of increased cell membrane permeability for otherwise poorly permeant molecules [1, 2]. If the intensity of the external electric field is below another threshold this effect is transient, the membrane reseals and the cell survives (the reversible electroporation), otherwise the electroporation leads to the cell death (the irreversible electroporation—IRE). Both types of electroporation are exploited in different areas as diverse as biomedicine and food processing technologies [1, 3]. Two clinical applications are considered in this paper—electrochemotherapy (ECT) and IRE ablation of tumors. In both, the effects of the therapy are localized to the area of electroporation with minimal side effects to the surrounding tissue.

Electrochemotherapy of tumors

In electrochemotherapy (ECT) of tumors reversible electroporation is combined with chemotherapy. A single dose of the chemotherapeutic drug (bleomycin or cisplatin) is injected intravenously or intratumorally before the application of electroporation pulses [4]. Transient increase of membrane permeability of tumor cells facilitates an increased cellular uptake of the hydrophilic drug molecules from the extracellular space [1, 5]. This leads to significantly potentiated cytotoxic effects due to entrapment of the drug after resealing of the membrane [6]. This is the main mechanism of antitumor effectiveness of ECT. However, two additional contributing mechanisms were identified—the vascular effects and the involvement of the immune response [6, 7]. Routine use of ECT and the number of clinical trials for new indications is constantly growing. ECT is an efficient and safe therapy for treatment of different types of solid malignancies in various superficial and internal tissues, including tumors in skin, head and neck, brain, bone and internal organs (visceral and deep-seated tumors) in human and veterinary medicine [8]. In a recent randomized Phase 3 study of electrochemotherapy on basal cell carcinoma, it was shown that ECT is equally efficient as surgery [9]. A typical protocol for ECT involves the application of a sequence of pulses for each active pair of electrodes (8 pulses per pair). Pulses of short duration (100 μs) and high voltage (e.g., at 1000 V/cm voltage-to-distance ratio) are used and delivered either individually at 1 Hz or in sequences of 4 pulses with a 5-kHz repetition rate within a sequence [10]. Pulse delivery is synchronized with the ECG when necessary. In clinical settings and for the largest inter-electrode distances (2–3 cm), the maximum voltages and currents can be as high as 3000 V and 50 A, respectively [8], and there can be as many as 12 electrode pairs that the electroporation pulses

are delivered to. Various types of needle-type electrodes were developed for different applications [6, 8, 11].

IRE ablation therapy

If the intensity, number and/or duration of applied pulses exceed irreversible threshold values, the affected cells die due to electroporation (IRE), largely due to irrecoverable loss of homeostasis [2]. IRE is thus used as a non-thermal ablation therapy with important advantages over the well-established conventional ablation methods [12, 13]. In IRE ablation, the cell death is predominantly a result of electroporation and not the temperature increase. However, local heating of tissue does occur, especially in the immediate vicinity of the electrodes and when large numbers of pulses are used [12, 14, 15]. IRE ablation has been used in clinical trials for treatment of tumors in internal organs such as liver, pancreas, kidneys and prostate [11, 16–19]. Compared to ECT, the number of pulses and voltages in IRE ablation of tumors are significantly larger. Typically, at least 70–90 pulses of 70–100 μs duration are used at the voltage-to-distance ratio of 1500 V/cm. The spacing between needle electrodes is 1.5–2 cm and their active length is 1–1.5 cm [12].

ECT and IRE ablation of tumors can benefit from the individualized treatment planning based on mathematical modeling and from coupling the treatment plan with a navigational system to provide more accurate positioning of the electrodes and optimized electrical parameters for the treatment [20, 21]. In this way, optimal coverage of the target tissue with sufficiently high electric field strength for the desired effect and minimal damage in the normal tissue can be achieved. Treatment planning also helps to avoid excessive heating and thermal damage of critical structures/tissues and to keep the current below the maximum output level of the device.

Cardiac and other safety considerations for electroporation-based therapies

When treating deep-seated internal tumors in vicinity of the heart (e.g., in the liver), there is an increased possibility for interactions of electroporation pulses with the cardiac activity. The risk of harmful interferences is minimized by synchronization of the delivery of electroporation pulses with the electrocardiogram (ECG). Synchronization is recommended for all electroporation-based therapies in thoracic cavity or close to the heart [12, 22]. However, as a safety precaution, the use of electroporation-based therapies remains contraindicated for patients with implanted cardiac pacemakers if the treatment zone is close to the implanted device [23]. Both manufacturers of clinically approved devices for generation of electroporation pulses, namely IGEA (Carpi, MO, Italy) for the Cliniporator system (for ECT) and Angiodynamics (Latham, NY, USA) for the NanoKnife system (for IRE ablation) consider cardiac pacemakers as contraindication for treatment [24, 25]. Angiodynamics further expands this to any implanted devices with metallic parts.

The presence of metallic implants within or in vicinity of the treatment zone may indeed negatively affect the outcome of electroporation-based treatments [26–28]. Metallic casing of the pacemaker has higher electrical conductivity than surrounding tissue and may therefore change the electric field distribution, which could potentially lead to undertreatment of the target tissue. It may also present an increased risk for thermal

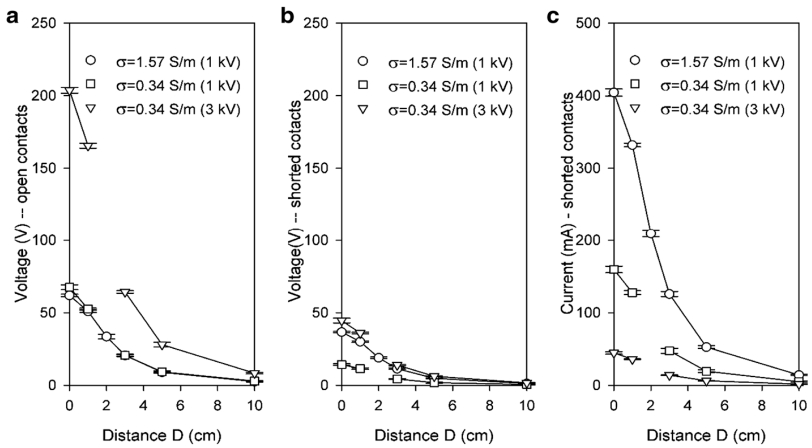

Fig. 1 Voltages and currents induced by electroporation pulses on the disconnected ventricular lead for open contacts (**a**—voltage only) and shorted contacts (**b**, **c**) as a function of the distance between the electroporation and the pacemaker electrodes. For the amplitudes of electroporation pulses 1000 V (both conductivities) and 3000 V (lower conductivity only). Mean average values and ± SD bars are shown ($N = 6–8$). See Fig. 5 for the definition of distance *D*

damage in the surrounding tissue, especially for IRE ablation. IRE ablation is usually considered a non-thermal method. However, several experimental in vivo and in silico studies have shown a significant increase in temperature during treatment [14, 15, 20, 29, 30]. Thermal coagulation has been observed a few millimeters from the electrodes in animal experimental studies [29–31]. The extent of thermal damage depends on tissue type, pulse parameters, electrode exposure length and inter-electrode distance. Furthermore, the presence of metal has been found to increase generation of heat [29].

Aims of the study

In this preliminary study two questions related to the contraindication of electroporation-based therapies for patients with pacemakers were addressed:

- Do the electroporation pulses electrically interfere with the function of the pacemaker in a way that could lead to its malfunction or even damage?
- Is the distribution of electric field in the tissue modified by the metal housing of the pacemaker to the extent that either the effective treatment zone is modified and/or that the tissue may be exposed to excessive heating?

The first question was addressed empirically by exposing a functioning pacemaker with its ventricular lead to electroporation pulses under various conditions and observing the effects, and the second question by numerical modeling of physical conditions encountered during application of electroporation pulses near the implanted pacemaker and pacemaker leads.

Results

Experimental evaluation of the effect of electroporation pulses on the pacemaker

Figure 1 presents steady-state voltages and currents (the interference) measured at the pacemaker ventricular electrodes without the pacemaker during application of a single 100-µs-long electroporation pulse. Two extremes are presented: with open ventricular lead contacts (the maximum voltage and zero current) and with shorted contacts (the maximum current at reduced voltage that represents the voltage drop on combined resistances of the anodic and cathodic leads). With the pacemaker connected, the combined resistance includes the internal resistance of the device, therefore voltages between those in Fig. 1a, b and currents lower than those in Fig. 1c are anticipated. As expected, the amplitude of the interference decreased rapidly with the distance of the electroporation electrodes from the pacemaker's ventricular lead.

Figure 2 presents a typical example of the effect of electroporation pulses on ventricular pacing pulse for one or four electroporation pulses at 1000 V amplitude delivered in the medium of the higher conductivity (physiological saline with the conductivity of 1.57 S/m).

Figure 3 shows unperturbed ventricular pacing pulses measured in both conductive media used in the study (panel a), a zoomed-out version of Fig. 2b for comparison of relative amplitudes of the ventricular pacing pulse and the artifacts caused by electroporation pulses (panel b), and a more detailed view of only the said artifacts (panel c). Note the declining amplitude of the artifacts caused by the technical limitation of the Cliniporator pulse generator, which does not recharge its output capacitors during delivery of pulses in high-frequency sequences.

Electroporation pulses resulted in distance-dependent voltage artifacts of expected polarities, duration and reproducible amplitudes (similar to those reported in Fig. 1b). No drastic changes in the characteristics of the pacing pulses were induced by the electroporation pulses delivered before or after the stimulating phase of the pacing pulse (Fig. 2 panels a, b, e, f).

Additional file 1: Figures S1 and S2 present the same kind of information as Fig. 2 for electroporation pulses delivered in the medium with decreased conductivity of 0.34 S/m, which is comparable to conductivities encountered in clinical practice in tissues such as human liver. This reduced conductivity also enabled the use of the highest available voltage for electroporation pulses, which is 3000 V (again comparable to clinical situation). It can be seen that the same kind of effects as described in Fig. 2 were also present in the medium of lower conductivity, but the effects were more pronounced here and the higher voltage resulted in considerably larger artifacts. In general, all observed effects were distance-dependent (decreasing the distance D between the electroporation and the pacemaker electrodes resulted in progressively larger interferences).

The shape of the pacing pulse was significantly perturbed and its amplitude reduced only for electroporation pulses delivered during the stimulating phase of the pacing pulse (panels c and d in Fig. 2, Additional file 1: Figures S1, S2). The effects were similar for all investigated conditions except that they were less or more pronounced, depending on the number of pulses or the amplitude of electroporation pulses. However, the most relevant observation was that all the described effects appeared only for pacing pulses coinciding with the electroporation pulse(s). There was no residual

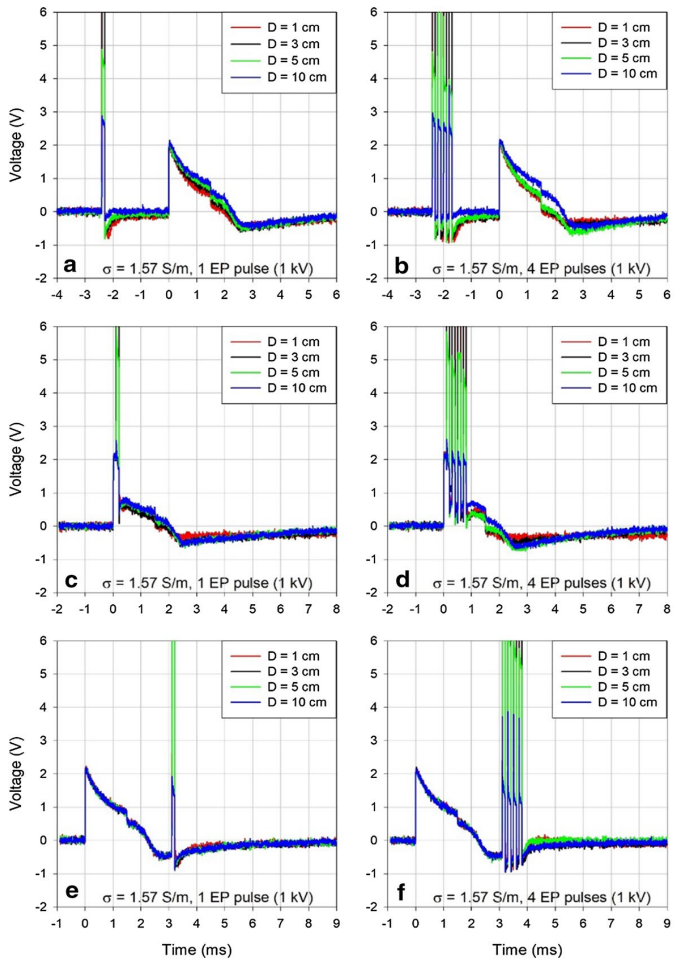

Fig. 2 The interference of a single electroporation pulse (**a**, **c**, **e**) and a sequence of four electroporation pulses (**b**, **d**, **f**) with 1000 V amplitude, 100 µs duration, and 5 kHz repetition rate. Electroporation pulses were delivered before (**a**, **b**), during (**c**, **d**) or after (**e**, **f**) the ventricular pacing pulse in the medium with conductivity of 1.57 S/m. For comparison with the effects observed in the media of lower conductivity at 1000 V and 3000 V amplitudes see Additional file 1: Figures S1 and S2

effect on the following pacing pulses. The pacemaker appeared completely immune to electroporation pulses.

Numerical modeling

The influence of the presence of pacemaker is similar for both treatments (ECT and IRE). In Fig. 4 only the results for IRE are shown because the impact of the pacemaker is more noticeable in IRE protocols due to higher number of pulses used.

In both treatments, the presence of the pacemaker without contact with the electrodes does not significantly affect the delivered electric currents when compared to control

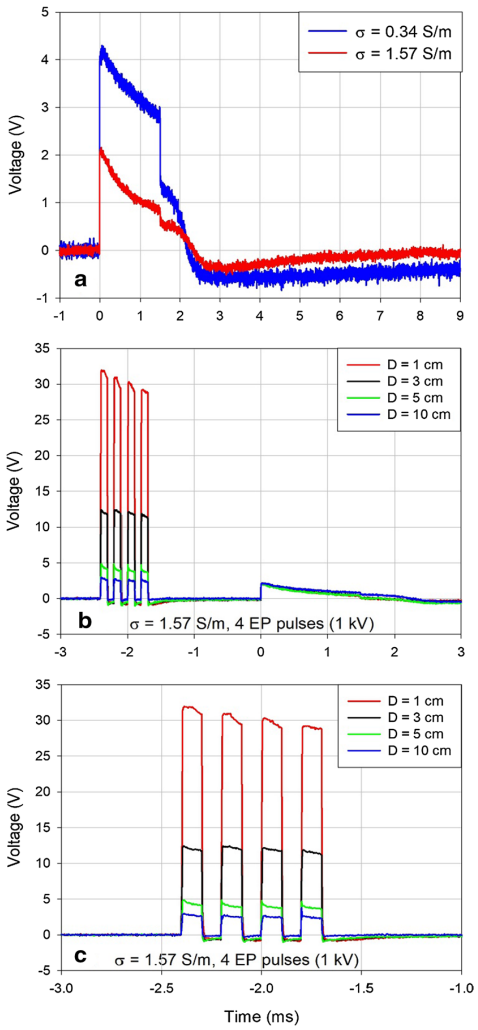

Fig. 3 **a** Unperturbed ventricular pacing pulse in two media of different conductivities. **b** Comparison of relative amplitudes of the electroporation pulse artifacts and the ventricular pacing pulse (same data as shown in Fig. 2b). **c** Electroporation pulse artifacts from panel **b** shown in more detail

values (0–2% change). Changes in electric field distribution are mainly observed in the healthy tissue, while electric field in the tumor remains mostly unaffected (Fig. 4b). Complete coverage of the tumor with sufficiently high electric field is achieved for both treatments. When compared to the control model (without pacemaker), the presence of the pacemaker does not cause any additional heating of tissue (Fig. 4e). Although both treatments are considered non-thermal, non-negligible tissue heating is observed at the electrodes, especially in IRE. The maximum calculated increase from base tissue

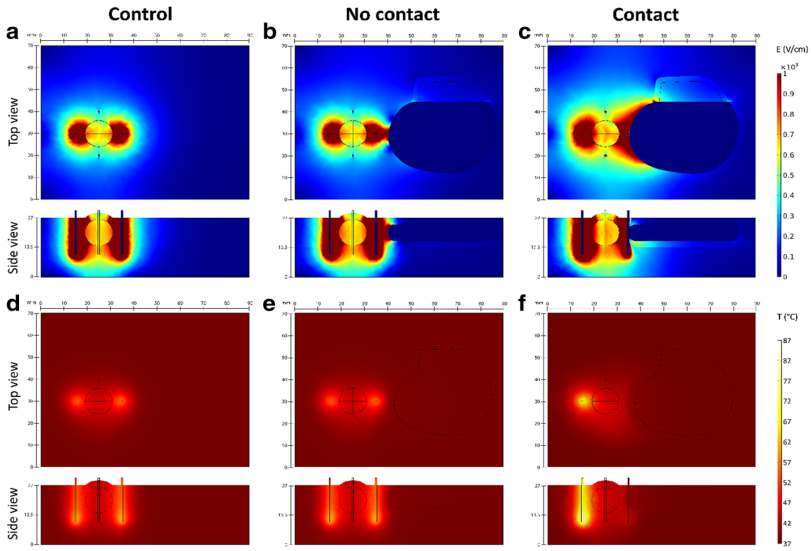

Fig. 4 The impact of the presence of metallic-encased pacemaker during IRE ablation of tumor. Images show computed results at the end of pulse delivery for one of six active electrode pairs in the simulated procedure. The simulated pulse protocol was 90 × 90 µs pulses delivered at 1 Hz with a pause of 3 s after each set of 10 pulses. Applied voltage to distance ratio was 1500 V/cm. **a**–**c** Electric field distribution in target tissue; **d**–**f** Temperature in the target tissue. In the control model, the pacemaker is not present in the simulation. In the no-contact model pacemaker is positioned 5 mm from the rightmost electrode. In the contact model, the pacemaker is in conductive contact with the rightmost electrode. The top and side views correspond with the model geometry shown in Fig. 6b

temperature (37 °C) is 9.6 °C and 40 °C for ECT and IRE ablation, respectively; the temperature rise is limited to immediate vicinity of the electrode tips.

When the pacemaker is in direct contact with one of the electrodes, its influence is more prominent. A significantly increased current draw is observed in the electrode pairs containing the contact electrode—the calculated electric current is approximately 50% higher when compared to control values. Electric field distribution changes drastically in electrode pairs containing the contact electrode as well. Since the pacemaker itself acts like an electrode, higher electric field is produced in the tumor and healthy tissue (Fig. 4c). A large volume of tissue surrounding the contact point is subject to IRE. Electric field in the tumor in this specific case is not impacted negatively: due to overall higher electric field, complete coverage of the tumor is achieved with fewer electrode pairs compared to the control and the no-contact models. Higher temperatures are observed in tissue for both treatments when compared to the control models. In the ECT model, up to 5.2 °C higher temperatures are observed in a pair-to-pair comparison; the temperature rise is most significant in the pairs containing the contact electrode (average 3.2 °C increase). However, this rise in temperature is limited to the immediate vicinity of the electrodes. The overall maximum calculated temperature is the same as in the control model without pacemaker. In the IRE model, contact with one of the electrodes results in significant heating

around the opposite electrode of the pair, however no significant heating is observed at the contact point (Fig. 4f). Up to 31.4 °C higher temperatures are observed in a pair-to-pair comparison to the control model. The temperature rise is most significant in pairs containing the contact electrode (average 24.1 °C increase). The overall maximum calculated increase from base tissue temperature is 70.4 °C (compared to 40 °C in the control model).

In the model some areas in immediate vicinity of the electrodes are heated to temperatures of more than 100 °C, because there is no term for boiling included in the numerical model. In reality, vaporization would occur at these high temperatures, which would drastically decrease bulk conductivity and further current increase.

The numerical results are shown in more detail in the tables in Additional file 2.

Discussion

Experimental evaluation of the effect of electroporation pulses on the pacemaker

The application of electroporation pulses induces significant changes in the shape of the pacemaker ventricular pacing pulse in experimental conditions only when the electroporation pulses coincides with the stimulating phase of the pacing pulse with no residual effects in the following pacing pulses for all tested conditions.

A decaying baseline voltage shift of the opposite polarity was observed when the pulses were delivered before the pacemaker pulse. Since the shift did not dissipate before the ventricular pacing pulse was delivered by the pacemaker, it visibly affected the absolute amplitude of the following pacing pulse (Fig. 2a, b). As all other effects, the magnitude of this shift decreased with the decreasing distance D (the horizontal distance between the electroporation electrodes and the pacemaker ventricular lead electrodes, see Fig. 5). We cannot fully explain this shift, but it was probably partially due to the combined resistive and inductive properties of the anodic and the cathodic parts of the ventricular lead. A similar effect of a decaying negative voltage shift that

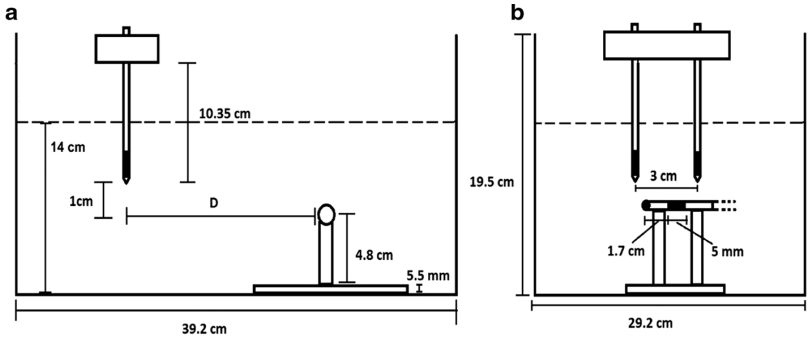

Fig. 5 Relative positions of the electroporation electrodes (suspended vertically from above) and the stimulating distal end of the pacemaker bipolar ventricular lead (fixed horizontally) in a container filled with conductive solution to the height of 14 cm [38]. Side view (**a**) and frontal view (**b**) of the container is shown. The active parts of the electrodes are shaded black. The distance D was adjusted between 0 and 10 cm as shown in Figs. 1 and 2

lasted more than 2 ms following the electroporation pulse was observed in the artifact induced by the electroporation pulse when the pacemaker was disconnected. In that case the ventricular lead was shorted at the other end thus permitting the maximum current to flow through serially connected anodic and cathodic leads during the delivery of the electroporation pulse. This effect was much less pronounced when the current was not flowing in the ventricular lead (the contacts of the ventricular lead left open). See also Additional file 1: Figure S3.

In general, all observed effects were distance-dependent (decreasing the distance D between the electroporation and the pacemaker electrodes resulted in progressively larger interferences). However, it needs to be pointed out that sometimes we observed some deviation to this rule. Most notably this can be seen in Additional file 1: Figure S1A, B (1000 V pulses) where the effects observed for the inter-electrode distance $D = 3$ cm did not fit with the distance-dependency rule and we do not have an explanation for this.

After testing in harsh conditions with $D = 1$ cm at the maximum available electroporation voltage of 3000 V and in a medium with conductivity comparable to tissue conductivity in ECT/IRE of deep-seated tumors we found no evidence of any malfunction of the pacemaker. However, without the proprietary data about the electrical protection of the Adapta pacemaker we cannot claim that the maximum voltages observed on the ventricular lead represent absolutely no risk for the pacemaker. Nevertheless, further mitigating circumstances should be considered for realistic applications. In clinical situations, the electrodes for delivery of electroporation pulses would never be placed as close to the pacemaker electrodes as in our study. Distances of at least about 3 cm or more between the two sets of electrodes can be expected unless the treatment zone was in the heart itself. At $D = 3$ cm the amplitude of the observed interference was less than 30 V. Furthermore, in clinical ECT (and also for IRE) of deep-seated tumors in thoracic cavity the delivery of electroporation pulses must always be synchronized with the absolute refractory period of the ventricles, which follows the depolarization of the atria and the ventricles. Therefore, for correct synchronization the electroporation pulses would be delivered after the unperturbed ventricular pacing pulse (or normal ventricular R wave) and therefore could not affect the shape of pacing pulses, atrial or ventricular. Furthermore, the moment of correctly delivered electroporation pulses immediately after depolarization of the ventricles would coincide with the blanking periods for both the atrial and ventricular channel (e.g., in case of the DDD pacing mode) and should therefore not interfere with the programmed function of the pacemaker [32]. Finally, pacemakers must be able to withstand the external defibrillation treatment. Even though not directly comparable, the total energy delivered to a pair of electroporation electrodes in ECT is typically only a fraction of the energy of a single defibrillation pulse. All this suggests that the application of ECT for deep-seated tumors in close vicinity of the heart should probably not be contraindicated, as also stated in the updated standard operating procedures for ECT of cutaneous tumors [10]. This conclusion could be extended to the IRE ablation therapy. Namely, even though the total number of delivered electroporation pulses (and consequently the total energy) is significantly larger than in ECT (typically 90 vs 8 pulses per each electrode pair for IRE vs ECT,

respectively), the pulses are delivered one at a time for IRE ablation and they are individually synchronized with the ECG [10, 12]. Therefore, the delivered energy in case of IRE is spread over a much longer period (more than an order of magnitude) than in case of ECT and therefore represents a less intensive instantaneous stress for the pacemaker.

Numerical modeling

Numerical results suggest for both therapies (ECT and IRE) that the presence of metal-encased pacemaker does not affect the coverage of the tumor tissue regardless of contact with the electrode and should thus not impair the effectiveness of the electroporation-based treatment. However, if the pacemaker is in contact with one of the electrodes, the entire housing acts as a large electrode resulting in an increased current draw from the electroporator. Consequently, overall higher electric fields are produced in target tissue, potentially achieving better coverage than without the pacemaker. However, this increased current draw also increases the probability of interruption of pulse delivery due to exceeded hardware-limited maximum values [33].

In both treatments, tissue heating is not increased in the presence of the pacemaker without contact with one of the electrodes. If contact with one of the electrodes is established, however, higher temperatures are observed in tissue. In ECT the rise in temperature is not as pronounced, which indicates that treatment safety should not be affected. In IRE a significant rise in temperature is observed at the site of the second active electrode in the pair. This observation agrees with the observation of heating around the electrodes when a metal stent was present within the treatment zone [26]. The metallic casing itself does not heat up during treatment, but rather acts like a heat sink, therefore thermal damage due to heating of metallic casing is unlikely.

Due to its limitations, our study should be considered preliminary and thus conclusions need further confirmation. One of the limitations of the numerical part of the study is the lack of validation of the model. Although the same model has been used in previous studies, and has also been validated for various tissues, such as liver, muscle and kidney [20, 34–37], it has not yet been validated for this specific tissue setting. Moreover, the potential negative impact of the presence of a metal-encased pacemaker on the efficacy of electroporation-based treatment has only been investigated in one simplified geometry. A patient-specific treatment plan is in any case advised.

The situation with the pacemaker in contact with more than one electrode has not been evaluated in this study. However, it is worth noting that such a condition would result in short circuit conditions. Pulse delivery would be terminated for all shorted electrode pairs due to excessive current, which would result in undertreatment of the target tissue.

Conclusions

In our study we found no evidence of harmful effects of electroporation pulses, such as those used in ECT or IRE of tumors, on functioning of a pacemaker even for pulses applied in immediate vicinity of the pacemaker electrodes. Transient voltage artifacts of up to almost 200 V were observed on the pacemaker electrodes during delivery of electroporation pulses in the most extreme situation (the maximum pulse voltage of 3000 V

and the unrealistically small distance between the electroporation and the pacemaker electrodes of 1 cm). In conditions resembling those encountered in clinical practice for the smallest realistic distance between the treatment and the pacemaker electrodes (i.e., 3 cm) the amplitude of voltage artifacts did not exceed 30 V. Due to similarity of electroporation pulses used for ECT and IRE treatments this observation is equally relevant for use of IRE ablation in patients with pacemakers. Numerical computation showed elevated temperatures in immediate vicinity of the electrode tips also without the presence of the pacemaker—up to 9.6 °C and 40 °C increase from base tissue temperature for ECT and IRE, respectively. The presence of the pacemaker without contact with the electrodes did not further contribute to tissue heating. When the pacemaker was in direct contact with one of the electrodes up to 9.6 °C and 70.4 °C increase from base tissue temperature was observed in ECT and IRE, respectively. In the modeled geometries, the presence of a metal-encased pacemaker did not negatively affect tumor coverage regardless of contact of one electrode with the pacemaker housing.

Our study should be considered preliminary and thus conclusions need further confirmation, however, the effectiveness of ECT or IRE, seem not to be impaired by the presence of a pacemaker or its leads in the vicinity of the treatment zone. Numerical modeling suggests that thermal damage due to heating of metallic casing of the pacemaker is unlikely.

Methods

Experimental evaluation of the effect of electroporation pulses on the pacemaker

The measurements were performed at room temperature (21 °C) in a glass container filled with either physiological saline (0.9% NaCl solution) or the saline diluted with distilled water at 1:4 ratio, thus resulting in two media with conductivities 1.57 and 0.34 S/m, respectively (the lower value mimicked the conductivities encountered in tissue during ECT of liver metastases). The conductivity was measured at 21 °C with SevenCompact S230 conductometer (Mettler Toledo, Columbus OH, USA). The experimental setup is presented in Fig. 4 [38].

In the first stage of the study, the bipolar ventricular lead (type CapSure Z Novus 5054) was not connected to the pacemaker; the connector (not submerged) allowed us to measure the maximum possible voltage or current (with the contacts open or shorted, respectively) between the pacemaker electrodes due to application of electroporation pulses. In the second stage, the ventricular lead was connected to an Adapta pacemaker (ADDR01 model, Medtronic, Minneapolis, USA) which was programmed into asynchronous D00 pacing mode and submerged. The atrial bipolar lead was also connected. Atrial pacing pulses were converted into adjustably delayed TTL pulses (0 V and 5 V output values) to trigger the generation of electroporation pulses. Thus, we were able to observe the effects on the pacemaker function for electroporation pulses delivered at different times with respect to the charge-balanced ventricular pacing pulse. The pacemaker is assumed to be in its most vulnerable state during generation of the pacing pulse due to relatively low internal impedance that could allow harmful currents flowing into the device due to electroporation interference.

Electroporation pulses were generated by Cliniporator Vitae device (IGEA, Carpi, MO, Italy) and delivered via two needle electrodes for clinical ECT (type VG-1230M20;

conductive length 3 cm, diameter 1.2 mm) submerged in parallel into the medium (Fig. 4). The inter-electrode distance was fixed at 3 cm, the maximum distance limited by the hardware capacity and also recommended in the standard operating procedures for ECT [10]. Standard rectangular pulses (1000 and 3000 V amplitude, 100 µs duration) were generated individually or in sequences of four pulses (repetition rate 5 kHz, i.e., 100 µs on, 100 µs off). The voltages appearing between the electrodes of the ventricular lead were sensed at the ventricular electrodes in the medium. The measurement instrumentation included HDO6104A oscilloscope, two HVD3605 differential high-voltage and two CP031A high-current probes (Teledyne LeCroy, Chestnut Ridge, NY, USA) for monitoring of generated electroporation pulses and interferences on the ventricular lead.

Numerical modeling

The impact of the presence of a metal-encased pacemaker on effectiveness and safety of electroporation-based therapies was further investigated by means of numerical computation. Two scenarios for treatment of a subcutaneous tumor were investigated: ECT and IRE. In both scenarios the influence of a metal-encased pacemaker was evaluated with the pacemaker in contact and without contact with one of the electrodes. A control scenario without the pacemaker was also evaluated. A previously designed numerical framework for planning of electroporation-based treatments was adapted for all computations [20, 28, 39].

All numerical computations were performed in COMSOL Multiphysics software (Comsol AB, Stockholm, Sweden), however the computations were set up and controlled in MATLAB (MathWorks, Natick, MA, USA) scripting environment through LiveLink. A simplified geometry including both the tumor and the pacemaker was used in this study. Placement of the pacemaker mimicked its position on the fascia of the pectoralis major muscle (Fig. 5). The tissue model consisted of three isotropic and homogeneous components: the spherical tumor (12 mm diameter), the fat tissue, and the underlying muscle tissue. The skin was not included in the model due to subcutaneous location of both the tumor and the pacemaker. The electrical and thermal properties of tissues and electrodes were taken from literature and databases and are listed in Table 1 along with the relevant references. The pacemaker model consisted of the titanium housing and the

Table 1 Electrical and thermal properties of modeled tissues taken from relevant literature (given in brackets)

	Fat	Tumor	Muscle
Initial electrical conductivity σ_0 (S/m)	0.080 [40, 41]	0.200 [39, 42]	0.135 [35, 39]
Final electrical conductivity σ_{end} (S/m)	0.240 [35, 39]	0.600 [35, 39]	0.405 [35, 39]
Threshold for reversible EP (V/cm)	100 [35, 39]	400 [35, 39]	200 [35, 39]
Threshold for irreversible EP (V/cm)	900 [35, 39]	900 [35, 39]	900 [35, 39]
Thermal conductivity k (W/m K)	0.21 [41]	0.52 [20, 40]	0.49 [41]
Specific heat capacity C_p (J/ kg K)	2348 [41]	3540 [20]	3421 [41]
Density ρ (kg/m^3)	911 [41]	1079 [41]	1090 [41]
Perfusion rate ω (1/s)	0.00043 [40]	0.01798 [40]	0.00069 [40]
Thermal coefficient of conductivity α_T (%/°C)	1.5 [20]	1.5 [20]	1.5 [20]

silicone-covered lead connectors. The built-in material properties from COMSOL were used (Titanium beta-21S and Silicon). An unstructured tetrahedral mesh was built in COMSOL and consisted of 27,643 elements for the ECT model and 21,623 elements for the IRE model. When compared to the finest possible mesh that was still manageable in the transient computation (197,119 elements for the ECT model and 138,480 elements for the IRE model), the use of a coarser mesh produced a < 1% error in calculated electric current and maximum temperature while greatly reducing the computation time.

For the ECT model (Fig. 5a) a hexagonal-electrode configuration of seven electrodes was used with a standard ECT protocol: eight 100 µs pulses per each of 12 active electrode pairs delivered in two sequences of four pulses with reversed pulse polarities. The sequences were delivered at 1 Hz and the pulses within each sequence at 5 kHz repetition rate. The applied voltage was 730 V [6, 10].

For the IRE model (Fig. 5b) four needle electrodes were modeled, surrounding the tumor in a rectangular configuration. IRE delivery protocol from [20] was used in the simulation: 90 pulses of 90 µs duration per electrode pair with a 1500 V/cm voltage-to-distance ratio delivered at 1 Hz with a pause of 3 s after each set of 10 pulses. The pacemaker was positioned either 5 mm from the nearest electrode (Fig. 5a) or in direct contact with the nearest electrode (Fig. 5b).

Electric field distribution in tissue is determined through solving the stationary Laplace partial differential equation for electric potential. The outer boundaries of model domain are considered electrically insulated while the continuity equation is applied to the inner domain boundaries. Electroporation is implemented as a non-linear electric field dependent increase in tissue electrical conductivity [20]. Electric field distribution is calculated separately for each active electrode pair in the treatment. The computed electric field for the n-th electrode pair is compared to computed field from all previous pairs (1 to $n-1$) and the maximum contributions from all pairs are combined into treatment equivalent field $E_{\mathrm{eq},n}$ of n-th electrode pair as follows:

$$E_{\mathrm{eq,n}} = \begin{cases} \max\left(\mathrm{E_{eq,n-1}}, \mathrm{E_n}\right); \mathrm{n} > 1 \\ E_n; n = 1 \end{cases}; \quad 1 \le n \le N,$$

where N is the total number of electrode pairs, $E_{\mathrm{eq},n}$ is the treatment equivalent field after application of pulses to the n-th electrode pair, $E_{\mathrm{eq},n-1}$ is the treatment equivalent field from electrode pairs 1 to $n-1$ and E_n is the actual computed electric field produced by the n-th electrode pair. The final electric field distribution in tissue is represented by the equivalent electric field after application of pulses to all N electrode pairs ($E_{\mathrm{eq},N}$). The percentage of tumor volume covered in target electric field strength, 400 V/cm for ECT and 650 V/cm for IRE ablation [39], was extracted from the final field distribution.

Computations of heat dissipation are performed separately with a transient model through solving the bioheat transfer equation [14, 28, 43]:

$$\rho C_p \frac{\partial T}{\partial t} + \nabla \bullet (-k\nabla T) = Q + \rho C_p \omega (T_{\mathrm{blood}} - T) + Q_{\mathrm{met}},$$

$$Q = \sigma \bullet E^2.$$

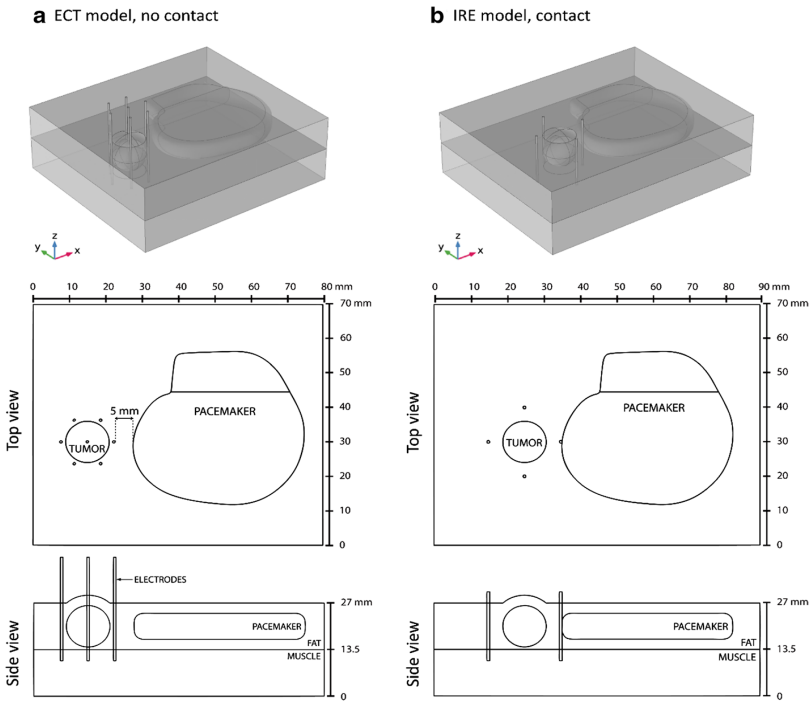

Fig. 6 **a** 3D model for the simulation of ECT treatment of a spherical subcutaneous tumor. The distance from the pacemaker casing to the nearest electrode is 5 mm. **b** 3D model for the simulation of IRE ablation of a spherical subcutaneous tumor. Pacemaker is in direct contact with rightmost electrode. Only one scenario (contact or no contact) is shown for each treatment

Right side of the equation represents the heat sources in the model—the heat source Q approximated by a Joule heating term and source terms representing tissue perfusion and metabolism. Similarly to the computation of electric field distribution, the outer boundaries of the model domain are thermally insulated, in order to create the "worst case" conditions, while continuity condition is applied to the inner boundaries. All parameters descriptions and values are provided in Table 1. Maximum tissue temperature is calculated at the end of pulse delivery for each electrode pair (Fig. 6).

Supplementary information

Supplementary information accompanies this paper at https://doi.org/10.1186/s12938-020-00827-7.

Additional file 1. Additional figures showing the interference of electroporation pulses delivered before, during and after the ventricular pacing pulse in the medium with a lower conductivity of 0.34 S/m. The figures show the effect of one pulse and a sequence of four pulses for pulse amplitude of 1000 V (**Figure S1**) and pulse amplitude 3000 V (**Figure S2**).

Additional file 2. Results of numerical computations. Additional tables containing results of numerical simulations for all six modeled treatment scenarios: delivered electric currents, maximum tissue temperatures, percentage of tumor volume covered in sufficiently high electric field (400 V/cm for ECT and 650 V/cm for IRE ablation) after delivery of pulses to each active electrode pair.

Abbreviations
ECT: Electrochemotherapy; IRE: Irreversible electroporation; ECG: Electrocardiogram.

Acknowledgements
Not applicable.

Authors' contributions
All authors contributed to drafting and revising of the manuscript. TJ co-designed, supervised and performed the experimental part of the study, analyzed the data, and drafted the manuscript. TK performed the experimental part of the study and analyzed the data. RM co-designed the experimental part of the study and provided the pacemaker hardware and expertise. BK and HC developed the numerical models of ECT and IRE treatments in the presence of the cardiac pacemaker, analyzed the computational results and drafted the numerical modeling part of the manuscript. DM generated the original idea for the study and supervised its execution. All authors read and approved the final manuscript.

Authors' informations
Tomaz Jarm received his Ph.D. degree in electrical engineering in from the University of Ljubljana in 1999. He is professor at the University of Ljubljana, Faculty of Electrical Engineering. He works in the area of biomedical engineering; his research interests include biomedical signal processing and measurement, instrumentation, and safety, in particular in relation to electroporation-based therapies.

Tadej Krmac received his M.Sc. degree in electrical engineering in 2018. He is junior researcher in Laboratory for Microelectronics of Faculty of Electrical Engineering, University of Ljubljana. His area of interest are innovating solutions for THz frequency-modulated continuous electromagnetic waves in various engineering areas.

Ratko Magjarevic received his Ph.D. degree in electrical engineering from the University of Zagreb in 1993. He is professor at the University of Zagreb, Faculty of Electrical Engineering and Computing where he received his Ph.D. in 1994. His scientific and professional interest is in bioelectric potential analysis and in cardiac pacing, methods based on electropermeabilization, and biomedical and health informatics. He is the president-elect of the IFMBE for the term 2021–24.

Bor Kos received his Ph.D. in Electrical Engineering from University of Ljubljana in 2013. He is currently Assistant Professor at the Faculty of Electrical Engineering, University of Ljubljana. His research field is bioelectromagnetics and biomedical engineering with main focus being on numerical modeling of electroporation. For his contributions to the field, he received the 2018 Alessandro Chiabrera award, presented by EBEA.

Helena Cindric received her M.Sc. degree in electrical engineering in 2018. She is a junior researcher in Laboratory of Biocybernetics, Faculty of Electrical Engineering, University of Ljubljana. Her main research interests lie in the field of finite element numerical modeling for electroporation-based treatments.

Damijan Miklavcic received his Ph.D. degree in electrical engineering from the University of Ljubljana in 1993. He is professor at the University of Ljubljana, Faculty of Electrical Engineering. His main research interests are in electroporation-based methods, including electrochemotherapy of tumors, cardiac ablation, gene therapy, biological experimentation, numerical modeling of biological processes and hardware development.

Funding
The research was supported by the Slovenian Research Agency (ARRS) through the Research Program—Electroporation-based Technologies and Treatments (P2-0249; 2015–2021), the Infrastructural Centre—Cellular Electrical Engineering, a part of the Infrasturctural Programme: Network of Research Infrastructure Centers at University of Ljubljana (MRIC UL IP-0510; 2015–2021) and by the Croatian–Slovenian Cooperation in Science and Technology—Safety Aspects of Electrochemotherapy for Patients with Implanted Devices: Numerical Model and Bench Testing (BI-HR/16-17-039; 2016–2017).

Availability of data and materials
The datasets generated and analyzed during the current study are not publicly available due to the still ongoing study, but are available from the corresponding author on reasonable request.

Ethics approval and consent to participate
Not applicable.

Consent for publication
Not applicable.

Competing interests
DM was in the past a consultant receiving consultancy fees and grants from IGEA S.p.A (Carpi, Modena, Italy) and has currently the same status with Medtronic (Minneapolis, MN, USA). BK is currently a consultant for Medtronic (Minneapolis, MN, USA). Apart from this, the authors declare that they have no other competing interests.

Author details
[1] University of Ljubljana, Faculty of Electrical Engineering, Trzaska 25, 1000 Ljubljana, Slovenia. [2] University of Zagreb, Faculty of Electrical Engineering and Computing, Unska 3, 10000 Zagreb, Croatia.

Received: 23 December 2019 Accepted: 30 October 2020
Published online: 16 November 2020

References
1. Kotnik T, Rems L, Tarek M, Miklavčič D. Membrane electroporation and electropermeabilization: mechanisms and models. Annu Rev Biophys. 2019;48:63–91.

2. Yarmush ML, Golberg A, Serša G, Kotnik T, Miklavčič D. Electroporation-based technologies for medicine: principles, applications, and challenges. Annu Rev Biomed Eng. 2014;16:295–320.
3. Miklavcic D, editor. Handbook of electroporation. Berlin: Springer International Publishing; 2017.
4. Marty M, Serša G, Garbay JR, Gehl J, Collins CG, Snoj M, et al. Electrochemotherapy—an easy, highly effective and safe treatment of cutaneous and subcutaneous metastases: results of ESOPE (European Standard Operating Procedures of Electrochemotherapy) study. Eur J Cancer Suppl. 2006;4(11):3–13.
5. Mir LM. Bases and rationale of the electrochemotherapy. Eur J Cancer Suppl. 2006;4(11):38–44.
6. Miklavčič D, Mali B, Kos B, Heller R, Serša G. Electrochemotherapy: from the drawing board into medical practice. Biomed Eng Online. 2014;13(1):29.
7. Serša G, Miklavčič D, Čemažar M, Belehradek J, Jarm T, Mir LM. Electrochemotherapy with CDDP on LPB sarcoma: comparison of the anti-tumor effectiveness in immunocompetent and immunodeficient mice. Bioelectrochem Bioenerg. 1997;43(2):279–83.
8. Campana LG, Edhemovic I, Soden D, Perrone AM, Scarpa M, Campanacci L, et al. Electrochemotherapy—emerging applications technical advances, new indications, combined approaches, and multi-institutional collaboration. Eur J Surg Oncol. 2019;45(2):92–102.
9. Clover AJP, Salwa SP, Bourke MG, McKiernan J, Forde PF, O'Sullivan ST, et al. Electrochemotherapy for the treatment of primary basal cell carcinoma; A randomised control trial comparing electrochemotherapy and surgery with five year follow up. Eur J Surg Oncol. 2020;46(5):847–54.
10. Gehl J, Sersa G, Matthiessen LW, Muir T, Soden D, Occhini A, et al. Updated standard operating procedures for electrochemotherapy of cutaneous tumours and skin metastases. Acta Oncol. 2018;57(7):874–82.
11. Geboers B, Scheffer HJ, Graybill PM, Ruarus AH, Nieuwenhuizen S, Puijk RS, et al. High-voltage electrical pulses in oncology: irreversible electroporation, electrochemotherapy, gene electrotransfer, electrofusion, and electroimmunotherapy. Radiology. 2020;295(2):254–72.
12. Wagstaff PG, Buijs M, van den Bos W, de Bruin DM, Zondervan PJ, de la Rosette JJ, et al. Irreversible electroporation: state of the art. OncoTargets Ther. 2016;9:2437–46.
13. Aycock KN, Davalos RV. Irreversible electroporation: background, theory, and review of recent developments in clinical oncology. Bioelectricity. 2019;1(4):214–34.
14. Garcia PA, Davalos RV, Miklavcic D. A numerical investigation of the electric and thermal cell kill distributions in electroporation-based therapies in tissue. PLoS ONE. 2014;9(8):e103083.
15. Agnass P, van Veldhuisen E, van Gemert MJC, van der Geld CWM, van Lienden KP, van Gulik TM, et al. Mathematical modeling of the thermal effects of irreversible electroporation for in vitro, in vivo, and clinical use: a systematic review. Int J Hyperth. 2020;37(1):486–505.
16. Scheffer HJ, Nielsen K, de Jong MC, van Tilborg AAJM, Vieveen JM, Bouwman ARA, et al. Irreversible electroporation for nonthermal tumor ablation in the clinical setting: a systematic review of safety and efficacy. J Vasc Interv Radiol JVIR. 2014;25(7):997–1011 (**quiz 1011**).
17. Verloh N, Jensch I, Lürken L, Haimerl M, Dollinger M, Renner P, et al. Similar complication rates for irreversible electroporation and thermal ablation in patients with hepatocellular tumors. Radiol Oncol. 2019;53(1):116–22.
18. Ruarus AH, Vroomen LGPH, Geboers B, van Veldhuisen E, Puijk RS, Nieuwenhuizen S, et al. Percutaneous irreversible electroporation in locally advanced and recurrent pancreatic cancer (PANFIRE-2): a multicenter, prospective, single-arm phase II study. Radiology. 2019;294(1):212–20.
19. Cohen EI, Field D, Lynskey GE, Kim AY. Technology of irreversible electroporation and review of its clinical data on liver cancers. Expert Rev Med Devices. 2018;15(2):99–106.
20. Kos B, Voigt P, Miklavcic D, Moche M. Careful treatment planning enables safe ablation of liver tumors adjacent to major blood vessels by percutaneous irreversible electroporation (IRE). Radiol Oncol. 2015;49(3):234–41.
21. Grošelj A, Kos B, Čemažar M, Urbančič J, Kragelj G, Bošnjak M, et al. Coupling treatment planning with navigation system: a new technological approach in treatment of head and neck tumors by electrochemotherapy. Biomed Eng Online. 2015;14(Suppl 3):S2.
22. Miklavčič D, Davalos RV. Electrochemotherapy (ECT) and irreversible electroporation (IRE)-advanced techniques for treating deep-seated tumors based on electroporation. Biomed Eng OnLine. 2015;14(3):I1.
23. Kalra N, Gupta P, Gorsi U, Bhujade H, Chaluvashetty SB, Duseja A, et al. Irreversible electroporation for unresectable hepatocellular carcinoma: initial experience. Cardiovasc Intervent Radiol. 2019;42(4):584–90.
24. Frequently Asked Questions | IGEA. https://www.igea.it/en/oncology/information-clinicians/frequently-asked-questions. Accessed 20 Aug 2019.
25. Risk Information. AngioDynamics. https://www.angiodynamics.com/about-us/risk-information/. Accessed 20 Aug 2019.
26. Scheffer HJ, Vogel JA, van den Bos W, Neal RE, van Lienden KP, Besselink MGH, et al. The influence of a metal stent on the distribution of thermal energy during irreversible electroporation. PLoS ONE. 2016;11(2):e0148457.
27. Martin RCG, Durham AN, Besselink MG, Iannitti D, Weiss MJ, Wolfgang CL, et al. Irreversible electroporation in locally advanced pancreatic cancer: a call for standardization of energy delivery. J Surg Oncol. 2016;114(7):865–71.
28. Cornelis FH, Cindrič H, Kos B, Fujimori M, Petre EN, Miklavčič D, et al. Peri-tumoral metallic implants reduce the efficacy of irreversible electroporation for the ablation of colorectal liver metastases. Cardiovasc Intervent Radiol. 2019;43:84–93.
29. Dunki-Jacobs EM, Philips P, Martin RCG. Evaluation of thermal injury to liver, pancreas and kidney during irreversible electroporation in an in vivo experimental model. Br J Surg. 2014;101(9):1113–21.
30. Faroja M, Ahmed M, Appelbaum L, Ben-David E, Moussa M, Sosna J, et al. Irreversible electroporation ablation: is all the damage nonthermal? Radiology. 2013;266(2):462–70.
31. Zmuc J, Gasljevic G, Sersa G, Edhemovic I, Boc N, Seliskar A, et al. Large liver blood vessels and bile ducts are not damaged by electrochemotherapy with bleomycin in pigs. Sci Rep. 2019;9(1):3649.
32. Korpas D. Implantable cardiac devices technology. Berlin: Springer; 2013.
33. Bertacchini C, Margotti PM, Bergamini E, Lodi A, Ronchetti M, Cadossi R. Design of an irreversible electroporation system for clinical use. Technol Cancer Res Treat. 2007;6(4):313–20.

34. Garcia PA, Rossmeisl JH, Neal RE, Ellis TL, Davalos RV. A parametric study delineating irreversible electroporation from thermal damage based on a minimally invasive intracranial procedure. Biomed Eng OnLine. 2011;10:34.
35. Corovic S, Lackovic I, Sustaric P, Sustar T, Rodic T, Miklavcic D. Modeling of electric field distribution in tissues during electroporation. Biomed Eng Online. 2013;12:16.
36. Gallinato O, de Senneville BD, Seror O, Poignard C. Numerical workflow of irreversible electroporation for deep-seated tumor. Phys Med Biol. 2019;64(5):055016.
37. López-Alonso B, Sarnago H, Burdío JM, Lucía O. Electro-thermal modeling of irreversible electroporation and validation method of electric field distribution. Int J Appl Electromagn Mech. 2020;63(S1):S41-50.
38. Jarm T, Krmac T, Miklavcic D, Magjarevic R. Cardiac Pacemaker exposed to electroporation pulses—an ex vivo study. In: Henriques J, Neves N, de Carvalho P, editors. XV mediterranean conference on medical and biological engineering and computing—MEDICON 2019 (IFMBE proceedings). Cham: Springer International Publishing; 2020. p. 439–46.
39. Kos B, Županič A, Kotnik T, Snoj M, Serša G, Miklavčič D. Robustness of treatment planning for electrochemotherapy of deep-seated tumors. J Membr Biol. 2010;236(1):147–53.
40. Duck FA. Physical properties of tissue: a comprehensive reference book. York: Institute of Physics and Engineering in Medicine; 2012. p. 360.
41. DATABASE » IT'IS Foundation. https://itis.swiss/virtual-population/tissue-properties/database/. Accessed 18 Feb 2020.
42. Marčan M, Kos B, Miklavčič D. Effect of blood vessel segmentation on the outcome of electroporation-based treatments of liver tumors. PLoS ONE. 2015;10(5):e0125591.
43. Lacković I, Magjarević R, Miklavčič D. Three-dimensional finite-element analysis of joule heating in electrochemotherapy and in vivo gene electrotransfer. IEEE Trans Dielectr Electr Insul. 2009;16(5):1338–47.

Publisher's Note

2.5 Paper 5

Title: **Electrochemotherapy of spinal metastases using transpedicular approach – A numerical feasibility study**

Authors: **Helena Cindrič**, Bor Kos, Giuseppe Tedesco, Matteo Cadossi, Alessandro Gasbarrini and Damijan Miklavčič

Publication: *Technology in Cancer Research and Treatment*, vol. 17, pp. 1-13, January 2018

Impact factor: 1.481 (2018)

Quartile: Q4

Rank: 211/230 (Oncology)

DOI: https://doi.org/10.1177/1533034618770253

Original Article

Technology in Cancer Research & Treatment
Volume 17: 1-13
© The Author(s) 2018
Reprints and permission:
sagepub.com/journalsPermissions.nav
DOI: 10.1177/1533034618770253
journals.sagepub.com/home/tct
SAGE

Electrochemotherapy of Spinal Metastases Using Transpedicular Approach—A Numerical Feasibility Study

Helena Cindrič, BSc[1], Bor Kos, PhD[1], Giuseppe Tedesco, MD[2], Matteo Cadossi, MD, PhD[2], Alessandro Gasbarrini, MD[2], and Damijan Miklavčič, PhD[1]

Abstract

Vertebral column is the most frequent site for bone metastases. It has been demonstrated in previous studies that bone metastases can be efficiently treated by electrochemotherapy. We developed a novel approach to treat spinal metastases, that is, transpedicular approach that combines electrochemotherapy with already established technologies for insertion of fixation screws in spinal surgery. In the transpedicular approach, needle electrodes are inserted into the vertebral body through pedicles and placed around the tumor. The main goal of our study was to numerically investigate the feasibility of the proposed treatment approach. Three clinical cases were used in this study—1 with a tumor completely contained within the vertebral body and 2 with tumors spread also to the pedicles and spinal canal. Anatomically accurate numerical models were built for all 3 cases, and numerical computations of electric field distribution in tumor and surrounding tissue were performed to determine the treatment outcome. Complete coverage of tumor volume with sufficiently high electric field is a prerequisite for successful electrochemotherapy. Close to 100% tumor coverage was obtained in all 3 cases studied. Two cases exhibited tumor coverage of >99%, while the coverage in the third case was 98.88%. Tumor tissue that remained untreated was positioned on the margin of the tumor volume. We also evaluated hypothetical damage to spinal cord and nerves. Only 1 case, which featured a tumor grown into the spinal canal, exhibited potential risk of neural damage. Our study shows that the proposed transpedicular approach to treat spinal metastases is feasible and safe if the majority of tumor volume is contained within the vertebral body. In cases where the spinal cord and nerves are contained within the margin of the tumor volume, a successful and safe treatment is still possible, but special attention needs to be given to evaluation of potential neural damage.

Keywords

electrochemotherapy, electroporation, numerical modeling, treatment planning, spinal metastases

Abbreviations

CT, computed tomography; IRE, irreversible electroporation; MR, magnetic resonance; MSE, mean square error; PET/CT, positron emission tomography/computed tomography; RE, reversible electroporation.

Received: September 20, 2017; Revised: December 19, 2017; Accepted: February 22, 2018.

Introduction

Bone cancers rarely originate from bone tissue or bone marrow but are rather metastasized from a primary tumor elsewhere in the body. Bone metastases usually develop in the later stages of cancer disease, and due to prolonged cancer survival, the number of patients with painful bone metastases has significantly increased in the modern day.[1]

[1] Laboratory of Biocybernetics, Faculty of Electrical Engineering, University of Ljubljana, Ljubljana, Slovenia
[2] Department of Oncologic and Degenerative Spine Surgery, Rizzoli Orthopedic Institute, Bologna, Italy

Corresponding Author:
Damijan Miklavčič, PhD, Laboratory of Biocybernetics, Faculty of Electrical Engineering, University of Ljubljana, Tržaška cesta 25, 1000 Ljubljana, Slovenia.
Email: damijan.miklavcic@fe.uni-lj.si

Vertebral column is the most frequent site for bone metastases. The incidence of spinal metastases in patients with cancer can reach up to 70% depending on primary tumor type. The highest incidence was observed for primary breast cancer, followed by prostate and lung cancer.[2,3] Bone metastases lead to a considerable decrease in patient's quality of life. They cause severe pain, pathological fractures, decreased mobility, neurological disorders as a consequence of hypercalcemia, and in case of spinal metastases, spinal cord, and nerve compression.[1,3]

It is commonly accepted that bone metastases are an expression of a systemic disease and therefore require multidisciplinary treatment. Several options to treat bone metastases are available: radiotherapy, surgery, cryosurgery (as an alternative to conventional surgery), chemotherapy, thermal (radiofrequency) ablation, and sometimes a combination of different therapies is used to achieve better results. The most common treatment option for bone metastases is radiotherapy. More aggressive approaches, such as surgery, are used in case of impending or pathological fractures, huge lesion, and in case of spinal cord compression.[1,4]

Spinal metastases have different shapes and behavior related to the large varieties of histotypes and spread modality of the primary tumor. The choice of the most appropriate treatment is of crucial importance for the patient who may be severely disabled by the presence of untreated spinal metastases. Moreover, these lesions may not only be the cause of severe deterioration in the quality of life but also direct or indirect cause of death. The major goal of treating spinal metastases is restoring spinal stability, cord decompression, and reducing pain. Treatment of spinal metastases is especially complicated because of the importance of vertebral column in bodily support and movement and because of the involvement of spinal cord and nerves. Controversy exists over the most appropriate treatment and despite the evolution of anesthesiological techniques, surgery remains a treatment with many risks and is not always feasible.[5] Therefore, novel and less aggressive treatments for spinal metastases are required, especially for the treatment of patients not responding to standard therapies (eg, radioresistant tumors), providing patients' relief from symptoms and improving their quality of life.

Electroporation is a technique that uses short intense electrical pulses to induce temporary pores in the cell membrane thus increasing its permeability. Electroporation can be controlled and achieved without compromising cells' viability. Electroporation has become a widespread technique in medicine, food, and biotechnology for facilitating transmembrane transport of larger or low permeant molecules.[6-10]

Electrochemotherapy combines the use of chemotherapeutic drugs with electroporation of the tumor volume, aiming at increasing drug uptake into tumor cells and thus increasing the cytotoxicity of some drugs, such as bleomycin and cisplatin.[11-13] In order for electrochemotherapy to be successful, the whole tumor volume needs to be covered in sufficiently high electric field (reversible electroporation threshold).[14] Various studies have demonstrated that electrochemotherapy is a safe and effective treatment and is minimally invasive and nontoxic to nontarget tissue. Electrochemotherapy has already been introduced into standard clinical practice and the increasing number of studies confirms its importance in treating cancer disease.[11]

It has been demonstrated in preclinical and clinical studies that bone metastases can be efficiently treated by electrochemotherapy.[15-18] A clinical study was presented by Bianchi *et al*, in which 29 patients were treated with electrochemotherapy in several skeletal sites.[15] There are few human patients with spinal metastases treated by electrochemotherapy, and to our knowledge, only 1 published case, presented by Gasbarrini *et al*.[18] Both clinical studies reported a significant decrease in pain and no adverse neural symptoms associated with the treatment. Furthermore, several preclinical studies have shown that electroporation causes no loss of bone density or cell organization and does not prevent new bone formation.[16,17] There is also evidence of possible bone and nerve tissue regeneration even after irreversible electroporation of tissue (nonthermal ablation).[19,20]

The study presented by Gasbarrini and colleagues[18] is the first reported clinical case using electrochemotherapy to treat spinal metastases. In this case, a partial hemilaminectomy was necessary in order to insert the electrodes directly into the vertebral body. No electrochemotherapy-related adverse events were observed during the procedure and overall improvement in pain outcome and global function after the treatment was excellent. The patient reported preoperative pain intensity of 10 according to visual analog scale, which dropped down to 2 already in the first month after treatment. Moreover, no spinal instability was reported after electrochemotherapy treatment.

The promising results of the first clinical case drove us to further investigate the possibilities for electrochemotherapy treatment for spinal metastases. In this article, we introduce a novel, minimally invasive approach that combines electrochemotherapy with already established technologies for transpedicular insertion of fixation screws in spinal surgery. In the proposed treatment approach, hereinafter referred to as transpedicular approach, needle electrodes are inserted into the vertebral body through the pedicles and placed around the tumor. The electrodes used in this approach have shorter conductive parts (1 cm rather than 3 cm) and are gradually retracted from the vertebral body, allowing to cover the tumor volume in segments rather than all at once and to manipulate various treatment parameters during procedure.

The goal of this study was to numerically investigate the feasibility of the transpedicular approach to treat spinal metastases. Three representative clinical cases, with different stages of vertebral body, pedicle, and spinal canal involvement, were used in the study. Anatomically accurate numerical models were built for all 3 cases, and numerical computations of electric field distribution in tumor and surrounding tissue were performed to determine the outcome of the proposed treatment. In addition to tumor coverage, we also evaluated the hypothetical risk of damage to the spinal cord and nerves.

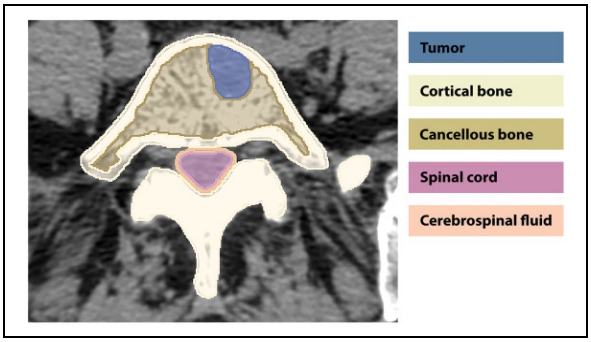

Figure 1. An example of tissue segmentation performed on a CT scan of fifth lumbar vertebra with a tumor. All tissues that were not directly included into segmentation were considered as background tissue and were assigned the properties of adipose tissue. CT indicates computed tomography.

Materials and Methods

We conducted a numerical feasibility study of transpedicular approach to treat spinal metastases. The study was approved by the ethical committee of the Rizzoli Orthopedic Institute (Prot.n.12458/15.05.2009—ES2IOR). All patients gave their written, informed consent to participate in the study. Three representative cases of spinal metastases were used for this study including the case presented by Gasbarrini *et al*.[18] An anatomical model based on medical images was developed for each case. Electrical properties of tissues were determined through an experimental numerical study and applied to the models. Applied voltages were optimized to ensure highest possible tumor coverage. Electric field strength distributions were calculated for each case in order to predict the outcome of the proposed treatment approach.

Anatomical Models

Geometry for the anatomical models was obtained from computed tomography (CT) and magnetic resonance (MR) scans of patients. 3D Slicer software platform (https://www.slicer.org/, Fedorov *et al.*[21]) was used to segment all relevant anatomical structures—tumor tissue, cortical bone, cancellous bone, spinal cord, cerebrospinal fluid, and intervertebral discs. All remaining tissue was considered as background and was assigned the properties of adipose tissue. An example of segmentation of the 5th lumbar vertebra with a tumor is presented in Figure 1.

Segmentation data were imported into Matlab R2016b (MathWorks, Natick, Massachusetts, USA) computing environment where three-dimensional models of the regions of interest were built. The models were based on initial electrical conductivity values and thresholds for reversible and irreversible electroporation of specific tissues found in the literature,[22-28] and numerically determined factors of electrical conductivity increase after electroporation. All tissues were considered homogeneous and isotropic. Osteoporosis effect on dielectric properties of bone tissue is negligible, thus it has not been accounted for in the models.[29,30] The assigned conductivity values before electroporation, that is initial conductivities, are presented in Table 1, along with the list of the literature from which the data were acquired. In some cases, a combination of different reported values was used due to discrepancies in reported results.

Table 1. Electrical Conductivities of Tissues in the Vertebral Column.

Tissue	Initial Electrical Conductivity (S/m)	List of References
Tumor	0.35	22,25,26
Cortical bone	0.02	24,27
Cancellous bone	0.07	23,24
Spinal cord	0.23	27
Cerebrospinal fluid	1.50	23
Intervertebral disc	1.00	28
Background (adipose tissue)	0.02	22

During the delivery of electric pulses, the electrical conductivity of tissues increases due to electroporation. The first approximation of factors of conductivity increase was set to 3.0 for all tissue types[22,25] except for cerebrospinal fluid, conductivity of which was kept unchanged. Factors of conductivity increase were later adjusted through a numerical optimization. The electric field strength threshold for all segmented tissue types was set to 400 V/cm for reversible and 800 V/cm for irreversible electroporation.[25,31-33] The threshold for reversible electroporation of background (adipose) tissue was set to 100 V/cm.[22]

Numerical Computations

The models were imported into the finite element analysis software Comsol Multiphysics 5.2 (Comsol Inc., Stockholm, Sweden), where all numerical computations were performed. A previously designed numerical framework for treatment planning of deep seated tumors, described in more detail in,[22,34-36] was used for the numerical computations. Live link for Matlab was used to control the method model setup and solving.

Four virtual needle electrodes (1.2 mm diameter and 1 cm conductive length) were inserted into each imported anatomical model as is shown in Figure 2. Two electrodes were inserted through each pedicle and positioned so as to surround the tumor volume. The upper 2 electrodes were parallel to the vertebral body plane while the lower 2 electrodes were positioned at a downward angle with respect to the upper electrodes. Electrode positions were determined based on medical images (CT and MR scans). Electrodes with shorter conductive parts than usual (1 cm rather than 3 cm) are used in this approach allowing us to target the tumor volume more precisely.

The electrodes were connected in pairs resulting in 6 combinations. Electric pulses were applied to each electrode pair. The applied voltage was adjusted based on the distance between centers of electrode tips and was later optimized to ensure highest possible tumor coverage. The minimum applied

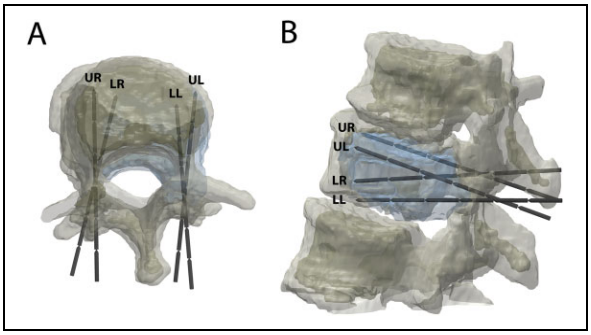

Figure 2. An example of electrode placement in the three-dimensional anatomical model of 11th thoracic vertebra in case of transpedicular approach in (A) axial and (B) sagittal view. LL indicates lower left electrode; LR, lower right electrode; UL, upper left electrode; UR, upper right electrode.

voltage was set to 500 V and the maximum to 3000 V since this is the possible range of output voltages provided by currently available devices.[37,38]

Electric field distribution in all tissues and electric currents were calculated after application of pulses to each active electrode pair as previously described.[34,36,39] The model was simplified so that the calculations for each electrode pair were performed independently from other pairs. A train of 8 pulses, delivered to each electrode pair, was modeled as a single pulse; otherwise the conductivity changes between each consecutive pulse in the train would need to be known and modeled.[22] At the beginning of the calculations for each pair, the initial electrical conductivity of all modeled tissues was considered homogenous. The dynamics of conductivity changes and electric fields during each pulse train were then approximated by a sequential model.[39] In each sequence of the model, electric field distribution in tissues was calculated and electrical conductivity values were increased accordingly. Tissue conductivity dependency on electric field distribution was approximated by a sigmoid function. Electrical conductivities defined in each sequence were used to calculate the electric field distribution in the following sequence, thus gradually increasing the total conductivity of tissues throughout the calculation. Our model was based on 6 sequences for each train of pulses. The final electric field distribution at the end of each train of pulses was calculated using the highest values from all previous sequences. Total electric current after the application of pulses was also calculated for each electrode pair.

The transpedicular approach assumes that the tumor volume is covered in segments, with electrodes being retracted a short distance after the application of pulses to all pairs. Upon completion of computations for all 6 active pairs (ie, all possible activations of 4 electrodes), the electrodes were retracted for a distance of 1 cm and computations were performed again. The number of retractions varies from case to case depending on the tumor and vertebra size.

Optimization of Tissue Conductivity Values

Although there are studies on electrical conductivities of human tissues, the data are scarce and reported results differ between individual studies. In order to develop a numerical model that reflects the conditions in the vertebral column as close as possible, we conducted a numerical study to determine the increase in electrical conductivity due to electroporation for bone and tumor tissue. Two sets of experimental data, published in previous studies,[17,18] were used for this purpose.

Electrical properties of bone tissue. Radiological images, acquired during the study of irreversible electroporation of sheep vertebrae,[17] enabled us to delineate a well-defined geometry of the sheep lumbar vertebra with 2 inserted electrodes. Combined with accurate current and voltage measurements for different electroporation protocols used in the procedure, we were able to fine tune the initial values of electrical conductivity and factors of conductivity increase for cortical and cancellous bone.

We designed an algorithm that iteratively changed the factor of conductivity increase for specific bone tissue in order to minimize the absolute error between measured and calculated current. The absolute (I_{abs}) and relative (I_{rel}) errors were calculated according to:

$$I_{abs} = |I_{meas} - I_{calc}|$$

$$I_{rel} = |\frac{I_{meas} - I_{calc}}{I_{meas}}|$$

where I_{meas} is electric current measured during the procedure and I_{calc} is numerically calculated electric current.

Current measurements of the protocol, that caused little or no electroporation of bone tissue (10 pulses, 100 μs, 1000 V),[17] were used to validate the initial conductivity values of bone tissue before electroporation. Current measurements of a second protocol (10 pulses, 100 μs, 3000 V), that caused electroporation of bone tissue, were used to determine the factors of conductivity increase.

Electrical properties of tumor tissue. In order to determine electrical conductivity values for tumor tissue, we numerically reconstructed the case presented previously.[18] For this purpose, we used the set of intraoperative images, fluoroscopic guidance images, treatment parameters (electrode pairs, distances between electrode tips), and currents and voltages measured during the procedure.

An anatomical model of the 5th lumbar vertebra, which was initially designed for evaluation of electrochemotherapy in case of transpedicular access, was reused for this purpose and adapted accordingly. Two electrodes were inserted through the left pedicle, the other 2 were inserted medially, directly into the vertebral body. Intraoperative images and fluoroscopic control images were used to determine approximate electrode positions. Further optimization of positioning was performed so that the distances, between electrode tips used in computation, matched the distances measured during the procedure as closely as possible (Figure 3). Since it was not registered which

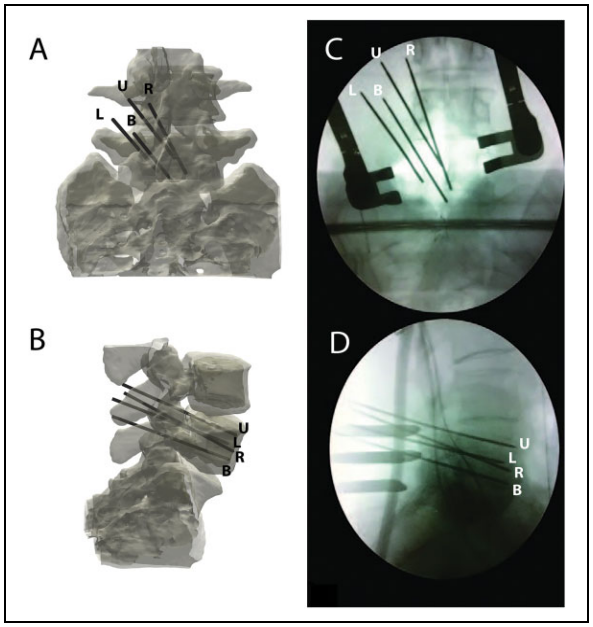

Figure 3. (A and B) Numerical reconstruction of the first clinical case of electrochemotherapy of spinal metastases[18]—three-dimensional model of fifth lumbar vertebra with inserted needle electrodes in (A) coronal and (B) sagittal view; (C and D) Fluoroscopic guidance images used in reconstruction of electrode positions. B indicates lower electrode; L, left electrode; R, right electrode; U, upper electrode.

distance corresponded to which electrode pair during operation, we determined the corresponding pairs for computation based on voltages and currents provided. The designed anatomical model with inserted electrodes is presented in Figure 3A and B, next to the fluoroscopic guidance images, which were taken from the study by Gasbarrini *et al*[18] and used for validation of electrode positions (Figure 3C and D).

Electrodes used in this model had a 3-cm-long conductive part and 1.8 mm diameter, mimicking the electrodes used in the actual treatment. The 4 electrodes formed 6 active pairs. The voltage applied to each pair was set to match the voltages used during treatment. Electrical properties of cortical and cancellous bone tissue determined in the sheep experimental study were used in this model.

Electric current and electric field distribution in tissues were calculated for all 6 electrode pairs. Calculated electric currents were then compared to measured electric currents and the mean square error (MSE) between the 2 currents was calculated. Mean square error was calculated according to:

$$\mathrm{MSE} = \frac{1}{n}\sum_{i=1}^{n}(I_{\mathrm{meas}} - I_{\mathrm{calc}})^2,$$

where I_{meas} is electric current measured during the procedure and I_{calc} is numerically calculated electric current and n is the index of the active electrode pair.

The algorithm developed for the sheep experimental study was used to calculate the factor of conductivity increase for tumor tissue by means of minimizing the MSE between the currents.

Optimization of Applied Voltage Values

The developed numerical models for 3 selected cases with different stages of vertebral body, pedicle, and spinal canal involvement were subjected to further optimization with respect to voltage values delivered to each electrode pair. The first approximation of voltage amplitudes, applied to the electrode pairs, was based on distance between centers of electrode tips. Each value was then optimized using a genetic algorithm.[36,40] The optimization algorithm was set to maximize the volume of the tumor tissue covered with electric field above the reversible threshold and minimize the volume of spinal cord tissue covered with electric field above the irreversible threshold. Applied voltages were varied in 5 steps of 100 V in both directions (lower and higher) from the initially assigned value, resulting in 10 possible values for each electrode pair. The minimum and maximum allowed values were set to 500 V and 3000 V.

First a population of possible candidates for all electrode pairs was generated. Candidates for optimal solution were selected from the population and evolved through 100 generations using operations of the genetic algorithm (crossover, mutations) and the fitness function:

$$F = V_T^{rev} - V_{SC}^{irr}$$

where F is fitness, V_T^{rev} is the volume of tumor tissue in $F = V_T^{rev} - V_{SC}^{irr}$ cubic centimeters covered in electric field above the reversible threshold and V_{SC}^{irr} is the volume of spinal cord tissue in cubic centimeters covered in electric field above the irreversible threshold.

Results

In this section, we present numerical results of tissue properties fitting, numerically calculated outcome of the reconstruction of the clinical case, and outcomes of the newly proposed transpedicular approach in 3 different cases of spinal metastases.

Electrical Properties of Tissues

Electrical properties of tissues, which were defined through the literature survey and numerical optimization, are presented in Table 2. So defined parameters minimized the errors between numerically calculated and actual measured currents for both reconstructed cases—sheep vertebra and Gasbarrini *et al* case. In case of sheep vertebra, the absolute error between calculated and measured current was 0.07 A for the first delivered protocol and 0.02 A for the second delivered protocol. The maximum relative error was 5.68%. Measured and calculated electric currents for both protocols and the absolute and relative errors are presented in Table 3.

Table 2. Electrical Properties of Tissues Used in the Numerical Model.

Tissue	Initial Electrical Conductivity (S/m)	Factor of Conductivity Increase After Electroporation (−)
Tumor	0.30	2.80
Cortical bone	0.02	3.00
Cancellous bone	0.07	2.90
Spinal cord	0.23	3.00
Cerebrospinal fluid	1.50	1.00
Intervertebral disc	1.00	3.00
Background	0.02	300

Table 3. Comparison of Measured and Calculated Currents for the Preclinical Case Presented Previously.[17]

Electroporation Protocol	Mean Measured Current (A)	Calculated Current (A)	Absolute Error (A)	Relative Error (−)
10 × 100 μs pulses; 1000 V	1.1859	1.1185	0.0674	0.0568
10 × 100 μs pulses; 3000 V	5.9515	5.9714	0.0199	0.0033

For the clinical case, presented by Gasbarrini *et al*, the MSE for calculated and measured electric currents was 2.61 A. Applied voltages, calculated electric currents, actual measured electric currents, and the absolute and relative errors between currents are presented in Table 4. The maximum relative error between measured and calculated current was 16%.

The reconstructed clinical case was also used to validate the adequacy of the designed numerical framework for planning electroporation-based treatments of spinal metastases. The numerical reconstruction predicted 100% (2.13 cm^3) coverage of tumor tissue with electric field strength equal or greater than the reversible threshold. The cumulative coverage curves for tumor tissue are presented in Figure 4. Each curve represents a volume fraction of tumor tissue with respect to electric field exposure for a single active electrode pair. It can be observed that complete coverage of the tumor with electric field of at least 400 V/cm, that is, reversible threshold, was achieved already after the third applied pulse sequence. After the delivery of pulse sequences to all 6 pairs of electrodes, 0.12 cm^3 of the total spinal cord volume modeled (7.29 cm^3) was covered with electric field strength above the reversible threshold and 0.016 cm^3 above irreversible threshold.

Transpedicular Approach

The outcome of the proposed treatment with transpedicular approach has been calculated for 3 cases of spinal metastases with different stages of vertebral body, pedicle, and spinal canal involvement. The cases featured tumors in fifth lumbar vertebra and in the sixth and 11th thoracic vertebrae, respectively.

Case 1—fifth lumbar vertebra. The case, which was presented previously[18] and also reconstructed for optimization purposes, presented a solid tumor completely contained within the body of fifth lumbar vertebra. Total volume of tumor tissue in the model was 2.13 cm^3. Electrodes were retracted once to cover the whole tumor volume with electric field above reversible threshold of 400 V/cm. Figure 5A shows the cumulative coverage curves for tumor tissue. Each curve represents a volume fraction of tumor tissue with respect to electric field exposure for a single active electrode pair (total 12). It can be observed in Figure 5A that approximately 90% of total tumor volume has been covered in sufficiently high electric field already after the third applied sequence of pulses. The remaining part of tumor tissue, positioned in the posterior area of vertebral body, has been covered with application of pulses to the remaining 9 electrode pairs resulting in 99.68% tumor coverage. None of the spinal cord tissue was exposed to electric field high enough to cause electroporation of tissue. The maximum delivered voltage used in this case was 2700 V and the maximum calculated current was 6.96 A.

For this case, we also calculated the outcome of treatment if electrodes with conductive part length of 3 cm were used since this length is common for treating bones. We used the same geometry and electrode positions but without electrode retraction. This treatment plan was submitted to the same optimization algorithm for voltage values as before. Table 5 shows compared results for both treatment plans. Tumor coverage is the same in both cases. No spinal cord tissue was electroporated in either case although the maximum electric field in spinal cord is higher in the case with 3 cm electrodes. The maximum calculated current in case of 3 cm electrodes is almost twice the value of maximum current in the case with 1 cm electrodes.

Case 2—11th thoracic vertebra. The second case featured a tumor in the 11th thoracic vertebra that had already grown out of vertebral body, into surrounding tissue, left pedicle, and posterior lamina. Total volume of tumor tissue in the model was 15.53 cm^3. Electrodes were retracted twice, each time for a distance of 1 cm, covering the tumor volume in 3 segments (deep, medial, and posterior). Coverage of tumor tissue at the end of all 18 applied pulse sequences was 98.88%. The cumulative coverage curves for tumor tissue are shown in Figure 5B. Tumor tissue that remained untreated was positioned on the margin of the tumor near the pedicle area (Figure 6B). The total volume of spinal cord tissue in the model was 7.31 cm^3, of which 1.228 cm^3 of tissue was exposed to electric field high above reversible threshold and 0.0002 cm^3 above irreversible threshold. The maximum delivered voltage used in this case was 2900 V and the maximum calculated current was 21.33 A.

Case 3—sixth thoracic vertebra. In the third case, the tumor was positioned in the posterior part of sixth thoracic vertebral body and had already grown into the pedicles and the spinal canal, compressing the spinal cord. Total volume of tumor tissue in the model was 15.33 cm^3. Electrodes were retracted twice, each time for a distance of 1 cm, covering the tumor volume in 3 segments.

Table 4. Comparison of Measured and Calculated Electric Currents for the Clinical Case Presented Previously.[18]

Electrode Pair	Applied Voltage (V)	Measured Electric Current (A)	Calculated Electric Current (A)	Absolute Error (A)	Relative Error (−)
U-L	1100	8.84	9.89	1.05	0.12
U-R	1000	11.91	10.05	1.86	0.16
U-B	1500	12.88	14.99	2.12	0.16
R-L	1500	14.11	12.79	1.31	0.09
B-L	1700	15.39	17.44	2.05	0.13
B-R	800	7.10	7.91	0.81	0.11

Abbreviations: B, lower electrode; L, left electrode; R, right electrode; U, upper electrode.

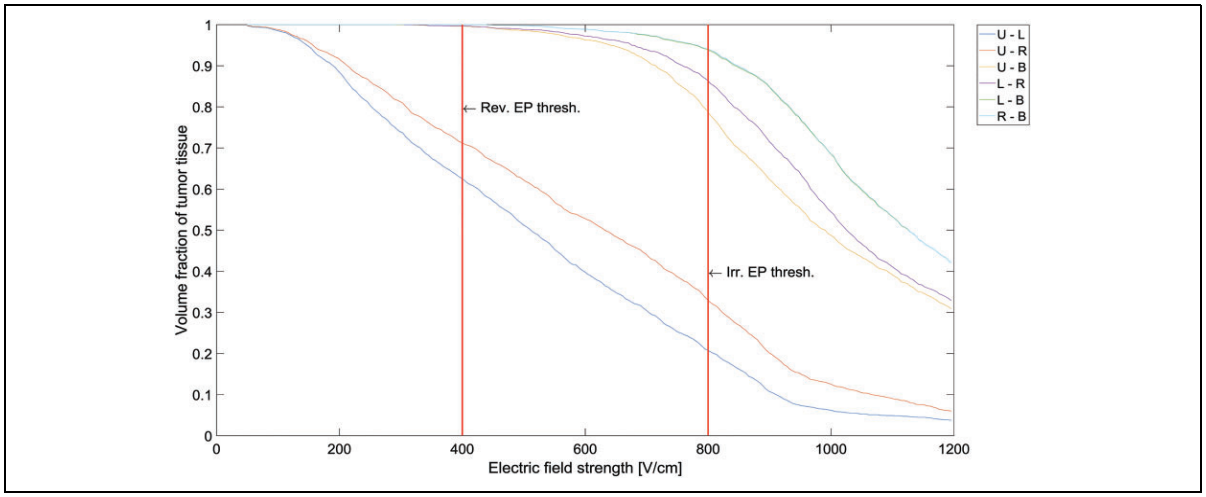

Figure 4. Cumulative coverage curves for tumor tissue for the numerically reconstructed clinical case[18] (5th lumbar vertebra). Each curve represents a volume fraction of tumor tissue with respect to electric field strength for a single active electrode pair. B indicates lower electrode; L, left electrode; R, right electrode; U, upper electrode.

The total coverage of tumor tissue was 99.42%. The cumulative coverage curves for tumor tissue are shown in Figure 5C. The total volume of spinal cord tissue in the model was 7.48 cm^3, of which 1.191 cm^3 of tissue was covered with electric field above the reversible threshold and 0.0124 cm^3 above irreversible threshold. The maximum delivered voltage used in this case was 3000 V and the maximum calculated current was 24.32 A.

Table 6 summarizes the outcomes (total tumor coverage) and other significant parameters for all 3 cases studied, using transpedicular approach. An example of numerically calculated electric field distribution in tumor and bone tissue for all 3 cases is shown in Figure 6. Blue areas represent electroporated tumor tissue while the orange areas represent electroporated bone tissue.

Discussion

In our study, we investigated feasibility of a novel approach for electrochemotherapy of spinal metastases with the insertion of electrodes through the pedicles, that is, transpedicular approach. For this purpose, we reworked the numerical framework, which was previously designed for planning of electroporation-based treatments of deep seated tumors, so that it can now also be used for planning of electrochemotherapy of spinal metastases.[22,34] We also investigated the spinal canal involvement and possible risk of neural damage.

Three representative cases have been used in this feasibility study, each showing a different stage of vertebral body, pedicle, and spinal canal involvement. In order for electrochemotherapy to be successful, an adequate concentration of a chemotherapeutic drug and sufficiently high electric field needs to be present in the whole tumor volume.[35] The focus of our study was to investigate the electric field distribution in tumor tissue in case of transpedicular electrode insertion. For this purpose, an individual treatment plan was prepared for each of the 3 cases.

Close to 100% tumor coverage with electric field above reversible threshold value was obtained in all 3 cases. Two cases, fifth lumbar vertebra and sixth thoracic vertebra, exhibited tumor coverage of >99%, while the coverage in 11th thoracic vertebra was 98.88%. In both cases in the thoracic vertebra, the percentage of irreversibly electroporated tumor tissue was quite high, 45% and 63% for the 11th and sixth thoracic vertebra, respectively. It has been revealed in a recent study, however, that threshold value for

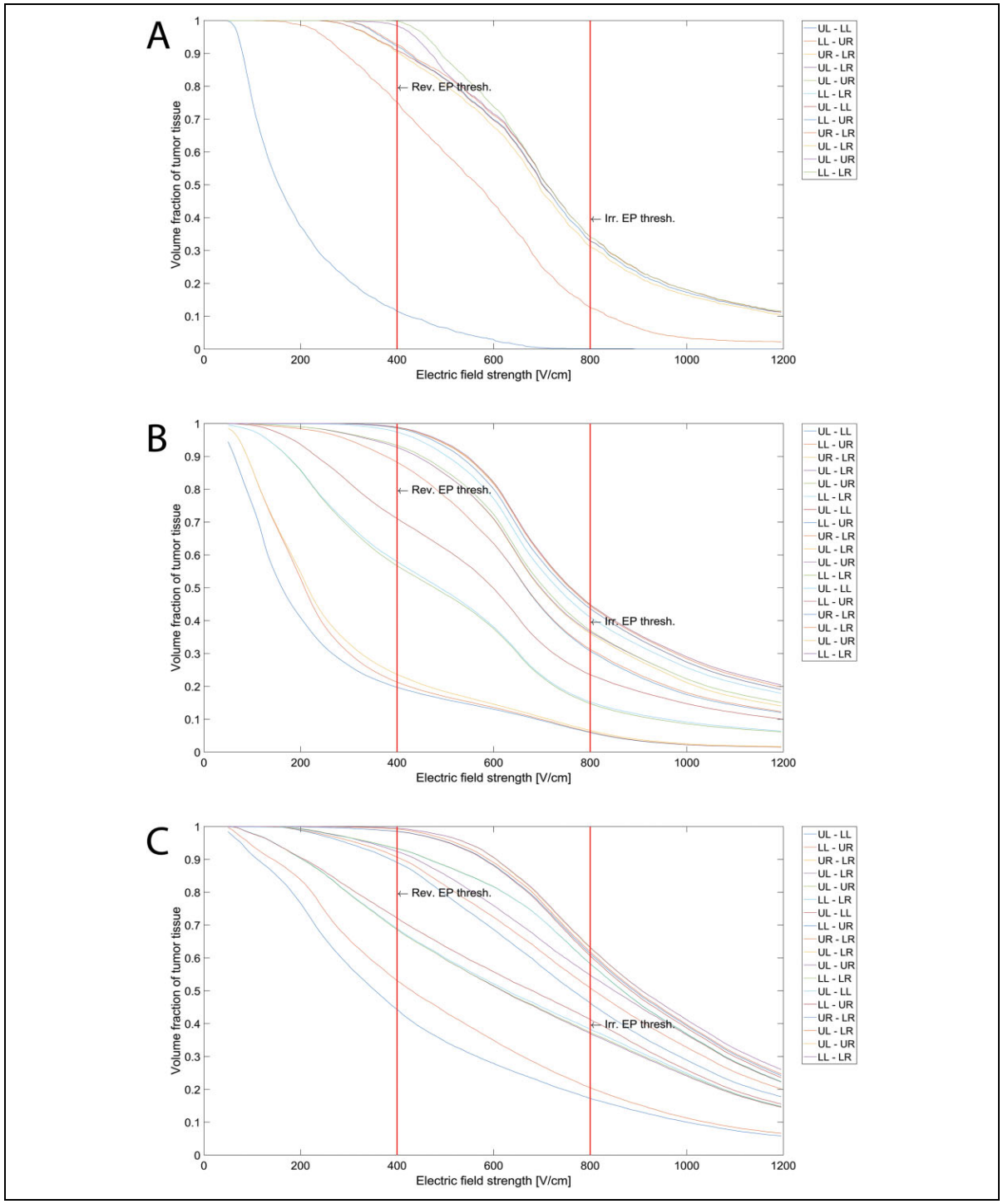

Figure 5. Cumulative coverage curves for tumor tissue for 3 studied cases; (A) fifth lumbar vertebra, (B) 11th thoracic vertebra, and (C) sixth thoracic vertebra. Each curve represents a volume fraction of tumor tissue with respect to electric field strength for a single active electrode pair. B indicates lower electrode; L, left electrode; R, right electrode; U, upper electrode.

Table 5. Comparison of Treatment for Electrodes With Different Conductive Part Length.

Parameter Description	Electrode Conductive Part Length: 3 cm	Electrode Conductive Part Length: 1 cm
Tumor coverage (%)	99.68	99.68
Maximum delivered voltage (V)	2600	2700
Maximum calculated current (A)	13.44	6.97
Volume of spinal cord tissue above reversible threshold (cm^3)	0	0
Maximum electric field in spinal cord tissue (V/cm)	230	140

irreversible electroporation of tumor tissue is in fact much higher than threshold values reported in the literature and used in our numerical model (800 V/cm)[41]; therefore, it is likely that the actual percentage of irreversibly electroporated tissue would be lower than that predicted by the model. Preclinical studies have demonstrated that in contrast to other ablative techniques, irreversible electroporation does not affect bone structure in the long term.[16,17,19] It only affects the cell membrane, while the tissue scaffold remains intact, thus preserving the mechanical competence of treated bone. Furthermore, irreversible electroporation does not affect or prevent osteogenic activity. On the contrary, there is emerging evidence that apoptotic cell death caused by electroporation even promotes bone growth and renewal.[20] Nevertheless, further limitations, such as percentage of irreversibly electroporated tumor and bone tissue, could be introduced into the constructed optimization algorithm to prevent unnecessarily high exposure of tissue to electric fields above irreversible threshold. This might result in lower tumor coverage in some cases, but it has been demonstrated in a study on ablation of brain tumors with irreversible electroporation that a complete response is possible even if a fraction of tumor tissue remains untreated.[42] Furthermore, it is also reported in the same study that electric field thresholds that produced good treatment outcomes were lower than the values commonly reported in the literature.

We would also like to point out that although an optimization algorithm was used for applied voltages, electrode positions were determined manually and were not subjected to optimization algorithm. Therefore, a similar algorithm, as was used for optimization of applied voltages, could also be used to optimize electrode positions and would perhaps result in even better tumor coverage. Furthermore, it can be observed in Figure 5 showing cumulative coverage curves for all 3 cases that some electrode pairs do not significantly contribute to total tumor coverage when compared to preceding electrode pairs. An optimization algorithm could identify and exclude such electrode pairs; therefore, it would not only optimize electrode positions to ensure highest tumor coverage but would also minimize exposure of tissues to high electric fields.

An important feature of the transpedicular approach are electrodes with shorter conductive parts. The length of the conductive part of electrodes used in this study was 1 cm instead of 3 cm, which is currently used for electroporation of bones.[15] Our study on the fifth lumbar vertebra demonstrates that lower maximum currents are delivered when electrodes with shorter conductive parts are used. Furthermore, lower electric field was observed in the spinal canal, which is due to more precise targeting of tumor volume. Also, the overall percentage of electroporated surrounding tissue was lower in case of electrodes with shorter conductive parts.

In constructing numerical models, some limitations need to be acknowledged. The numerical models are based on electrical conductivity values for tissues and factors of conductivity increase due to electroporation. Although there are reports on electrical conductivities of human tissue in the low frequency range needed for electroporation, the data are scarce and the reported results differ considerably between individual studies.[23,24,27,28] The impact of electroporation on conductivity increase is even harder to come by. We thus used 2 sets of experimental data acquired during preclinical and clinical studies of electroporation in vertebra to fine-tune factors of electrical conductivity increase for bone and tumor tissue. Results of the fitting show good agreement between measured and calculated electric currents in tissue, however, further validation is needed. Namely, the data size on which this fitting was performed was small and not acquired specifically for this purpose. More accurate measurements with the exact purpose of investigating the behavior of tissue conductivity subjected to electroporation are thus needed.

The next major uncertainty of the designed model are electroporation thresholds for the treated tumor and surrounding tissues. There are extensive studies on electroporation thresholds for specific tissues, such as liver, muscle, and brain, and on tumors present in these tissues,[25,26,32,43,44] but only a few preclinical studies on the effect of electroporation on bone and nerve tissue.[17,19,27,45,46] Thresholds for bone, bone tumors, and spinal cord have not yet been determined. Reported results on thresholds for electroporation of tumor tissue vary, depending on tumor histology and pulse parameters.[22,25,31,32,43,47] Since there are no reported results on bone tumors, the highest reported threshold for reversible electroporation of tumor tissue was used in this model to prevent overly optimistic prediction of electroporated area. For spinal cord tissue, however, the lowest threshold for irreversible electroporation was used in order to alert of potential risk of neural damage.

Further limitations of the model are mostly related to tissue structure and segmentation complexity. All tissue was considered homogenous and isotropic, although it is known that the actual situation is much more complex—for example, bone tissue, especially cortical bone, is distinctively anisotropic and so is its electrical conductivity.[23] Furthermore, only the most relevant tissues were segmented for the anatomical model. However, previous studies that used a similar modeling approach showed good agreement between calculated and measured data.[25,35]

Upon completion of the model and numerical method setup, the outcome of the reconstructed clinical case presented previously[18] was calculated. Numerical computations

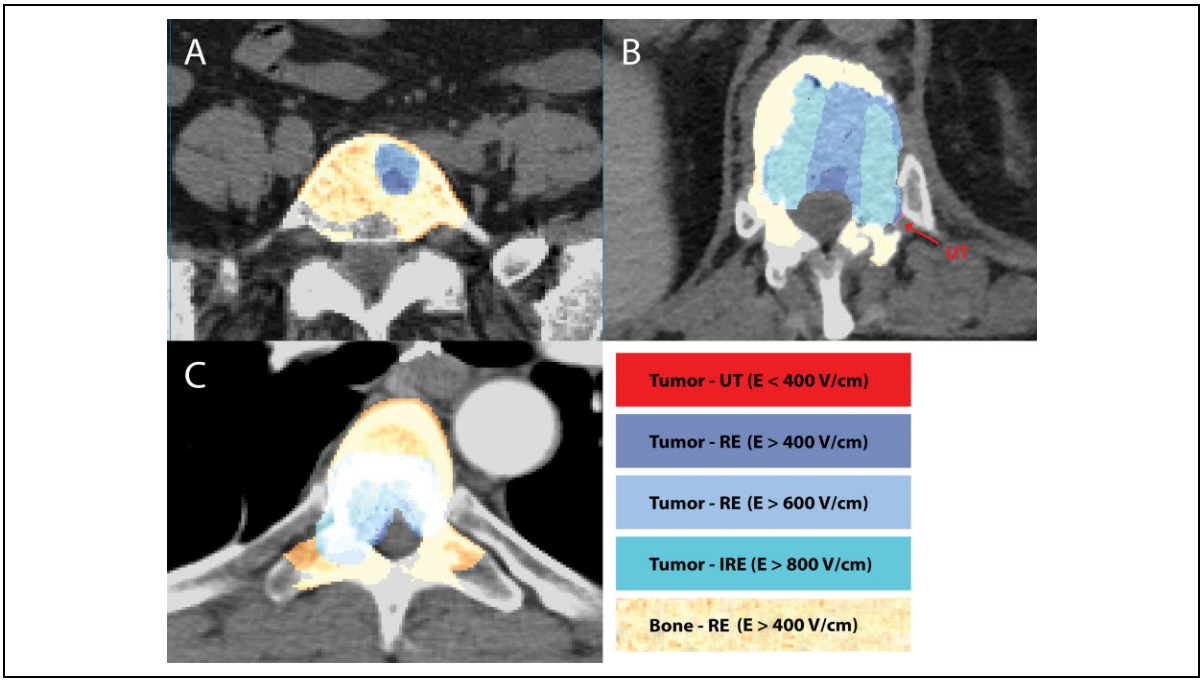

Figure 6. Visualization of numerically calculated electric field distribution overlaid onto the corresponding CT images of (A) fifth lumbar vertebra, (B) 11th thoracic vertebra, and (C) sixth thoracic vertebra. The colored areas represent tumor and bone tissue covered in electric field above the reversible electroporation threshold. The arrow indicates some of the untreated tumor tissue in the 11th thoracic vertebra. CT indicates computed tomography; IRE, irreversible electroporation; REP, reversible electroporation; UT, untreated tissue.

Table 6. Calculated Treatment Outcomes and Other Significant Parameters.

Patient Case	Total Tumor Coverage (%)	Tumor Coverage Above Irreversible Threshold (%)	Volume of Spinal Cord Tissue Above Reversible Threshold (cm^3)	Volume of Spinal Cord Tissue Above Irreversible Threshold (cm^3)	Maximum Electric Field in Spinal Cord Tissue (V/cm)
Case 1: fifth lumbar vertebra[a]	99.68	34.01	0	0	140
Case 2: 11th thoracic vertebra	98.88	44.93	1.228	0.0002	821
Case 3: sixth thoracic vertebra	99.42	63.26	1.191	0.0124	953

[a]The case presented by Gasbarrini *et al*.[18]

predicted 100% tumor electroporation already after the third applied pulse sequence. On the first glance, this result might contradict the actual outcome of the treatment, where a positive positron emission tomography/computed tomography (PET/CT) scan was found at 6-month follow-up which indicated a possible recurrence. However, it has been demonstrated in previous studies that electroporation does not prevent new bone synthesis.[16,19] Moreover, osteogenesis was observed also after irreversible electroporation of the bone.[19] It is thus possible since bone regeneration is associated with increased cell metabolism, that in the Gasbarrini *et al* case, new bone formation was shown in the PET/CT scans rather than cancer recurrence. But since electrochemotherapy treatment of bone metastases is not yet in clinical practice, preventive measures needed to be taken.

When treating spinal metastases, the potential damage to spinal cord and nerves needs to be considered, especially because both structures are commonly located within the margin of the tumor. Our study showed no electroporation of spinal cord tissue when tumor was located in the anterior part of vertebral body. Both cases in the thoracic vertebra, where the tumor was located also in the posterior part of vertebral body and the pedicles, indicated however some electroporation of spinal cord tissue and possibly some irreversible

electroporation. In both cases, approximately 1 cm^3 of spinal cord tissue was covered with electric field above the assumed threshold for reversible electroporation. It has been demonstrated in a study of single-cell electroporation of neurons that electric properties of recovered cells were indistinguishable from nonelectroporated cells.[48] These findings are also in agreement with the preclinical studies[17,27] and the clinical outcome of the Gasbarrini *et al* case[18] where no long-term adverse effects associated with reversible electroporation were reported. The numerical reconstruction of the clinical case predicted that some of the spinal cord tissue was subjected to electric field high enough to cause reversible and even irreversible electroporation, nevertheless no neural symptoms were observed in the patient. Study of the case in the 11th thoracic vertebra showed that less than 1 mm^3 of spinal cord tissue was exposed to electric field above irreversible threshold. Given the conservative threshold values used in our study, it is probably safe to presume that no neural damage occurred in this case. On the other hand, the case in the sixth thoracic vertebra showed that approximately 12 mm^3 of spinal cord tissue was covered with electric field above the assumed irreversible threshold. These findings could indicate possible neural damage. However, the thresholds used in our numerical study were purposefully conservative in order to prevent overly optimistic outcomes since the effect of reversible and irreversible electroporation of spinal cord tissue has not yet been thoroughly investigated. Recent preclinical studies have shown that the actual threshold for irreversible electroporation of spinal cord and nerve tissue is much higher (at least 1000 V/cm) than the threshold used in our study (800 V/cm), and there is also possible evidence of neural regeneration even after irreversible electroporation.[45,46] Also, a recent study of a direct irreversible electroporation ablation of the spinal canal in pigs[49] showed that irreversible electroporation can be performed directly adjacent to the spinal cord with minimal adverse effects, possibly due to the structure of the spinal canal. The epidural fat surrounding the spinal cord namely acts as a protective layer also in electrical sense. Due to the low electrical conductivity of adipose tissue, the major voltage drop and consequently electric field strength occur in epidural space not in the spinal cord.

Based on our study, we can conclude that with a careful selection of patients, the proposed method to treat spinal metastases with the insertion of electrodes through the pedicles is a feasible approach that should be further investigated. If the majority of tumor volume is contained within vertebral body, the method is minimally invasive and poses minimal risk for neural damage. If the tumor has grown outside of the vertebral body and somewhat into the pedicle area, a successful treatment is still possible but more extensive planning is needed with special attention given to possible involvement of spinal cord and nerves. There is evidence, however, that if the tumor has grown too much into the region of the vertebral arch, we might not be able to cover these regions of tumor volume with sufficiently high electric field without risking damage to the spinal cord tissue. When using needle electrodes, electric field strength drops rapidly with distance from the electrode surface.[14] In case of transpedicular access, the distance between the electrodes usually increases as we approach insertion point; therefore, it is ever harder to produce electric field high enough to electroporate the tumor volume positioned in the area of vertebral arch. Ever higher voltage amplitudes are needed, which are limited by currently available devices. Another limitation of the approach is our ability to completely surround the tumor with electrodes inserted through the pedicles. The pedicles are mechanically the strongest part of a vertebra but are also the narrowest, and since the electrodes must not penetrate the vertebral wall, we are very limited in terms of positions and angles of the electrodes. Another drawback of electrochemotherapy in bone tissue in general is a difficult follow-up of the treated lesion with standard imaging techniques. Considering that the tumor volume will decrease over time, a close monitoring with MR imaging, CT, or PET/CT becomes necessary to evaluate tumor shrinking.

However, due to many advantages, electrochemotherapy with transpedicular approach could prove to be a successful minimally invasive alternative to other already established treatments of spinal metastases. For example, in the case presented by Gasbarrini *et al*, temporal dislodging of the cauda on the right side after a partial hemilaminectomy was necessary in order to achieve correct electrode positions. In case of transpedicular approach, all 4 electrodes could be inserted through the pedicles and not directly into vertebral body; therefore, laminectomy would not be necessary, thus keeping the treatment minimally invasive. Furthermore, in contrast to other treatment modalities, such as radiotherapy and thermal ablation, electroporation does not cause tissue necrosis and does not compromise bone stability. Neural structures, eventually included in the treatment area, are also far less susceptible to damage caused by electroporation than, for example, to thermal damage. Electrochemotherapy could therefore potentially also be used for the treatment of patients not amenable to other treatments or not responding to standard therapies. The use of electrodes with shorter conductive parts enable targeting tumor tissue more precisely, resulting in minimal damage to the surrounding tissue, and reducing maximum delivered electric currents therefore reducing negative side effects of the treatment. Finally, the transpedicular approach combines electrochemotherapy, which has already proved to be successful in treating other malignancies as well as bone metastases, with insertion of electrodes through the pedicles, which is a similar technique to already established orthopedic procedures. Insertion of fixation screws is the most frequent technique in vertebral fixation surgery.[50] The technology developed for automated screw insertion trajectory planning and intraoperative guidance could thus, with some adaptation, also be used for electrode insertion for electrochemotherapy purpose.[50-52]

Further studies on electrical properties of tissues and effects of reversible and irreversible electroporation on vital anatomical structures are needed to fully understand the limitations and risks of electrochemotherapy to metastases in the vertebrae. However, the results of this numerical feasibility study provide the basis and evidence that should encourage further analysis

and experiments, either additional numerical computations on more samples or experimental studies on animal models. We have shown that electrochemotherapy with transpedicular approach could prove to be a safe and minimally invasive treatment of spinal metastases.

Authors' Note

This study was conducted within the scope of the European Associated Laboratory on the Electroporation in Biology and Medicine (LEA-EBAM).

Declaration of Conflicting Interests

The author(s) declared the following potential conflicts of interest with respect to the research, authorship, and/or publication of this article. Damijan Miklavčič holds patents on electrochemotherapy that have been licensed to IGEA S.p.a (Carpi, Italy) and is also consultant to various companies with interest in electroporation-based technologies and treatments. Matteo Cadossi is Vice President of IGEA S.p.A. (Carpi, Italy) and holds 10% of the shares of the Company.

Funding

The author(s) disclosed receipt of the following financial support for the research, authorship, and/or publication of this article: This study was supported by the Slovenian Research Agency (ARRS) [grant numbers P2-0249, Z3-7126].

ORCID iD

Bor Kos, PhD http://orcid.org/0000-0001-6219-7046

References

1. Biermann JS, Holt GE, Lewis VO, Schwartz HS, Yaszemski MJ. Metastatic bone disease: diagnosis, evaluation, and treatment. *J Bone Joint Surg Am*. 2009;91(6):1518-1530.
2. Choi D, Crockard A, Bunger C, et al. Review of metastatic spine tumour classification and indications for surgery: the consensus statement of the Global Spine Tumour Study Group. *Eur Spine J*. 2010;19(2):215-222. doi:10.1007/s00586-009-1252-x.
3. Weilbaecher KN, Guise TA, McCauley LK. Cancer to bone: a fatal attraction. *Nat Rev Cancer*. 2011;11(6):411-425. doi:10.1038/nrc3055.
4. Ecker RD, Endo T, Wetjen NM, Krauss WE. Diagnosis and treatment of vertebral column metastases. *Mayo Clin Proc*. 2005;80(9):1177-1186. doi:10.4065/80.9.1177.
5. Sundaresan N, Rothman A, Manhart K, Kelliher K. Surgery for solitary metastases of the spine: rationale and results of treatment. *Spine*. 2002;27(16):1802-1806.
6. Rems L, Miklavčič D. Tutorial: electroporation of cells in complex materials and tissue. *J Appl Phys*. 2016;119(20):201101. doi:10.1063/1.4949264.
7. Yarmush ML, Golberg A, Serša G, Kotnik T, Miklavčič D. Electroporation-based technologies for medicine: principles, applications, and challenges. *Annu Rev Biomed Eng*. 2014;16:295-320. doi:10.1146/annurev-bioeng-071813-104622.
8. Kotnik T, Frey W, Sack M, Haberl Meglič S, Peterka M, Miklavčič D. Electroporation-based applications in biotechnology. *Trends Biotechnol*. 2015;33(8):480-488. doi:10.1016/j.tibtech.2015.06.002.
9. Mahnič-Kalamiza S, Vorobiev E, Miklavčič D. Electroporation in food processing and biorefinery. *J Membr Biol*. 2014;247(12):1279-1304. doi:10.1007/s00232-014-9737-x.
10. Golberg A, Sack M, Teissie J, et al. Energy-efficient biomass processing with pulsed electric fields for bioeconomy and sustainable development. *Biotechnol Biofuels*. 2016;9(1):94.
11. Miklavčič D, Mali B, Kos B, Heller R, Serša G. Electrochemotherapy: from the drawing board into medical practice. *Biomed Eng Online*. 2014;13(1):29. doi:10.1186/1475-925X-13-29.
12. Sersa G, Cemazar M, Miklavcic D. Antitumor effectiveness of electrochemotherapy with cis-diamminedichloroplatinum(II) in mice. *Cancer Res*. 1995;55(15):3450-3455.
13. Orlowski S, Belehradek J, Paoletti C, Mir LM. Transient electropermeabilization of cells in culture: increase of the cytotoxicity of anticancer drugs. *Biochem Pharmacol*. 1988;37(24):4727-4733. doi:10.1016/0006-2952(88)90344-9.
14. Miklavčič D, Čorović S, Pucihar G, Pavšelj N. Importance of tumour coverage by sufficiently high local electric field for effective electrochemotherapy. *Eur J Cancer Suppl*. 2006;4(11):45-51. doi:10.1016/j.ejcsup.2006.08.006.
15. Bianchi G, Campanacci L, Ronchetti M, Donati D. Electrochemotherapy in the treatment of bone metastases: a phase II trial. *World J Surg*. 2016;40(12):3088-3094. doi:10.1007/s00268-016-3627-6.
16. Fini M, Salamanna F, Parrilli A, et al. Electrochemotherapy is effective in the treatment of rat bone metastases. *Clin Exp Metastasis*. 2013;30(8):1033-1045. doi:10.1007/s10585-013-9601-x.
17. Tschon M, Salamanna F, Ronchetti M, et al. Feasibility of electroporation in bone and in the surrounding clinically relevant structures: a preclinical investigation. *Technol Cancer Res Treat*. 2016;15(6):737-748. doi:10.1177/1533034615604454.
18. Gasbarrini A, Campos WK, Campanacci L, Boriani S. Electrochemotherapy to metastatic spinal melanoma: a novel treatment of spinal metastasis? *Spine*. 2015;40(24): E1340-1346. doi:10.1097/BRS.0000000000001125.
19. Fini M, Tschon M, Ronchetti M, et al. Ablation of bone cells by electroporation. *J Bone Joint Surg Br*. 2010;92(11):1614-1620. doi:10.1302/0301-620X.92B11.24664.
20. Song Y, Zheng J, Yan M, et al. The effect of irreversible electroporation on the femur: experimental study in a rabbit model. *Sci Rep*. 2015;5:18187. doi:10.1038/srep18187.
21. Fedorov A, Beichel R, Kalpathy-Cramer J, et al. 3D Slicer as an image computing platform for the quantitative imaging network. *Magnetic Resonance Imaging*. 2012;30(9):1323-1341.
22. Kos B, Županič A, Kotnik T, Snoj M, Serša G, Miklavčič D. Robustness of treatment planning for electrochemotherapy of deep-seated tumors. *J Membr Biol*. 2010;236(1):147-153. doi:10.1007/s00232-010-9274-1.
23. Gabriel C, Peyman A, Grant EH. Electrical conductivity of tissue at frequencies below 1 MHz. *Phys Med Biol*. 2009;54(16):4863. doi:10.1088/0031-9155/54/16/002.
24. Gabriel C, Gabriel S, Corthout E. The dielectric properties of biological tissues: I. Literature survey. *Phys Med Biol*. 1996;41(11):2231-2249.
25. Pavšelj N, Bregar Z, Cukjati D, Batiuskaite D, Mir LM, Miklavčič D. The course of tissue permeabilization studied on a

mathematical model of a subcutaneous tumor in small animals. *IEEE Trans Biomed Eng*. 2005;52(8):1373-1381. doi:10.1109/TBME.2005.851524.

26. Cukjati D, Batiuskaite D, André F, Miklavcic D, Mir LM. Real time electroporation control for accurate and safe in vivo non-viral gene therapy. *Bioelectrochemistry Amst Neth*. 2007;70(2):501-507. doi:10.1016/j.bioelechem.2006.11.001.
27. Tam AL, Abdelsalam ME, Gagea M, et al. Irreversible electroporation of the lumbar vertebrae in a porcine model: is there clinical-pathologic evidence of neural toxicity? *Radiology*. 2014;272(3):709-719. doi:10.1148/radiol.14132560.
28. IT'IS Foundation. Low frequency (conductivity). https://www.itis.ethz.ch/virtual-population/tissue-properties/database/low-frequency-conductivity/. Accessed August 19, 2017.
29. Barger-Lux MJ, Recker RR. Bone microstructure in osteoporosis: transilial biopsy and histomorphometry. *Top Magn Reson Imaging*. 2002;13(5):297-305.
30. Williams PA, Saha S. The electrical and dielectric properties of human bone tissue and their relationship with density and bone mineral content. *Ann Biomed Eng*. 1996;24(2):222-233.
31. Šemrov D, Miklavčič D. Calculation of the electrical parameters in electrochemotherapy of solid tumours in mice. *Comput Biol Med*. 1998;28(4):439-448.
32. Šel D, Maček Lebar A, Miklavčič D. Feasibility of employing model-based optimization of pulse amplitude and electrode distance for effective tumor electropermeabilization. *IEEE Trans Biomed Eng*. 2007;54(5):773-781. doi:10.1109/TBME.2006.889196.
33. Kranjc M, Markelc B, Bajd F, et al. In situ monitoring of electric field distribution in mouse tumor during electroporation. *Radiology*. 2015;274(1):115-123. doi:10.1148/radiol.14140311.
34. Marčan M, Pavliha D, Kos B, Forjanič T, Miklavčič D. Web-based tool for visualization of electric field distribution in deep-seated body structures and planning of electroporation-based treatments. *Biomed Eng Online*. 2015;14(suppl 3):S4. doi:10.1186/1475-925X-14-S3-S4.
35. Miklavčič D, Snoj M, Županič A, et al. Towards treatment planning and treatment of deep-seated solid tumors by electrochemotherapy. *Biomed Eng Online*. 2010;9:10. doi:10.1186/1475-925X-9-10.
36. Županič A, Kos B, Miklavčič D. Treatment planning of electroporation-based medical interventions: electrochemotherapy, gene electrotransfer and irreversible electroporation. *Phys Med Biol*. 2012;57(17):5425-5440. doi:10.1088/0031-9155/57/17/5425.
37. Pirc E, Reberšek M, Miklavčič D. Dosimetry in electroporation-based technologies and treatments. In: *Dosimetry in Bioelectromagnetics*. 1st ed. Boca Raton: CRC Press; 2017:233-268.
38. Bertacchini C, Margotti PM, Bergamini E, Lodi A, Ronchetti M, Cadossi R. Design of an irreversible electroporation system for clinical use. *Technol Cancer Res Treat*. 2007;6(4):313-320. doi:10.1177/153303460700600408.
39. Šel D, Cukjati D, Batiuskaite D, Slivnik T, Mir LM, Miklavčič D. Sequential finite element model of tissue electropermeabilization. *IEEE Trans Biomed Eng*. 2005;52(5):816-827. doi:10.1109/TBME.2005.845212.
40. Županič A, Čorović S, Miklavčič D. Optimization of electrode position and electric pulse amplitude in electrochemotherapy. *Radiol Oncol*. 2008;42(2):93-101.
41. Kranjc M, Kranjc S, Bajd F, Serša G, Serša I, Miklavčič D. Predicting irreversible electroporation-induced tissue damage by means of magnetic resonance electrical impedance tomography. *Sci Rep*. 2017;7(1):10323. doi:10.1038/s41598-017-10846-5.
42. Garcia PA, Kos B, Rossmeisl JH, Pavliha D, Miklavčič D, Davalos RV. Predictive therapeutic planning for irreversible electroporation treatment of spontaneous malignant glioma. *Med Phys*. 2017;44(9):4968-4980. doi:10.1002/mp.12401.
43. Kranjc M, Markelc B, Bajd F, et al. In situ monitoring of electric field distribution in mouse tumor during electroporation. *Radiology*. 2015;274(1):115-123. doi:10.1148/radiol.14140311.
44. Miklavčič D, Šemrov D, Mekid H, Mir LM. A validated model of in vivo electric field distribution in tissues for electrochemotherapy and for DNA electrotransfer for gene therapy. *Biochim Biophys Acta*. 2000;1523(1):73-83.
45. Schoellnast H, Monette S, Ezell PC, et al. Acute and subacute effects of irreversible electroporation on nerves: experimental study in a pig model. *Radiology*. 2011;260(2):421-427. doi:10.1148/radiol.11103505.
46. Schoellnast H, Monette S, Ezell PC, et al. The delayed effects of irreversible electroporation ablation on nerves. *Eur Radiol*. 2013;23(2):375-380. doi:10.1007/s00330-012-2610-3.
47. Qin Z, Jiang J, Long G, Lindgren B, Bischof JC. Irreversible electroporation: an in vivo study with dorsal skin fold chamber. *Ann Biomed Eng*. 2013;41(3):619-629. doi:10.1007/s10439-012-0686 -1.
48. Nevian T, Helmchen F. Calcium indicator loading of neurons using single-cell electroporation. *Pflugers Arch*. 2007;454(4):675-688. doi:10.1007/s00424-007-0234-2.
49. Tam AL, Figueira TA, Gagea M, et al. Irreversible electroporation in the epidural space of the porcine spine: effects on adjacent structures. *Radiology*. 2016;281(3):763-771. doi:10.1148/radiol.2016152688.
50. Knez D, Mohar J, Cirman RJ, Likar B, Pernuš F, Vrtovec T. Determination of the pedicle screw size and trajectory in CT images of thoracic spinal deformities: a comparison between manual and computer-assisted preoperative planning. *Slov Med J*. 2017;85(11-12). http://vestnik.szd.si/index.php/ZdravVest/article/view/1747. Accessed July 18, 2017.
51. Tian N-F, Huang Q-S, Zhou P, et al. Pedicle screw insertion accuracy with different assisted methods: a systematic review and meta-analysis of comparative studies. *Eur Spine J*. 2011;20(6):846-859. doi:10.1007/s00586-010-1577-5.
52. Koktekir E, Ceylan D, Tatarli N, Karabagli H, Recber F, Akdemir G. Accuracy of fluoroscopically-assisted pedicle screw placement: analysis of 1,218 screws in 198 patients. *Spine J*. 2014;14(8):1702-1708. doi:10.1016/j.spinee.2014.03.044.

2.6 Paper 6

Title: **Optimization of transpedicular electrode insertion for electroporation-based treatments of vertebral tumors**

Authors: Helena Cindrič, Damijan Miklavčič, Francois H. Cornelis and Bor Kos

Publication: *Cancers*, vol. 14, iss. 21, pp. 1-16, November 2022

Impact factor: 6.575 (2021)

Quartile: Q1

Rank: 60/246 (Oncology)

DOI: https://doi.org/10.3390/cancers14215412

cancers

MDPI

Article

Optimization of Transpedicular Electrode Insertion for Electroporation-Based Treatments of Vertebral Tumors

Helena Cindrič [1], Damijan Miklavčič [1], Francois H. Cornelis [2] and Bor Kos [1,*]

[1] Faculty of Electrical Engineering, University of Ljubljana, 1000 Ljubljana, Slovenia
[2] Memorial Sloan-Kettering Cancer Center, New York, NY 10065, USA
* Correspondence: bor.kos@fe.uni-lj.si

Simple Summary: Electroporation has sparked great interest regarding its use in medicine. When planning electroporation-based treatments, the main goal is to determine the best possible electrode position and voltage amplitude that will ensure treatment of the entire target tissue's volume. However, this process is still mainly performed manually or using computationally intensive genetic algorithms. This study presents an algorithm for optimizing electrode positions based on spatial information of the electric field distribution in the target tissue. The algorithm is currently designed for the electrochemotherapy of vertebral tumors via a transpedicular approach but could be adapted to other anatomic sites in the future. The algorithm performs successfully for different spinal segments, tumor sizes, and locations within the vertebra. Application of the algorithm significantly reduces the time and expertise required to create a treatment plan for the electrochemotherapy of vertebral tumors.

Abstract: Electroporation-based treatments such as electrochemotherapy and irreversible electroporation ablation have sparked interest with respect to their use in medicine. Treatment planning involves determining the best possible electrode positions and voltage amplitudes to ensure treatment of the entire clinical target volume (CTV). This process is mainly performed manually or with computationally intensive genetic algorithms. In this study, an algorithm was developed to optimize electrode positions for the electrochemotherapy of vertebral tumors without using computationally intensive methods. The algorithm considers the electric field distribution in the CTV, identifies undertreated areas, and uses this information to iteratively shift the electrodes from their initial positions to cover the entire CTV. The algorithm performs successfully for different spinal segments, tumor sizes, and positions within the vertebra. The average optimization time was 71 s with an average of 4.9 iterations performed. The algorithm significantly reduces the time and expertise required to create a treatment plan for vertebral tumors. This study serves as a proof of concept that electrode positions can be determined (semi-)automatically based on the spatial information of the electric field distribution in the target tissue. The algorithm is currently designed for the electrochemotherapy of vertebral tumors via a transpedicular approach but could be adapted for other anatomic sites in the future.

Keywords: treatment planning; numerical modeling; bone tumors; tumor treatment; minimally invasive treatment

Citation: Cindrič, H.; Miklavčič, D.; Cornelis, F.H.; Kos, B. Optimization of Transpedicular Electrode Insertion for Electroporation-Based Treatments of Vertebral Tumors. *Cancers* **2022**, *14*, 5412. https://doi.org/10.3390/cancers14215412

Academic Editor: Ahmed Hassanein

Received: 5 October 2022
Accepted: 31 October 2022
Published: 2 November 2022

Publisher's Note: MDPI stays neutral with regard to jurisdictional claims in published maps and institutional affiliations.

1. Introduction

Electroporation is a phenomenon in which short high voltage electric pulses are used to change the structural integrity of the cell membrane and consequently increase the membrane permeability. Depending on the pulse parameters, the phenomenon can be either reversible, meaning that the cells remain unchanged in the long term, or irreversi-

ble, meaning that the cells cannot recover from the changes in the membrane and eventually die [1–4]. Both reversible and irreversible electroporation have sparked great interest regarding their use in medicine. Reversible electroporation can be used in combination with chemotherapeutic agents, a treatment known as electrochemotherapy (ECT) [5–8], or with genetic material, a treatment known as gene electrotransfer (GET) [9,10]. Irreversible electroporation (IRE) has emerged as a promising alternative to thermal methods for the ablation of tumors and soft tissues [11–17]. It is generally accepted that electroporation occurs in tissues at a specific electric field strength, i.e., the electroporation threshold. A complete coverage of the target tissue volume with an electric field above a certain value is required to achieve a therapeutic effect in all electroporation-based treatments [18,19].

When planning electroporation-based treatments, the main goal is to determine the best possible electrode position and applied voltage amplitude that will ensure the electroporation of the clinical target volume (CTV) and cause minimal damage to the surrounding healthy tissue [19–21]. The most common method for predicting the outcome of an electroporation-based treatment is to apply a tissue-specific threshold to the computed electric field distribution and determine the coverage of the CTV, i.e., to calculate the fraction of the target volume covered by an electric field strength of at least the (tissue-specific) threshold value [19,22–24]. However, by calculating the fraction of the CTV above the threshold, the computation results are reduced to a single numerical value, and the spatial information about the distribution and local strength of the electric field that the calculation provides is lost.

The determination of the optimal electrode positions is still mainly performed by hand. Most attempts to optimize electrode positions and voltages are based on either genetic algorithms (GA) or parametric sweeps [25–27], which are time-consuming and require significant computational power. Moreover, the criteria used for optimization are mainly the fraction of CTV coverage and the total volume of damaged healthy tissue, thus failing to exploit the valuable spatial information provided by the computation.

In this study, we present an algorithm for the optimization of electrode positions for the electrochemotherapy of vertebral tumors without using computationally intensive genetic algorithms. The developed algorithm considers the electric field distribution in the target tissue, identifies the regions not covered by a sufficiently high electric field (i.e., undertreated regions) in the CTV, and uses this information to iteratively move the electrodes from their initial positions to their final positions to cover the whole CTV. The applied voltage is also adjusted by the optimization process. Technological constraints such as ensuring the appropriate electrode spacing and accounting for the limitations (e.g., maximum current and voltage) of commercially available pulse generators are also considered by the algorithm.

The algorithm is developed for the treatment of vertebral tumors using two needle electrodes inserted through the pedicles into the vertebral body. The concept is based on our previous studies on the electrochemotherapy of spinal metastases using a transpedicular approach [28,29]. However, the algorithm is designed according to the modular principle and can be adapted to other anatomic sites in the future by adding new "modules" and reusing some of the existing ones. The algorithm's source code and all models of the vertebral tumors created in this study are available in an open database at https://doi.org/10.6084/m9.figshare.21270111.v1 (accessed on 5 October 2022).

2. Materials and Methods

2.1. Dataset Preparation

To construct anatomical models of vertebrae, six lumbar and six thoracic vertebrae (of the lower thoracic region T8–T12) were segmented from medical images of three patients using Slicer 3D [30] and Mimics 24.0 (Materialise NV, Leuven, Belgium). First, a threshold was applied to the medical image to obtain a rough mask of the bone, which was then sliced into individual vertebral masks, smoothed, and manually corrected. The

individual vertebral masks were saved as surface meshes and further smoothed and uniformly re-meshed using the 3-matric 16.0 (Materialise NV, Leuven, Belgium).

Each completed vertebral mesh was imported into COMSOL Multiphysics (COMSOL Inc., Stockholm, Sweden), where a model of a spherical tumor was inserted at one of the three different locations in the vertebral body: central position (Figure 1a), anterior-lateral position (Figure 1b), and posterior-inferior position (Figure 1c). Each tumor was modelled with three different radii: 5 mm, 7.5 mm, and 10 mm. Therefore, 9 different tumor models were created for each of the 12 vertebrae, resulting in a total of 108 models, which served as the dataset for the computation. A block was built around each vertebral model representing the surrounding healthy tissue. Two needle electrodes were added to each model, modelled in COMSOL as cylinders with a fixed radius of 0.6 mm and exposure length of 20 mm.

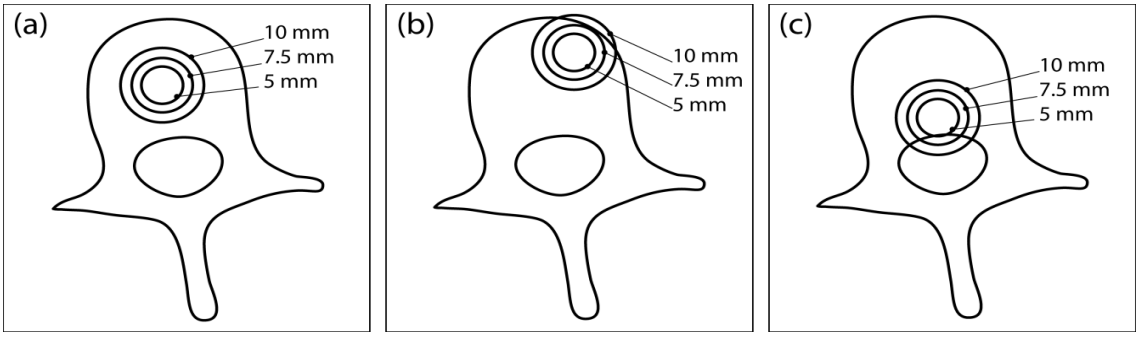

Figure 1. Three different tumor locations within the vertebral body: (**a**) central location, (**b**) anterior-lateral location, and (**c**) posterior-inferior location. At each location, the tumor is modelled with three different radii: 5 mm, 7.5 mm, and 10 mm. This illustration was created from an axial CT section of an L3 vertebra and does not show the actual geometry of the numerical model used for computation.

A mesh convergence study was performed in COMSOL to ensure that the discretization error was minimal. A physics-controlled mesh was used, and the element size varied from "extremely fine" to "normal." The volume of tissue exceeding 400 V/cm, CTV coverage, and computation time were evaluated at each mesh size and compared to the extremely fine mesh. Using the "fine" mesh size resulted in no change in CTV coverage, a 1% change in total electroporated tissue volume, and a 96% decrease in computational cost, so it was selected as the final mesh size.

The block of healthy tissue also served as the boundary of the computational domain, and convergence with respect to the size of the boundary block was assessed. The size of the boundary block was gradually decreased in 5 mm increments in every spatial direction, until the relative change in the electroporated tissue volume surpassed 1% between two successive boundary block sizes. The CTV coverage remained unaffected at all tested sizes. The final size of the boundary block was 130 × 120 × 75 mm, which was the same in all models.

2.2. Computational Approach

COMSOL Multiphysics, a finite element analysis software, was used for the computations of electric field distribution in the models. MATLAB (MathWorks, Natick, MA, USA) via LiveLink was used to control the model's setup and solution. The electrode positions and orientations are determined by the algorithm in each iteration, and the electrode parameters in COMSOL geometry are corrected accordingly. The applied voltage is also determined by the algorithm and corrected accordingly in the model. The electric field distribution is computed independently in each iteration with new electrode positions.

The electric field distribution E in the target tissue is computed indirectly by solving the partial differential equation for electric potential V (Equation (1)) for stationary conditions, governed by the equation:

$$\nabla \cdot \left(\sigma(-\nabla V)\right) = 0, \quad (1)$$

where σ is the tissue conductivity, and V is the electric potential. The external domain boundaries are set as electrically insulating. The increase in tissue conductivity due to local electric field (Equation (2)) is modelled with a smoothed Heaviside function (with continuous second derivative), which is defined for each tissue separately. Thus, the conductivity in eq. 1 becomes a function of the local electric field:

$$\sigma \to \sigma(|E|). \quad (2)$$

The parameters of the smoothed Heaviside function for each modelled tissue are listed in Table 1. A detailed description of the computational approach can be found in previous studies [28,31].

Table 1. Electrical properties of modelled tissues and electrodes are taken from [28]. The surrounding tissue was assigned the properties of adipose tissue.

Tissue Property	Bone	Tumor	Surrounding Tissue	Electrodes
Initial electrical conductivity [S/m]	0.07	0.30	0.02	10^6
Factor of electrical conductivity increase	2.9	2.8	3.0	-
Center of transition zone [V/cm]	600	600	300	-
Size of transition zone [V/cm]	400	400	400	-

2.3. Algorithm Structure

The algorithm was developed entirely in MATLAB, but the computations are performed in COMSOL and connected to MATLAB via LiveLink (see Section 2.2 Computational Approach). From the entire model dataset, 12 models were randomly selected, involving 4 samples of tumors in each radius studied. This group of models was used as the "training set" for the development of the algorithm.

The algorithm was developed through computational experimentation with the training set; a series of evaluations was performed and analyzed to obtain the best overall performance. The algorithm iteratively changes the positions of two electrodes within the vertebral body. The goal is to achieve complete coverage of the clinical target volume with a sufficiently high electric field in as few iterations as possible. The flowchart of the algorithm's structure is shown in Figure 2, while the algorithm's structure is explained in detail in Sections 2.3.1–2.3.5.

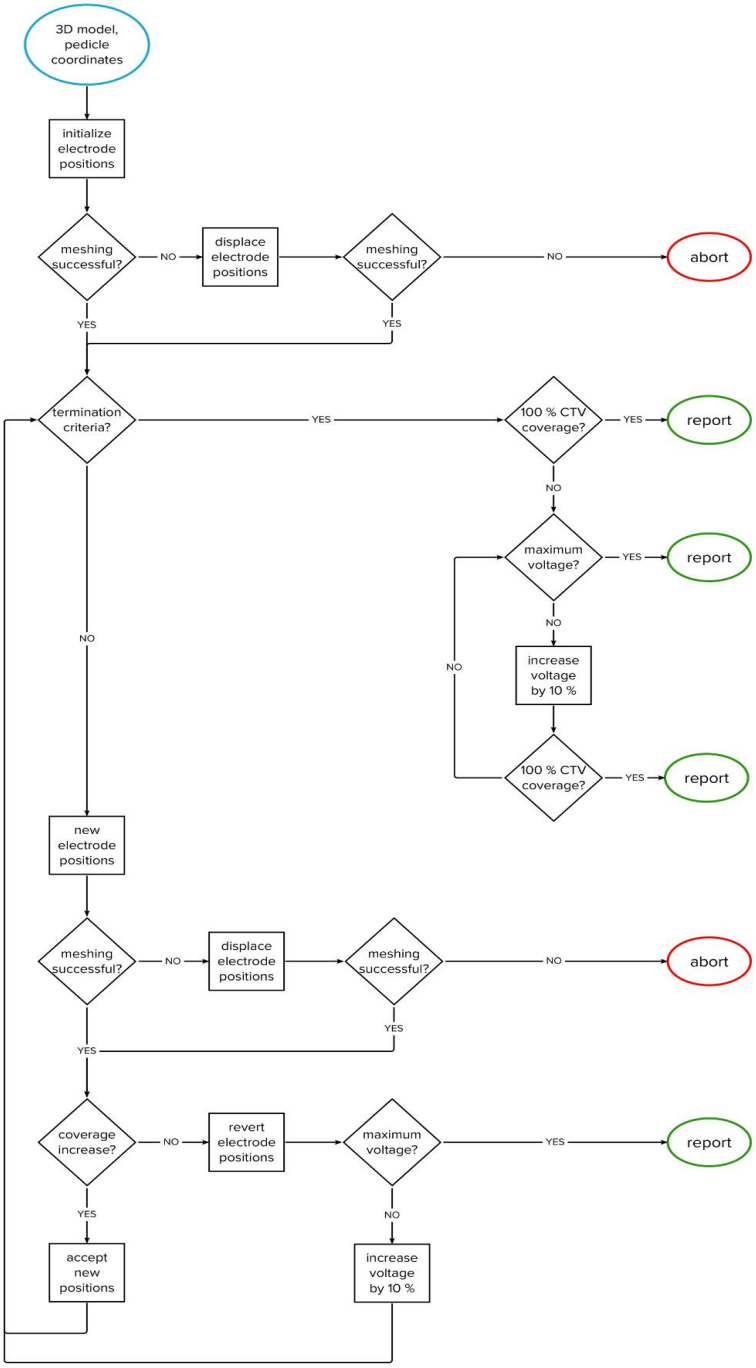

Figure 2. Flowchart of the algorithm.

2.3.1. Clinical Target Volume Coverage

The boundary between gross tumor volume (GTV—i.e., total tumor volume as seen on medical imaging) and healthy tissue is usually not sharp; the presence of tumor cells outside the tumor volume depends on the tumor's type and growth pattern. Therefore, in clinical practice, it is common to treat not only the GTV but also a margin of healthy tissue (5–10 mm), i.e., a safety margin, around the tumor volume to treat possible tumor cells or micrometastases. The tumor, together with the safety margin, forms the so-called clinical target volume (CTV).

For safety reasons, the thresholds for electroporation used in practice are generally quite high, and sometimes it may be difficult to cover the entire CTV for larger tumor radii. However, if the safety margin is taken into account, very few or no cells are expected at the outer edge of the CTV; therefore, the so-called soft coverage of the CTV is introduced in this study, in which the threshold for electroporation at the outer edge of the CTV is not strictly enforced. For this purpose, a weighting map of the CTV was created, where each voxel in the map is assigned a weight based on how far the voxel is from the boundary of the GTV. The GTV has a weight of 1, which means that it must be covered (at least) by the threshold electric field. In the safety margin, the weighting decreases linearly and reaches zero outside the CTV. The weighting map can be easily adapted to the tumor type. For example, in metastatic tumors, a higher weight (e.g., 0.5) can be assigned to the outer edge of the CTV to provide additional safety.

When calculating the center of mass of undertreated areas of the CTV (below the desired threshold), the weighting map is taken into account; therefore, the resulting center of mass is closer to the GTV boundary than to the outer boundary of the CTV. In the current implementation, the safety margin for all tumor radii is set at 5 mm. The margin can be easily adjusted (e.g., 10 mm) for different tumor types. An example of the CTV's weighting map is shown in Figure 3.

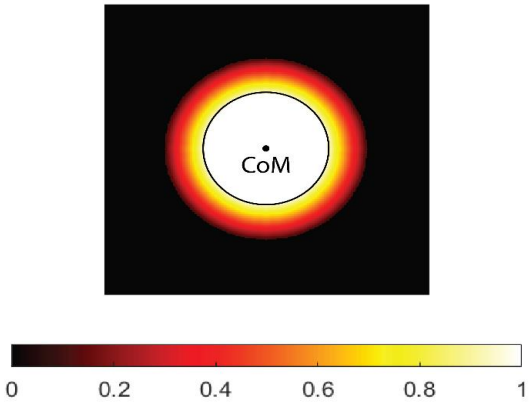

Figure 3. A weighting map of the clinical target volume (CTV). The contour (black) and center of mass (CoM) of the tumor gross volume (GTV, black circle) are shown. The weight uniformly decreases with distance from tumor border and reaches zero on the outer border of the CTV.

2.3.2. Input and Initialization

The operator must identify two points in the CT scan of the vertebra for each pedicle: the entry point, positioned in the narrowest part of the pedicle, and a second point that indicates the pedicle's orientation/direction, as shown on Figure 4a–c. The position of each electrode is determined with the coordinates of the electrode tip and the direction vector

pointing from the electrode tip to the entry point. The operator-selected points determine the starting position of the electrode, with the second point serving as the electrode tip (Figure 4d). Throughout the optimization, the entry point remains fixed to ensure transpedicular insertion, while the electrode tip is iteratively changed by the algorithm. For this reason, the entry point must be chosen with care.

At the beginning of the optimization process, the electrode's geometry is pulled towards the tumor's center of mass (Figure 4e)—as described in Section 2.3.3, Optimization of Electrode Positions—to compute the initial field distribution. This initialization step significantly decreases the solution time, compared to using the starting positions, selected by the operator.

2.3.3. Optimization of Electrode Positions

The algorithm is constructed in a modular form, with different "forces" acting on the electrodes. The final force acting on the electrode, and, therefore, effectively moving the electrode to a new position, is a weighted sum of all acting forces. In the current implementation, three main processes controlling the electrode positions are considered: attractive force toward the tumor's center of mass (CoM), attractive force toward the undertreated areas of the CTV, and the repulsive force between the electrodes, maintaining appropriate inter-electrode distance to prevent short-circuit. In the future, the algorithm can be adapted for other anatomic sites by adding new forces and reusing some of the existing ones.

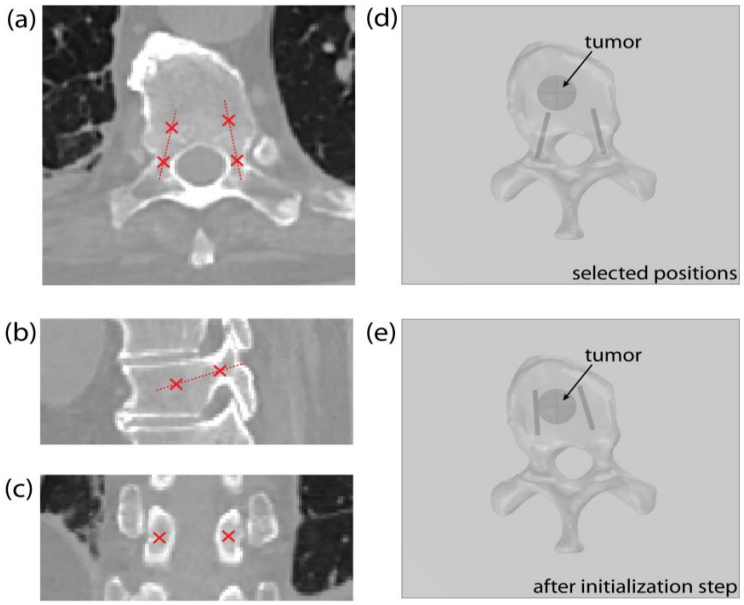

Figure 4. An example of point selection shown on the (**a**) axial, (**b**) sagittal, and (**c**) coronal CT slice of a thoracic vertebra. (**d**) An example of the model's geometry in COMSOL Multiphysics, showing a thoracic vertebra and a spherical tumor, with starting electrode positions, obtained from the selected points. (**e**) Corrected electrode positions after algorithm initialization step.

Attractive Force to Tumor's Center of Mass

By seemingly connecting the point of the first electrode to the rear of the second electrode and vice versa, two lines are obtained. The line segment that is the shortest distance between the lines is calculated; the point in the middle of this line segment is

considered the center of electrode geometry (illustrated on Figure 5a). The force F_{geo} is the vector pointing from the center of the electrode geometry to the CoM of the tumor. The point of application of F_{geo} is at the tip of the electrode.

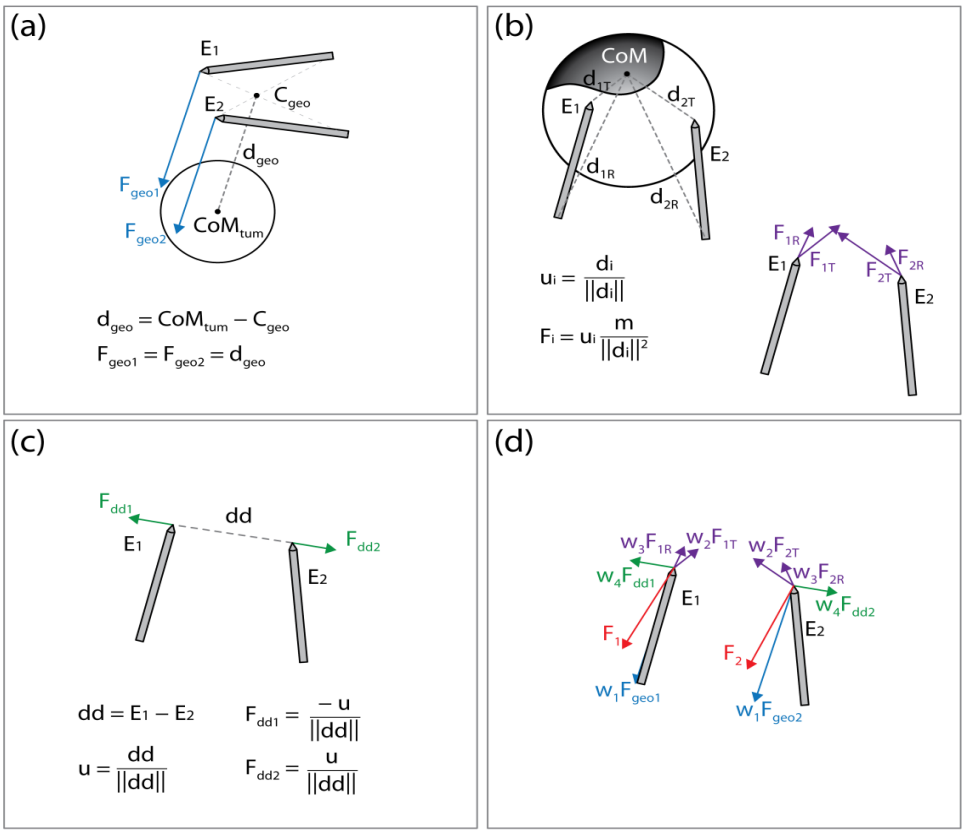

Figure 5. Illustration of the forces acting on the electrodes. (**a**) Attractive force (F_{geo1}, F_{geo2}) toward the tumor's center of mass (CoM_{tum}). (**b**) Attractive force (at the electrode tip, F_{iT}, and rear F_{iR}) toward the undertreated areas of the clinical target volume. (**c**) Repulsive force (F_{dd1}, F_{dd2}) maintaining appropriate distance between electrodes. (**d**) Final forces (F_1 and F_2) acting on the electrodes are a weighted sum of all forces. This figure is for illustration of the concept only; distances, vectors, and sums do not represent actual values.

Attractive Forces to Undertreated Regions of the Clinical Target Volume

The areas of the CTV where the local electric field strength does not reach the threshold for electroporation (400 V/cm) are considered undertreated regions. The undertreated region is often disconnected, resulting in n undertreated "islands" within the CTV. The islands that are less than 10% of the size of the largest island are discarded and the CoM of each remaining island is calculated. Note that while computing the CoM of the island, the weighting map of the CTV is considered as well (see Section 2.3.1. Clinical Target Volume Coverage). The distance from each electrode rear and tip to CoM of each island I (illustrated on Figure 5b) is calculated. The forces acting on the electrode tip ($F_{i,T}$) or rear ($F_{i,R}$) are defined to mimic the gravitation force:

$$F_{i,T} = \frac{m_i}{\|d_{i,T}\|^2} \cdot \frac{d_{i,T}}{\|d_{i,T}\|}, i = 1, \ldots, n \quad (3)$$

$$F_{i,R} = \frac{m_i}{\|d_{i,R}\|^2} \cdot \frac{d_{i,R}}{\|d_{i,R}\|}, i = 1, \ldots, n \quad (4)$$

where m_i is the mass of the i-th island, calculated as the weighted number of voxels in the island; $d_{i,T}$ and $d_{i,R}$ are the vectors from electrode tip (T) or rear (R) to the i-th islands CoM. The application points of forces $F_{i,T}$ and $F_{i,R}$ are at the tips of the electrodes.

Repulsive Force between the Electrodes

To prevent an event where both electrodes would be pulled into the same position, or very close together, the electrodes are forced apart. The repulsive force is proportional to the inverse of distance between the electrode tips:

$$F_{dd} = \frac{1}{\|dd\|} \cdot \frac{dd}{\|dd\|}, \quad (5)$$

where dd is the vector from tip of the electrode 1 toward tip of the electrode 2 (illustrated in Figure 5c). The application point of force F_{dd} is at the tip of electrode 2 and the application point of force $-F_{dd}$ is at the tip of electrode 1.

Sum of Forces

The final forces F_{ele1} and F_{ele2}, acting on the electrodes, and, therefore, effectively moving the electrodes to new positions, are a weighted sum of all acting forces:

$$F_{ele1} = w_1 \cdot F_{geo} + w_2 \cdot \sum_i F_{1\,i,T} + w_3 \cdot \sum_i F_{1\,i,R} + w_4 \cdot (-F_{dd}), \quad (6)$$

$$F_{ele2} = w_1 \cdot F_{geo} + w_2 \cdot \sum_i F_{2\,i,T} + w_3 \cdot \sum_i F_{2\,i,R} + w_4 \cdot F_{dd}. \quad (7)$$

The concept of the forces acting on the electrodes is illustrated in Figure 5. After the new electrode positions are generated, the new voltage amplitude is calculated by multiplying the voltage-to-distance ratio, set to 1000 V/cm, and the distance between the electrode middle points, and rounded to 100 V. The electrode positions are changed in each iteration according to Equations (3)–(7). If the new electrode positions produce a decrease in CTV coverage, the algorithm reverts the positions to positions from the previous iteration and increases the applied voltage amplitude to 10% of the original value. The voltage-to-distance ratio is also increased accordingly and kept at an increased value through the rest of the optimization process.

2.3.4. Termination and Handling of Errors

The optimization is terminated if 100% soft coverage of the CTV is achieved, if the change in CTV coverage between iterations is less than 0.1 percentage point (i.e., tolerance), or if either the maximum number of iterations (50 iterations), maximum allowed voltage (3000 V), or maximum allowed electric current (45 A) are reached.

In case a meshing error occurs after moving the electrodes (usually due to self-intersecting faces), the electrodes are displaced by 0.5 mm in a random direction. If the error persists after correction, the optimization is terminated, and the last computed results are saved.

In case the CTV is not completely covered after the optimization of electrode positions, the final step is to increase the applied voltage in steps of 100 V until either complete coverage of CTV or the maximum allowed voltage (3000 V) is reached.

2.3.5. Algorithm Output

The output of the algorithm provides the final coordinates of the electrode's entry point and the electrode tip, which correspond to the local coordinate system of the medical image used for initialization. The amplitude of the applied voltage and the expected current draw are also provided, as well as the expected coverage of the GTV and CTV with the selected electric field threshold (e.g., 400 V/cm). The total computation time and the number of iterations are also stored. All steps performed by the algorithm are stored in a log text file so that detailed information about the optimization process is available.

2.4. Full Factorial Experiment

The uncertainties in the algorithm stem from the four weights (*w1*, *w2*, *w3*, and *w4*) belonging to the forces in the final sum (Equations (6)–(7)). To understand the effects of the weights on the algorithm's performance, a two-stage (low and high), four-factor, full-factorial experiment was conducted. Each weight was tested at a low and high stages and all combinations of the four weights were tested, resulting in a total of 16 groups, each with 108 replicates (models). The tested levels of parameters are listed in Table 2. The algorithm's performance was measured with respect to computation time, number of iterations, and number of meshing errors. The goal was to achieve full coverage with minimum number of iterations, errors, and the shortest time. The measured data (computation time, number of iterations, and number of errors) in all 16 groups had the same non-normal distribution. Therefore, the Kruskal–Wallis test was used to statistically determine the effects of the weights. The Kruskal–Wallis test is a nonparametric version of the classic one-way ANOVA and uses ranks of the data rather than numerical values to calculate the test statistics.

Table 2. Results of the full factorial experiments for weights w1–w4.

w1	w2	w3	w4	Average Time (s)	Average Iterations (–)	Number of Errors (–)	Average Voltage (V)	Group Score (–)
0.7	0.1	0.02	5	81	5.1	3	2659	14
0.7	0.1	0.02	15	82	4.9	4	2687	11
0.7	0.1	0.14	5	84	5.5	2	2662	18
0.7	0.1	0.14	15	83	5.1	6	2682	20
0.7	0.7	0.02	5	84	5.6	4	2656	27
0.7	0.7	0.02	15	87	5.5	6	2689	28
0.7	0.7	0.14	5	86	5.7	2	2663	29
0.7	0.7	0.14	15	88	5.5	7	2693	34
1.3	0.1	0.02	5	71	4.9	5	2663	8 *
1.3	0.1	0.02	15	79	4.9	6	2694	12
1.3	0.1	0.14	5	72	4.9	8	2664	17
1.3	0.1	0.14	15	78	4.9	6	2693	11
1.3	0.7	0.02	5	83	5.5	8	2665	29
1.3	0.7	0.02	15	88	5.5	7	2690	34
1.3	0.7	0.14	5	85	5.6	7	2662	36
1.3	0.7	0.14	15	87	5.5	9	2693	37

The group with the lowest score (shadowed and indicated with *) has the best overall performance and was selected as the set of final algorithm weights.

3. Results

3.1. Full Factorial Experiment

The results of the full factorial experiment showed no significant effect of the algorithm weights on the performance (p = 0.917); therefore, no further optimization of the weights was performed. The algorithm's performance is determined by three factors: the mean computation time, mean number of iterations, and number of meshing errors. All 16 weight groups were sorted and ranked (from 1–16) according to each performance factor. The three ranks were summed in each group to obtain the groups' total scores, and the group with the lowest score was selected as the set of final algorithm weights. The results of the full factorial experiment along with the group scores are shown in Table 2.

3.2. Algorithm Performance

The performance of the algorithm was evaluated on realistic models of six lumbar (L1–L5) and six thoracic (T8–T12) vertebrae (created from patient images) with a total of 108 synthetic spherical tumors (created for simulation). The average computation time was 71 s (range: 17–253 s); the average and median number of iterations were 4.9 and 4.5, respectively (range: 1–15); and the average applied voltage amplitude was 2663 V (range: 1800–3000 V). The algorithm successfully completed the optimization in 103 models, while a meshing error occurred in five models. In 87/108 models, 100% coverage of CTV and GTV was achieved. In 17/108 models, a CTV coverage of more than 99% and a GTV coverage of 100% were achieved. In four models, the CTV coverage was greater than 94% and the GTV coverage was greater than 98%.

A meshing error occurred in 5/108 models, corresponding to 4.63%. All five errors occurred in the anterior-lateral tumor locations in the thoracic vertebral region with tumor radii of 7.5 mm or 10 mm. In all five models, 100% CTV and GTV coverage was achieved by an additional voltage increase after the last successful iteration. The termination criteria were complete CTV coverage in 70 models, maximum voltage in 22 models, minimum tolerance in 11 models, and meshing error in 5 models.

The dependence of the computation time and the number of iterations on the following variables was evaluated: vertebra type (lumbar/thoracic), tumor location, and tumor radius. Since the distribution of the data (computation time and number of iterations) does not follow a normal distribution, a nonparametric Kruskal–Wallis test was used. According to the test, the only variable with a statistically significant effect is the tumor radius (p < 0.01). This result is to be expected because only two electrodes were used, which makes it more difficult to cover larger tissue volumes. Table 3 shows the average computation time, number of iterations, and applied voltage for each tumor radius group.

Table 3. Tumor radius is the only variable affecting the algorithm's performance. The average computation time, iterations, and applied voltage are shown for each modelled tumor radius.

Tumor Radius (mm)	Average Time (s)	Average Iterations (–)	Average Voltage (V)
5	31	1	2331
7.5	70	5	2667
10	113	9	2992

4. Discussion

This study is one of the first attempts to use spatial information about the electric field distribution in tissues to optimize electrode positioning and pulse amplitude without using computationally intensive genetic algorithms. The algorithm is developed for the treatment of vertebral tumors using two needle electrodes inserted through the pedicles into the vertebral body. The concept is based on our previous studies on the electrochemotherapy of spinal metastases using a transpedicular approach [28,29]. The vertebral column is the most common site for bone metastases, with the incidence reaching up to 70% depending on the primary cancer type [32]. Electroporation offers several advantages over

other treatment options, as it preserves the integrity of bone tissue, enables bone regeneration, and has low neural toxicity [33–36]. Studies have shown that bone metastases can be effectively treated with ECT with significant improvements in patients' pain level and quality of life [29,33,37–39]. The transpedicular approach is a well-established technique used for tumor ablation, cement injection, and for the insertion of fixation screws in spinal fixation surgery [40–42]. Combining ECT with the technology used for transpedicular access could facilitate the introduction of the ECT or IRE ablation of vertebral tumors into clinical practice to further improve tumor control [28,43].

The treatment planning for electroporation-based treatments is still in the early stages of development [22,44,45]. The treatment plans are made prior to the procedure, and the electrode positions and voltage amplitudes are still primarily determined manually (by hand). This process usually requires several iterations where the operator changes the electrode positions between computations. After each iteration, the operator must visually inspect the electric field (usually as an overlay over the medical image), determine the potentially undertreated areas of the CTV, reposition the electrodes accordingly, and repeat the process. This approach requires a high level of expertise in the distribution of the electric field in inhomogeneous tissue and the impact of electrode positioning and pulse parameters [44,46].

When designing the algorithm, we followed the concept of the manual approach; however, the goal was to automate the process so as to require minimal operator input. The algorithm is modular, in a sense, and considers various requirements. For example, an appropriate distance between electrodes needs to be maintained at all times to avoid short circuits; it is also intuitive to move the electrodes toward the center of mass of the tumor or toward large regions of undertreated tissue. Furthermore, the concept of soft coverage is introduced, where we consider an electric field strength below the threshold in the CTV margin to be acceptable. The reason for this decision is that the thresholds currently used in treatment planning are only a very rough estimate. The threshold itself is a difficult property to determine. The determined threshold values are influenced by biological variability (small and large animals and humans), the condition of the tissue sample (in vivo vs. ex vivo), and the measurement method, among other factors. Therefore, there are a range of values in the literature, even for the same tissue type. Whether the tissue is electroporated also depends on the pulse protocol used, i.e., the number of pulses, pulse duration, and repetition rate. In addition, certain parts of the tissue may be cumulatively exposed to more pulses than other parts due to multiple pairs of active electrodes. Studies suggest that electroporation can occur at lower thresholds when the exposure time is increased with more and/or longer pulses [47–50].

The current implementation considered the technical limitations of the Cliniporator Vitae (IGEA S.p.A., Carpi, Italy), a commercially available pulse generator for electrochemotherapy. The allowed voltage amplitudes are 500–3000 V, rounded to 100 V, which correspond to the default step size of the generator, and is commonly used in clinical practice. With pulse generators, it is possible to set the voltage step size manually; therefore, this parameter was also included in the algorithm. However, decreasing the voltage step also increases the number of iterations required to obtain the optimal solution. The current limit is set at 45 A, which is 5 A lower than the pulse generator's limit (50 A). Biological tissue is a very inhomogeneous material, and its actual electrical conductivity can vary significantly from the modelled values. Bones have low electrical conductivity compared to other tissues; therefore, the current is unlikely to reach the limit. However, in tissues with high conductivity, this may become a legitimate concern, and the algorithm's limit should be set to lower values, since high current consumption will immediately terminate the pulse's delivery.

The performance of the algorithm was evaluated on realistic vertebral models of the lower thoracic (T8–T12) and lumbar (L1–L5) segments (created from patient images) with inserted synthetic spherical tumor models of different sizes (created for simulation), re-

sulting in 108 models in total. The results have shown that the algorithm performs successfully for different segments of the spine, different tumor sizes, and different locations within the vertebral body. A meshing error occurred in 4.63% of models; however, the algorithm still achieved complete coverage of the CTV and GTV. The most time-consuming step of the optimization process is the creation of the anatomical model based on medical imaging. However, this step is also required for any other treatment-planning concept. Once the model is completed, the operator only needs to select two points per pedicle in the patient's medical image, and the treatment parameters are calculated within a few minutes. The average time to find a solution using the algorithm was 71 s (range: 17–253 s), and the average number of iterations was 4.9 (range: 1–15). This is a significant improvement over the solution-finding ability of a genetic algorithm, which requires at least 100 generations (equivalent to iterations in this case). It can also be assumed that optimization with the algorithm is faster than determining electrode positions by hand, since it essentially automates the same process, and a significantly lower level of expertise is required from the operator. It is worth noting that the process of image segmentation could also be automated to some degree, given the high contrast of bone tissue in CT imaging.

The algorithm returns the coordinates of the final electrode positions, which correspond to the coordinates of the medical image used for initialization. To produce an output that is useful to the surgeon performing the procedure, the electrode positions can be written into the DICOM files of the medical images by manipulating the brightness of the pixels in a manner that corresponds to the electrode positions. This way, the optimal positions can be inspected using medical image-viewing software that is available in hospitals. Alternatively, the electrode coordinates can be transformed into a set of morphological parameters that are commonly used to position transpedicular screws in spinal fixation surgery: the transversal angle, sagittal angle, distance from the sagittal plane (entry point), and insertion depth [51].

The main limitation of this study is the lack of validation towards realistic vertebral tumors. Before a treatment-planning workflow can be established, validation must be performed towards real clinical cases, either prospectively or retrospectively. A realistic tumor geometry could lead to some meshing issues that have not currently been encountered and would need further investigation. Another limitation is that the current implementation of the algorithm allows for the use of only two electrodes, which limits its use to tumors located mainly within the vertebral body, i.e., to the earlier stages of the disease.

In the future, additional electrodes could be added either in the same vertebra or in adjacent vertebrae using a similar concept, which would allow for the treatment of larger tumor volumes that are less well-contained (extend outside of the vertebral body). When adding new electrodes, the overlapping contributions of the different electrode pairs should be investigated and considered when calculating the soft coverage of the CTV. Furthermore, the size of the safety margin and the length of electrode exposure could be adjusted to the tumor size, the entry point could be shifted within the pedicle to allow for even better electrode positioning, and additional boundary conditions could be introduced, such as defining the minimum allowed distance to the center of the spinal cord, to ensure treatment safety, especially in IRE ablation, where high voltages are used and a substantial temperature rise around the electrodes is expected. [52–54]. Adapting the algorithm for other anatomic treatment sites, such as deep-seated soft tissue tumors, would require a slightly different approach to determining electrode placement, for example, in relation to the center of mass of the tumor. However, most of the concepts remain the same or require minimal modification.

5. Conclusions

This study introduces and presents an algorithm developed for the optimization of electrode positions (and pulse amplitudes) based on the spatial information of the electric field distribution within the target tissue. The algorithm is currently designed for the elec-

trochemotherapy (and potentially irreversible electroporation ablation) of vertebral tumors using a transpedicular access but could be adapted to new anatomic sites in the future. The algorithm performed successfully for different segments of the spine, tumor sizes, and locations within the vertebral body. This study serves as a proof of concept that the electrode positions can be determined (semi)automatically based on the spatial information of the electric field distribution in the target tissue. The algorithm's source code and all models of vertebral tumors created in this study are available in an online repository.

Author Contributions: Conceptualization, D.M. and B.K.; Methodology, B.K. and H.C.; Software, H.C.; Validation, H.C. and B.K.; Formal Analysis, H.C.; Investigation, F.H.C. and H.C.; Resources, F.H.C. and D.M.; Data Curation, H.C.; Writing—Original Draft Preparation, H.C.; Writing—Review & Editing, H.C., B.K., D.M., F.H.C.; Visualization, H.C.; Supervision, B.K.; Project Administration, D.M. and B.K.; Funding Acquisition, D.M. All authors have read and agreed to the published version of the manuscript.

Funding: The Slovenian Research Agency (ARRS), grants P2-0249 and 17-MR.R910 supported this work. MSKCC is funded through the NIH/NCI Cancer Center Support Grant P30 CA008748.

Institutional Review Board Statement: Patient data (medical images) used in this study were obtained from clinical procedures performed in the past for which informed consent was obtained from all patients. All patient data used in this study were fully anonymized, so IRB approval was not required under local regulations.

Informed Consent Statement: Informed consent was obtained from all subjects involved in the study.

Data Availability Statement: The algorithm source codes and all 3D models of vertebral tumors created in this study are openly available in the FigShare repository at https://doi.org/10.6084/m9.figshare.21270111.v1 (accessed on 5 October 2022). No patient data or medical images are shared in the database.

Acknowledgments: 3D Slicer (https://www.slicer.org/), a free open-source platform for medical image analysis, was used for the construction of anatomical models of vertebrae from medical images. The authors also acknowledge the use of a MATLAB function "Shortest Distance Between Two Lines in N dimensions" created by Alexander Brodsky, accessible at MATLAB Central File Exchange (https://www.mathworks.com/matlabcentral/fileexchange/29130-shortest-distance-between-two-lines-in-n-dimensions).

Conflicts of Interest: The funder had no role in the study design, data analysis, decision to publish, or preparation of the manuscript. D.M. is the inventor of several patents pending and granted, is receiving royalties, and is consulting for different companies and organizations, which are active in electroporation and electroporation-based technologies and treatments. The rest of the authors declare no conflict of interest.

References

1. Neumann, E.; Rosenheck, K. Permeability Changes Induced by Electric Impulses in Vesicular Membranes. *J. Membr. Biol.* **1972**, *10*, 279–290. https://doi.org/10.1007/BF01867861.
2. Kotnik, T.; Pucihar, G.; Miklavčič, D. The Cell in the Electric Field. In *Clinical Aspects of Electroporation*; Springer: New York, NY, 2011; pp. 19–29, ISBN 978-1-4419-8362-6.
3. Kotnik, T.; Rems, L.; Tarek, M.; Miklavčič, D. Membrane Electroporation and Electropermeabilization: Mechanisms and Models. *Annu. Rev. Biophys.* **2019**, *48*, 63–91. https://doi.org/10.1146/annurev-biophys-052118-115451.
4. Batista Napotnik, T.; Polajžer, T.; Miklavčič, D. Cell Death Due to Electroporation—A Review. *Bioelectrochemistry* **2021**, *141*, 107871. https://doi.org/10.1016/j.bioelechem.2021.107871.
5. Mir, L.M.; Orlowski, S.; Belehradek, J.; Paoletti, C. Electrochemotherapy Potentiation of Antitumour Effect of Bleomycin by Local Electric Pulses. *Eur. J. Cancer Oxf. Engl.* **1991**, *27*, 68–72.
6. Serša, G.; Miklavčič, D. Electrochemotherapy of Tumours. *J. Vis. Exp.* **2008**, *22*, 1038.
7. Miklavčič, D.; Mali, B.; Kos, B.; Heller, R.; Serša, G. Electrochemotherapy: From the Drawing Board into Medical Practice. *Biomed. Eng. Online* **2014**, *13*, 29. https://doi.org/10.1186/1475-925X-13-29.

8. Campana, L.G.; Edhemovic, I.; Soden, D.; Perrone, A.M.; Scarpa, M.; Campanacci, L.; Cemazar, M.; Valpione, S.; Miklavčič, D.; Mocellin, S.; et al. Electrochemotherapy—Emerging Applications Technical Advances, New Indications, Combined Approaches, and Multi-Institutional Collaboration. *Eur. J. Surg. Oncol. J. Eur. Soc. Surg. Oncol. Br. Assoc. Surg. Oncol.* **2019**, *45*, 92–102. https://doi.org/10.1016/j.ejso.2018.11.023.
9. Rosazza, C.; Meglic, S.H.; Zumbusch, A.; Rols, M.-P.; Miklavcic, D. Gene Electrotransfer: A Mechanistic Perspective. *Curr. Gene Ther.* **2016**, *16*, 98–129.
10. Gothelf, A.; Gehl, J. Gene Electrotransfer to Skin; Review of Existing Literature and Clinical Perspectives. *Curr. Gene Ther.* **2010**, *10*, 287–299. https://doi.org/10.2174/156652310791823443.
11. Davalos, R.V.; Mir, I.L.M.; Rubinsky, B. Tissue Ablation with Irreversible Electroporation. *Ann. Biomed. Eng.* **2005**, *33*, 223–231.
12. Edd, J.F.; Horowitz, L.; Davalos, R.V.; Mir, L.M.; Rubinsky, B. In Vivo Results of a New Focal Tissue Ablation Technique: Irreversible Electroporation. *IEEE Trans. Biomed. Eng.* **2006**, *53*, 1409–1415. https://doi.org/10.1109/TBME.2006.873745.
13. Rubinsky, B. Irreversible Electroporation in Medicine. *Technol. Cancer Res. Treat.* **2007**, *6*, 255–259. https://doi.org/10.1177/153033460700600401.
14. Jiang, C.; Davalos, R.V.; Bischof, J.C. A Review of Basic to Clinical Studies of Irreversible Electroporation Therapy. *IEEE Trans. Biomed. Eng.* **2015**, *62*, 4–20. https://doi.org/10.1109/TBME.2014.2367543.
15. Reddy, V.Y.; Koruth, J.; Jais, P.; Petru, J.; Timko, F.; Skalsky, I.; Hebeler, R.; Labrousse, L.; Barandon, L.; Kralovec, S.; et al. Ablation of Atrial Fibrillation With Pulsed Electric Fields: An Ultra-Rapid, Tissue-Selective Modality for Cardiac Ablation. *JACC Clin. Electrophysiol.* **2018**, *4*, 987–995. https://doi.org/10.1016/j.jacep.2018.04.005.
16. Wittkampf, F.H.M.; van Es, R.; Neven, K. Electroporation and Its Relevance for Cardiac Catheter Ablation. *JACC Clin. Electrophysiol.* **2018**, *4*, 977–986. https://doi.org/10.1016/j.jacep.2018.06.005.
17. Stewart, M.T.; Haines, D.E.; Verma, A.; Kirchhof, N.; Barka, N.; Grassl, E.; Howard, B. Intracardiac Pulsed Field Ablation: Proof of Feasibility in a Chronic Porcine Model. *Heart Rhythm* **2019**, *16*, 754–764. https://doi.org/10.1016/j.hrthm.2018.10.030.
18. Miklavčič, D.; Čorović, S.; Pucihar, G.; Pavšelj, N. Importance of Tumour Coverage by Sufficiently High Local Electric Field for Effective Electrochemotherapy. *Eur. J. Cancer Suppl.* **2006**, *4*, 45–51. https://doi.org/10.1016/j.ejcsup.2006.08.006.
19. Miklavčič, D.; Snoj, M.; Županič, A.; Kos, B.; Čemažar, M.; Kropivnik, M.; Bracko, M.; Pečnik, T.; Gadzijev, E.; Serša, G. Towards Treatment Planning and Treatment of Deep-Seated Solid Tumors by Electrochemotherapy. *Biomed. Eng. OnLine* **2010**, *9*, 10. https://doi.org/10.1186/1475-925X-9-10.
20. Kos, B.; Županič, A.; Kotnik, T.; Snoj, M.; Serša, G.; Miklavčič, D. Robustness of Treatment Planning for Electrochemotherapy of Deep-Seated Tumors. *J. Membr. Biol.* **2010**, *236*, 147–153. https://doi.org/10.1007/s00232-010-9274-1.
21. Edd, J.F.; Davalos, R.V. Mathematical Modeling of Irreversible Electroporation for Treatment Planning. *Technol. Cancer Res. Treat.* **2007**, *6*, 275–286. https://doi.org/10.1177/153303460700600403.
22. Pavliha, D.; Kos, B.; Zupanič, A.; Marčan, M.; Serša, G.; Miklavčič, D. Patient-Specific Treatment Planning of Electrochemotherapy: Procedure Design and Possible Pitfalls. *Bioelectrochemistry Amst. Neth.* **2012**, *87*, 265–273. https://doi.org/10.1016/j.bioelechem.2012.01.007.
23. Čorović, S.; Županič, A.; Miklavčič, D. Numerical Modeling and Optimization of Electric Field Distribution in Subcutaneous Tumor Treated With Electrochemotherapy Using Needle Electrodes. *IEEE Trans. Plasma Sci.* **2008**, *36*, 1665–1672. https://doi.org/10.1109/TPS.2008.2000996.
24. Kos, B. Treatment Planning for Electrochemotherapy and Irreversible Electroporation of Deep-Seated Tumors. In *Handbook of Electroporation*; Miklavčič, D., Ed.; Springer International Publishing: Cham, Switzerland, 2017; pp. 1001–1017. ISBN 978-3-319-32886-7.
25. Adeyanju, O.O.; Al-Angari, H.M.; Sahakian, A.V. The Optimization of Needle Electrode Number and Placement for Irreversible Electroporation of Hepatocellular Carcinoma. *Radiol. Oncol.* **2012**, *46*, 126–135. https://doi.org/10.2478/v10019-012-0026-y.
26. Županič, A.; Čorović, S.; Miklavčič, D. Optimization of Electrode Position and Electric Pulse Amplitude in Electrochemotherapy. *Radiol. Oncol.* **2008**, *42*, 93–101.
27. Županič, A.; Kos, B.; Miklavčič, D. Treatment Planning of Electroporation-Based Medical Interventions: Electrochemotherapy, Gene Electrotransfer and Irreversible Electroporation. *Phys. Med. Biol.* **2012**, *57*, 5425–5440. https://doi.org/10.1088/0031-9155/57/17/5425.
28. Cindrič, H.; Kos, B.; Tedesco, G.; Cadossi, M.; Gasbarrini, A.; Miklavčič, D. Electrochemotherapy of Spinal Metastases Using Transpedicular Approach—A Numerical Feasibility Study. *Technol. Cancer Res. Treat.* **2018**, *17*, 1533034618770253. https://doi.org/10.1177/1533034618770253.
29. Cornelis, F.H.; Ben Ammar, M.; Nouri-Neuville, M.; Matton, L.; Benderra, M.A.; Gligorov, J.; Fallet, V.; Mir, L.M. Percutaneous Image-Guided Electrochemotherapy of Spine Metastases: Initial Experience. *Cardiovasc. Intervent. Radiol.* **2019**, *42*, 1806–1809. https://doi.org/10.1007/s00270-019-02316-4.
30. Fedorov, A.; Beichel, R.; Kalpathy-Cramer, J.; Finet, J.; Fillion-Robin, J.-C.; Pujol, S.; Bauer, C.; Jennings, D.; Fennessy, F.; Sonka, M.; et al. 3D Slicer as an Image Computing Platform for the Quantitative Imaging Network. *Magn. Reson. Imaging* **2012**, *30*, 1323–1341. https://doi.org/10.1016/j.mri.2012.05.001.
31. Kos, B.; Voigt, P.; Miklavcic, D.; Moche, M. Careful Treatment Planning Enables Safe Ablation of Liver Tumors Adjacent to Major Blood Vessels by Percutaneous Irreversible Electroporation (IRE). *Radiol. Oncol.* **2015**, *49*, 234–241. https://doi.org/10.1515/raon-2015-0031.

32. Choi, D.; Crockard, A.; Bunger, C.; Harms, J.; Kawahara, N.; Mazel, C.; Melcher, R.; Tomita, K. Review of Metastatic Spine Tumour Classification and Indications for Surgery: The Consensus Statement of the Global Spine Tumour Study Group. *Eur. Spine J.* **2010**, *19*, 215–222. https://doi.org/10.1007/s00586-009-1252-x.
33. Fini, M.; Salamanna, F.; Parrilli, A.; Martini, L.; Cadossi, M.; Maglio, M.; Borsari, V. Electrochemotherapy Is Effective in the Treatment of Rat Bone Metastases. *Clin. Exp. Metastasis* **2013**, *30*, 1033–1045. https://doi.org/10.1007/s10585-013-9601-x.
34. Tschon, M.; Salamanna, F.; Ronchetti, M.; Cavani, F.; Gasbarrini, A.; Boriani, S.; Fini, M. Feasibility of Electroporation in Bone and in the Surrounding Clinically Relevant Structures: A Preclinical Investigation. *Technol. Cancer Res. Treat.* **2016**, *15*, 737–748. https://doi.org/10.1177/1533034615604454.
35. Song, Y.; Zheng, J.; Yan, M.; Ding, W.; Xu, K.; Fan, Q.; Li, Z. The Effect of Irreversible Electroporation on the Femur: Experimental Study in a Rabbit Model. *Sci. Rep.* **2015**, *5*, 18187. https://doi.org/10.1038/srep18187.
36. Tam, A.L.; Abdelsalam, M.E.; Gagea, M.; Ensor, J.E.; Moussa, M.; Ahmed, M.; Goldberg, S.N.; Dixon, K.; McWatters, A.; Miller, J.J.; et al. Irreversible Electroporation of the Lumbar Vertebrae in a Porcine Model: Is There Clinical-Pathologic Evidence of Neural Toxicity? *Radiology* **2014**, *272*, 709–719. https://doi.org/10.1148/radiol.14132560.
37. Bianchi, G.; Campanacci, L.; Ronchetti, M.; Donati, D. Electrochemotherapy in the Treatment of Bone Metastases: A Phase II Trial. *World J. Surg.* **2016**, *40*, 3088–3094. https://doi.org/10.1007/s00268-016-3627-6.
38. Gasbarrini, A.; Campos, W.K.; Campanacci, L.; Boriani, S. Electrochemotherapy to Metastatic Spinal Melanoma: A Novel Treatment of Spinal Metastasis? *Spine* **2015**, *40*, E1340-1346. https://doi.org/10.1097/BRS.0000000000001125.
39. Campanacci, L.; Bianchi, G.; Cevolani, L.; Errani, C.; Ciani, G.; Facchini, G.; Spinnato, P.; Tognù, A.; Massari, L.; Cornelis, F.H.; et al. Operating Procedures for Electrochemotherapy in Bone Metastases: Results from a Multicenter Prospective Study on 102 Patients. *Eur. J. Surg. Oncol. J. Eur. Soc. Surg. Oncol. Br. Assoc. Surg. Oncol.* **2021**, *47*, 2609–2617. https://doi.org/10.1016/j.ejso.2021.05.004.
40. Tian, N.-F.; Huang, Q.-S.; Zhou, P.; Zhou, Y.; Wu, R.-K.; Lou, Y.; Xu, H.-Z. Pedicle Screw Insertion Accuracy with Different Assisted Methods: A Systematic Review and Meta-Analysis of Comparative Studies. *Eur. Spine J. Off. Publ. Eur. Spine Soc. Eur. Spinal Deform. Soc. Eur. Sect. Cerv. Spine Res. Soc.* **2011**, *20*, 846–859. https://doi.org/10.1007/s00586-010-1577-5.
41. Knez, D.; Likar, B.; Pernuš, F.; Vrtovec, T. Computer-Assisted Screw Size and Insertion Trajectory Planning for Pedicle Screw Placement Surgery. *IEEE Trans. Med. Imaging* **2016**, *35*, 1420–1430. https://doi.org/10.1109/TMI.2016.2514530.
42. Levy, J.; Hopkins, T.; Morris, J.; Tran, N.D.; David, E.; Massari, F.; Farid, H.; Vogel, A.; O'Connell, W.G.; Sunenshine, P.; et al. Radiofrequency Ablation for the Palliative Treatment of Bone Metastases: Outcomes from the Multicenter OsteoCool Tumor Ablation Post-Market Study (OPuS One Study) in 100 Patients. *J. Vasc. Interv. Radiol.* **2020**, *31*, 1745–1752. https://doi.org/10.1016/j.jvir.2020.07.014.
43. Mohme, M.; Riethdorf, S.; Dreimann, M.; Werner, S.; Maire, C.L.; Joosse, S.A.; Bludau, F.; Mueller, V.; Neves, R.P.L.; Stoecklein, N.H.; et al. Circulating Tumour Cell Release after Cement Augmentation of Vertebral Metastases. *Sci. Rep.* **2017**, *7*, 7196. https://doi.org/10.1038/s41598-017-07649-z.
44. Gallinato, O.; de Senneville, B.D.; Seror, O.; Poignard, C. Numerical Workflow of Irreversible Electroporation for Deep-Seated Tumor. *Phys. Med. Biol.* **2019**, *64*, 055016. https://doi.org/10.1088/1361-6560/ab00c4.
45. Perera-Bel, E.; Yagüe, C.; Mercadal, B.; Ceresa, M.; Beitel-White, N.; Davalos, R.V.; Ballester, M.A.G.; Ivorra, A. EView: An Electric Field Visualization Web Platform for Electroporation-Based Therapies. *Comput. Methods Programs Biomed.* **2020**, *197*, 105682. https://doi.org/10.1016/j.cmpb.2020.105682.
46. Beyer, L.P.; Pregler, B.; Michalik, K.; Niessen, C.; Dollinger, M.; Müller, M.; Schlitt, H.J.; Stroszczynski, C.; Wiggermann, P. Evaluation of a Robotic System for Irreversible Electroporation (IRE) of Malignant Liver Tumors: Initial Results. *Int. J. Comput. Assist. Radiol. Surg.* **2017**, *12*, 803–809. https://doi.org/10.1007/s11548-016-1485-1.
47. Pucihar, G.; Krmelj, J.; Reberšek, M.; Napotnik, T.B.; Miklavčič, D. Equivalent Pulse Parameters for Electroporation. *IEEE Trans. Biomed. Eng.* **2011**, *58*, 3279–3288. https://doi.org/10.1109/TBME.2011.2167232.
48. Dermol, J.; Miklavčič, D. Mathematical Models Describing Chinese Hamster Ovary Cell Death Due to Electroporation In Vitro. *J. Membr. Biol.* **2015**, *248*, 865–881. https://doi.org/10.1007/s00232-015-9825-6.
49. García-Sánchez, T.; Leray, I.; Ronchetti, M.; Cadossi, R.; Mir, L.M. Impact of the Number of Electric Pulses on Cell Electrochemotherapy in Vitro: Limits of Linearity and Saturation. *Bioelectrochemistry Amst. Neth.* **2019**, *129*, 218–227. https://doi.org/10.1016/j.bioelechem.2019.05.021.
50. Perera-Bel, E.; Mercadal, B.; Garcia-Sanchez, T.; Gonzalez Ballester, M.A.; Ivorra, A. Modeling Methods for Treatment Planning in Overlapping Electroporation Treatments. *IEEE Trans. Biomed. Eng.* **2021**, *69*, 1318–1327. https://doi.org/10.1109/TBME.2021.3115029.
51. Lien, S.-B.; Liou, N.-H.; Wu, S.-S. Analysis of Anatomic Morphometry of the Pedicles and the Safe Zone for Through-Pedicle Procedures in the Thoracic and Lumbar Spine. *Eur. Spine J.* **2007**, *16*, 1215–1222. https://doi.org/10.1007/s00586-006-0245-2.
52. Faroja, M.; Ahmed, M.; Appelbaum, L.; Ben-David, E.; Moussa, M.; Sosna, J.; Nissenbaum, I.; Goldberg, S.N. Irreversible Electroporation Ablation: Is All the Damage Nonthermal? *Radiology* **2013**, *266*, 462–470. https://doi.org/10.1148/radiol.12120609.
53. Garcia, P.A.; Davalos, R.V.; Miklavcic, D. A Numerical Investigation of the Electric and Thermal Cell Kill Distributions in Electroporation-Based Therapies in Tissue. *PLoS ONE* **2014**, *9*, e103083. https://doi.org/10.1371/journal.pone.0103083.
54. Dunki-Jacobs, E.M.; Philips, P.; Martin, R.C.G. Evaluation of Thermal Injury to Liver, Pancreas and Kidney during Irreversible Electroporation in an in Vivo Experimental Model. *Br. J. Surg.* **2014**, *101*, 1113–1121. https://doi.org/10.1002/bjs.9536.

3 Discussion

3.1 Validation of the model of irreversible electroporation ablation of liver tumors

A large number of parameters in complex numerical models introduces a degree of uncertainty, so the accuracy and robustness of the models must be validated before they can be used for clinical applications. The first part of the doctoral studies was dedicated to the validation of the numerical model of irreversible electroporation (IRE) ablation of liver tumors using existing clinical data and is presented in the first paper (Cindrič *et al* 2022, pages 69–82).

Previously developed numerical model [60], [63], [103], [104] was adapted specifically to the treatment of liver tumors with IRE ablation. The main difference from the predominantly steady-state models used for treatment planning was the use of a time-domain computation that allowed computation of tissue heating and thermal damage during treatment. Due to the difference in pulse length (typically 100 µs) and the inter-pulse delay (typically about 1 s), which span several orders of magnitude, modeling separate pulses is not feasible from a computational standpoint. In practice, individual pulses are synchronized with the patient's ECG and are delivered in sequences of 10 pulses, followed by a delay required to charge the pulse generator. We incorporated a semi pulsing scheme into our model, in which sequences of 10 pulses are modeled together as one long pulse, followed by a delay corresponding to 3 patient ECG cycles. Measurements of the patient's heart rate are used to tailor the pulsing scheme to each patient. The delays after each sequence of 10 pulses also introduce important cooling dynamics during IRE ablation. The adjusted numerical model was used

in a retrospective study in which 18 clinical cases of IRE ablation of liver tumors were numerically reconstructed and treatment outcomes were calculated. The simulated treatment outcomes were compared with ablation outcomes on patient follow-up imaging.

The aim of this study was to determine the electric field threshold in the numerical model corresponding to successful ablation of the target tissue, as seen in patient follow-up. This would allow us to determine at what electric field threshold *in silico* we expect complete ablation *in vivo* and thus validate the ability of the numerical model to predict outcomes for treatment planning of IRE ablation of liver tumors. For each case, six simulated ablation volumes corresponding to *in silico* electric field thresholds of 400–900 V/cm were extracted and compared with ablation volumes manually segmented from follow-up T1 weighted MRI. The current standard clinical practice for follow-up after IRE ablation of liver tumors is 24 hours after treatment for the assessment of treatment technical success, and 6 weeks after treatment for initial assessment of the tumor response to treatment. Originally, the MRI acquired 24 hours after the procedure was to be used for comparison with the simulated results, as earlier imaging is thought to better represent the actual area of ablated tissue at the time of treatment. However, due to massive edema in the treatment zone, it was impossible to identify the ablated tissue, so this data set was discarded. Instead, MRI images 6 weeks after ablation were used for comparison.

The chosen metric for comparison of the simulated and segmented ablation zones was the surface deviation, calculated as the average absolute error (AAE) between the surfaces of the two volumes. Based on the results of a similar study on RFA of hepatic tumors [105], an AAE of < 4 mm between simulated and segmented ablation volume should be sufficient for clinical demands and would effectively validate the numerical model. The lowest mean AAE obtained in our study was 5.6 mm $\pm$ 1.5 mm (standard deviation) obtained with the *in silico* electric field threshold of 900 V/cm. We know from the literature that a threshold of 900 V/cm is higher than that required for complete IRE ablation of liver tissue; the threshold is estimated to be 500–700 V/cm [58], [103], [106]–[108].

However, comparison with the simulated volumes at lower thresholds shows an even greater discrepancy between segmented and simulated ablation volumes,

with simulated volumes consistently larger than segmented volumes. There are several possible reasons for this discrepancy. In contrast to thermal ablation, where necrotic tissue can be easily delineated from viable tissue and its appearance does not change on follow-up within the time frame examined, the healing dynamics of electroporated tissue make it difficult to determine the actual size of the ablation zone on follow-up imaging. Recent studies on MRI findings after IRE ablation of liver primary [109] and secondary tumors [110] have also shown that the ablation zone shrinks rapidly in size in the first 2–4 weeks after the procedure. Padia *et al* [109] report a marked decrease of ablation zone size especially in the first 4 weeks after IRE procedure. Barabasch *et al* [110] also report a rapid decrease in ablation size in the 2 weeks after the IRE procedure, and a moderate decrease afterwards.

It is very likely that the follow-up period of 6 weeks was too long and that the ablation zone had already shrunk considerably. Because the numerical model is intended to compute the ablation size on the day of treatment, the threshold determined in this study is largely overestimated, so we were unable to validate the model in a way that would be useful for treatment planning. Our results suggest that lesions visible on MRI 6 weeks after IRE represent tissue areas that experienced a local electric field strength of 900 V/cm or greater during treatment. We hypothesize that better correlation with contours at lower electric field thresholds (e.g., 500–700 V/cm) could be achieved if follow-up at an earlier time point, when lesions have not yet shrunk, were available for comparison with simulated ablation volumes. Based on the collective knowledge of the estimated threshold for IRE of liver tissue and the MRI findings of Barabasch *et al* and Padia *et al*, we hypothesize that the best time point for comparison with our computed results would be somewhere between 1 and 2 weeks after the IRE procedure. A future prospective study with multiple follow-up examinations, for example, 3 to 5 days (when inflammation should have already resolved), 1 week, and 2 weeks after IRE, would allow better comparison of the calculated electric field with the ablation size at different time points after IRE and would allow determination of a more realistic electric field threshold .

In addition to the IRE threshold determination, the heat-generating effect of the classic IRE ablation protocol was numerically evaluated. Although IRE ablation is considered a nonthermal technique, several studies have shown mild

hyperthermic as well as thermal ablation effects during and after IRE [43], [83], [88], [111]. It needs to be emphasized that the thermal ablation component could potentially be problematic, as IRE is currently presented as a nonthermal modality for use in cases and anatomical sites where thermal injury is unacceptable. Our computational results showed that significant heating of the treated tissue occurred, particularly in the more clinically challenging cases where many electrodes were used (i.e., many pulses were delivered). In fact, in 7 of 18 reconstructed cases, heating sufficient to cause thermal damage occurred in more than 50 % of the tumor volume. It is possible that our model overestimates the extent of thermal injury to some degree. However, as parts of the tissue are cumulatively exposed to hundreds of pulses during IRE ablation, unwanted heating and thermally induced necrosis are inevitable. The highest increase in temperature was observed at the electrode surface where the current density is the highest, which can negatively affect treatment safety, should the electrodes be in contact or in the immediate vicinity of critical anatomical structures.

We also demonstrate the utility of treatment planning to improve future IRE procedures, for example, by performing IRE ablation without potentially harmful thermal effects. Two cases in which reconstructions suggested a high percentage of thermal damage in the target tissue were selected for optimization and development of a hypothetical treatment plan. In both cases, we were able to completely eliminate thermal damage while maintaining coverage of the target volume with a sufficiently high electric field. In this study, only the applied voltage magnitudes were optimized, while the electrode positions remained the same. Due to uncertainties in the size of the ablation zone, multiple sessions of electrode retraction are often performed in clinical practice. In one of the selected cases, we were able to omit electrode retraction and achieved complete coverage of the tumor volume and safety margin in one session, which also shortened the overall procedure time.

In this study, a method for validating the numerical model for treatment planning was developed and refined. Based on these results, a future prospective study can be effectively designed to provide the necessary data to validate the predictive ability of the model and ensure sufficient accuracy to meet clinical needs. A database containing all case information, models, and computational results has been made publicly available in an online repository https://doi.org/10.6084/m9.figshare.12961646.v1.

3.2 Electrochemotherapy in the liver at the mesoscale

To better understand the physical phenomenon of electroporation, numerical models are being developed at various scales, ranging from bulk tissue models intended for treatment planning [59], [70], [71], [103], to models of densely packed cells [112]–[115], models of single cells, and models of cell membrane electroporation [3], [116]. A prerequisite for the success of electroporation-based treatments is the complete coverage of the target tissue volume with a sufficiently high electric field. The distribution of the electric field in biological tissue is highly dependent on the electrical properties of the tissues in the region to be treated; this is particularly important in heterogeneous organs, where conductivities of different tissues span over a wide range of values [59], [107], [117], [118].

The liver is a highly heterogeneous organ, permeated with a network of blood vessels and biliary tracts. The liver parenchyma also has a distinct microstructure consisting of functional units called hepatic lobules, each containing a centrilobular vein (CV). The lobules relate to a network of connective tissue, blood vessels and bile ducts (portal triads), called the interlobular septa. Several studies have already shown the importance of considering liver macrostructures, such as large blood vessels and bile ducts, when constructing models for electroporation-based treatments in the liver [106], [107], [119]. The impact of liver microstructures, however, has not yet been investigated. We hypothesized that the natural heterogeneity of the liver structure might have an impact on the distribution of the electric field and, consequently, on the outcome of electroporation-based treatments in the liver.

In the second paper (Cindrič *et al.* 2022, pages 83–96), we thus investigated how the heterogeneous anatomical structure of the liver affects the electric field distribution during electrochemotherapy (ECT). We constructed a mesoscale model of the liver that incorporates both liver macro- and microstructures and is comparable to findings from microscopic images. To obtain realistic geometries we numerically reconstructed four ECT procedures in healthy porcine liver, performed in a recent *in vivo* animal model study by Zmuc et al [98]. Special attention was given to select samples where several major hepatic vessels and portal spaces were involved in the treatment area. The electric field distribu-

tion was calculated with our previously developed numerical model for planning electroporation-based treatments in the liver and compared with the histopathological changes observed in the microscopic images of tissue samples after ECT of healthy porcine liver.

Because the electrical properties of the individual microstructures, namely the hepatic lobules, interlobular septa, and CVs, are not known, we performed a parametric study in which we varied the conductivity (functions) of the individual structures. We investigated whether the inclusion of liver microstructures and the variability of their electrical conductivity affect the distribution of the electric field to an extent relevant for comparison with the microscopic images and thus with the histopathological findings. Figure 3 in Paper 2 (page 88) shows an example of the electric field computed with the heterogeneous mesoscale model (incorporating liver microstructures), compared to a homogeneous bulk model of the liver parenchyma (generally used in treatment planning). In the heterogeneous model, we observe a peak in electric field strength at the edge of the lumen of the CV, which is a consequence of the much higher conductivity of the blood compared to the surrounding tissue, followed by a drop in the area of the CV lumen. A decrease in electric field strength is also observed in the domain of the interlobular septa. The numerical model is also consistent with the histological findings, in which the damage was more pronounced in the centri- and midlobular areas, with CVs no longer visible in the damaged areas. We postulate that the damage in the centrilobular area is due to disruption of the central vasculature of the lobules because of spikes in the electric field, whereas the outer parts of the lobules are less affected because of a vasculature (the interlobular septa) that is still functioning.

In the example shown in on Figure 3 (page 88), the mean relative error between the electric field computed with a heterogeneous model and a homogeneous bulk model of the liver parenchyma is 7 % with a standard deviation of 12 %, whereas the median relative error is 3 %. The low median error indicates that there is no significant difference in the gross electric field distribution. According to the parametric study, the only scenario in which the inclusion of the interlobular septa would significantly affect the gross electric field distribution is when the conductivity of the septa is much lower (e.g., 10 %) than the conductivity of the surrounding hepatic tissue. However, this is highly unlikely because of the com-

position of the interlobular septa. Our results indicate that the microstructures of the liver do not significantly affect the distribution of the electric field on the mesoscale, so that the use of a homogeneous bulk model of the liver parenchyma is sufficient for planning electroporation-based treatments in the liver. The presence of large hepatic vessels, on the other hand, affects the gross electric field distribution. In Figures 1–2 in Paper 2 (pages 87–88), we can see an increase in electric field strength at the side of the vessel parallel to the external electric field, and a decrease in field strength at the side perpendicular to the external electric field, which is in agreement with previous studies [106], [107], [119].

Histological examination of the treated porcine liver samples showed acute changes in the tissue, with clear zonation. The area immediately around the electrode insertion site showed coagulation necrosis with complete loss of liver microstructure. Surrounding this area was a zone of partially damaged liver parenchyma, which was attributed to irreversible electroporation of the tissue. We fitted the electric field computed with the mesoscale model with homogeneous liver parenchyma to the microscopic images of the treated area, and determined the thresholds that best fit the appearance of both zones. The mean *in silico* electric field that best fit the zone of partially damaged liver parenchyma was 810 V/cm, which was sufficient to cause irreversible electroporation of hepatic tissue using pulse protocols designed for reversible electroporation [70], [107], [120]. The mean *in silico* electric field threshold that best fit the zone of coagulation necrosis was 1225 V/cm. Despite the necrotic appearance of the tissue, Zmuc *et al* postulated that it was unlikely that these changes were caused by heating of the tissue during pulse delivery, which has now been confirmed by our computations, as no significant tissue heating was observed in the models. The highest calculated temperature reached 47°C, but only for a very short time, which was not sufficient to cause thermal damage to the tissue. The necrosis observed in our samples may be related to the pH changes around the electrodes, however, further research is needed to verify this speculation.

In summary, in this study we have confirmed that the microstructures of the liver (hepatic lobules, interlobular septa, and centrilobular veins) do not significantly affect the distribution of the electric field at the mesoscale. Therefore, the use of a completely homogeneous model of the liver parenchyma is appropriate for the numerical computations of the electric field in the liver used for

planning electroporation treatments. However, the large hepatic vessels and portal vein spaces should be included in the model because these macrostructures significantly affect the electric field distribution, as suggested previously.

3.3 Does the presence of metallic implants affect the safety and efficacy of electroporation-based treatments?

As a safety precaution, the use of electroporation-based treatment remains contraindicated for patients with metallic implants when the treatment zone is near the implanted device. Due to the high electrical conductivity of metal compared to biological tissue, the presence of metallic objects within or in close proximity to the treatment zone may alter the distribution of the electric field, potentially resulting in under-treatment of the target tissue. There may also be an increased risk of thermal damage to surrounding tissue, especially during IRE ablation. The effects of metallic implants on the safety and efficacy of ECT and IRE ablation have been investigated in two studies.

In the third paper (Cornelis *et al*, pages 97–108), we investigated the effect of metallic surgical clips in IRE ablation of unresectable colorectal liver metastases (CRLM). The presence of surgical clips at the treatment site is a common clinical scenario in the management of unresectable liver malignancies, as patients have often already been treated. According to Angiodynamics (Latham, NY, USA), the manufacturer of the NanoKnife pulse generator for IRE ablation, the presence of any implanted devices with metal parts is considered a contraindication to treatment [121]. However, the presence of smaller implants, such as surgical clips, is often overlooked in practice. Our hypothesis was that surgical clips also reduce the efficacy of IRE ablation of CRLM and that patient-specific numerical models can be used to identify the mechanism by which metallic implants affect the outcomes of the treatment.

We used patient-specific numerical models as tools to understand the etiology and factors underlying IRE failure in treating CRLM patients with metallic surgical clips at the site of ablation. Our simulations showed that metallic clips

induce microscopic distortions in the distribution of the electric field in the tissue (Figure 5 E-F in Paper 3, page 104). The presence of metallic clips resulted in a reduction of the electric field strength in their immediate vicinity (< 1 mm), with a maximum distortion at the center of the clip, along the longitudinal axis. The reduction in electric field strength at the site of such distortions was sufficient to reduce the probability of cell death (Figure 5D in Paper 3, page 104). This might reduce treatment efficacy if the tumor cells are present in the areas within and around the clips. However, no difference was found in the gross volume of the tumor that had an electric field strength above the IRE threshold when the simulations were compared with and without the clips.

While IRE has a predominantly nonthermal cell-killing mechanism, our models suggest that thermal damage is present in a substantial portion of treated tissue regardless of the presence of the metallic clips. We speculate that the he aggressive pulsing protocol currently used in IRE ablation may be responsible. Since metal is a good thermal and electrical conductor, the presence of metallic implants at the treatment site does not cause them to heat up directly. Any heating of the clip is merely by conduction from the ambient tissue; moreover, the metallic clip may even act as a heat sink, reducing the thermal energy released into tissue [122].

Several preclinical studies have examined the effects of the presence of metallic implants on IRE ablation. Neal *et al* [123] examined the effects of prostate brachytherapy seeds on electric field distribution and ablation volume and found no adverse effects. On the other hand, a preclinical *in vivo* assessment by Ben-David *et al* [124] showed that the presence of metal in the IRE treatment zone can distort the size and shape of the ablation. Scheffer *et al* [125] and Dunki-Jacobs *et al* [111] then showed that IRE can cause local heating, with the presence of metal increasing thermal damage at the treatment site. We add to these findings by reporting that the presence of metallic surgical clips may affect the efficacy of IRE ablation of CRLM, but does not appear to affect treatment safety.

Two major manufacturers of clinically approved pulse generators, namely IGEA (Carpi, MO, Italy) for the Cliniporator system used in ECT and Angiodynamics (Latham, NY, USA) for the NanoKnife system used for IRE ablation, consider implanted pacemakers a contraindication to treatment [121], [126]. In the

fourth paper (Jarm *et al*, 2020, pages 109–128), we numerically investigated the influence of the presence of a metal-encased pacemaker, positioned on the fascia of the pectoralis major muscle, on the efficacy and safety of electrochemotherapy (ECT) and irreversible electroporation (IRE) ablation of a subcutaneous tumor. Three scenarios were studied for both treatment options: a pacemaker in contact with one of the electrodes, a pacemaker near the tumor but not in contact with the electrodes, and a control scenario without a pacemaker.

The presence of a pacemaker has a similar effect in both treatments. Without contact with the electrodes, the presence of a pacemaker has no significant effect on the gross electric field distribution and the delivered electric current compared with the control situation. Changes in the electric field are observed mainly in the adjacent healthy tissue, whereas the electric field in the tumor remains unaffected. Moreover, no additional heating of the tissue was observed. When the pacemaker is in contact with one of the electrodes, the entire housing acts as one large electrode, resulting in increased current draw from the pulse generator; the calculated electric current was about 50 % higher than in the control situation. The higher current draw increases the risk of interruption of pulse delivery due to exceeding the maximum values limited by the hardware. In both treatments, the resulting electric field is higher overall, and a significant amount of IRE is also observed in healthy tissue near the contact site. In addition, higher temperatures are observed near the electrodes. In ECT, the temperature increase is not as pronounced, but in IRE ablation, a significant temperature increase is observed at the site of the other active electrode in the pair (paired with the contact electrode). This observation is consistent with the observation of heating around the electrodes when a metal stent was present within the treatment zone [125]. The metal housing of the pacemaker itself does not heat up during treatment, but rather acts as a heat sink, so thermal damage due to heating of the metal housing is unlikely.

Our study has shown that the presence of a metal-encased pacemaker has no effect on tumor tissue coverage, regardless of contact with the electrode, and thus should not impair treatment efficacy. The study should be considered preliminary, and the conclusions therefore require further confirmation. Nevertheless, these results should help make electroporation-based treatments accessible to patients with implanted pacemakers.

3.4 Introducing a new approach to the treatment of spinal tumors

Bones, especially the spine, are one of the most common sites for cancer metastases. The incidence of spinal metastases in cancer patients can reach up to 70 %, depending on the type of primary tumor. Preclinical and clinical studies have shown that bone metastases can be effectively treated by electrochemotherapy, and significant reductions in pain and no adverse neural symptoms associated with treatment have been reported [127]–[130]. In the fifth paper (Cindrič *et al* 2018, pages 129–144), we present a novel, minimally invasive approach, hereafter referred to as the transpedicular approach, in which the needle electrodes for electrochemotherapy are inserted into the vertebral body through the pedicles, similar to the placement of the pedicular screws for spinal fixation surgery. The electrodes are shorter than what is currently used for electroporation of bones, 1 cm rather than 3 cm, allowing for more precise targeting of the tumor. The aim of this study was to numerically evaluate the feasibility and safety of the proposed approach for the treatment of spinal metastases.

Three representative clinical cases of spinal tumors with different stages of vertebral body, pedicle, and spinal canal involvement were used for the study. For all three cases, anatomically accurate numerical models were created from the patients' medical images, and an individual treatment plan was developed for each case. The numerical model of electroporation is based on the values of electrical conductivity of tissues and the factors of the conductivity increase due to electroporation. However, data are sparse, especially for the latter, and reported results differ considerably between studies. We therefore used experimental data from a preclinical study on a sheep vertebra [129] and the first clinical case of ECT of a vertebral tumor [128] to fine-tune the factors for the increase in electrical conductivity during electroporation for bone and tumor tissues, respectively. Calculations of the distribution of the electric field in the tumor and surrounding tissue were performed to determine the outcome of the proposed treatment approach, and the potential risk of nerve damage was assessed.

Tumor coverage with the selected threshold of 400 V/cm for ECT of bone tissue was > 99 % in two cases and > 98.9 % in the third case, which was considered

a successful treatment. The undertreated tumor tissue was located at the margin of the tumor volume. In one case where the tumor had grown into the spinal canal, the calculation showed IRE in 12.4 mm^3 of the spinal cord, which could pose a risk for nerve damage. However, it should be noted that the thresholds for electroporation of different tissues are still not well defined; for this reason, we use very conservative thresholds in the models to avoid overly optimistic coverage of the target tissue and underestimation of the risk of damage. It is likely that the nerve tissue would not be damaged. Computations suggest that a significant portion of the tumor tissue (34-63 %) was exposed to an electric field strong enough to cause IRE. However, studies have shown that IRE does not affect the mechanical competence of the treated bone in the long term [127], [129], [131], and there is also emerging evidence that electroporation-induced apoptotic cell death even promotes osteogenic activity [132]. The use of electrodes with shorter conducting parts allows more precise targeting of tumor tissue, resulting in minimal damage to surrounding tissue and reducing the maximum electric currents delivered and thus the negative side effects of treatment. A genetic algorithm was used to optimize the applied voltage amplitudes, but the electrode positions were determined manually and not optimized. The use of an algorithm to optimize electrode positions would potentially lead to even better tumor coverage with an even lower risk of nerve damage.

The results of this study suggest that the proposed treatment approach is feasible and carries little risk of nerve damage if the majority of the tumor volume is within the vertebral body. If the tumor is outside the vertebral body and has grown somewhat into the pedicle area, effective treatment is still possible, but more extensive planning is required, with special attention to possible spinal cord and nerve involvement. Therefore, with careful patient selection, the proposed approach to spinal metastases is a feasible treatment option that should be further investigated. Insertion of electrodes through the pedicles is a technique similar to the well established orthopedic procedures; insertion of fixation screws is the most common technique in spinal fixation surgery [133]. The technology developed for automated screw trajectory planning and intraoperative guidance could probably be used for electrode insertion for electrochemotherapy [134]–[136], facilitating the introduction of the new treatment approach into clinical practice.

3.5 Optimization of electrode positions for the treatment of spinal tumors

The sixth paper (Cindrič *et al.* 2022, pages 145–162) builds on the concept of the transpedicular approach for electrochemotherapy of spinal tumors, presented previously [41], [101]. Generally, the treatment planning process consists of determining the best possible electrode positions and voltage amplitudes to ensure treatment of the entire clinical target volume (CTV). This process is still mainly performed manually, requiring a high level of expertise, or with computationally intensive genetic algorithms. The study presented in this paper is one of the first attempts to use spatial information about the electric field distribution in the tissue to optimize electrode positioning and pulse amplitude without using computationally intensive genetic algorithms.

Unfortunately, treatment planning for electroporation-based treatments is still in its early stages of development. Treatment plans are created prior to the procedure, and the electrode positions and voltage amplitudes are still primarily determined manually. This process typically requires multiple iterations where the operator changes the electrode positions between computations. After each iteration, the operator must visually inspect the electric field (usually as an overlay over the medical image), identify potentially undertreated areas of the CTV, reposition the electrodes accordingly, and repeat the computation. The entire process is then iterated until the entire CTV is covered by sufficiently high electric field. This approach requires a high level of expertise in the distribution of the electric field in inhomogeneous tissue and the effects of electrode positioning and pulse parameters. Furthermore, in our experience, this iterative process takes at least 30 minutes.

In developing the algorithm, we followed the concept of the manual approach; however, the goal was to automate the iterative process so that minimal operator input is required. The algorithm computes the distribution of the electric field in the CTV, identifies potentially undertreated regions, and uses this information to iteratively move the electrodes from their initial positions to cover the entire CTV. The algorithm is somewhat modular and takes into account several conditions; for example, an appropriate distance between electrodes must always be maintained

to avoid short circuits; it is also intuitive to move the electrodes toward the center of mass of the tumor or toward large regions of undertreated tissue. The technical limitations of a commercially available pulse generator for ECT are also respected.

For safety reasons, the thresholds for electroporation used in practice are generally quite high, and sometimes it may be difficult to cover the entire CTV in larger tumors. However, if the safety margin is taken into account, very few or no cells are expected at the outer edge of the CTV; therefore, we introduced the so-called soft coverage of the CTV, where the threshold for electroporation at the outer edge of the CTV is not strictly enforced. In this study, the CTV represents the tumor mass with a safety margin of 5 mm. A weighting map of the CTV was created in which each voxel in the map is assigned a weight based on how far the voxel is from the boundary of the tumor volume, with the weight decreasing linearly toward the edge of the CTV. The electroporation thresholds currently used in treatment planning are only a very rough estimate. The threshold itself is a difficult property to determine, influenced by biological variability, tissue sample condition, and measurement method, among other factors. Therefore, it is not surprising that different values are reported in the literature, even for the same tissue type. In addition, whether the tissue is electroporated or not depends on the pulsing protocol used in the treatment and the cumulative exposure time in cases where treatment is performed by multiple electrodes. Studies suggest that electroporation may occur at lower thresholds when the exposure time is increased with more and/or longer pulses.

We tested the performance of the algorithm using realistic vertebral models of the lower thoracic (T8–T12) and lumbar (L1–L5) spinal segments. The models were created from patients' medical images, to which synthetic spherical tumor models of different sizes were added, resulting in a total of 108 test models. The results have shown that the algorithm performs successfully for different spinal segments, different tumor sizes, and different tumor locations within the vertebral body. The most time-consuming step of the optimization process is the creation of the anatomical model based on medical imaging. However, this step is also required for other treatment planning concepts. Once the model is completed, the operator needs to select two points per pedicle in the patients medical image, and the treatment parameters are calculated within a few minutes. The average

time to find a solution using the proposed algorithm was 71 s (range: 17–253 s), and the average number of iterations was 4.9 (range: 1–15). This is a significant improvement over finding a solution with a genetic algorithm, which requires at least 100 generations (equivalent to iterations in this case) or by hand (which takes at least 30 minutes). It should also be emphasized that the process is essentially automated and therefore requires a much lower level of expertise on the part of the operator.

The main limitation of this study is the lack of validation on realistic vertebral tumors. Before a treatment planning workflow can be established, validation must be performed towards real clinical cases, either prospectively or retrospectively. Another limitation is that the current implementation of the algorithm only allows the use of two electrodes, which limits its application to tumors located mainly in the vertebral body, i.e., the earlier stages of the disease. This study serves as a proof of concept that the electrode positions can be determined (semi-) automatically based on the spatial information of the electric field distribution in the target tissue. The algorithm is currently designed for ECT (and IRE ablation by adopting a different electric field threshold) of vertebral tumors via a transpedicular approach, but could be adapted for other anatomical sites in the future. The source code of the algorithm and all models of vertebral tumors created in the study have been made publicly available in an online repository https://doi.org/10.6084/m9.figshare.21270111.v1.

4 Conclusions

The clinical applicability of treatment planning for electroporation-based treatments has been demonstrated previously. However, the numerical models used for treatment planning have not yet been systematically validated for irreversible electroporation (IRE) ablation. We have developed a method to validate the numerical model using clinical data from patients whose liver tumors were treated with IRE ablation. Based on the comparison of the ablation zone predicted by the numerical model with the actual ablation zone detected at the patients' follow-up imaging, we determined the *in silico* electric field threshold that gave the best agreement with the successful ablation *in vivo*. Our results suggest that lesions visible on MRI 6 weeks after IRE represent tissue areas that experienced a local electric field strength of 900 V/cm or greater during treatment. The study was limited by its retrospective nature and the suboptimal timing of the clinical follow-up imaging. Because the numerical model is intended to compute the ablation zone on the day of the treatment, the comparison with the 6-week follow-up resulted in an overestimation of the IRE threshold, so we were unable to validate the predictive ability of the model. Nevertheless, based on the methodology and results presented in this work, a future prospective clinical trial can be effectively designed to provide the necessary data to further validate the numerical model and ensure sufficient accuracy for clinical needs.

In addition, we developed a mesoscale model, comparable to microscopic images to evaluate whether the heterogeneous structure of the liver organ and its variability in electrical properties affect the electric field at a level important for treatment planning. We established that the microstructure of the liver parenchyma does not significantly affect the distribution of the electric field at the mesoscale and that the use of a homogeneous model of the liver parenchyma

is appropriate for planning electroporation-based treatments. Nevertheless, the large hepatic vessels and portal spaces should be included in the model because these macrostructures significantly affect the electric field distribution, as suggested previously. Moreover, we determined the *in silico* electric field thresholds consistent with the histopathological changes observed on microscopic images after treatment. The mean electric field threshold that best matched the zone of coagulation necrosis was 1225 V/cm, whereas the mean threshold that best matched the zone of partially damaged liver parenchyma attributed to IRE was 805 V/cm.

Numerical models are an important tool for investigating new treatment approaches, testing new electrode designs, and analyzing different clinical scenarios without the need for animal testing and clinical trials. Two studies were conducted to investigate the efficacy and safety aspects of electrochemotherapy (ECT) and IRE ablation in different clinical scenarios commonly encountered in practice. According to the manufacturers' instructions (of pulse generators) metallic implants are a contraindication for electroporation-based treatments. We have shown that for implanted pacemakers, the risk of treatment failure or safety problems due to the presence of the pacemaker is negligible. Our results should render electroporation-based treatments more accessible to patients. On the other hand, we have shown that in liver metastases, the presence of metallic clips within the treatment zone may reduce the efficacy of the treatment due to the Faraday cage effect. In light of these findings, the presence of surgical clips should not be disregarded when deciding on treatment options for these patients. We have shown that the presence of metallic implants does not cause additional heating however, throughout the works we also demonstrate a significant heat-generating effect of IRE ablation. IRE ablation is often referred to as a nonthermal ablation method and is therefore considered for use in organs and anatomic sites where thermal damage to surrounding tissue is unacceptable. The medical community needs to be made aware of the thermal component of IRE ablation and that the tissue temperature must be controlled and considered when planning the procedure.

We also developed a new approach for the treatment of spinal metastases with ECT and numerically evaluated its efficacy and safety. The treatment of spinal metastases is particularly complicated because of the importance of the

mechanical stability of the spine in supporting and moving the body and the involvement of the spinal cord and nerves. Surgery remains the most common treatment option, but carries many risks and is not always feasible. Therefore, new and less aggressive treatments for spinal metastases are needed to relieve patients' symptoms and improve their quality of life. We have shown that ECT with a transpedicular approach could be a safe and minimally invasive treatment for spinal metastases. The results of our study provide the foundation and evidence that should stimulate further analysis and experimentation with this potential treatment option for an otherwise poorly treatable disease.

The last part of the thesis was devoted to the optimization of the numerical model of electroporation to meet the requirements of treatment planning in real-time. The main goal in planning electroporation-based treatments is to determine the best possible electrode position and voltage amplitude that ensures treatment of the entire target tissue volume.This process is still mainly performed manually or with computationally intensive genetic algorithms. The latter are particularly unsuitable for real-time treatment planning. We have therefore developed an algorithm that optimizes electrode positions based on spatial information about the distribution of the electric field in the target tissue. The algorithm is currently designed for the ECT of spinal tumors via a transpedicular approach, but could be adapted for IRE ablation and other anatomical sites in the future. The algorithm performs successfully for different spinal segments, for different tumor sizes, and at different sites within the vertebral body. Most importantly, the proposed algorithm significantly reduces the time and expertise required to create a treatment plan for the ECT of vertebral tumors.

5 Original scientific contributions

Validation of the numerical model for planning electroporation-based treatments

The numerical model for planning electroporation-based treatments has not yet been systematically validated for irreversible electroporation (IRE) ablation. In this dissertation, we developed a sophisticated method to validate the numerical model using clinical data from patients whose liver tumors were treated with IRE ablation. The study was limited because of its retrospective nature and the suboptimal timing of standard clinical follow-up, so we could not validate the predictive ability of the model. Nevertheless, based on the methodology and results presented in this work, a future prospective clinical trial can be effectively designed to provide the necessary data to fully validate the numerical model and ensure sufficient accuracy for clinical needs. A database containing all image segmentations, computed 3D electric field distributions, 3D surface models of the liver, tumors, and ablation volumes has been made publicly available in an online repository and can be used for future research.

We also developed a mesoscale model, comparable to microscopic images to evaluate whether the heterogeneous structure of the liver organ and its variability in electrical properties affect the electric field at a level important for treatment planning. We showed that the microstructure of the liver parenchyma does not significantly affect the distribution of the electric field at the mesoscale and that the use of a completely homogeneous model of the liver parenchyma is appropriate for planning electroporation-based treatments. In addition, we determined the *in silico* electric field thresholds consistent with the histopathological changes seen on post-treatment microscopic images, namely the zone of coagulation necrosis

and the zone of partially damaged liver parenchyma attributable to IRE.

Numerical evaluation of safety aspects and new approaches to electroporation-based treatments

We have investigated the efficacy and safety of electrochemotherapy (ECT) and IRE ablation in two frequently occurring clinical scenarios: the presence of metallic surgical clips in the liver within the treated tissue volume, and treatment near an implanted pacemaker. Throughout the works we also demonstrated the significant heat-generating effect of IRE ablation, which could prove detrimental if not considered when planning the treatment. Finally, we developed a new approach for the treatment of spinal metastases with ECT via transpedicular approach. We numerically evaluated its efficacy and safety and demonstrated that the proposed approach could be a safe, minimally invasive treatment for spinal metastases. The results of the study provide the foundation and evidence that should stimulate further analysis and development of this treatment option for an otherwise poorly treatable disease.

Optimization of the numerical model of electroporation and preparation of workflow for real-time computer-assisted treatment planning for clinical applications of electroporation

The last part of the doctoral study was devoted to the optimization of the numerical model of electroporation to meet the requirements of treatment planning in real-time. We developed an algorithm to determine optimal electrode positions and applied voltage amplitudes for ECT of spinal metastases using the transpedicular approach. The study was the first attempt to use the spatial information of the electric field distribution in the tissue to optimize the treatment parameters. We have shown that the algorithm significantly reduces the time and expertise required to create the treatment plan. With the algorithm, the average time to find the optimal treatment parameters was 71 s and the maximum time was 253 s, which is acceptable for real-time computation. Thus, the developed algorithm is expected to make an important contribution to the future development of real-time computer-assisted treatment planning. The algorithm source code and all models created in the study have been made publicly available in an online repository and can be used for future research.

References

[1] E. Neumann and K. Rosenheck, "Permeability changes induced by electric impulses in vesicular membranes", *The Journal of Membrane Biology*, vol. 10, no. 1, pp. 279–290, Dec. 1972, ISSN: 0022-2631, 1432-1424. DOI: 10.1007/BF01867861.

[2] T. Kotnik, G. Pucihar, and D. Miklavčič, "The cell in the electric field", in *Clinical Aspects of Electroporation*, S. T. Kee, J. Gehl, and E. W. Lee, Eds. New York, NY: Springer New York, 2011, pp. 19–29, ISBN: 978-1-4419-8363-3. DOI: 10.1007/978-1-4419-8363-3_3.

[3] T. Kotnik, L. Rems, M. Tarek, and D. Miklavčič, "Membrane Electroporation and Electropermeabilization: Mechanisms and Models", *Annual Review of Biophysics*, Feb. 2019, ISSN: 1936-1238. DOI: 10.1146/annurev-biophys-052118-115451.

[4] L. Rems and D. Miklavčič, "Tutorial: Electroporation of cells in complex materials and tissue", *Journal of Applied Physics*, vol. 119, no. 20, p. 201 101, May 2016, ISSN: 0021-8979. DOI: 10.1063/1.4949264.

[5] M. L. Yarmush, A. Golberg, G. Serša, T. Kotnik, and D. Miklavčič, "Electroporation-based technologies for medicine: Principles, applications, and challenges", *Annual Review of Biomedical Engineering*, vol. 16, pp. 295–320, Jul. 2014, ISSN: 1545-4274. DOI: 10.1146/annurev-bioeng-071813-104622.

[6] S. Mahnič-Kalamiza, D. Miklavčič, and E. Vorobiev, "Dual-porosity model of solute diffusion in biological tissue modified by electroporation", *Biochimica Et Biophysica Acta*, vol. 1838, no. 7, pp. 1950–1966, Jul. 2014, ISSN: 0006-3002. DOI: 10.1016/j.bbamem.2014.03.004.

[7] T. Kotnik, W. Frey, M. Sack, S. Haberl Meglič, M. Peterka, and D. Miklavčič, "Electroporation-based applications in biotechnology", *Trends in Biotechnology*, vol. 33, no. 8, pp. 480–488, Aug. 2015, ISSN: 1879-3096. DOI: 10.1016/j.tibtech.2015.06.002.

[8] B. Geboers, H. J. Scheffer, P. M. Graybill, *et al.*, "High-Voltage Electrical Pulses in Oncology: Irreversible Electroporation, Electrochemotherapy, Gene Electrotransfer, Electrofusion, and Electroimmunotherapy", *Radiology*, vol. 295, no. 2, pp. 254–272, May 2020, ISSN: 1527-1315. DOI: 10.1148/radiol.2020192190.

[9] L. M. Mir, M. Belehradek, C. Domenge, *et al.*, "[Electrochemotherapy, a new antitumor treatment: first clinical trial]", *Comptes rendus de l'Academie des sciences. Serie III, Sciences de la vie*, vol. 313, no. 13, pp. 613–618, 1991, ISSN: 0764-4469.

[10] G. Serša, D. Miklavcic, M. Cemazar, Z. Rudolf, G. Pucihar, and M. Snoj, "Electrochemotherapy in treatment of tumours", *European Journal of Surgical Oncology*, vol. 34, no. 2, pp. 232–240, Feb. 2008, ISSN: 0748-7983, 1532-2157. DOI: 10.1016/j.ejso.2007.05.016.

[11] T. Stepišnik, T. Jarm, A. Grošelj, *et al.*, "Electrochemotherapy – An effective method for treatment of tumors with combination of chemotherapeutic agent and electric field", *Slovenian Medical Journal*, vol. 85, no. 1, Feb. 2016, ISSN: 1581-0224.

[12] C. Rosazza, S. H. Meglic, A. Zumbusch, M.-P. Rols, and D. Miklavcic, "Gene Electrotransfer: A Mechanistic Perspective", *Current Gene Therapy*, vol. 16, no. 2, pp. 98–129, 2016, ISSN: 1875-5631.

[13] A. Gothelf and J. Gehl, "Gene electrotransfer to skin; review of existing literature and clinical perspectives", *Current Gene Therapy*, vol. 10, no. 4, pp. 287–299, Aug. 2010, ISSN: 1875-5631. DOI: 10.2174/156652310791823443.

[14] R. V. Davalos, I. L. M. Mir, and B. Rubinsky, "Tissue ablation with irreversible electroporation", *Annals of Biomedical Engineering*, vol. 33, no. 2, pp. 223–231, Feb. 2005, ISSN: 0090-6964.

[15] C. Livia, A. Sugrue, T. Witt, *et al.*, "Elimination of Purkinje Fibers by Electroporation Reduces Ventricular Fibrillation Vulnerability", *Journal of the American Heart Association*, vol. 7, no. 15, e009070, Aug. 2018, ISSN: 2047-9980. DOI: 10.1161/JAHA.118.009070.

[16] J. F. Edd, L. Horowitz, R. V. Davalos, L. M. Mir, and B. Rubinsky, "In vivo results of a new focal tissue ablation technique: Irreversible electroporation", *IEEE transactions on bio-medical engineering*, vol. 53, no. 7, pp. 1409–1415, Jul. 2006, ISSN: 0018-9294. DOI: 10.1109/TBME.2006.873745.

[17] B. Rubinsky, G. Onik, and P. Mikus, "Irreversible Electroporation: A New Ablation Modality — Clinical Implications", *Technology in Cancer Research & Treatment*, vol. 6, no. 1, pp. 37–48, Feb. 2007, ISSN: 1533-0346. DOI: 10.1177/153303460700600106.

[18] M. R. Meijerink, H. J. Scheffer, and G. Narayanan, Eds., *Irreversible Electroporation in Clinical Practice*. Springer International Publishing, 2018, ISBN: 978-3-319-55112-8.

[19] C. Jiang, R. V. Davalos, and J. C. Bischof, "A review of basic to clinical studies of irreversible electroporation therapy", *IEEE transactions on biomedical engineering*, vol. 62, no. 1, pp. 4–20, Jan. 2015, ISSN: 1558-2531. DOI: 10.1109/TBME.2014.2367543.

[20] H. J. Scheffer, K. Nielsen, M. C. de Jong, *et al.*, "Irreversible electroporation for nonthermal tumor ablation in the clinical setting: A systematic review of safety and efficacy", *Journal of vascular and interventional radiology: JVIR*, vol. 25, no. 7, 997–1011, quiz 1011, Jul. 2014, ISSN: 1535-7732. DOI: 10.1016/j.jvir.2014.01.028.

[21] V. Y. Reddy, J. Koruth, P. Jais, *et al.*, "Ablation of Atrial Fibrillation With Pulsed Electric Fields: An Ultra-Rapid, Tissue-Selective Modality for Cardiac Ablation", *JACC: Clinical Electrophysiology*, vol. 4, no. 8, pp. 987–995, Aug. 2018, ISSN: 2405-5018, 2405-500X. DOI: 10.1016/j.jacep.2018.04.005.

[22] F. H. M. Wittkampf, R. van Es, and K. Neven, "Electroporation and its Relevance for Cardiac Catheter Ablation", *JACC. Clinical electro-*

physiology, vol. 4, no. 8, pp. 977–986, Aug. 2018, ISSN: 2405-5018. DOI: 10.1016/j.jacep.2018.06.005.

[23] M. T. Stewart, D. E. Haines, A. Verma, *et al.*, "Intracardiac pulsed field ablation: Proof of feasibility in a chronic porcine model", *Heart Rhythm*, vol. 16, no. 5, pp. 754–764, May 2019, ISSN: 1556-3871. DOI: 10.1016/j.hrthm.2018.10.030.

[24] D. Miklavčič, S. Čorović, G. Pucihar, and N. Pavšelj, "Importance of tumour coverage by sufficiently high local electric field for effective electrochemotherapy", *European Journal of Cancer Supplements*, Electrochemotherapy, vol. 4, no. 11, pp. 45–51, Nov. 2006, ISSN: 1359-6349. DOI: 10.1016/j.ejcsup.2006.08.006.

[25] L. M. Mir, J. Gehl, G. Sersa, *et al.*, "Standard operating procedures of the electrochemotherapy: Instructions for the use of bleomycin or cisplatin administered either systemically or locally and electric pulses delivered by the CliniporatorTM by means of invasive or non-invasive electrodes", *European Journal of Cancer Supplements*, Electrochemotherapy, vol. 4, no. 11, pp. 14–25, Nov. 2006, ISSN: 1359-6349. DOI: 10.1016/j.ejcsup.2006.08.003.

[26] J. Gehl, G. Sersa, L. W. Matthiessen, *et al.*, "Updated standard operating procedures for electrochemotherapy of cutaneous tumours and skin metastases", *Acta Oncologica (Stockholm, Sweden)*, vol. 57, no. 7, pp. 874–882, Jul. 2018, ISSN: 1651-226X. DOI: 10.1080/0284186X.2018.1454602.

[27] G. Serša, M. Cemazar, and D. Miklavcic, "Antitumor effectiveness of electrochemotherapy with cis-diamminedichloroplatinum(II) in mice", *Cancer Research*, vol. 55, no. 15, pp. 3450–3455, Aug. 1995, ISSN: 0008-5472.

[28] L. M. Mir, "Bases and rationale of the electrochemotherapy", *European Journal of Cancer Supplements*, Electrochemotherapy, vol. 4, no. 11, pp. 38–44, Nov. 2006, ISSN: 1359-6349. DOI: 10.1016/j.ejcsup.2006.08.005.

[29] T. Jarm, M. Cemazar, D. Miklavcic, and G. Sersa, "Antivascular effects of electrochemotherapy: Implications in treatment of bleeding metastases", *Expert Review of Anticancer Therapy*, vol. 10, no. 5, pp. 729–746, May 2010, ISSN: 1744-8328. DOI: 10.1586/era.10.43.

[30] G. Serša, D. Miklavčič, M. Čemažar, J. Belehradek, T. Jarm, and L. M. Mir, "Electrochemotherapy with CDDP on LPB sarcoma: Comparison of the anti-tumor effectiveness in immunocompotent and immunodeficient mice", *Bioelectrochemistry and Bioenergetics*, vol. 43, no. 2, pp. 279–283, Aug. 1997, ISSN: 0302-4598. DOI: 10.1016/S0302-4598(96)05194-X.

[31] D. Miklavčič, G. Pucihar, M. Pavlovec, *et al.*, "The effect of high frequency electric pulses on muscle contractions and antitumor efficiency in vivo for a potential use in clinical electrochemotherapy", *Bioelectrochemistry*, vol. 65, no. 2, pp. 121–128, Feb. 2005, ISSN: 1567-5394. DOI: 10.1016/j.bioelechem.2004.07.004.

[32] A. Zupanic, S. Ribaric, and D. Miklavcic, "Increasing the repetition frequency of electric pulse delivery reduces unpleasant sensations that occur in electrochemotherapy", *Neoplasma*, vol. 54, no. 3, pp. 246–250, 2007, ISSN: 0028-2685.

[33] R. Cannon, S. Ellis, D. Hayes, G. Narayanan, and R. C. G. Martin, "Safety and early efficacy of irreversible electroporation for hepatic tumors in proximity to vital structures", *Journal of Surgical Oncology*, vol. 107, no. 5, pp. 544–549, Apr. 2013, ISSN: 1096-9098. DOI: 10.1002/jso.23280.

[34] B. Mali, V. Gorjup, I. Edhemovic, *et al.*, "Electrochemotherapy of colorectal liver metastases - an observational study of its effects on the electrocardiogram", *BioMedical Engineering OnLine*, vol. 14, no. 3, S5, Aug. 2015, ISSN: 1475-925X. DOI: 10.1186/1475-925X-14-S3-S5.

[35] M. Linnert, H. K. Iversen, and J. Gehl, "Multiple brain metastases - current management and perspectives for treatment with electrochemotherapy", *Radiology and Oncology*, vol. 46, no. 4, pp. 271–278, Nov. 2012, ISSN: 1318-2099. DOI: 10.2478/v10019-012-0042-y.

[36] D. Miklavčič, G. Serša, E. Brecelj, *et al.*, "Electrochemotherapy: Technological advancements for efficient electroporation-based treatment of internal tumors", *Medical & Biological Engineering & Computing*, vol. 50, no. 12, pp. 1213–1225, Dec. 2012, ISSN: 1741-0444. DOI: 10.1007/s11517-012-0991-8.

[37] L. Tarantino, G. Busto, A. Nasto, *et al.*, "Percutaneous electrochemotherapy in the treatment of portal vein tumor thrombosis at hepatic hilum in patients with hepatocellular carcinoma in cirrhosis: A feasibility study", *World Journal of Gastroenterology*, vol. 23, no. 5, pp. 906–918, Feb. 2017, ISSN: 1007-9327. DOI: 10.3748/wjg.v23.i5.906.

[38] M. Djokic, M. Cemazar, P. Popovic, *et al.*, "Electrochemotherapy as treatment option for hepatocellular carcinoma, a prospective pilot study", *European Journal of Surgical Oncology: The Journal of the European Society of Surgical Oncology and the British Association of Surgical Oncology*, vol. 44, no. 5, pp. 651–657, May 2018, ISSN: 1532-2157. DOI: 10.1016/j.ejso.2018.01.090.

[39] M. Djokic, M. Cemazar, M. Bosnjak, *et al.*, "A Prospective Phase II Study Evaluating Intraoperative Electrochemotherapy of Hepatocellular Carcinoma", *Cancers*, vol. 12, no. 12, E3778, Dec. 2020, ISSN: 2072-6694. DOI: 10.3390/cancers12123778.

[40] L. G. Campana, I. Edhemovic, D. Soden, *et al.*, "Electrochemotherapy - Emerging applications technical advances, new indications, combined approaches, and multi-institutional collaboration", *European Journal of Surgical Oncology: The Journal of the European Society of Surgical Oncology and the British Association of Surgical Oncology*, vol. 45, no. 2, pp. 92–102, Feb. 2019, ISSN: 1532-2157. DOI: 10.1016/j.ejso.2018.11.023.

[41] F. H. Cornelis, M. Ben Ammar, M. Nouri-Neuville, *et al.*, "Percutaneous Image-Guided Electrochemotherapy of Spine Metastases: Initial Experience", *Cardiovascular and Interventional Radiology*, vol. 42, no. 12, pp. 1806–1809, Dec. 2019, ISSN: 1432-086X. DOI: 10.1007/s00270-019-02316-4.

[42] H. Falk Hansen, M. Bourke, T. Stigaard, *et al.*, "Electrochemotherapy for colorectal cancer using endoscopic electroporation: A phase 1 clinical study", *Endoscopy International Open*, vol. 8, no. 2, E124–E132, Feb. 2020, ISSN: 2364-3722. DOI: 10.1055/a-1027-6735. (visited on 12/29/2022).

[43] P. A. Garcia, R. V. Davalos, and D. Miklavcic, "A numerical investigation of the electric and thermal cell kill distributions in electroporation-based therapies in tissue", *PloS One*, vol. 9, no. 8, e103083, 2014, ISSN: 1932-6203. DOI: 10.1371/journal.pone.0103083.

[44] E. Maor, A. Ivorra, J. Leor, and B. Rubinsky, "The effect of irreversible electroporation on blood vessels", *Technology in Cancer Research & Treatment*, vol. 6, no. 4, pp. 307–312, Aug. 2007, ISSN: 1533-0346. DOI: 10.1177/153303460700600407.

[45] O. Sutter, J. Calvo, G. N'Kontchou, *et al.*, "Safety and Efficacy of Irreversible Electroporation for the Treatment of Hepatocellular Carcinoma Not Amenable to Thermal Ablation Techniques: A Retrospective Single-Center Case Series", *Radiology*, vol. 284, no. 3, pp. 877–886, Apr. 2017, ISSN: 0033-8419. DOI: 10.1148/radiol.2017161413.

[46] M. B. Sano, R. E. Neal, P. A. Garcia, D. Gerber, J. Robertson, and R. V. Davalos, "Towards the creation of decellularized organ constructs using irreversible electroporation and active mechanical perfusion", *BioMedical Engineering OnLine*, vol. 9, p. 83, Dec. 2010, ISSN: 1475-925X. DOI: 10.1186/1475-925X-9-83.

[47] C. B. Arena, M. B. Sano, J. H. Rossmeisl, *et al.*, "High-frequency irreversible electroporation (H-FIRE) for non-thermal ablation without muscle contraction", *Biomedical Engineering Online*, vol. 10, p. 102, Nov. 2011, ISSN: 1475-925X. DOI: 10.1186/1475-925X-10-102.

[48] V. M. Ringel-Scaia, N. Beitel-White, M. F. Lorenzo, *et al.*, "High-frequency irreversible electroporation is an effective tumor ablation strategy that induces immunologic cell death and promotes systemic anti-tumor immunity", *EBioMedicine*, vol. 44, pp. 112–125, Jun. 2019, ISSN: 2352-3964. DOI: 10.1016/j.ebiom.2019.05.036.

[49] C. Yao, S. Dong, Y. Zhao, *et al.*, "Bipolar Microsecond Pulses and Insulated Needle Electrodes for Reducing Muscle Contractions During Irreversible Electroporation", *IEEE transactions on bio-medical engineering*, vol. 64, no. 12, pp. 2924–2937, Dec. 2017, ISSN: 1558-2531. DOI: 10.1109/TBME.2017.2690624.

[50] A. Cvetkoska, A. Maček-Lebar, P. Trdina, D. Miklavčič, and M. Reberšek, "Muscle contractions and pain sensation accompanying high-frequency electroporation pulses", *Scientific Reports*, vol. 12, 1 2022, ISSN: 2045-2322. DOI: 10.1038/s41598-022-12112-9.

[51] E. Maor, A. Sugrue, C. Witt, *et al.*, "Pulsed electric fields for cardiac ablation and beyond: A state-of-the-art review", *Heart Rhythm*, vol. 16, no. 7, pp. 1112–1120, Jul. 2019, ISSN: 1556-3871. DOI: 10.1016/j.hrthm.2019.01.012.

[52] R. Heller and L. C. Heller, "Chapter Eight - Gene Electrotransfer Clinical Trials", in *Advances in Genetics*, ser. Nonviral Vectors for Gene Therapy, L. Huang, D. Liu, and E. Wagner, Eds., vol. 89, Academic Press, Jan. 2015, pp. 235–262. DOI: 10.1016/bs.adgen.2014.10.006.

[53] U. Lampreht Tratar, L. Loiacono, M. Cemazar, *et al.*, "Gene Electrotransfer of Plasmid-Encoding IL-12 Recruits the M1 Macrophages and Antigen-Presenting Cells Inducing the Eradication of Aggressive B16F10 Murine Melanoma", *Mediators of Inflammation*, vol. 2017, e5285890, May 2017, ISSN: 0962-9351. DOI: 10.1155/2017/5285890.

[54] T. Potočnik, A. Maček Lebar, Š. Kos, *et al.*, "Effect of experimental electrical and biological parameters on gene transfer by electroporation: A systematic review and meta-analysis", *Pharmaceutics*, vol. 14, no. 12, 2022, ISSN: 1999-4923. DOI: 10.3390/pharmaceutics14122700.

[55] T. Potočnik, S. Sachdev, T. Polajžer, A. Maček Lebar, and D. Miklavčič, "Efficient gene transfection by electroporation — in vitro and in silico study of pulse parameters", *Applied Sciences*, vol. 12, no. 16, 2022, ISSN: 2076-3417. DOI: 10.3390/app12168237.

[56] J. H. Rossmeisl, P. A. Garcia, T. E. Pancotto, *et al.*, "Safety and feasibility of the NanoKnife system for irreversible electroporation ablative treatment of canine spontaneous intracranial gliomas", *Journal of Neurosurgery*, vol. 123, no. 4, pp. 1008–1025, Oct. 2015, ISSN: 1933-0693. DOI: 10.3171/2014.12.JNS141768.

[57] P. A. Garcia, B. Kos, J. H. Rossmeisl, D. Pavliha, D. Miklavčič, and R. V. Davalos, "Predictive therapeutic planning for irreversible electroporation treatment of spontaneous malignant glioma", *Medical Physics*, vol. 44, no. 9, pp. 4968–4980, Jun. 2017, ISSN: 2473-4209. DOI: 10.1002/mp.12401.

[58] O. Gallinato, B. D. de Senneville, O. Seror, and C. Poignard, "Numerical workflow of irreversible electroporation for deep-seated tumor", *Physics*

in Medicine and Biology, vol. 64, no. 5, p. 055 016, Mar. 2019, ISSN: 1361-6560. DOI: 10.1088/1361-6560/ab00c4.

[59] D. Miklavčič, M. Snoj, A. Županič, *et al.*, "Towards treatment planning and treatment of deep-seated solid tumors by electrochemotherapy", *BioMedical Engineering OnLine*, vol. 9, p. 10, Feb. 2010, ISSN: 1475-925X. DOI: 10.1186/1475-925X-9-10.

[60] A. Županič, B. Kos, and D. Miklavčič, "Treatment planning of electroporation-based medical interventions: Electrochemotherapy, gene electrotransfer and irreversible electroporation", *Physics in Medicine and Biology*, vol. 57, no. 17, pp. 5425–5440, Sep. 2012, ISSN: 1361-6560. DOI: 10.1088/0031-9155/57/17/5425.

[61] B. Kos, "Treatment Planning for Electrochemotherapy and Irreversible Electroporation of Deep-Seated Tumors", in *Handbook of Electroporation*, D. Miklavčič, Ed., Cham: Springer International Publishing, 2017, pp. 1001–1017, ISBN: 978-3-319-32886-7. DOI: 10.1007/978-3-319-32886-7_2.

[62] D. Pavliha, B. Kos, M. Marčan, A. Zupanič, G. Serša, and D. Miklavčič, "Planning of electroporation-based treatments using Web-based treatment-planning software", *The Journal of Membrane Biology*, vol. 246, no. 11, pp. 833–842, Nov. 2013, ISSN: 1432-1424. DOI: 10.1007/s00232-013-9567-2.

[63] M. Marčan, D. Pavliha, B. Kos, T. Forjanič, and D. Miklavčič, "Web-based tool for visualization of electric field distribution in deep-seated body structures and planning of electroporation-based treatments", *Biomedical Engineering Online*, vol. 14 Suppl 3, S4, 2015, ISSN: 1475-925X. DOI: 10.1186/1475-925X-14-S3-S4.

[64] E. Perera-Bel, K. N. Aycock, Z. S. Salameh, *et al.*, "Piret — a platform for treatment planning in electroporation-based therapies", *IEEE Transactions on Biomedical Engineering*, pp. 1–9, 2022. DOI: 10.1109/TBME.2022.3232038.

[65] A. Grošelj, B. Kos, M. Čemažar, *et al.*, "Coupling treatment planning with navigation system: A new technological approach in treatment of head and neck tumors by electrochemotherapy", *Biomedical Engineering*

Online, vol. 14 Suppl 3, S2, 2015, ISSN: 1475-925X. DOI: 10.1186/1475-925X-14-S3-S2.

[66] I. Fuhrmann, U. Probst, P. Wiggermann, and L. Beyer, "Navigation Systems for Treatment Planning and Execution of Percutaneous Irreversible Electroporation", *Technology in Cancer Research & Treatment*, vol. 17, p. 1 533 033 818 791 792, Jan. 2018, ISSN: 1533-0338. DOI: 10.1177/1533033818791792.

[67] L. P. Beyer, B. Pregler, K. Michalik, *et al.*, "Evaluation of a robotic system for irreversible electroporation (IRE) of malignant liver tumors: Initial results", *International Journal of Computer Assisted Radiology and Surgery*, vol. 12, no. 5, pp. 803–809, May 2017, ISSN: 1861-6429. DOI: 10.1007/s11548-016-1485-1.

[68] O. O. Adeyanju, H. M. Al-Angari, and A. V. Sahakian, "The optimization of needle electrode number and placement for irreversible electroporation of hepatocellular carcinoma", *Radiology and Oncology*, vol. 46, no. 2, pp. 126–135, Apr. 2012, ISSN: 1318-2099. DOI: 10.2478/v10019-012-0026-y.

[69] A. Županič, S. Čorović, and D. Miklavčič, "Optimization of electrode position and electric pulse amplitude in electrochemotherapy", *Radiology and Oncology*, vol. 42, no. 2, pp. 93–101, Jun. 2008.

[70] D. Šel, D. Cukjati, D. Batiuskaite, T. Slivnik, L. M. Mir, and D. Miklavčič, "Sequential finite element model of tissue electropermeabilization", *IEEE transactions on bio-medical engineering*, vol. 52, no. 5, pp. 816–827, May 2005, ISSN: 0018-9294. DOI: 10.1109/TBME.2005.845212.

[71] J. F. Edd and R. V. Davalos, "Mathematical modeling of irreversible electroporation for treatment planning", *Technology in Cancer Research & Treatment*, vol. 6, no. 4, pp. 275–286, Aug. 2007, ISSN: 1533-0346. DOI: 10.1177/153303460700600403.

[72] S. Čorović, A. Županič, and D. Miklavčič, "Numerical Modeling and Optimization of Electric Field Distribution in Subcutaneous Tumor Treated With Electrochemotherapy Using Needle Electrodes", *IEEE Transactions on Plasma Science*, vol. 36, no. 4, pp. 1665–1672, Aug. 2008, ISSN: 0093-3813. DOI: 10.1109/TPS.2008.2000996.

[73] D. Cukjati, D. Batiuskaite, F. André, D. Miklavcic, and L. M. Mir, "Real time electroporation control for accurate and safe in vivo non-viral gene therapy", *Bioelectrochemistry (Amsterdam, Netherlands)*, vol. 70, no. 2, pp. 501–507, May 2007, ISSN: 1567-5394. DOI: 10.1016/j.bioelechem.2006.11.001.

[74] A. Ivorra, B. Al-Sakere, B. Rubinsky, and L. M. Mir, "In vivo electrical conductivity measurements during and after tumor electroporation: Conductivity changes reflect the treatment outcome", *Physics in Medicine & Biology*, vol. 54, no. 19, p. 5949, 2009, ISSN: 0031-9155. DOI: 10.1088/0031-9155/54/19/019.

[75] R. E. Neal, P. A. Garcia, J. L. Robertson, and R. V. Davalos, "Experimental characterization and numerical modeling of tissue electrical conductivity during pulsed electric fields for irreversible electroporation treatment planning", *IEEE transactions on bio-medical engineering*, vol. 59, no. 4, pp. 1076–1085, Apr. 2012, ISSN: 1558-2531. DOI: 10.1109/TBME.2012.2182994.

[76] N. Beitel-White, S. Bhonsle, R. C. G. Martin, and R. V. Davalos, "Electrical Characterization of Human Biological Tissue for Irreversible Electroporation Treatments", *Conference proceedings: ... Annual International Conference of the IEEE Engineering in Medicine and Biology Society. IEEE Engineering in Medicine and Biology Society. Annual Conference*, vol. 2018, pp. 4170–4173, Jul. 2018, ISSN: 1557-170X. DOI: 10.1109/EMBC.2018.8513341.

[77] Y. Zhao, S. Zheng, N. Beitel-White, H. Liu, C. Yao, and R. V. Davalos, "Development of a Multi-Pulse Conductivity Model for Liver Tissue Treated With Pulsed Electric Fields", *Frontiers in Bioengineering and Biotechnology*, vol. 8, 2020, ISSN: 2296-4185. DOI: 10.3389/fbioe.2020.00396.

[78] N. Pavšelj, Z. Bregar, D. Cukjati, D. Batiuskaite, L. M. Mir, and D. Miklavčič, "The course of tissue permeabilization studied on a mathematical model of a subcutaneous tumor in small animals", *IEEE Transactions on Biomedical Engineering*, vol. 52, no. 8, pp. 1373–1381, Aug. 2005, ISSN: 0018-9294. DOI: 10.1109/TBME.2005.851524.

[79] S. Corovic, I. Lackovic, P. Sustaric, T. Sustar, T. Rodic, and D. Miklavcic, "Modeling of electric field distribution in tissues during electroporation", *Biomedical Engineering Online*, vol. 12, p. 16, Feb. 2013, ISSN: 1475-925X. DOI: 10.1186/1475-925X-12-16.

[80] H. Cindrič, B. Kos, and D. Miklavčič, "Electrodes and electric field distribution in clinical practice", in *Electroporation in Veterinary Oncology Practice: Electrochemotherapy and Gene Electrotransfer for Immunotherapy*, J. A. Impellizeri, Ed. Cham: Springer International Publishing, 2021, pp. 21–59, ISBN: 978-3-030-80668-2. DOI: 10.1007/978-3-030-80668-2_2.

[81] I. Lacković, R. Magjarević, and D. Miklavčič, "Three-dimensional Finite-element Analysis of Joule Heating in Electrochemotherapy and in vivo Gene Electrotransfer", *IEEE Transactions on Dielectrics and Electrical Insulation*, vol. 16, no. 5, pp. 1338–1347, Oct. 2009, ISSN: 1070-9878. DOI: 10.1109/TDEI.2009.5293947.

[82] R. V. Davalos, S. Bhonsle, and R. E. Neal, "Implications and considerations of thermal effects when applying irreversible electroporation tissue ablation therapy", *The Prostate*, vol. 75, no. 10, pp. 1114–1118, Jul. 2015, ISSN: 1097-0045. DOI: 10.1002/pros.22986.

[83] W. van den Bos, H. J. Scheffer, J. A. Vogel, *et al.*, "Thermal Energy during Irreversible Electroporation and the Influence of Different Ablation Parameters", *Journal of vascular and interventional radiology: JVIR*, vol. 27, no. 3, pp. 433–443, Mar. 2016, ISSN: 1535-7732. DOI: 10.1016/j.jvir.2015.10.020.

[84] J. Langus, M. Kranjc, B. Kos, T. Šuštar, and D. Miklavčič, "Dynamic finite-element model for efficient modelling of electric currents in electroporated tissue", *Scientific Reports*, vol. 6, no. 1, pp. 1–11, May 2016, ISSN: 2045-2322. DOI: 10.1038/srep26409.

[85] M. Pintar, J. Langus, I. Edhemović, *et al.*, "Time-Dependent Finite Element Analysis of In Vivo Electrochemotherapy Treatment", *Technology in Cancer Research & Treatment*, vol. 17, p. 1 533 033 818 790 510, Jan. 2018, ISSN: 1533-0338. DOI: 10.1177/1533033818790510.

[86] D. Voyer, A. Silve, L. M. Mir, R. Scorretti, and C. Poignard, "Dynamical modeling of tissue electroporation", *Bioelectrochemistry*, vol. 119, pp. 98–110, Feb. 2018, ISSN: 1567-5394. DOI: 10.1016/j.bioelechem.2017.08.007.

[87] H. H. Pennes, "Analysis of Tissue and Arterial Blood Temperatures in the Resting Human Forearm", *Journal of Applied Physiology*, vol. 85, no. 2, pp. 93–122, Aug. 1948, ISSN: 8750-7587. DOI: 10.1152/jappl.1948.1.2.93.

[88] P. Agnass, E. van Veldhuisen, M. J. C. van Gemert, *et al.*, "Mathematical modeling of the thermal effects of irreversible electroporation for in vitro, in vivo, and clinical use: A systematic review", *International Journal of Hyperthermia: The Official Journal of European Society for Hyperthermic Oncology, North American Hyperthermia Group*, vol. 37, no. 1, pp. 486–505, 2020, ISSN: 1464-5157. DOI: 10.1080/02656736.2020.1753828.

[89] C. Rossmanna and D. Haemmerich, "Review of temperature dependence of thermal properties, dielectric properties, and perfusion of biological tissues at hyperthermic and ablation temperatures", *Critical Reviews in Biomedical Engineering*, vol. 42, no. 6, pp. 467–492, 2014, ISSN: 0278-940X.

[90] M. Trujillo and E. Berjano, "Review of the mathematical functions used to model the temperature dependence of electrical and thermal conductivities of biological tissue in radiofrequency ablation", *International Journal of Hyperthermia: The Official Journal of European Society for Hyperthermic Oncology, North American Hyperthermia Group*, vol. 29, no. 6, pp. 590–597, Sep. 2013, ISSN: 1464-5157. DOI: 10.3109/02656736.2013.807438.

[91] P. A. Garcia, J. H. Rossmeisl, R. E. Neal, T. L. Ellis, and R. V. Davalos, "A Parametric Study Delineating Irreversible Electroporation from Thermal Damage Based on a Minimally Invasive Intracranial Procedure", *BioMedical Engineering OnLine*, vol. 10, p. 34, Apr. 2011, ISSN: 1475-925X. DOI: 10.1186/1475-925X-10-34.

[92] M. Peleg, "A model of microbial survival after exposure to pulsed electric fields", *Journal of the Science of Food and Agriculture*, vol. 67, no. 1, pp. 93–99, 1995, ISSN: 1097-0010. DOI: 10.1002/jsfa.2740670115.

[93] A. Golberg and B. Rubinsky, "A statistical model for multidimensional irreversible electroporation cell death in tissue", *BioMedical Engineering OnLine*, vol. 9, p. 13, Feb. 2010, ISSN: 1475-925X. DOI: 10.1186/1475-925X-9-13.

[94] J. Dermol and D. Miklavčič, "Mathematical Models Describing Chinese Hamster Ovary Cell Death Due to Electroporation In Vitro", *The Journal of Membrane Biology*, vol. 248, no. 5, pp. 865–881, Oct. 2015, ISSN: 1432-1424. DOI: 10.1007/s00232-015-9825-6.

[95] S. Sharabi, B. Kos, D. Last, *et al.*, "A statistical model describing combined irreversible electroporation and electroporation-induced blood-brain barrier disruption", *Radiology and Oncology*, vol. 50, no. 1, pp. 28–38, 2016, ISSN: 1581-3207. DOI: 10.1515/raon-2016-0009.

[96] H. Cindrič, P. Mariappan, L. Beyer, *et al.*, "Retrospective Study for Validation and Improvement of Numerical Treatment Planning of Irreversible Electroporation Ablation for Treatment of Liver Tumors", *IEEE Transactions on Biomedical Engineering*, vol. 68, no. 12, pp. 3513–3524, Dec. 2021, ISSN: 1558-2531. DOI: 10.1109/TBME.2021.3075772.

[97] H. Cindric, G. Gasljevic, I. Edhemovic, *et al.*, "Numerical mesoscale tissue model of electrochemotherapy in liver based on histological findings", *Scientific Reports*, vol. 12, no. 1, p. 6476, Apr. 2022, ISSN: 2045-2322. DOI: 10.1038/s41598-022-10426-2.

[98] J. Zmuc, G. Gasljevic, G. Sersa, *et al.*, "Large Liver Blood Vessels and Bile Ducts Are Not Damaged by Electrochemotherapy with Bleomycin in Pigs", *Scientific Reports*, vol. 9, no. 1, p. 3649, Mar. 2019, ISSN: 2045-2322. DOI: 10.1038/s41598-019-40395-y.

[99] F. H. Cornelis, H. Cindrič, B. Kos, *et al.*, "Peri-tumoral Metallic Implants Reduce the Efficacy of Irreversible Electroporation for the Ablation of Colorectal Liver Metastases", *CardioVascular and Interventional Radiology*, Aug. 2019, ISSN: 1432-086X. DOI: 10.1007/s00270-019-02300-y.

[100] T. Jarm, T. Krmac, R. Magjarevic, B. Kos, H. Cindric, and D. Miklavcic, "Investigation of safety for electrochemotherapy and irreversible electroporation ablation therapies in patients with cardiac pacemakers", *BioMedical*

Engineering OnLine, vol. 19, no. 1, p. 85, Nov. 2020, ISSN: 1475-925X. DOI: 10.1186/s12938-020-00827-7.

[101] H. Cindrič, B. Kos, G. Tedesco, M. Cadossi, A. Gasbarrini, and D. Miklavčič, "Electrochemotherapy of Spinal Metastases Using Transpedicular Approach—A Numerical Feasibility Study", *Technology in Cancer Research & Treatment*, vol. 17, p. 1 533 034 618 770 253, Jan. 2018, ISSN: 1533-0346. DOI: 10.1177/1533034618770253.

[102] H. Cindrič, D. Miklavčič, F. H. Cornelis, and B. Kos, "Optimization of transpedicular electrode insertion for electroporation-based treatments of vertebral tumors", *Cancers*, vol. 14, 21 2022, ISSN: 2072-6694. DOI: 10.3390/cancers14215412.

[103] B. Kos, P. Voigt, D. Miklavcic, and M. Moche, "Careful treatment planning enables safe ablation of liver tumors adjacent to major blood vessels by percutaneous irreversible electroporation (IRE)", *Radiology and Oncology*, vol. 49, no. 3, pp. 234–241, Sep. 2015, ISSN: 1318-2099. DOI: 10.1515/raon-2015-0031.

[104] B. Kos, A. Županič, T. Kotnik, M. Snoj, G. Serša, and D. Miklavčič, "Robustness of treatment planning for electrochemotherapy of deep-seated tumors", *The Journal of Membrane Biology*, vol. 236, no. 1, pp. 147–153, Jul. 2010, ISSN: 1432-1424. DOI: 10.1007/s00232-010-9274-1.

[105] M. Moche, H. Busse, J. J. Futterer, *et al.*, "Clinical evaluation of in silico planning and real-time simulation of hepatic radiofrequency ablation (ClinicIMPPACT Trial)", *European Radiology*, vol. 30, no. 2, pp. 934–942, Feb. 2020, ISSN: 1432-1084. DOI: 10.1007/s00330-019-06411-5.

[106] R. Qasrawi, L. Silve, F. Burdío, Z. Abdeen, and A. Ivorra, "Anatomically Realistic Simulations of Liver Ablation by Irreversible Electroporation: Impact of Blood Vessels on Ablation Volumes and Undertreatment", *Technology in Cancer Research & Treatment*, vol. 16, no. 6, pp. 783–792, Dec. 2017, ISSN: 1533-0338. DOI: 10.1177/1533034616687477.

[107] M. Marčan, B. Kos, and D. Miklavčič, "Effect of Blood Vessel Segmentation on the Outcome of Electroporation-Based Treatments of Liver Tumors", *PLOS ONE*, vol. 10, no. 5, e0125591, May 2015, ISSN: 1932-6203. DOI: 10.1371/journal.pone.0125591.

[108] R. E. Neal, P. A. Garcia, H. Kavnoudias, *et al.*, "In vivo irreversible electroporation kidney ablation: Experimentally correlated numerical models", *IEEE transactions on bio-medical engineering*, vol. 62, no. 2, pp. 561–569, Feb. 2015, ISSN: 1558-2531. DOI: 10.1109/TBME.2014.2360374.

[109] S. A. Padia, G. E. Johnson, R. S. Yeung, J. O. Park, D. S. Hippe, and M. J. Kogut, "Irreversible Electroporation in Patients with Hepatocellular Carcinoma: Immediate versus Delayed Findings at MR Imaging", *Radiology*, vol. 278, no. 1, pp. 285–294, Jan. 2016, ISSN: 1527-1315. DOI: 10.1148/radiol.2015150031.

[110] A. Barabasch, M. Distelmaier, P. Heil, N. A. Krämer, C. K. Kuhl, and P. Bruners, "Magnetic Resonance Imaging Findings After Percutaneous Irreversible Electroporation of Liver Metastases: A Systematic Longitudinal Study", *Investigative Radiology*, vol. 52, no. 1, p. 23, Jan. 2017. DOI: 10.1097/RLI.0000000000000301.

[111] E. M. Dunki-Jacobs, P. Philips, and R. C. G. Martin, "Evaluation of thermal injury to liver, pancreas and kidney during irreversible electroporation in an in vivo experimental model", *The British Journal of Surgery*, vol. 101, no. 9, pp. 1113–1121, Aug. 2014, ISSN: 1365-2168. DOI: 10.1002/bjs.9536.

[112] T. R. Gowrishankar and J. C. Weaver, "Electrical behavior and pore accumulation in a multicellular model for conventional and supra-electroporation", *Biochemical and Biophysical Research Communications*, vol. 349, no. 2, pp. 643–653, Oct. 2006, ISSN: 0006-291X. DOI: 10.1016/j.bbrc.2006.08.097.

[113] T. Murovec, D. C. Sweeney, E. Latouche, R. V. Davalos, and C. Brosseau, "Modeling of Transmembrane Potential in Realistic Multicellular Structures before Electroporation", *Biophysical Journal*, vol. 111, no. 10, pp. 2286–2295, Nov. 2016, ISSN: 0006-3495. DOI: 10.1016/j.bpj.2016.10.005.

[114] J. Dermol-Černe and D. Miklavčič, "From Cell to Tissue Properties—Modeling Skin Electroporation With Pore and Local Transport Region Formation", *IEEE Transactions on Biomedical Engineering*, vol. 65, no. 2, pp. 458–468, Feb. 2018, ISSN: 1558-2531. DOI: 10.1109/TBME.2017.2773126.

[115] M. Pavlin, V. Leben, and D. Miklavčič, "Electroporation in dense cell suspension—Theoretical and experimental analysis of ion diffusion and cell permeabilization", *Biochimica et Biophysica Acta (BBA) - General Subjects*, vol. 1770, no. 1, pp. 12–23, Jan. 2007, ISSN: 0304-4165. DOI: 10.1016/j.bbagen.2006.06.014.

[116] G. Pucihar, D. Miklavcic, and T. Kotnik, "A time-dependent numerical model of transmembrane voltage inducement and electroporation of irregularly shaped cells", *IEEE transactions on bio-medical engineering*, vol. 56, no. 5, pp. 1491–1501, May 2009, ISSN: 1558-2531. DOI: 10.1109/TBME.2009.2014244.

[117] L. G. Campana, M. Bullo, P. Di Barba, *et al.*, "Effect of Tissue Inhomogeneity in Soft Tissue Sarcomas: From Real Cases to Numerical and Experimental Models", *Technology in Cancer Research & Treatment*, vol. 17, p. 1 533 033 818 789 693, Jan. 2018, ISSN: 1533-0346. DOI: 10.1177/1533033818789693.

[118] A. Denzi, L. Strigari, F. Di Filippo, *et al.*, "Modeling the positioning of single needle electrodes for the treatment of breast cancer in a clinical case", *BioMedical Engineering OnLine*, vol. 14, no. Suppl 3, S1, Aug. 2015, ISSN: 1475-925X. DOI: 10.1186/1475-925X-14-S3-S1.

[119] A. Golberg, B. G. Bruinsma, B. E. Uygun, and M. L. Yarmush, "Tissue heterogeneity in structure and conductivity contribute to cell survival during irreversible electroporation ablation by "electric field sinks"", *Scientific Reports*, vol. 5, no. 1, p. 8485, Feb. 2015, ISSN: 2045-2322. DOI: 10.1038/srep08485.

[120] D. Miklavčič, D. Šemrov, H. Mekid, and L. M. Mir, "A validated model of in vivo electric field distribution in tissues for electrochemotherapy and for DNA electrotransfer for gene therapy", *Biochimica Et Biophysica Acta*, vol. 1523, no. 1, pp. 73–83, Sep. 2000, ISSN: 0006-3002.

[121] *Risk Information*, http://www.angiodynamics.com/about-us/risk-information/, [Date accessed: February 2023].

[122] C. W. van der Geld, R. T. van Gaalen, H. J. Scheffer, *et al.*, "Maxwell's equations explain why irreversible electroporation will not heat up a metal stent", *International Journal of Heat and Mass Transfer*, vol. 169,

p. 120 962, 2021, ISSN: 0017-9310. DOI: https://doi.org/10.1016/j.ijheatmasstransfer.2021.120962.

[123] R. E. Neal, R. L. Smith, H. Kavnoudias, *et al.*, "The effects of metallic implants on electroporation therapies: Feasibility of irreversible electroporation for brachytherapy salvage", *Cardiovascular and Interventional Radiology*, vol. 36, no. 6, pp. 1638–1645, Dec. 2013, ISSN: 1432-086X. DOI: 10.1007/s00270-013-0704-1.

[124] E. Ben-David, M. Ahmed, M. Faroja, *et al.*, "Irreversible electroporation: Treatment effect is susceptible to local environment and tissue properties", *Radiology*, vol. 269, no. 3, pp. 738–747, Dec. 2013, ISSN: 1527-1315. DOI: 10.1148/radiol.13122590.

[125] H. J. Scheffer, J. A. Vogel, W. van den Bos, *et al.*, "The Influence of a Metal Stent on the Distribution of Thermal Energy during Irreversible Electroporation", *PloS One*, vol. 11, no. 2, e0148457, 2016, ISSN: 1932-6203. DOI: 10.1371/journal.pone.0148457.

[126] *Frequently Asked Questions — IGEA*, https://www.igea.it/en/oncology/information-clinicians/frequently-asked-questions, [Date accessed: August 2019].

[127] M. Fini, F. Salamanna, A. Parrilli, *et al.*, "Electrochemotherapy is effective in the treatment of rat bone metastases", *Clinical & Experimental Metastasis*, vol. 30, no. 8, pp. 1033–1045, Dec. 2013, ISSN: 1573-7276. DOI: 10.1007/s10585-013-9601-x.

[128] A. Gasbarrini, W. K. Campos, L. Campanacci, and S. Boriani, "Electrochemotherapy to Metastatic Spinal Melanoma: A Novel Treatment of Spinal Metastasis?", *Spine*, vol. 40, no. 24, E1340–1346, Dec. 2015, ISSN: 1528-1159. DOI: 10.1097/BRS.0000000000001125.

[129] M. Tschon, F. Salamanna, M. Ronchetti, *et al.*, "Feasibility of Electroporation in Bone and in the Surrounding Clinically Relevant Structures: A Preclinical Investigation", *Technology in Cancer Research & Treatment*, vol. 15, no. 6, pp. 737–748, Dec. 2016, ISSN: 1533-0338. DOI: 10.1177/1533034615604454.

[130] G. Bianchi, L. Campanacci, M. Ronchetti, and D. Donati, "Electrochemotherapy in the Treatment of Bone Metastases: A Phase II Trial", *World Journal of Surgery*, vol. 40, no. 12, pp. 3088–3094, 2016, ISSN: 0364-2313. DOI: 10.1007/s00268-016-3627-6.

[131] M. Fini, M. Tschon, M. Ronchetti, *et al.*, "Ablation of bone cells by electroporation", *The Journal of Bone and Joint Surgery. British Volume*, vol. 92, no. 11, pp. 1614–1620, Nov. 2010, ISSN: 2044-5377. DOI: 10.1302/0301-620X.92B11.24664.

[132] Y. Song, J. Zheng, M. Yan, *et al.*, "The Effect of Irreversible Electroporation on the Femur: Experimental Study in a Rabbit Model", *Scientific Reports*, vol. 5, p. 18 187, Dec. 2015, ISSN: 2045-2322. DOI: 10.1038/srep18187.

[133] D. Knez, J. Mohar, R. J. Cirman, B. Likar, F. Pernuš, and T. Vrtovec, "Determination of the pedicle screw size and trajectory in CT images of thoracic spinal deformities: a comparison between manual and computer-assisted preoperative planning", *Slovenian Medical Journal*, vol. 85, no. 11-12, Jan. 2017, ISSN: 1581-0224.

[134] A. P. Keszei, B. Berkels, and T. M. Deserno, "Survey of Non-Rigid Registration Tools in Medicine", *Journal of Digital Imaging*, vol. 30, no. 1, pp. 102–116, Feb. 2017, ISSN: 0897-1889. DOI: 10.1007/s10278-016-9915-8.

[135] N.-F. Tian, Q.-S. Huang, P. Zhou, *et al.*, "Pedicle screw insertion accuracy with different assisted methods: A systematic review and meta-analysis of comparative studies", *European Spine Journal: Official Publication of the European Spine Society, the European Spinal Deformity Society, and the European Section of the Cervical Spine Research Society*, vol. 20, no. 6, pp. 846–859, Jun. 2011, ISSN: 1432-0932. DOI: 10.1007/s00586-010-1577-5.

[136] E. Koktekir, D. Ceylan, N. Tatarli, H. Karabagli, F. Recber, and G. Akdemir, "Accuracy of fluoroscopically-assisted pedicle screw placement: Analysis of 1,218 screws in 198 patients", *The Spine Journal*, vol. 14, no. 8, pp. 1702–1708, Aug. 2014, ISSN: 1529-9430. DOI: 10.1016/j.spinee.2014.03.044.

[137] F. Hecht, "New development in freefem++", *Journal of Numerical Mathematics*, vol. 20, no. 3-4, pp. 251–266, Dec. 2012, ISSN: 1569-3953. DOI: 10.1515/jnum-2012-0013.

Permissions

SPRINGER NATURE LICENSE
TERMS AND CONDITIONS

Feb 03, 2023

This Agreement between University of Ljubljana, Faculty of Electrical Engineering -- Helena Cindrič ("You") and Springer Nature ("Springer Nature") consists of your license details and the terms and conditions provided by Springer Nature and Copyright Clearance Center.

License Number	5481241383259
License date	Feb 03, 2023
Licensed Content Publisher	Springer Nature
Licensed Content Publication	CardioVascular and Interventional Radiology
Licensed Content Title	Peri-tumoral Metallic Implants Reduce the Efficacy of Irreversible Electroporation for the Ablation of Colorectal Liver Metastases
Licensed Content Author	Francois H. Cornelis et al
Licensed Content Date	Aug 5, 2019
Type of Use	Thesis/Dissertation
Requestor type	academic/university or research institute
Format	print and electronic
Portion	full article/chapter
Will you be translating?	no
Circulation/distribution	1 - 29

Author of this Springer Nature content	yes
Title	Numerical modeling and treatment planning for clinical applications of electroporation
Institution name	University of Ljubljana, Faculty of Electrical Engineering
Expected presentation date	Feb 2023
Requestor Location	University of Ljubljana, Faculty of Electrical Engineering Tržaška cesta 25 Ljubljana, Select One 1000 Slovenia Attn: University of Ljubljana, Faculty of Electrical Engineering
Total	0.00 EUR

Terms and Conditions

Springer Nature Customer Service Centre GmbH Terms and Conditions

The following terms and conditions ("Terms and Conditions") together with the terms specified in your [RightsLink] constitute the License ("License") between you as Licensee and Springer Nature Customer Service Centre GmbH as Licensor. By clicking 'accept' and completing the transaction for your use of the material ("Licensed Material"), you confirm your acceptance of and obligation to be bound by these Terms and Conditions.

1. Grant and Scope of License

1. 1. The Licensor grants you a personal, non-exclusive, non-transferable, non-sublicensable, revocable, world-wide License to reproduce, distribute, communicate to the public, make available, broadcast, electronically transmit or create derivative works using the Licensed Material for the purpose(s) specified in your RightsLink Licence Details only. Licenses are granted for the specific use requested in the order and for no other use, subject to these Terms and Conditions. You acknowledge and agree that the rights granted to you under this License do not include the right to modify, edit, translate, include in collective works, or create derivative works of the Licensed Material in whole or in part unless expressly stated in your RightsLink Licence Details. You may use the Licensed Material only as permitted under this Agreement and will not reproduce, distribute, display, perform, or otherwise use or exploit any Licensed Material in any way, in whole or in part, except as expressly permitted by this License.

1. 2. You may only use the Licensed Content in the manner and to the extent permitted by these Terms and Conditions, by your RightsLink Licence Details and by any

applicable laws.

1. 3. A separate license may be required for any additional use of the Licensed Material, e.g. where a license has been purchased for print use only, separate permission must be obtained for electronic re-use. Similarly, a License is only valid in the language selected and does not apply for editions in other languages unless additional translation rights have been granted separately in the License.

1. 4. Any content within the Licensed Material that is owned by third parties is expressly excluded from the License.

1. 5. Rights for additional reuses such as custom editions, computer/mobile applications, film or TV reuses and/or any other derivative rights requests require additional permission and may be subject to an additional fee. Please apply to journalpermissions@springernature.com or bookpermissions@springernature.com for these rights.

2. Reservation of Rights

Licensor reserves all rights not expressly granted to you under this License. You acknowledge and agree that nothing in this License limits or restricts Licensor's rights in or use of the Licensed Material in any way. Neither this License, nor any act, omission, or statement by Licensor or you, conveys any ownership right to you in any Licensed Material, or to any element or portion thereof. As between Licensor and you, Licensor owns and retains all right, title, and interest in and to the Licensed Material subject to the license granted in Section 1.1. Your permission to use the Licensed Material is expressly conditioned on you not impairing Licensor's or the applicable copyright owner's rights in the Licensed Material in any way.

3. Restrictions on use

3. 1. Minor editing privileges are allowed for adaptations for stylistic purposes or formatting purposes provided such alterations do not alter the original meaning or intention of the Licensed Material and the new figure(s) are still accurate and representative of the Licensed Material. Any other changes including but not limited to, cropping, adapting, and/or omitting material that affect the meaning, intention or moral rights of the author(s) are strictly prohibited.

3. 2. You must not use any Licensed Material as part of any design or trademark.

3. 3. Licensed Material may be used in Open Access Publications (OAP), but any such reuse must include a clear acknowledgment of this permission visible at the same time as the figures/tables/illustration or abstract and which must indicate that the Licensed Material is not part of the governing OA license but has been reproduced with permission. This may be indicated according to any standard referencing system but must include at a minimum 'Book/Journal title, Author, Journal Name (if applicable), Volume (if applicable), Publisher, Year, reproduced with permission from SNCSC'.

4. STM Permission Guidelines

4. 1. An alternative scope of license may apply to signatories of the STM Permissions Guidelines ("STM PG") as amended from time to time and made available at https://www.stm-assoc.org/intellectual-property/permissions/permissions-guidelines/.

4. 2. For content reuse requests that qualify for permission under the STM PG, and which may be updated from time to time, the STM PG supersede the terms and conditions contained in this License.

4. 3. If a License has been granted under the STM PG, but the STM PG no longer apply at the time of publication, further permission must be sought from the Rightsholder. Contact journalpermissions@springernature.com or bookpermissions@springernature.com for these rights.

5. Duration of License

5. 1. Unless otherwise indicated on your License, a License is valid from the date of purchase ("License Date") until the end of the relevant period in the below table:

Reuse in a medical communications project	Reuse up to distribution or time period indicated in License
Reuse in a dissertation/thesis	Lifetime of thesis
Reuse in a journal/magazine	Lifetime of journal/magazine
Reuse in a book/textbook	Lifetime of edition
Reuse on a website	1 year unless otherwise specified in the License
Reuse in a presentation/slide kit/poster	Lifetime of presentation/slide kit/poster. Note: publication whether electronic or in print of presentation/slide kit/poster may require further permission.
Reuse in conference proceedings	Lifetime of conference proceedings
Reuse in an annual report	Lifetime of annual report
Reuse in training/CME materials	Reuse up to distribution or time period indicated in License
Reuse in newsmedia	Lifetime of newsmedia
Reuse in coursepack/classroom materials	Reuse up to distribution and/or time period indicated in license

6. Acknowledgement

6. 1. The Licensor's permission must be acknowledged next to the Licensed Material in print. In electronic form, this acknowledgement must be visible at the same time as the figures/tables/illustrations or abstract and must be hyperlinked to the journal/book's homepage.

6. 2. Acknowledgement may be provided according to any standard referencing system and at a minimum should include "Author, Article/Book Title, Journal name/Book imprint, volume, page number, year, Springer Nature".

7. Reuse in a dissertation or thesis

7. 1. Where 'reuse in a dissertation/thesis' has been selected, the following terms apply: Print rights of the Version of Record are provided for; electronic rights for use only on institutional repository as defined by the Sherpa guideline (www.sherpa.ac.uk/romeo/) and only up to what is required by the awarding institution.

7. 2. For theses published under an ISBN or ISSN, separate permission is required. Please contact journalpermissions@springernature.com or bookpermissions@springernature.com for these rights.

7. 3. Authors must properly cite the published manuscript in their thesis according to current citation standards and include the following acknowledgement: '*Reproduced with permission from Springer Nature*'.

8. License Fee

You must pay the fee set forth in the License Agreement (the "License Fees"). All amounts payable by you under this License are exclusive of any sales, use, withholding, value added or similar taxes, government fees or levies or other assessments. Collection and/or remittance of such taxes to the relevant tax authority shall be the responsibility of the party who has the legal obligation to do so.

9. Warranty

9. 1. The Licensor warrants that it has, to the best of its knowledge, the rights to license reuse of the Licensed Material. **You are solely responsible for ensuring that the material you wish to license is original to the Licensor and does not carry the copyright of another entity or third party (as credited in the published version).** If the credit line on any part of the Licensed Material indicates that it was reprinted or adapted with permission from another source, then you should seek additional permission from that source to reuse the material.

9. 2. EXCEPT FOR THE EXPRESS WARRANTY STATED HEREIN AND TO THE EXTENT PERMITTED BY APPLICABLE LAW, LICENSOR PROVIDES THE LICENSED MATERIAL "AS IS" AND MAKES NO OTHER REPRESENTATION OR WARRANTY. LICENSOR EXPRESSLY DISCLAIMS ANY LIABILITY FOR ANY CLAIM ARISING FROM OR OUT OF THE CONTENT, INCLUDING BUT NOT LIMITED TO ANY ERRORS, INACCURACIES, OMISSIONS, OR DEFECTS CONTAINED THEREIN, AND ANY IMPLIED OR EXPRESS WARRANTY AS TO MERCHANTABILITY OR FITNESS FOR A PARTICULAR PURPOSE. IN NO EVENT SHALL LICENSOR BE LIABLE TO YOU OR ANY OTHER PARTY OR ANY OTHER PERSON OR FOR ANY SPECIAL, CONSEQUENTIAL, INCIDENTAL, INDIRECT, PUNITIVE, OR EXEMPLARY DAMAGES, HOWEVER CAUSED, ARISING OUT OF OR IN CONNECTION WITH THE DOWNLOADING, VIEWING OR USE OF THE LICENSED MATERIAL REGARDLESS OF THE FORM OF ACTION, WHETHER FOR BREACH OF CONTRACT, BREACH OF WARRANTY, TORT, NEGLIGENCE, INFRINGEMENT OR OTHERWISE (INCLUDING, WITHOUT LIMITATION, DAMAGES BASED ON LOSS OF PROFITS, DATA, FILES, USE, BUSINESS OPPORTUNITY OR CLAIMS OF THIRD PARTIES), AND WHETHER OR NOT THE PARTY HAS BEEN ADVISED OF THE POSSIBILITY OF SUCH DAMAGES. THIS LIMITATION APPLIES NOTWITHSTANDING ANY FAILURE OF ESSENTIAL PURPOSE OF ANY LIMITED REMEDY PROVIDED HEREIN.

10. Termination and Cancellation

10. 1. The License and all rights granted hereunder will continue until the end of the applicable period shown in Clause 5.1 above. Thereafter, this license will be terminated and all rights granted hereunder will cease.

10. 2. Licensor reserves the right to terminate the License in the event that payment is not received in full or if you breach the terms of this License.

11. General

11. 1. The License and the rights and obligations of the parties hereto shall be construed, interpreted and determined in accordance with the laws of the Federal Republic of Germany without reference to the stipulations of the CISG (United

Nations Convention on Contracts for the International Sale of Goods) or to Germany´s choice-of-law principle.

11. 2. The parties acknowledge and agree that any controversies and disputes arising out of this License shall be decided exclusively by the courts of or having jurisdiction for Heidelberg, Germany, as far as legally permissible.

11. 3. This License is solely for Licensor's and Licensee's benefit. It is not for the benefit of any other person or entity.

Questions? For questions on Copyright Clearance Center accounts or website issues please contact springernaturesupport@copyright.com or +1-855-239-3415 (toll free in the US) or +1-978-646-2777. For questions on Springer Nature licensing please visit https://www.springernature.com/gp/partners/rights-permissions-third-party-distribution

Other Conditions:

Version 1.4 - Dec 2022

Questions? customercare@copyright.com or +1-855-239-3415 (toll free in the US) or +1-978-646-2777.